Swansea University
Prifysgol Abertawe

Understanding the Fundamentals of Chromium-free Pre-treatments

Andrew Christian Mescall

Thesis Submitted to Swansea University in fulfilment of the requirements for the Degree of Doctor of Engineering
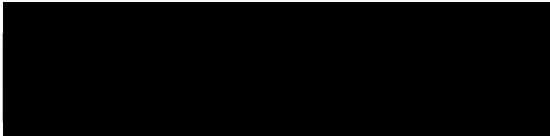
2022

Declaration: This work has not previously been accepted in substance for any degree and is not being concurrently submitted in candidature for any degree.

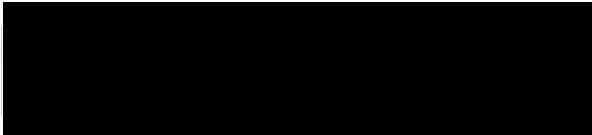Signed ███████████████████████ (candidate)

Date: 16/12/2022

Statement: This thesis is the result of my own investigations, except where otherwise stated. Other sources are acknowledged by footnotes giving explicit references. A bibliography is appended.

Signed ███████████████████████ (candidate)

Date: 16/12/20232

Statement 2: I hereby give consent for my thesis, if accepted, to be available for photocopying and for inter-library loan, and for the title and summary to be made available to outside organisations.

Signed ███████████████████████ (candidate)

Date: 16/12/2022

Abstract

The work described in this thesis sets out to investigate the influence of alkaline cleaning on the surface chemistry and electrochemical corrosion behaviour of commercial galvanised steel (hot-dip galvanised (HDG) and Zn-Al(4.8%) (Galvalloy/ZA) provided by Tata Steel) in aqueous chloride containing solutions and under conditions where the surface is overcoated with a model protective organic coating. Alkaline cleaning is an important stage in the preparation of organically coated steel (OCS) in order to appropriately prepare the surface for subsequent organic coating application. Post-cleaned galvanised steel surfaces are pre-treated using an inorganic conversion coating which provides additional corrosion protection to the surface and allows an improved surface for adhesion of organic coatings. The work here also investigates the influence of alkaline cleaning conditions on the surface chemistry and corrosion protection characteristics of surfaces following the application of a commercial titanium hexafluoride-based pre-treatment. X-ray Photoelectron Spectroscopy (XPS) was employed to determine surface chemistry of HDG, ZA and pre-treated HDG, with Titanium X-ray fluorescence (XRF) used to determine the Ti-weighting of the pre-treatment coating. Electrochemical techniques (potentiodynamic experiments and linear polarisation) were used to investigate the surface behaviour as a function of alkaline cleaning regime, prior to and following pre-treatment. Additionally, the performance of a model organic coating on applied to cleaned surfaces with/without pre-treatment was evaluated through a combination of time-lapse photography and scanning Kelvin Probe (SKP) techniques under atmospheric corrosion conditions. XPS analysis showed that intensive cleaning removed: surface aluminium; decreased ZnO content, and; increased metallic Zn content on both HDG and ZA. Cathodic-going polarisation curves showed that alkaline cleaning of HDG and ZA produced a progressively more reactive surface with both increasing temperature and time of cleaning compared to an uncleaned sample. Anodic polarisation curves exhibited similar behaviour for all cleaning conditions, with limited passive regions present, Corrosion current density values calculated from linear polarisation curves showed a correlation of increased corrosion rate with both cleaning temperature and holding time. Cathodic disbondment investigations on organic coated surfaces showed that increased cleaning intensity led to progressively higher coating failure rates for both HDG and ZA steels. In contrast when a Ti-based surface pre-treatment was present, coating delamination rates were significant lower compared with equivalent cleaned surfaces and there was a progressive decrease in disbondment kinetics with cleaning temperature used prior to pre-treatment. Alkaline cleaned HDG and ZA

specimens exhibited parabolic delamination rate kinetics, whereas linear kinetics were observed using pre-treated HDG samples. The difference is ascribed to the blocking of underfilm electron transfer by the presence of the Ti-based surface layer, making cathodic oxygen reduction rather than cation migration the rate limiting step in the cathodic disbondment process.

Acknowledgements

First, I would like to thank my academic supervisors Prof. Geraint Williams and Prof. Peter Holliman. Geraint was a great source of knowledge and wisdom for all things corrosion and was a supportive constant in organising my project throughout the COVID-19 pandemic, for which he has my everlasting gratitude.

I would like to thank the European Social Fund (ESF), for sponsoring the project alongside my industrial sponsorship from Tata Steel Colours. I would also like to thank my industrial supervisors Dr. Peter Barker, Dr. Digvijay Thakur, and Neil Metherell who were always available to discuss my work and field questions, no matter how trivial or obvious the answer was.

A huge thanks goes to Dr. Chris Griffiths and Dr. Calvin Richards who were always in the office to discuss my work over a cup of coffee, keeping the SKP running and helping to interpret my data. A big thanks goes to Dr. James McGettrick, who trained me up on the XPS and let me loose on a £250,000 piece of equipment, which I may (definitely) have broken….multiple times. A big thanks to all those students/staff based in the PMRC Baglan and the M2A office and labs, who have made coming in to work a genuine pleasure. I doubt I will ever laugh as much in a workplace again.

I want to give a huge thanks to my parents who have supported my every step of the way with their love and support, to my grandmother Mam Chris who claims all credit for my (incorrectly) perceived intelligence, and to my late grandfather Dad John who would always talk about his time as a welder at British Steel in Port Talbot when I chatted about my work and wished he was here to see me submit this body of work.

Finally, my biggest thanks goes to my ever suffering wife-to-be Rachel for being there every step of the way. She has witnessed the anger, tears, frustration, and happiness that comes with conducting research. Hopefully at the time of our wedding she'll be marrying "Dr" Mescall.

"The most exciting phrase to hear in science is not "Eureka" but "that's funny" – Isaac Asimov.

Table of Contents

Table of Figures

Table of Tables.

Chapter 1 – Introduction and Literature Review

The research described in this EngD thesis assesses the influence of alkaline cleaning has on the performance of organically coated hot dip galvanised (HDG) and 4.8%-Al (ZA) steels and investigates the ability of hexaflourotitanate pre-treatment to inhibit cathodic disbondment of hot dip galvanised steel when applied after cleaning and before application of an organic coating. There has been high demand in recent years to find a suitable replacement for hexavalent chromium which was the industrial standard corrosion inhibitor but is now banned through REACH legislation due to it being considered a genotoxic carcinogen. Conversion coatings, or pre-treatments which previously contained hexavalent chrome have now been replaced with hexafluoro-compounds based on titanium or zirconium, which provide a lower toxicity replacement but do lack the performance in corrosion protection achieved using hexavalent chromate. Potentiodynamic techniques are employed to measure the behaviour of cleaned and pre-treated substrates in aggressive electrolytes. A scanning Kelvin probe technique is employed to measure organic coating performance on cleaned and pre-treated surfaces and X-ray photoelectron spectroscopy (XPS) and microwave-plasma atomic emission spectroscopy are employed to monitor in-situ behaviour of steels in alkaline cleaning solution and surface chemistry post-cleaning.

Chapter 1. Chapter 1 consists of a literature review of topics relevant to the subject matter of the programme of research, with principal emphasis on current state of the art in chromate-free pre-treatments.

Chapter 2. Chapter 2 consists of details of the experimental equipment, methodology and techniques used to gather the results presented in this body of research. .

The subsequent chapters investigate the potentiodynamic behaviour and corrosion driven cathodic disbondment performance of HDG and ZA steels after alkaline cleaning and pre-treatment application.

Chapter 3. Chapter 3 investigates how alkaline cleaning parameters influence the surface chemistry and corrosion behaviour of HDG substrates. Alkaline cleaning is used to prepare galvanised steel prior to pre-treatment and organic coating application for use in multi-coating organic paint systems. Varying alkaline cleaning parameters are used on HDG steel and the influence these conditions have on the potentiodynamic response is measured by anodic, cathodic, and linear polarisation. The cathodic disbondment behaviour is measured by scanning Kelvin probe and time-lapse photography. and surface chemistry measured by X-ray photoelectron spectroscopy.

Chapter 4. Chapter 4 investigates how alkaline cleaning parameters influence the surface and corrosion behaviour of ZA substrates. A study using time-lapse photography, SKP, XPS and potentiodynamic techniques to determine the influence alkaline cleaning has on 4.8%-Al steel and how these influences the organic coating performance in comparison to HDG. Experiments are conducted using the Stratmann cell techniques to analyse coating performance. Influence of cleaning on the 4.8%-Al steel surface is analysed using XPS.

Chapter 5. Chapter 5 investigates how the addition of a titanium based conversion coating applied to the surface of alkaline cleaned HDG influences the corrosion behaviour of HDG substrates. The cathodic disbondment of organic coatings using the SKP technique and electrochemical performance of hexaflourotitanate pre-treated HDG after alkaline cleaning at varying intensities are studied. Surface chemistry of the pre-treatment is analysed by XPS and titanium specific XRF.

Chapter 6. Chapter 6 investigates how ageing of titanium based conversion coating applied to the surface of alkaline cleaned HDG influences the corrosion behaviour of HDG substrates. Investigation of the cathodic disbondment behaviour of organic coatings using the

SKP technique and electrochemical performance of hexaflourotitanate pre-treated HDG which has been aged at ambient storage conditions for varying amounts of time after alkaline cleaning at varying temperature. Surface chemistry of the pre-treatment is analysed by XPS and titanium specific XRF.

1.1 Corrosion

Corrosion is deterioration of materials such as polymers and metals due to a chemical interaction between the material and the surrounding environment. In the case of metals, this interaction converts a refined metal into a more stable oxide, sulphide, chloride, or hydroxide, which often resulting in failure of the metal. The term corrosion is generally applied to metal but can also be used for the degradation and failure of other materials, such as plastics, concrete and composites.

The global economic effect of corrosion is very high. This is considering the general effect corrosion would have of construction, infrastructure and transport networks and the implicated costs in repairing or replacing corrosion affected sections of these networks. Findings stated in the "Hoar Report" found that the costs of corrosion on the UK economy was between 2-3% of the GNP (Gross National Product). Which would be approximately £16 billion for the year 2019. [1] For perspective, a 2002 study by NACE (National Association for Corrosion Engineers) put the cost of corrosion in the USA at $276 billion, accounting for inflation, this is over $1 trillion in 2019. [2] Corrosion is also a serious cause of natural resource loss, with 1 tonne of steel being completely converted to rust every 90 seconds in the UK alone. [3,4] This results in the waste of energy and the materials used in steel manufacturing.

Besides the scientific implications of corrosion, it also has extensive social implications, having a considerable impact on human beings and sometimes being the cause of injury or death. An example of this would be the explosion of a sewer in Guadalajara, Spain. This was caused by corrosion of water pipes in the sewage system, resulting in water release into gas pipes causing subsequent corrosion of the gas pipes and gas leakage into the sewer. This explosion killed 252 people, injured a further 1500 and left 15,000 residents homeless. [5]

Most metals can be found naturally as an ore (usually as a metal oxide), as this is their lowest energy state, and thus the most stable form. To extract a metal from its ore, energy needs to

be used to raise the energy of the system to a higher energy state, resulting in a more thermodynamically unstable state in the atmosphere. The second law of thermodynamics states that a spontaneous change occurs with the release of free energy from the system to the surroundings at a constant temperature and pressure. The thermodynamic principal of corrosion is the movement of a metal from a high energy state back to a low energy state, this does not necessarily mean that the metal will be converted back to its ore, but to another low energy state, usually in the form of an oxide. An energy profile, Figure 1.1, can be used to illustrate the free energy changes that occur during corrosion. For the corrosion process to occur the ore must be refined into metal, which can be described as a metastable state, which requires activation energy to occur, represented as $\Delta G^{\neq}$ in Figure 1.1. The change in Gibbs free energy associated with corrosion, represented as ΔG in Figure 1.1, is negative (due to entropy) and is the driving force of corrosion.
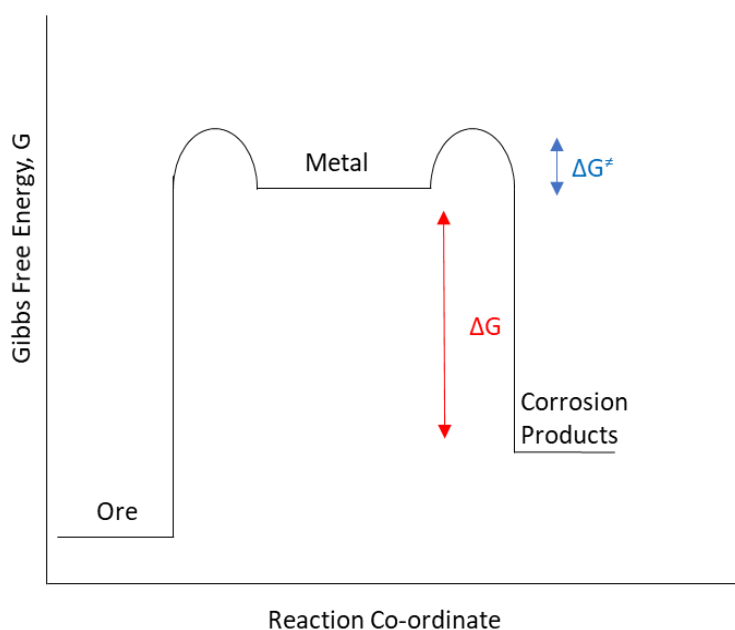
Figure 1.1. The thermodynamic life cycle of a processes metal. [6]

The activation energy barrier $\Delta G^{\neq}$, prevents all metals from spontaneously forming their oxides. A large activation energy barrier will result in a very slow corrosion rate whilst a low activation energy barrier will result in a faster corrosion rate. When water is present the mechanisms of corrosion are such that the activation energy for corrosion is lowered and so corrosion proceeds at a faster rate whilst also providing a conducting pathway for electrons to travel between anode and cathode.

1.1.1 Electrochemistry of corrosion

Aqueous corrosion, or wet corrosion, is referred to as corrosion of a metal that occurs in the presence of water or an aqueous electrolyte. Natural electrolytes are typically a salt solution from rain or seawater. When corrosion occurs, an electrochemical cell is formed on the corrosion sites. This electrochemical cell is formed of four components: an anodic site (where oxidation occurs), a cathodic site (where reduction occurs), an electrolyte and an electrical connection.

The electrical connection between anode and cathode can be achieved via an external circuit or by contact between two dissimilar metals, but typically occurs on the same metal surface. Corrosive behaviour can be separated into two distinct types:

General corrosion is when anode and cathode sites are indistinguishable as distinct areas on the corrosion surface. Anode and cathode surfaces are numerous and can move position as the two reactions occur over time as a result in changing surface and chemical properties.

Localised corrosion is when anodic and cathodic sites are spatially distinct from one another. As the anodic site is focussed in one area, this can cause significant damage in a short space of time.

At anodic sites, an oxidation process called metal dissolution occurs on the metal surface through equation 1.1.

$$M_{(s)} \rightarrow M^{n+}_{(aq)} + ne^- \hspace{5cm} \text{Equation 1.1}$$

The cathodic reaction subsequently balances the anodic reaction. The electrons released during metal dissolution are transported through the metal substrate (the electrical connection) and are used in the cathodic reaction. The cathodic reaction can vary depending on the conditions of the electrolyte such as pH and the concentration of dissolved oxygen.

Oxygen reduction occurs when local conditions are at a neutral pH (7);

$$2H_2O_{(l)} + O_{2\,(g)} + 4e^- \rightleftharpoons 4OH^- \hspace{4cm} \text{Equation 1.2}$$

When the pH of the electrolyte is lower than neutral then hydrogen evolution will occur.

$$2H^+_{(aq)} + 2e^- \rightleftharpoons H_{2\,(g)} \hspace{5cm} \text{Equation 1.3}$$

1.1.2 Corrosion thermodynamics

The thermodynamics of a corrosion reaction can be understood using a Pourbaix diagram which can be seen in Figure 1.2. A Pourbaix diagram shows the most stable corrosion species for a metal with regards to the potential and pH of the system. In a Pourbaix diagram there are three conditions that can be assigned to a metal; corroding, immune, or passive. [7,8] The metal will be considered to be corroding if the concentration of the ions in the solutions is $>10^{-6}$ M (Moles) and will be considered immune if the ion concentration is $<10^{-6}$ M. Passivity is a more complex process which does not only consider the ion concentration. This is a result of the insoluble corrosion product that forms on the metal surface as result of corrosion reactions which prevents electrolytes from reacting with the metal surface, which considerably slows the rate of corrosion.[7] Metal corrosion may contain complex reactions and is highly dependent on temperature, pH and the electrolyte composition.
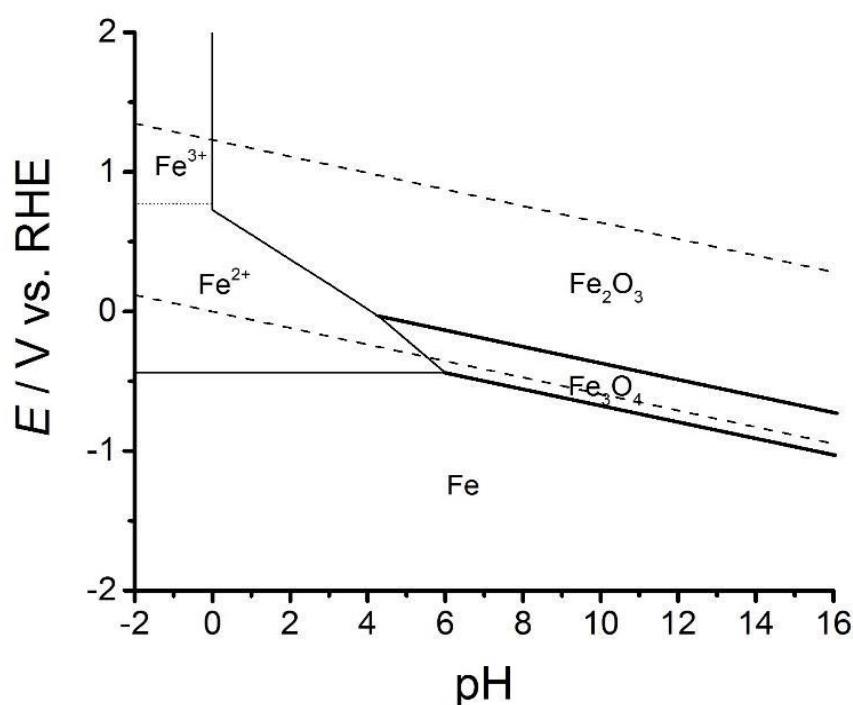
Figure 1.2. Pourbaix diagram of iron in pure water. [9]

The Pourbaix diagram in Figure 1.2 is for iron in pure water. The different sections show the most thermodynamically favourable states of the iron at the set conditions. The two sloping

dashed lines represent the two other possible reactions that can occur in aqueous solution. The top line is the water oxidation reaction that occurs to produce oxygen gas and the bottom line represents hydrogen reduction that produces hydrogen gas.

1.1.3 Corrosion kinetics

The rate at which corrosion occurs is dictated by the current densities of both the anodic and cathodic reactions. The current density is defined as the current strength per unit of surface area. The anodic current density is represented by i_a and the cathodic current density by i_c, and at equilibrium $i_a = i_c$. At equilibrium the value is known as the exchange current density, i_0.[10]

When anodic and cathodic areas are established on a metal surface the corroding metal is described as a polyelectrode, which is defined as a system where there are two of more couples, not in thermodynamic equilibrium acting simultaneously at a single electrode surface.[11] Wagner and Traud derived the additivity principle, which states that when a metal is corroding freely, the total current flowing into an external circuit is the sum of the currents produced by individual couples on the corroding metal surface.[12] This is shown in Equation 1.4:

$$\sum i_{anode} = \sum -i_{cathode} = i_{corr} \qquad\qquad \text{Equation 1.4}$$

Where:

$\sum i_{anode}$ is the current density of the anode.

$\sum -i_{cathode}$ is the current density of the cathode.

i_{corr} is the rate of corrosion at the metal surface, expressed as a current.

The electrochemical currents are dependent on potential and so the corroding metal will have a unique potential which is known as the free corrosion potential $\sum_{corr}$.

Julius Tafel discovered the relationship between current and potential which can be expressed as:

$$I_{anodic} \; \alpha \; \exp(E) \qquad\qquad \text{Equation 1.5}$$

$$I_{cathodic} \; \alpha \; \exp(-E) \qquad\qquad \text{Equation 1.6}$$

A Tafel plot can be produced by plotting E against log (i), which produces a straight line. An Evans diagram can then be produced by combining the Tafel plots of individual electrodes; this can be seen below in Figure 1.3.
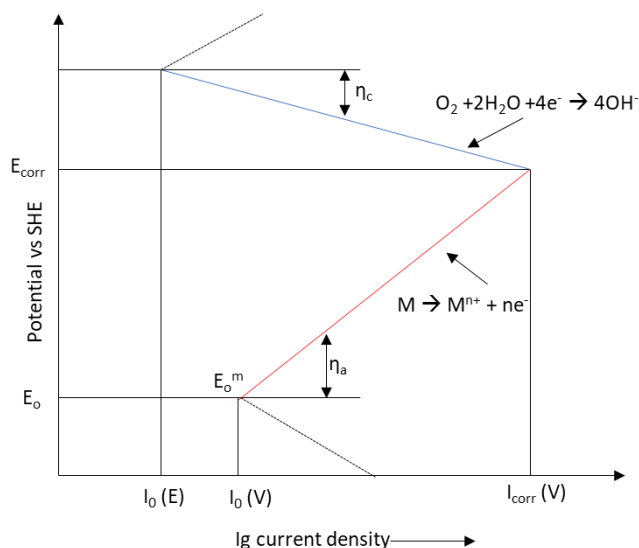
Figure 1.3: An Evans schematic – a metal reacting with an aerated electrolyte.

The Evans schematic in Figure 1.3 represents a corrosion reaction that occurs when a metal is in contact with an electrolyte. The thermodynamic driving force for the reaction is the free corrosion potential (E_{corr}). During corrosion anodic activity will produce metal ions and excess electrons; the quantity of these will reduce as the metal continues to corrode, causing the anodes (η_a) to become increasingly positive. The cathode will receive the electrons produced by the anode and becomes increasingly negative which will shift the potential downwards (η_c). The free corrosion current density, Equation 1.4, defines the point at which the anodic and cathodic current densities are zero and is shown in Figure 1.3 as the intersection of the Tafel slopes. The free corrosion potential of the system (E_{corr}) can be determined by using the Evans diagram.

1.1.4 Redox and corrosion potentials

Within a system, a metal immersed in an electrolyte containing ions of the same metal will establish a dynamic equilibrium whereby the reduced and oxidised states of the system will be present within the solution. The large concentration of metal cations at the metal surface

and the negative charge of the metal due to remaining electrons will result in the formation of an electrochemical double-layer.

This double layer causes the metal to have a different potential to the surrounding electrolyte, which is known as the Galvani Potential (Φ). The difference in the Galvani potential between the metal and the surrounding electrolyte is known as the electrode potential (E). The relationship between the electrode potential and the metal ion concentration can be represented using the Nernst equation:

$$E = E^0 - \frac{RT}{zF} \ln \frac{[products]}{[reactants]}$$ Equation 1.7

Where E^0 is the standard cell potential, [reactants] and [products] represent the concentrations of the oxidants and reductants respectively, R is the universal gas constant (8.31 J mol^{-1} K^{-1}), T is temperature (Kelvin), z is the number of electrons involved in the reaction and F is Faradays constant (96394 C mol^{-1}).

The standard electrode potential for all metals can be calculated using the Nernst Equation and this can be seen in Table 1.1. When two or more metals are coupled together, the metal with the more positive/less negative electrode potential will be more likely to be reduced and the less positive/more negative electrode potential will be preferentially oxidised.

Table 1.1. standard electrode potential for a selection of common metals.

Metal	Potential E^0 (V vs SHE)
Pt	+ 1.20
Ag	+ 0.80
Fe	+ 0.77
Cu	+ 0.34
H	0
Ni	-0.26
Fe	-0.44
Zn	-0.76
Al	-1.68
Ca	-2.87

Increasing metal oxide activity

Increasing metal activity

1.2 Zinc Corrosion

Hot dipped galvanised steel is covered in a layer of zinc which acts as a sacrificial anode for the underlying steel substrate when subjected to a corrosive environment. A Pourbaix diagram can be used to determine the corrosion of zinc, which shows the electrochemical potential versus pH for a metal undergoing corrosion and shows how the zinc will behave under different pH.
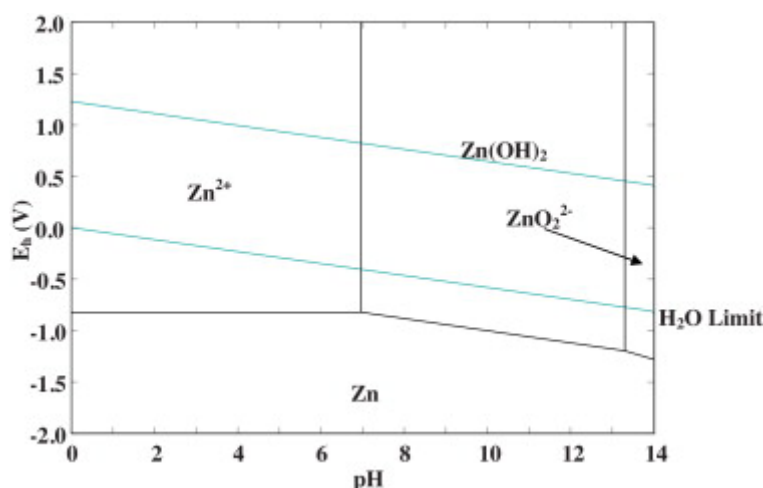
Figure 1.4. Pourbaix diagram of zinc in water. [13]

The Pourbaix diagram of zinc in Figure 1.4 indicates that zinc corrosion is most active between pH 0-8 where Zn^{2+} ions are formed from zinc dissolution. Below a potential of ca. -0.98 V vs SHE between pH 0-8 zinc is immune to corrosion. Increasing the pH between to between 8.5-10.5 will form $Zn(OH)_2$ and above pH 14 will form ZnO_2^{2-}.

1.3.1 Zinc corrosion in a NaCl environment

When zinc is placed in a NaCl containing electrolyte and in atmospheric conditions the zinc will corrode to produce a zinc hydroxychloride and a zinc hydroxycarbonate.[14] This is shown in the following reactions:

Hydroxide formation at the cathode:

$$O_2 + 2H_2O + 4e^- \rightarrow 4OH^-$$ Equation 1.8

Metal dissolution at the anode:

$$Zn \rightarrow Zn^{2+} + 2e^-$$
<div align="right">Equation 1.9</div>
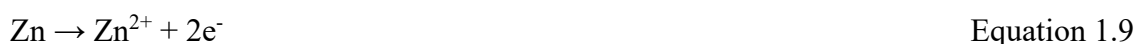
The Zn^{2+} and OH^- will react to form zinc hydroxide:

$$Zn^{2+} + 2OH^- \rightarrow Zn(OH)_2$$
<div align="right">Equation 1.10</div>

When hot dipped galvanised steel undergoes corrosion, zinc hydroxide is a common precipitate that forms, resulting in a passive layer forming on the steel surface. The passive layer acts as a semiconductor with a band gap of approximately $E_g = 3.2$ eV.[15] This relatively large band gap would indicate that zinc hydroxide will behave as an electrically insulating layer and would result in electron transfer being reduced when part of an electrochemical cell.

Under alkaline conditions (>10) zincate will preferentially form:

$$Zn(OH)_2 + 2OH^- \rightarrow Zn(OH)_4^{2-}$$
<div align="right">Equation 1.11</div>

When Cl^- ions migrate the anode, zinc hydroxychloride can form:

$$5Zn(OH)_2 + 2Cl^- + H_2O \rightarrow Zn(OH)_8Cl_2.H_2O + 2OH^-$$
<div align="right">Equation 1.12</div>
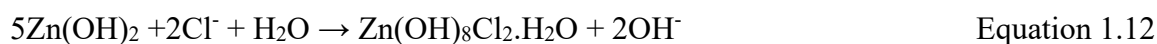
When zinc is in contact with aqueous NaCl, the corrosion products formed are zinc hydroxychloride ($Zn(OH)_8Cl_2$) and zinc hydroxycarbonate ($Zn_5(OH)_6(CO_3)_2$) as shown in Equations 1.13-1.15.[16]

The absorption of CO_2 from the atmosphere is what drives the formation of zinc hydroxycarbonate:

$$CO_2 + 2OH^- \rightarrow CO_3^{2-} + H_2O$$
<div align="right">Equation 1.13</div>

$$CO_3^{2-} + H_2O \rightarrow HCO_3^- + OH^-$$
<div align="right">Equation 1.14</div>

$$5Zn(OH)_2 + 2HCO_3^- + 2H^+ \rightarrow Zn_5(OH)_6(CO_3)_2 + 4H_2O$$
<div align="right">Equation 1.15</div>
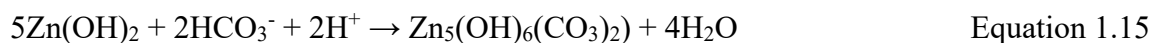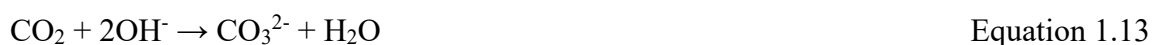
The corrosion of zinc in aqueous sodium chloride has been studied by Wint et al, who used scanning vibrating electrode technique (SVET) to study the localised corrosion of unpolarised zinc. Zinc is a suitable system to experimentally investigation of how electrolyte concentration can affect the spatial behaviour of pitting corrosion under near neutral corrosion due to the limited range of pH over which Zn exhibits passive behaviour. As previously mentioned, when immersed in NaCl electrolyte Zn undergoes corrosive attack

with anodic zinc dissolution and cathodic oxygen reduction occurring, producing hydroxides on the surface. Areas of anodic zinc dissolution can be detected using scanning vibrating electrode technique (SVET) when the concentration of NaCl is varied. In lower concentrations of NaCl (≤0.1%), circular features typical of pitting corrosion are observed, and in higher NaCl concentrations (1% w/v) corrosion on the surface is observed to be more general with few localised corrosion features observed. These differences are observed under SVET through measurement of the produced current. The areas that show pitting corrosion illustrate multiple localised areas of anodic current density set against a cathodic surface, with larger areas of general corrosion showing large irregular areas of anodic currents against a cathodic current, with the number of pits being formed decreasing as NaCl concentration increases.[17]

1.3. Sacrificial Protection of Steel by Zinc

Zinc is frequently used as a sacrificial metal on steel due to preferential corrosion instead of the iron base of the steel it is deposited on. Thereby acting as a protective barrier to protect the steel from oxidising. When zinc is in contact with iron galvanic corrosion typically occurs. This is a very common and rapid form of corrosion; however, it can be used as a method to protect a metal substrate against corrosion.

For galvanic corrosion to take place, a corrosion cell must be in an environment where the anode and cathode consists of two (or more) metals that occupy different positions in the galvanic series, thus having differing electrode potentials. The least noble metal (most negative potential) will corrode preferentially to the metal with a more positive potential. This behaviour is referred to as sacrificial protection. When the free corrosion potential of a metal is low (negative), the reactivity of the metal increases due to its ability to be more readily oxidised. This a common cause of corrosion throughout industry but can be avoided with careful design and material selection.

The sacrificial protection of metals is widely used in engineering to protect structural metals from corrosion. In the case of zinc or aluminium coated steels, the zinc or aluminium will corrode preferentially as they are the least noble metals in the steel structure and protects the steel from corrosion if subjected to aqueous conditions. Therefore, the galvanising process is used to coat the entire iron surface in order to prevent iron and zinc from coupling and

causing further damage to the metals, whereas galvanising allows the zinc to sacrifice itself on the steel surface. At the point where galvanised steel suffers damage a galvanic cell is formed and the zinc around the point of damage preferentially corrodes and corrosion products form on the steel surface to protect it, with the steel being further protected as it is cathodic in relation to the zinc coating.

The corrosion of zinc as a function of pH has been studied by Thomas et al using anodic and cathodic polarisation in 0.1M with pH ranging from 1-13. [18] At acidic pH (1-4), zinc corrosion proceeds via cathodic control and the kinetics of hydrogen evolution reaction dictates the overall corrosion rate with Zn forming Zn^{2+}. In the pH range of 4-11, there is no significant variation in the corrosion rates due to a change in the cathodic reaction from hydrogen evolution to oxygen reduction, with zinc oxides being thermodynamically predicted to form at pH 7-10. The surface oxides formed over zinc do not serve as an effective corrosion protection barrier. In alkaline conditions, zinc reacts forming different oxides and complexes based on the local pH and potential. Zinc oxides that protect the surface are formed when the local solution is between 11-12, and the electrode potential is -1.15$V_{SCE.}$ Minimal corrosion rates are measured between pH 10-12, where there is limited influence of metal hydrolysis or alkaline dissolution of zinc due to well defined passivity of the surface occurring due to hydroxide formation on the surface.

The corrosion phenomena that occurs in galvanised steels has been studied using scanning reference electrode technique (SRET). The SRET is used to investigate the time dependent galvanic corrosion processes that occur in coating defects and cut edges of HDG steel. When HDG steel is immersed in solution, an intact coating exhibits immediate localised anode formation, which does not extend over the surface over 24 hours. On a steel surface with coating defect, electrolyte sites of anodic activity are highly localised and occur principally on the zinc covered portion of the sample. The cathodic activity is initially distributed across both the exposed and intact steel surfaces, and after 40 minutes begins to focus on the exposed steel. Over time anodic activity becomes more generalised and the cathodic activity becomes associated with the steel and after 100 minutes the typical representation of cathodic steel protection by a sacrificial anode coating is revealed by SRET mapping. [19]

1.4. The effect of aluminium additions on zinc coated steels

Aluminium has been used as an alloying addition to zinc for metal coatings to improve the overall corrosion performance. The addition of Al has shown to provide superior corrosion protection compared to traditional hot dipped galvanised steels. [20]

Zinc coatings corrode because of the dissolution of zinc from the surface. However, zinc possesses the ability to "self-heal", whereby protective layers of Zn-based carbonates, oxides or hydrated sulphides can form, depending on the environment.[21] When these corrosive products have formed, the corrosion rate is greatly reduced. However, the ability of zinc to maintain a protective layer is dependent on local pH as a result of the amphoteric oxide formed by zinc which can dissolve in acidic and alkaline conditions. This makes the protective layer susceptible to acidic of alkaline conditions, which interferes with zinc's ability to form protective layers due to impairing the ability for zinc to "self-heal", so alloying additions are needed to improve the performance of metals against corrosion. [22]

Alloying additions to Zn coatings, such as Al, have been shown to markedly improve the corrosion performance. The addition of Al results in a change in the microstructure of the alloy (compared to steel coated with Zn) and allows for the formation of a protective aluminium oxide (Al_2O_3) to form on the surface and results in lower corrosion and oxidation rates compared to pure-Zn coatings. [23,24,25]

When Zinc-based coatings are exposed to a corrosive environment, corrosion products are formed which results in a slowing of corrosion rate. These products can consist of a thin layer of hydrozincite ($Zn_5(OH)_6CO_3$) in humid environments, which often evolves into a crystalline form over time. If the surrounding environment contains any chlorides, zinc hydroxychloride is formed ($Zn_5(OH)_8Cl_2.H_2O$) locally on the surface via Equation 1.12, which gradually forms a sodium zinc hydroxychlorosulfate ($Na_4Zn_4SO_4(OH)_6Cl_2.6H_2O$). Chen et al studied atmospheric corrosion of zinc metal in the presence of NaCl which showed that the main corrosion product formed was $Zn_5(OH)_8Cl_2.H_2O$. [26]These corrosion products are key to inhibiting further corrosion as they block the anodic and cathodic sites driving the corrosion reactions.

In a corrosive environment such as a marine environment, preferential Zn dissolution results in the formation of an Al-rich porous structure. Aluminium, in this porous structure, can be passivated and is cathodic with respect to the steel substrate.[27] The corrosion resistance afforded to aluminium is a result of the passive oxide on the surface which bonds strongly to

the surface and reforms almost immediately if damaged. The passive oxide provided by aluminium addition is only seen in zinc alloy coatings possessing <40% Al.

Zn coatings which contain >40% Al have microstructures which do not allow for the formation of an aluminium surface oxide. At these increased Al contents an Al-rich α-phase contains up to 70% Zn and does not possess the ability to form the barrier oxide film when it coexists with the Zn-rich β-phase. The microstructure of Galvalume^{TM} which possesses 55%-Al can be seen in Figure 1.5.
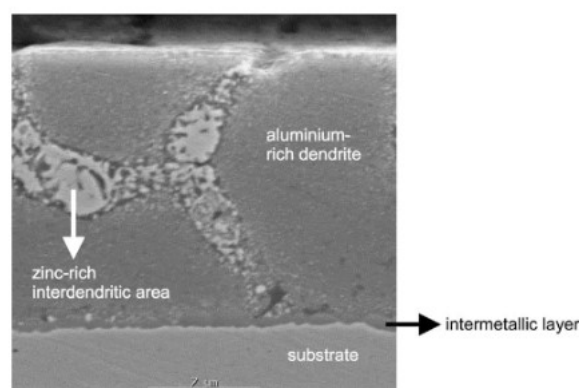
Figure 1.5 Scanning Electron Microscope cross section of commercial grade Galvalume.[28]

The standard electrode potential of pure aluminium is much more negative than that of pure zinc, -1.68 V (vs SHE) and -0.76 V (vs SHE) respectively. [29] As a result, when the two metals are electrochemically coupled, the aluminium will be the anode if it is not covered by a protective oxide film. When fully decomposed through the eutectoid reaction, the α-phase could still contain over 1% Zn. The electrolytic solution potential of a decomposed α-phase is about 1.06 V using a 0.1 N Calomel electrode is only slightly more anodic than that for zinc at 1.01 V. It is, therefore, expected than the a-phase will corrode first and slightly faster than the β-Zn in decomposed primary a-phase pockets resulting in a decreased corrosion rate.[30]

As well as the reactions which occur in the section above, the addition of aluminium to a zinc coating results in the formation of additional corrosion products which aid by decreasing the corrosion rate. These include zinc aluminium carbonates ($Zn_6Al_2(OH)_{16}CO_3.4H_2O$) and zinc aluminium hydroxychlorides ($Zn_2Al(OH)_6Cl.2H_2O$). [31, 32] The formation of these hydroxycarbonates generally forms as a layered double hydroxide, which slows ion-transfer through the layers, slowing the rate of corrosion. [21]. However, these studies tend to investigate the behaviour of 55% Al coated steel, generally referred to as Galvalume^{TM}.

The purpose of the review is to investigate the ZnAl-coated steel known as Galvalloy[TM], which consists of 95.2% Zn and 4.8% Al. Alloys consisting of higher Al content, such as Galvalume[TM] (55% Al, 1.5% Si), have a complex and sub-micron sized heterogenous microstructure. Galvalloy[TM] by comparison consists of a relatively simple microstructure, with corrosion initiation taking place in the zinc-rich interdentritic phases, with the Al-rich interdentritic phases only beginning to corrode after longer immersion times or in a much more aggressive environment. [33] The microstructure of Galvalloy is characterised as a two-phase structure. A Zn-rich η-proeutectic phase surrounded by a eutectic type phase consisting of β-Al and η-Zn lamellae. [34] An SEM image of the microstructure of Galvalloy can be seen in Figure 1.6.
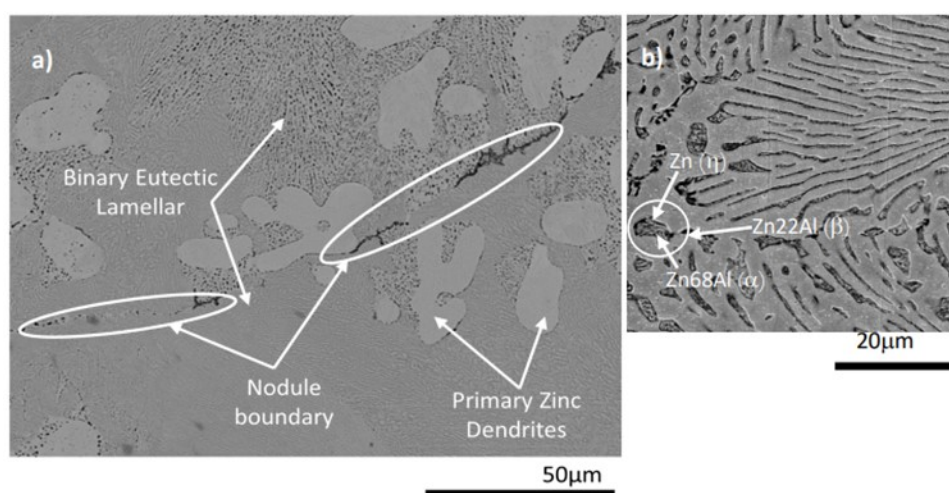
Figure 1.6. SEM image of the microstructure of Galfan. (a) Shows the Zn primary dendrites surrounded by the binary eutectic lamellar phase of Zn-Al. b) Magnified image of eutectic phase showing Zn (η) (light) and Zn22Al (β) (darker) lamellar. The Zn22Al (β) has a sub-microstructure within its lamellae composed of Zn (η) and Zn68Al (α).[35]

It was found that the protectoid η-Zn phase possesses improved corrosion resistance compared to the eutectic colonies.[30] This was supported by Yang et al, who proposed a corrosion model in which the eutectic phase was prone to preferential attack when ZnAl alloys were immersed in a simulated acid rain environment.[36] Although the Zn-rich phases of Galvalloy are the phases which undergo preferential corrosion, the Al-rich phase does become prone to corrosive attack after 5 days. Due to the increased corrosion resistivity of the Al-rich phase compared to the Zn-rich eutectic phase, as the ratio of Al rich to Zn rich phases increases, the rate of corrosion does decrease. The $Zn_6Al_2(OH)_{16}CO_3.4H_2O$ content of

corrosion products formed by the ZnAl coating under a corrosive environment increase as the Al content of ZnAl increases. Coatings with higher Al content results in a lower corrosion rate, with corrosion rate also decreasing as time in corrosive media increased. Weight loss of the metal due to corrosion was also substantially greater with coatings with lower Al content (<8%) as time went on. This is a result of the passivating behaviour caused by corrosion products formed, with a greater Al content creating thicker "fixed" layers, compared to lower Al content creating more "loose" corrosion products. This results in the trend seen in the corrosion rate and the subsequent weight losses. [36]

In a simulated acid rain environment, the corrosion reaction proceeds as follows:

a) Al-rich phases are attacked due to galvanic effects of primary Zn-rich and Al-rich phases. Corrosion products mainly cover the Al-rich phases.

b) After a longer immersion time, the whole grain becomes corroded, resulting in deep corrosion pits and product film formation on alloy surface.

c) Formation of Al-based corrosion products results in the rate of corrosion slowing down over time.

However acid rain has a pH of 4-5, whereas chloride rich marine environments have a pH of 8. Xian Zhang et al. investigated the atmospheric corrosion of Galfan in chloride-rich environments (4 µg $NaCl/cm^2$ and 70-90& relative humidity). [37] At a relative humidity (RH) of 70%, very thin oxides of ZnO, Al_2O_3 and $ZnAl_2O_4$ covering most of the surface and at 90% RH, ZnO and $Zn_6Al_2(OH)_{16}CO_3.4H_2O$ formation dominates. Corrosion products begin to form on the η-Zn phase adjacent to the β-Al phase and, as a result of the slightly higher Al-content, the β-Al phase could be expected to be the anode. However, oxide formation on the surface appears to reverse the conditions so that the β-Al phase acts more noble than the η-Zn phase. Over extended periods of time, corrosion products begin to spread from the η-Zn phase over the entire surface, with $Zn_6Al_2(OH)_{16}CO_3.4H_2O$ as the dominating phase. OH-production in cathodic areas results in a local pH increase in the aqueous ad-layer, instability of Al_2O_3, enhanced Al-dissolution and the formation of local clusters of $Zn_6Al_2(OH)_{16}CO_3.4H_2O$. [37] Generally, in a chloride containing environment, Cl^- ions compete with OH^- in the oxides present on the surface, which results in local depassivation and areas which are more susceptible to transient dissolution of metal ions. This chloride competition can result in adsorption to the oxide surface, resulting in metal-chloride complexes on the surface which are less strongly bound to the oxide matrix. This results in an

increasing rate of local dissolution and film growth is poisoned Thinning of the passive layer occurs at a faster rate resulting in localised depassivation, the Cl^- then compete with OH^- for metal surface adsorption, which hinders repassivation if there is not a sufficient OH^- supply.[38]

As well as chloride deposition in marine environments, there is also the deposition of SO_4^{2-}, which is present in the atmosphere and dissolved into sea water. Extended exposure (>2 weeks) of Galfan to a marine environment result in the formation of an additional layered phase: sodium zinc chlorohydroxosulfate, $Na_4Zn_4SO_4(OH)_6Cl_2.6H_2O$. This chlorohydroxosulfate is the final corrosion product which forms from an initial phase zinc hydroxycarbonate and an intermediate phase zinc hydroxychlorides.[39]

Without NaCl, the dissolution of Zn^{2+} and Al^{3+} from the surface creates conditions for the rapid formation of $Zn_6Al_2(OH)_{16}CO_3.4H_2O$, a ZnAl phase previously reported on Galfan in non-chloride containing environments.[40] The formation of this hydroxycarbonate is a result of OH^- in cathodic areas results in an increase in pH in the aqueous adlayer, decreased stability of Al_2O_3, enhanced Al-dissolution and local cluster formation of hydroxycarbonates. [41] This phase has a highly complicated structure and forms in the initial stages of corrosion, which suggests formation directly in the aqueous adlayer through a multi-ion reaction, rather than a gradual dissolution-precipitation reaction. Due to its unique crystal structure, $Zn_6Al_2(OH)_{16}CO_3.4H_2O$ possesses ion-exchange properties and when placed in a chloride containing environment, the Cl^- ions can replace the CO_3^{2-} ions and become inactive for further repassivation of the Galvalloy surface.[41, 42] This $Zn_6Al_2(OH)_{16}CO_3.4H_2O$ phase was suggested to be the main reason for the enhanced corrosion resistance to Zn-Al-Mg coatings compare to HDG Zn coatings. [43]

In a humid environment, instantaneous formation of ZnO, $ZnAl_2O_3$ and Al_2O_3 will form on the Galfan surface. Further production of surface phases are then produced depending on the local environment. In a CO_2 containing atmosphere, the formation of $Zn_6Al(OH)_{16}CO_3.4H_2O$ (hydrotalcite). When placed in marine environments in the presence of chloride and sulphide ions, Galvalloy forms hydroxychlorides and hydroxysulphides, existing as $Zn_5Cl_2(OH)_8.H_2O/Zn_2Al(OH)_6)Cl.H_2O$, $Na_4Zn_4SO_4(OH)_6Cl_2.6H_2O$ respectively and can exist at the same time on the same surface, these can be seen in Figure 1.7 The formation of these corrosion products (particularly hydroxychlorides) has been shown to have improved barrier coating properties compared to galvanised steel. [43]

$$\text{Galfan} \xrightarrow[\text{Corrosion}]{\text{General}} \text{ZnO/ZnAl}_2\text{O}_3/\text{Al}_2\text{O}_3$$

Marine Environment → $Zn_5Cl_2(OH)_8.H_2O/Zn_2Al(OH)_6Cl.H_2O$

Marine Environment → $Na_4Zn_4SO_4(OH)_6Cl_2.6H_2O$

CO_2-containing atmosphere → $Zn_6Al_2(OH)_{16}CO_3.4H_2O$.
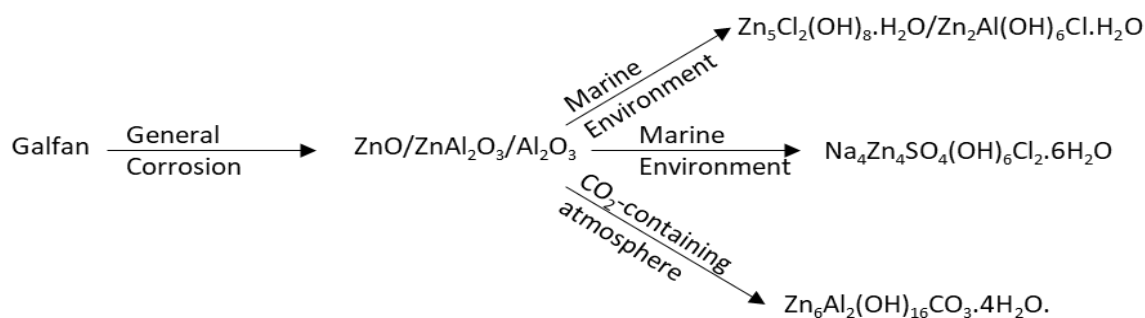
Figure 1.7. Sequence of corrosion products formed on surface of Galfan.[44]

1.5. Alkaline cleaning behaviour on galvanised steel

The first step to applying an organic coating to HDG steel , and the main topic of this short review, is alkaline cleaning. Alkaline cleaning is done to remove any organic contaminants and to prepare surface for coating. Cleaning occurs prior to the application of a conversion coating, which aids in adhesion of the final organic coating layer. This whole process results in a finished product which has increased corrosion resistance compared to a non-conversion coated steel product.
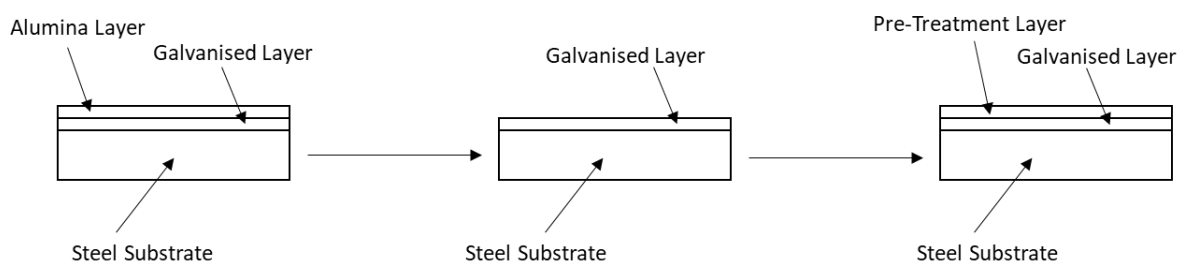
Figure 1.8. Schematic of how alkaline cleaning influences the surface of steel prior to pre-treatment application.

Hot Dip Galvanised (HDG) steel is covered in a surface aluminium oxide layer, which is present as a homogenous film over the entire surface. In a galvanised zinc coating, aluminium has been reported to consist of three main forms: (i) as Fe-Al intermetallic compounds at the steel-zinc interface, (ii) in segregated Al-moieties and (iii) as a continuous thin film of aluminium and oxygen that covers the entire zinc surface. [45] The diffusion of aluminium from the bulk of the galvanised coating towards the surface helps create the oxide layer. The affinity for aluminium to react with oxygen, which is abundant on the surface, drives this process, with analysis of Al in the bulk showing highly limited quantities of Al. This is a

thermodynamically driven process, as it is not favourable for Al to be dissolved in Zn as the temperature drops during zinc solidification.[46] The presence of the Al_2O_3 on the surface protects the surface from further oxidation prior to application of organic coating, however this needs to be removed before a pre-treatment is applied as any residual aluminium oxide film hinder the reactivity of hexaflourotitanate pre-treatments with the zinc surface due to formation of non-uniform coating at aluminium rich sites [47] Improper surface activation can cause wettability and adhesion issues of subsequent layers place on top of the activated surface, as a result of foreign matter remaining on or imbedded in the surface. [48]

To achieve a uniform coverage and efficient bonding of the conversion coating to the steel substrate, the optimisation of the cleaning process is required.. Alkaline cleaners are used at the beginning of a colour-coat process to remove residual surface impurities before further coating. [49] The purpose of alkaline cleaning is not just to degrease the steel surface but to etch the surface ready to be passivated by a conversion coating. The inert Al_2O_3 on the surface can be detrimental to the reactivity of zinc and aluminium substrates and reduces the adhesion of paint to the surface. The etching reaction caused by alkaline cleaning removes the surface oxides, increasing the surface reactivity. The hydroxide ions present in an alkaline cleaner dissolve the amphoteric oxide layer and the underlying metal, this dissolution can be shown by the following reactions: [50]

$$Al_2O_3 + 2OH^- + 3H_2O \rightarrow 2Al(OH)_4^- \qquad\qquad \text{Equation 1.11}$$

$$Zn + 2OH^- + 2H_2O \rightarrow Zn(OH)^{2-} + H_2 \qquad\qquad \text{Equation 1.12}$$

The alkaline etching reaction that occurs on the surface generates a zinc rich surface, composed of differing zinc compounds and a reduced presence of aluminium and carbon.[51]

In a study by Schoeman et al, for an effective pre-treatment to be formed on the surface, complete removal of the alumina layer is essential. This would result in a uniform distribution of TiO_2 on the zinc layer, with a desired concentration range of 4-8 mg/m^2. In order to achieve the removal of the alumina layer, the free alkalinity of the alkaline cleaner must be at least 3.2 meq/L. The free alkalinity is the measure of the concentration of charged basic species that can be neutralised by a strong acid. [52]

Berger et al evaluated how cleaning temperature and time influence HDG. Under mild cleaning conditions (40 °C, 10 seconds), carbon compounds present from contamination via the atmosphere, handling, and storage are removed from the surface but with much of the

aluminium oxide coating remaining on the surface. [53] Under more moderate cleaning parameters (60 °C, 30 seconds), the aluminium oxide coating removal is more substantial. This would indicate that the surface would be more preferential for pre-treatment deposition. Atomic Emission Spectroscopy analysis further shows that as cleaning temperatures and times are increased, the surface of HDG shows a much reduced aluminium concentration. X-ray Photoelectron Spectroscopy analysis of an alkaline cleaned surface show a dominant presence of zinc oxides and hydroxides after cleaning. [53]

Saarima et al in an initial study on the chemistry and morphology of hexafluorotitante pre-treatments on HDG showed that on a non-etched surface, 30% of the atoms in the outermost few nanometres were aluminium, with the remaining 70% consisting mostly of oxygen and small amounts of zinc and carbon. When treated with alkaline cleaner, the aluminium concentration decreases and the Al:Zn atomic ratio decreases rapidly even at low concentrations of the cleaning solution. When a 2 g/L solution is used, there is a further decrease in the Al:Zn ratio, indicating the ratio continues to drop at greater concentration. This is shown by a decrease of 50% in the Al-% content of the surface and a drop of 90% in the Al:Zn ratio. The Al:Zn atomic ratio has been used as a method of depicting the actual aluminium content of a surface since the Al-content percentage are usually small. [54] In order to achieve good adhesion of the pre-treatment layer and the subsequent corrosion resistance properties that come with an effective pre-treatment, an Al removal of 70% is required. [55] However, extensive Al removal requires a severe etching reaction to occur, which may not be economically feasible due to the cost of energy, and through losses made through slowing the line cleaning step down which impacts the amount of final product that can be made. [51]

HDG when exposed to mild alkaline cleaning showed that the Al:Zn atomic ratio decreases rapidly. XPS analysis of the cleaned HDG surface showed an increased Zn signal intensity which indicates removal of the Al_2O_3 layer. XPS analysis has also showed a thicker pre-treatment barrier coating when Al_2O_3 was removed. The dissolution of Al_2O_3 occurred more easily at deformation twinning, which results in a more reactive surface area available for an etching reaction to occur, whereas Al_2O_3 removal was slower at dendritic valleys and grain boundaries. Deformation twinning occurs when there is a homogenous shear of the lattice structure, forming deformation twins. This deformation caused by the gliding along rows of atoms in the lattice structure cause displacement laterally along the glide plane, resulting in a more reactive surface area. [56]

Further analysis of grain boundaries using Helium Ion microscopy imaging and Electron Probe Micro Analysis (EPMA) measurements showed greater accumulation of pre-treatment chemical in these areas, possibly the result of greater reactivity at the grain boundaries with a greater reactive area of the surface depressions present in these areas as a result of the drying effect. [57]

In a further study, Saarimaa et al analysed HDG which had been alkaline cleaned at varying levels of free alkalinity and evaluated the surface activation by exposing the cleaned surface in a humid supercritical CO_2 environment. This environment results in the formation of zinc corrosion products at activated surface sites. XRF was then used to quantify the oxidised zinc in the subsequent corrosion products after extraction using glycine. To measure the changes in surface activity, samples were pre-treated by applying a hexaflourotitanate solution and measuring the uniformity of the formed barrier coating.

Uncleaned specimens showed very little surface activity; however, the most active sites were at the grain boundaries and intermetallic particles. Corrosion was initiated at these sites due to potential differences between these areas and the surrounding substrate, which creates microscale electrochemical cells.

After an initial high cathodic activity at these sites, activity diminished, resulting in a low overall activity of the uncleaned HDG during exposure to humid $_{sc}CO_2$. When the free alkalinity of the alkaline cleaning solution was increased from 0.5 to 4.0 meq/L, a large increase in the surface activity occurs, which is confirmed by a significant improvement in the uniformity of the pre-treatment layer.

The surface activity increases as a result of Al_2O_3 dissolution from the HDG surface, which also enables the surface between grain boundaries to become gradually activated. As stated by Maeda, a severe etching reaction needs to occur to fully remove the Al_2O_3 layer, which would not be economically feasible due to the cost of raw materials and energy. [51] In this study, full Al_2O_3 removal, which is accompanied by high zinc activity and uniform pre-treatment layer formation is only achieved with a free alkalinity of 60 mEq/L, which is not feasible on an industrial scale due to the time and energy constraints under which industry operates. [58]

1.6. Conversion coatings

A conversion coating involves altering the chemistry of a metal surface via a chemical reaction between the surface and the coating. The reaction of a conversion solution with a metal surface generates a layer that covers the metal surface. The conversion coating allows for greater adhesion of subsequent organic coatings due to the presence of chemical bonds and an intermediate layer between the coating and the underlying metal.[59] This type of coating system is used in organically coated steel systems such as the Colorcoat Prisma produced by TATA steel.
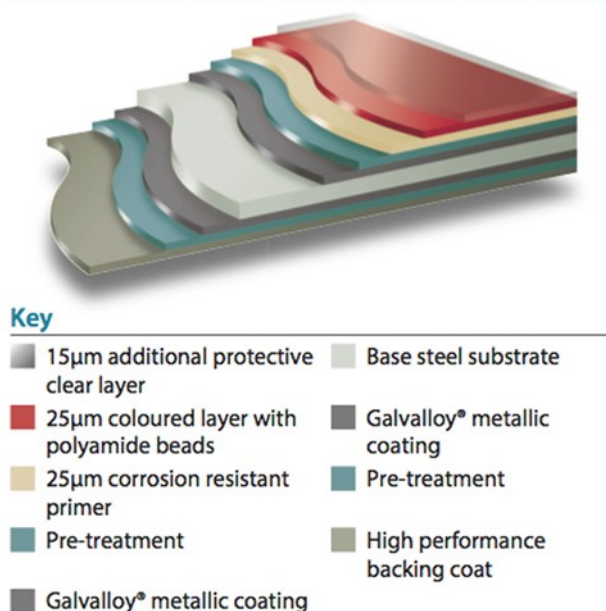
Figure 1.9. Schematic of multicoating system present in Tata Steel Colorcoat Prisma product. [60]

An increase in corrosion performance has been attributed to the use of a conversion coating compared to an uncoated sample.[61] The conversion coating, when applied, reacts with the steel surface which precipitates as a thin film coating the metal surface, inhibiting corrosion from occurring. The aim of a conversion coating is to increase the polarisation resistance of the surface and decreases the current and potential corrosion rates. This is done through neutralising the potential of local anodic and cathodic galvanic corrosion sites. [62] These films also acts as an absorption base for improving the adhesion of subsequent of organic layers applied on top.

1.6.1 Chromate conversion coatings

In the environment, chromium exists as the stable Cr^{3+} and Cr^{6+} ions. This variability in oxidation state allows chromium to have varying behaviours and characteristics.[63] Whilst trivalent chromium is an essential trace element for the proper function of a living organism, however, in high enough concentrations will cause chromium toxicity. Hexavalent chromium is highly toxic to a living organism due to its ability to be reduced to Cr^{3+} in cells, which causes DNA damage. Hexavalent chromium is a highly soluble and mobile ion, meaning it can be easily washed into the environment, where it can come into contact with living organisms, and cause health problems. [64]

The Cr^{3+} oxidation state is the most stable and considerable energy is required to convert it to the Cr^{6+} oxidation state. This can be seen in the Frost diagram in Figure 1.10, with varying potentials (nE) required for chromium to change oxidation number.[65] The Frost diagram illustrates that the +3 oxidation state of chromium is the most stable relative to free energy. It also illustrates that the +6 oxidation state requires a considerable input of energy in order to convert from the +3 to the +6 oxidation state.
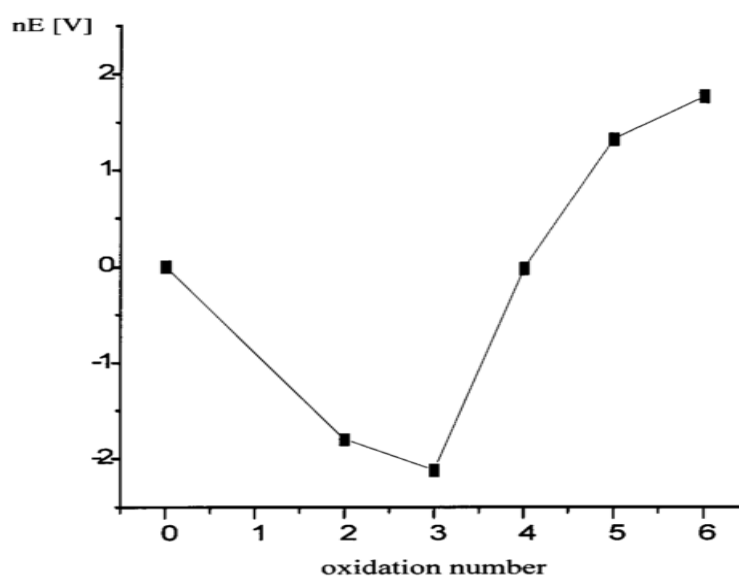
Figure 1.10 A Frost diagram for metallic chromium species in acidic solution.[61]

The pH of a solution and the potential of the metal also plays a large part in the formation of chromate ions, the more alkaline a solution is, the more likely that Cr^{6+} will be formed,

producing higher electrode potentials. The chromium Pourbaix diagram given in Figure 1.11 shows the stable redox state of chromium as a function of pH. For example, the deposition of a trivalent chromium oxide onto zinc by a Cr^{6+} containing solution is due to a redox reaction whereby zinc dissolution is coupled to a reduction of chromate via reaction 1.13. Studying Figure 1.11 the passive Cr^{3+} oxide is formed at a higher pH range of $5 - 12$, with the electrode potential of the surface playing a role in the formation at a particular pH. If the electrode potential is more negative, a more alkaline pH is required to form this inert oxide, and if the electrode potential is more positive, a more acidic pH is required.

$$CrO_4^{2-}{}_{(aq)} \ + \ 5H_2O \ + \ 3e^- \ \rightleftharpoons \ Cr(OH)_{3(s)} + 5OH^- \qquad\qquad \text{Reaction 1.13}$$
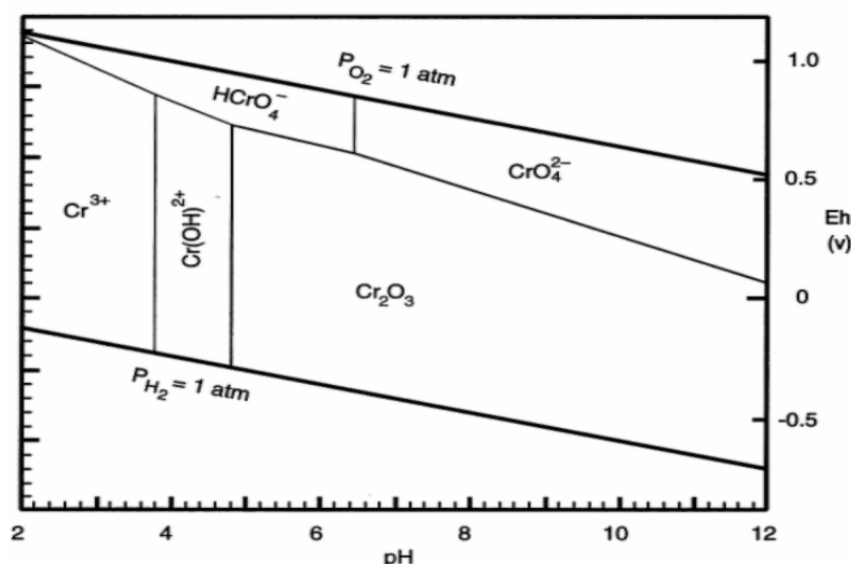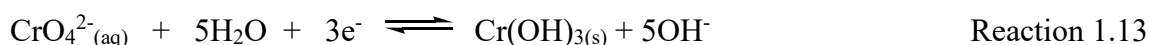
Figure 1.11 A simplified Pourbaix diagram for chromium. Taken from reference 62.[66]

Chromium based conversion coatings have been used to provide corrosion resistance for various metals and metal alloys due to their ability to inhibit corrosion occurring on the surface. Cr^{6+} ions are highly mobile in solution, which allows them to easily migrate to sites of corrosion, where they are irreversibly adsorbed to the surface and reduced to Cr^{3+}. This inhibits oxygen reduction that may occur on the metal surface. [67] Self-repairing chromium oxides for the protection of zinc has been reviewed by Thomas et al. with short term protection the zinc surface being achieved through chromate conversion coatings, with dual oxidation states Cr^{3+} and Cr^{6+} existing on the formed coating. Cr_2O_3 which serves as a protective barrier and Cr^{6+} exists as soluble CrO_4^{2-} which can self-repair defects on the

surface layer. In the long-term, protection of zinc is achieved through its own corrosion products formed during atmospheric corrosion. [68]

Chromate conversion coatings (CCC) deposited on aluminium alloys and placed in highly acidic fluoride or chloride solutions have been used for years to inhibit aluminium corrosion. The thickness of CCC's are typically around 100 nm, however thickness between 200-300 nm thick with coating weight proportional to coating thickness and the redox rate of formation of Cr(III) and the solubility of Cr(III) oxides has been shown in sol-gel coatings.[69,70] It's believed that the CCC involves the destabilisation of the passive oxide film on the metal surface by fluoride, followed by reduction of chromate by the exposed aluminium surface.[71] The mechanisms of corrosion inhibition have been proposed as involving blocking of active sites by the Cr^{3+} film,[71] dynamic repair of newly created defects in the creative film, [72] or an increase in the electrical resistance of the conversion coating. [73] One study, conducted by Zhao et al. used Raman spectroscopy to study the surface species present on an aluminium surface when covered with a CCC in an aqueous NaCl solution. [74] Raman spectra of the CCC film identified a characteristic Cr^{VI} band, which was distinct from CrO_4^{2-} and $Cr_2O_7^{2-}$.

The success of chromate lies in its ability to switch oxidation states and its smart release transportability. Schuman TP *et al*. has proposed that CCC's inhibit corrosion by using Cr(III) as an insoluble cathodic inhibitor and Cr(VI) as a soluble, transportable anodic inhibitor. [75]

1.6.2 Phosphate conversion coatings

Phosphate conversion coatings are used on steel and metal alloys such as magnesium, and aluminium, for corrosion protection, lubrication, or as a foundation for subsequent coatings and can vary between 1-50 μm thick or have a coating weight of 1.5-100 g/m^2.[76] A phosphate conversion coating is made up of thin crystalline layers that adhere to the surface of the metal substrate. These phosphate crystals are porous and can be formed from solutions of zinc phosphates, manganese phosphates, and iron phosphates solutions, all of which give slightly different properties.[77]

When iron substrate is pickled in a phosphate solution, a reaction occurs where iron dissolution is initiated at the microanodes present on the surface by the free phosphoric acid present in the solution. Hydrogen evolution occurs at the corresponding microcathodic sites:

$$3Fe^{2+} + 6H^+ + 2PO_4^{2-} \rightarrow 2Fe^{2+} + 2PO_4^{3-} + 3H_2 \qquad \text{Equation 1.14}$$
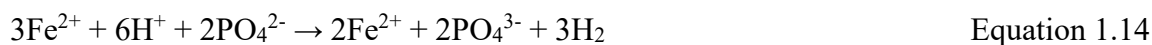
The consumption of phosphoric acid during the reaction results in a drop in solution acidity of the solution in the layer adjacent to the surface. As the pH of the solution becomes more neutral, the solubility of the phosphate layer is lowered, resulting in precipitation of the phosphate salt:[76]

$$nM^{z+} + 2PO_4^{3-} \rightarrow M_n(PO_4)_2 \qquad \text{Equation 1.15}$$

1.6.2.1 Zinc phosphate conversion coatings

Zinc phosphate coatings were the initial replacements for chromate-based conversion coatings. They do not exhibit the toxic properties associated with chromate conversion coatings and provide corrosion protection to metal alloys by forming a $Zn_3(PO_3)_2 \cdot 4H_2O$ film.[78] Niu et al. conducted a study and application of a zinc phosphate coating onto AZ91D magnesium alloy [79] XRD analysis discovered that the coating was composed of mixed metal phosphates with a microporous structure. Corrosion testing on AZ91D vs C1008 steel showed poor performance of C1008 related to no crystalline zinc present on the surface, with corrosion inhibition of zinc phosphate being related to the presence of zinc in the coating. It is believed that the zinc in the coating will be corroded first, and the many fine zinc particles in the coating on AZ91D would disperse the corrosion current and decrease the corrosion rate, which produces the difference in anti-corrosion performance. Further corrosion testing was conducted on a paint coating with the zinc phosphate, finding similar corrosion resistance to that of paint plus a chromium conversion coating, and exhibits increased adhesion to the alloy surface. [79]

In addition to zinc phosphate conversion coatings, calcium can be used as an additive to create a calcium-modified zinc phosphate conversion coating. This Ca-modified coating mainly consists of a distinct crystalline phase of $Ca_2Zn(PO_4)_2.2H_2O$. [80] Experimentally, the corrosion resistance of a calcium-modified zinc phosphate coating has been conducted on an aluminium-magnesium alloy. Potentiodynamic polarisation techniques have been used to test the corrosion resistance of a Ca-modified phosphate coating. [81] When compared to a zinc

phosphate coating, the Ca-zinc phosphate has a much-decreased current density (11.5 $\mu A/cm^2$) compared to that of zinc phosphate (41.8 $\mu A/cm^2$). This shows that the presence of calcium phosphate nuclei in the coating has a significant influence on the corrosion resistance. The influence of microstructure on the corrosion resistance of Ca-Zn Phosphate coatings using SEM and optical microscopy on AZ31 and AM30 alloys has also been studied. [82] Through surface analysis it was determined that the alloy microstructure (grain size, phases), with a greater surface roughness resulting from greater grain sizes have a large effect on the corrosion rate, and chemical composition of the alloy substrate (higher zinc and lower manganese content results in greater corrosion resistance) have a significant influence on the formation and corrosion resistance of the Ca-Zn phosphate coating.

1.6.2.2 Manganese phosphate conversion coatings

Manganese phosphates are used for reducing wear and to improve the running of gearboxes. During the phosphating process, phosphoric acid pickles the surface and forms with manganese ions a layer of phosphate crystals with a high oil affinity, which aids in the reduction of wear.[83] Of the three main phosphate coatings, manganese phosphate has the highest hardness and superior corrosion and wear resistance.[84] Manganese phosphate coatings are generally composed of $(Mn,Fe)_5H_2(PO_4)_4 \cdot 4H_2O$. The incorporated iron phosphate is only composed $(Fe)_5H_2(PO_4)_4 \cdot 4H_2O$. Iron phosphate is usually formed as a by-product due to the chemical reactions that occur during the reaction between the metal (generally ferrous) surface and the orthophosphoric acid which is present in the bath which leads to incorporation into the final product. [85]

Reactions occurring between the phosphating solution and metal surface are shown in the equations below.[86] At the beginning of the process, dissociation of H_3PO_4 into $H_2PO_4^-$ ion between pH 1 to 3 takes place via equation 1.15

$$H_3PO_4 \rightarrow H_2PO_4^- + H^+ \qquad\qquad \text{Equation 1.16}$$

$$3Mn^{2+} + 2H_2PO_4^- \rightarrow Mn_3(PO_4)_2 + 4H^+ \qquad\qquad \text{Equation 1.17}$$
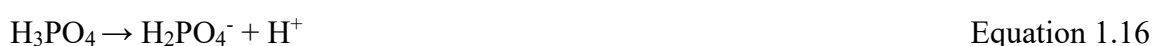
Phosphoric acid reacts with metal which is oxidized to ferrous cation (Fe^{2+}) followed by reaction a between phosphate anion and ferrous anion, resulting in the formation of ferric phosphate. During this reaction, the protons from an acidic solution and are reduced to hydrogen (H_2). according to the reactions shown below:

$$Fe \rightarrow Fe^{2+} + 2e^-$$

Equation 1.18

$$2H^+ + 2e^- \rightarrow H_2$$

Equation 1.19

$$Fe^{2+} + PO_4{}^{3-} \rightarrow FePO_4 + e^-$$

Equation 1.20

Finally, the manganese phosphate is precipitated (Equations (8) and (9)). The optimal pH is above 2.5 .

$$3Mn^{2+} + 2H_2PO_4{}^- \rightarrow Mn_3(PO_4)_2 + 4H^+$$

Equation 1.21

$$5Mn^{2+} + 4H_2PO_4{}^- \rightarrow Mn_2H_2(PO_4)_4 + 6H^+$$

Equation 1.22

The use of a reaction accelerator such as nitric acid prevents interaction between the metal surface and emitted bubbles of hydrogen. The presence of iron on the second oxidation rate in the bath results in the formation of a coating consisting of a mixed hureaulite, i.e., a mixed iron–manganese orthophosphate with the sum formula $(Mn, Fe)_5H_2(PO_4)_2 \cdot 4H_2O$.

Depending on the concentration of the phosphate bath, manganese phosphate coatings tend to precipitate as a combination of secondary and tertiary phosphates, which are formed from soluble primary phosphates in the bath. [87] Manganese phosphate coatings, like all phosphate coatings, are thin insulating films with pores which are formed as a result of the various crystal sizes of the coating which cover the surface. This results in the film not being directly involved in any electrochemical reaction and tend to exhibit greater porosity than other phosphate based coatings but decreased insulating ability in comparison to iron and zinc phosphate coatings resulting in suppression of anodic and cathodic reactions on any metal substrate. Since corrosion can occur at the bottom of the pore, corrosion resistance is increased as film thickness is increased, since the rate of transport of corrosive species is increased. [88] As a steel coating, manganese phosphate coatings can be successfully produced at 90 °C.[89] At 90 °C, two distinct phosphate layers form, an Fe-rich inner layer and a Mn-rich outer layer, which was caused by early-stage iron dissolution causing a high Fe^{2+} concentration and increasing pH would produce favourable conditions for Fe and mn co-precipitation. At lower temperatures, the deposition of phosphate from the conversion bath was less favourable.

1.6.2.3. Iron phosphate conversion coatings

Iron phosphate coatings can be created on steel surfaces by immersion in phosphate baths at a pH pf 3.5 - 5.5, where fine crystals of $FePO_4$ and $Fe_3(PO_4)_2$ are formed [90] A limiting factor in the use of iron-phosphate coatings is the reduced surface coverage of the metal surface, which results in an increased corrosion rate of coated metal substrates. This problem is remedied through the addition of nitrite containing additives which allows the formation of smaller phosphate crystals more closely packed together. It was also found that increased immersion time caused the formation of needle-like phosphate crystals with a greater phosphate concentration, which also resulted in greater surface coverage. [91] Like other conversion coatings, iron phosphate coatings must provide optimal adhesion between the metal substrate and subsequent coatings. The addition of sodium nitrite in the phosphating bath as an accelerator is key for the subsequent corrosion stability and adhesion characteristics of polyester coatings on steel. [92] It was shown that without the addition of nitrite accelerants to the phosphate bath, the porosity of the iron-phosphate coating decreased. Electrochemical impedance measurements of the polyester coating found a higher impedance of pre-treated steel, compared to bare steel, and decreases more slowly in the presence of a corroding agent compared to bare steel, which indicates good corrosion resistance properties. When nitrate and nitrate-free phosphate coatings were compared, it was found that nitrate-free coatings had a higher pore resistance and lower coating capacitance than phosphate coatings with nitrates, indicating greater stability of nitrate-free coatings in corrosive environments. The measurements of time-dependent double layer capacitance (C_{dl}) and charge transfer resistance (R_{cT}) illustrate the disbondment of the organic coating and underfilm corrosion. Nitrate-free coatings showed one-time constant behaviour, so C_{dl} and R_{cT} could not be determined, which confirmed the increased corrosion stability. However nitrated coatings showed a constant value of R_{CT} and a slow increase in $C_{dl,}$ which shows that accelerator free baths are more efficient coatings than phosphating baths with accelerators present.

1.6.3 Metal oxide conversion coatings

The corrosion resistant coatings that are the subject of this thesis for use on colour-coated steel is based on metal oxides, such as zirconia and titania. These coatings are environmentally benign and produce sufficient corrosion resistance. The coating baths normally used to form these conversion coatings are aqueous solutions of hexafluorotitanic

acid or hexafluorozirconic acid. For aluminium parts, the cleaning process creates an oxide layer on the surface, which is subsequently dissolved by the aggressive fluoride ions present in the bath according to the following:

$$Al^{3+} + ZrF_6^{2-} \rightarrow AlF_6^{3-} + Zr^{4+}$$ Equation 1.23

$$3Zn^{2+} + ZrF_6^{2-} \rightarrow 3ZnF_2 + Zr^{4+}$$ Equation 1.24

$$Al^{4+} + TiF_6^{2-} \rightarrow AlF_6^{3-} + Ti^{4+}3Zn^{2+} + TiF_6^{2-} \rightarrow 3ZnF_2 + Ti^{4+}$$ Equation 1.25
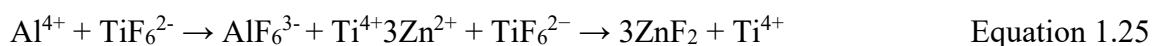
Oxygen reduction and hydrogen evolution then occurs at the cathodic sites:

$$O_2 + 4H^+ + 4e^- \rightarrow 2H_2O$$ Equation 1.26

$$2H^+ + 2e^- \rightarrow H_2$$ Equation 1.27

The cathodic reactions cause local alkalisation resulting in an increase in pH which drives the hydrolysis of the fluorometalates to form precipitated hydrated metal oxide layers, as shown:[93]

$$ZrF_6^{2-} \text{ (aq)} + 4OH^- \rightarrow ZrO_2 \cdot 2H_2O \text{ (s)} + 6F^-_{\text{(aq)}}$$ Equation 1.28

$$TiF_6^{2-} \text{ (aq)} + 4OH^- \rightarrow TiO_2 \cdot 2H_2O \text{ (s)} + 6F^-_{\text{(aq)}}$$ Equation 1.29

$$Ti^{4+} + 3H_2O \rightarrow TiO_2 \cdot 2H_2O + 4H^+$$ Equation 1.30

$$Zr^{4+} + 3H_2O \rightarrow ZrO_2 \cdot 2H_2O + 4H_2$$ Equation 1.31

The use of hexafluorozirconate on Al alloys also contributes to the formation of a Al-Zr-O-F hydrated layer within the conversion coating structure. This layer increases the hydrophilicity of the surface. This hydrated layer consists of aqueous fluoride ions which continue to further etch the surface of the substrate and subsequently results in a lower corrosion resistance of the surface [94]

On steel substrates, the process of zinc corrosion in Ti- or Zr-conversion baths is a combination of anodic zinc dissolution, and cathodic hydrogen evolution or oxygen reduction. which is the rate determining process. [95] During the initial stage of conversion layer formation, the primary zinc layer on the steel surface is etched and replaced by a thin Zr-based oxide/hydroxide layer.[96] Hydrogen evolution occurs and hydrated oxides of Zr, Ti and Zn form, accompanied by HF and H_2 evolution. HF can dissolve Zn and ZnO to form ZnF_2.[97] Native Zn oxide layer can also be dissolved by "free" hexafluorides or fluorides as shown:[98]

$$Zn(OH)_2 + xF^- \rightarrow ZnF_x^{(2-x)} + 2OH^- \hspace{3cm} \text{Equation 1.31}$$

Zinc from the galvanised steel surface is incorporated into the conversion layer consisting of ZnO, ZnF_2 and $Zn (OH)_2$. The formation of $Zn(OH)_2$ forms a greater protective layer due to its lower electrical conductivity, helping to suppress corrosion reactions on the surface. [99]

Both zirconium and titanium-based coatings have been used to provide corrosion protection as a result of the health and environmental issues associated with chromate and phosphate coatings. Ti and Zr coatings are significantly thinner than chromate and phosphate coatings, with coating thicknesses generally between 10 - 80 nm and are generally transparent, which provides a unique problem in knowing when the coating has been deposited.

Recently research has been conducted on the formation and analysis of Ti, Zr and mixed Ti/Zr based coatings.[100] In a study by Chen et al. a coloured zirconium based coating was prepared from potassium hexafluorozirconate and the morphology and composition of the coating was analysed by optical microscopy, scanning electron microscopy (SEM) energy dispersive x-ray spectroscopy (EDX) and x-ray diffraction (XRD). [101] Optical microscopy clearly showed a colour change from a silver white to dark grey, indicating the formation of a coating. The coating microstructure was analysed by SEM, which reveals the coating is composed of needle or ribbon-like microcrystals which are orientated parallel to the substrate surface. This forms a microcrystalline and microporous structure, which is expected to improve paint adhesion due to the formation of mechanical interlocks between the paint and coating.

The corrosion performance of zirconium-based coatings has also been studied on aluminium alloys with the corrosion performance and morphological properties of zirconium coatings on aluminium through variation in the pH, immersion time, temperature and Zr concentration. [102] SEM/EDX analysis revealed that the Zr coating covered the aluminium heterogeneously, with increased deposition on or around intermetallic particles which are cathodic sites that the pre-treatment preferentially deposits from. These intermetallic particles were covered by the coating, which resulted in increased resistance to pitting corrosion as a result of the reduced cathodic activity of the intermetallics on the surface. Measurements performed by EDX and open circuit potential (OCP) demonstrated a high stability of the zirconium on the surface of the aluminium even at immersion times of 6 minutes in corrosive solution. The dissolution rate of aluminium in corrosive media was at its lowest when treated at a pH of 4.5, an immersion time of 3 minutes, a bath temperature of 25 °C and a Zr concentration of 100 mg/l.

The zirconium coating also provided increased adhesion of epoxy paint to the aluminium compared to untreated aluminium.

1.6.4 Titanium-based conversion coatings

As well as zirconium-based conversion coatings, titanium-based conversion coatings (TCC) are also a good alternative to CCCs in coating metal alloys, with Tata Steel using titanium oxide as the basis for their coating on their organically coated steel range. Titanium coatings are based on titanium tetrachloride or hexafluorotitanic acid, with phosphoric, boric or nitric acid added to adjust the pH and fluoride additives to increase surface activation and act as cathodic inhibitors, inhibiting cathodic oxygen reduction. [93]

The mechanism of deposition of a TCC on steel undergoes the following steps. After initial immersion, fluoride ions present in the conversion bath attack and remove the naturally formed oxide layer on the surface of the steel. This is known as an etch-deposition process, where the pre-treatment etches off the oxide layer on the surface before deposition of the protective layer. Intermetallic present on the surface are suitable sites for cathodic oxygen reduction and hydrogen evolution, resulting in an increase of local pH on and around these intermetallic sites, which allows deposition of the TCC and complete surface coverage occurs shortly thereafter.

Within academia, research has been conducted on TCCs since the 1990s on a variety of substrates, such as aluminium or steel. Initially TCCs were seen as a novel coating alternative to CCCs, which have now become a reality due to the phasing out of CCCs. Coloma *et al* studied the use of TCCs (along with other inorganic salts) on aluminium alloys for aircrafts [103] In the experiments performed, potassium permanganate and sodium molybdate corrosion inhibitors were combined with potassium hexafluorozirconate and two different aluminium alloys, known as AA20204 and AA7075, were immersed for 3 minutes at a temperature of 20 °C and a pH of 5. The amount of $KMnO_4$ and Na_2MoO_4 were kept at 20 g/L and K_2TiO_6 was varied at concentrations of 4 and 8 g/L respectively and the concentration of H_2ZrF_6 was kept between 6 - 8 g/L. This can be seen in Table 1.2 below.

Table 1.2. Concentrations of salts and inhibitors used by Caloma et al. [104]

Reference Bath	K_2TiO_6 (g/L)	H_2ZrF_6 (g/L)	$KmnO_4$ (g/L)	Na_2MoO_4 (g/L)
1	4	6	20	20
2	0	8	20	20
3	0	0	20	20
4	8	0	20	20

All four coatings improved the corrosion resistance of the alloys, but the best performing coatings consisted of zirconium. With H_2ZrF_6, the oxides, hydroxides and fluorides present in the conversion baths preferentially deposited on the intermetallics present on the surface of the alloys. This led to a reduction of the electrochemical potential difference between the intermetallics and the bulk aluminium and provided significant corrosion protection. In comparison, the presence of Ti in the conversion baths led to detrimental salt deposition on the surface of the alloys, leading to reduced corrosion protection. The corrosion potential (E_{corr}), the pitting potential (E_{pit}), the corrosion current density (J_{corr}), the Tafel slopes for the anodic (βa) and cathodic (βc) can be seen below in Table 1.3.

Table 1.3. Values of corrosion potential, pitting potential, corrosion current density and anodic and cathodic Tafel slopes obtained for the two aluminium alloys.

Reference Alloy and Bath	E_{corr} (V)	E_{pit} (V)	J_{corr} (A/cm^2)	βa (mV/Dec)	βc (mV/Dec)
2024 - Bare	-0.197	-0.197	1.74×10^{-6}	7.5	22
2024 – 1	-0.523	-0.227	1.35×10^{-6}	184	173
2024 – 2	-0.44	-0.224	5.55×10^{-7}	161	159
2024 – 3	-0.43	-0.097	1.59×10^{-6}	216	161
2024 – 4	-0.769	-0.252	9.29×10^{-7}	327	208
7075 - Bare	-0.436	-0.436	1.33×10^{-6}	5.6	360
7075 – 1	-0.565	-0.152	1.54×10^{-7}	164	115
7075 – 2	-0.625	-0.128	1.34×10^{-7}	112	131
7075 – 3	-0.694	-0.104	3.2×10^{-7}	284	133
7075 – 4	-0.666	-0.329	1.97×10^{-7}	150	128

What can be shown is that AA7075 generally has more negative E_{corr} values and less negative E_{pit} values, this is a result of the greater Cu content of the alloy. This allows a more favourable deposition of inorganic salts on the Cu rich intermetallics present on the surface, which aids in the prevention of corrosion occurring.

Several studies have been conducted on titanium conversion coatings on steel. On a galvanised steel, a titanium conversion coating forms a thin film of TiO_2 on the surface of the steel. This was shown in a study by Zhu *et al.* who studied the corrosion resistance of electro-galvanised steel treated with a TCC. [105] In this study, *Zhu et al.* used $TiCl_4$ and HNO_3 to create the TiO_2 coating and H_2SiF_6 was used to supply F^- that etch the surface of the steel ready for titanium deposition. The coating was deposited through immersing the galvanised steel in the conversion bath. XPS was used to better understand the chemical composition of the conversion coating, this produced values of Ti 21.39, Si 4.68, Zn 9.50, O 64.43 (atomic %). The XPS of Ti produced peaks of 464.4 eV and 458.5 eV (Ti 2P $_{1/2}$ and Ti 2P $_{3/2}$). The peak for O 1s appeared at 530.1 eV. Zn 2P $_{1/2}$ and Zn 2P $_{3/2}$ produced peaks at 1044.9 eV and 1021.7 eV. The Si 2P spectrum exhibits a peak at 101.8 eV. Based on the XPS results, it can

be concluded that the TCC on the zinc layer consists of ZnO, TiO$_2$ and Zn$_4$Si$_2$O$_7$(OH)$_2$. Through salt spray testing, the influence of immersion time and subsequent coating thickness was evaluated. A lower immersion time (>30 seconds) produced coatings with a low Ti and Si content, resulting in decreased efficacy. An immersion time of 240 seconds produced the best results, however for industrial applications, this immersion time is too long. An immersion time of 60 – 90 seconds was shown to have the ability to inhibit the cathodic corrosion reaction, which is what is required on an industrial scale. Longer immersion times results in the formation of a heterogenous surface and the formation of micro-cracks which allow the cathodic and anodic corrosion reactions to continue.

The process of the formation of a TCC is as follows: firstly, anodic zinc dissolution and cathodic hydrogen ion and oxygen reduction occurs, which results in an increase in pH and then formation of titanium dioxide hydrate, zinc hydroxide and silicon hydroxide. The Si(OH)$_4$ then condenses with any OH containing surface compounds which it can react with, generally Zn(OH)$_4$. This results in Zn disilicates forming on the surface, creating Zn$_4$Si$_2$O$_7$(OH)$_2$. This is followed by dehydration of these compounds on the zinc surface and forms the TCC.

In a different study, Bamoulid *et al.* combined a conversion layer and TiO$_2$ deposit on the surface of stainless steel via a sol-gel process. [106] A conversion coating was created via chemical oxidation of steel substrate in a bath of acidic solution containing thiosulfate and propargyl alcohol before subsequent sol-gel formation of TiO$_2$. Salt spray analysis of these coatings shows that the application of a conversion layer alone is not sufficient to protect the steel substrate, whereas a combination of conversion layer/TiO$_2$ showed very good corrosion resistance showing no rust formation after 192 hours of salt spray testing, illustrating the effectiveness of titania based coatings.

1.6.5. Influence of ageing on conversion coatings.

The influence of ageing on conversion coatings has been studied on aluminium and its alloys using chromium based conversion coatings. Liu et al studied ageing of Cr^{VI} based pre-treatment up to 48 hours and found the thickness of the deposited coating was similar after ageing in air for 1-48 hours compared to a freshly deposited layer which was attributed to loss of free or weakly bound water from the coating which limits any restructuring of the coating. [107] The effect of ageing temperature and time on Cr^{III} based pre-treatment on

aluminium alloy was investigated by Li and Swain, who aged the coating overnight in temperatures up to 150°C and aged at room temperature for 1-7 days. When the ageing temperature was increased, the coating was found to undergo dehydration at elevated temperatures. This causes a coating with more hydrophobic properties to form which increases corrosion resistance which was linked to the loss of weakly bound water and improved barrier properties to the transport of reactants through the coating, although ageing at 150°C causes excessive cracking of the coating and detachment from the metal surface. Increasing the ageing time was found to increase corrosion resistance of the coating by a factor of 4 by forming an aluminium oxide layer on exposed metal sites, and again increases the hydrophobicity of the surface, with the best performance observed after 7 days of ageing. [108]

In influence of ageing of non-chromate based pre-treatment on zinc substrates has not been extensively studied, with aluminium being a typically studied substrate with chromate based pre-treatments. [109,110] The ageing of commercial zirconic acid pre-treatment on HDG substrates has been studied in an investigation by Puomi et al. who studied the wetting behaviour of polyurethane coatings deposited on pre-treated HDG. [111] Contact angle measurements showed an increase in the measured contact angle as ageing is increased up to 100 hours, indicating that the nature of the surface.

1.6.6 Protection of organic coatings using conversion coatings

Organic coatings act as a protective barrier against corrosion and consist of an organic backbone and generally classified from the resin they are composed from, such as vinyl or acrylic based resins. The efficiency of organic coatings to resist corrosion relies on their ability to hinder the transport of water, oxygen, and ions through the coating. For an organic coating not possessing pigments the transfer rate for oxygen and water would be relatively high, so the limiting factor for any corrosion would be ionic transfer.[112] The rate of ionic movement between anodic and cathodic sites on the surface is reduced by an organic coating as it is believed the coating acts as an electrical resistor, therefore a coated surface will have a significantly reduced rate of charge transfer compared to that of a non-coated metal surface. The adhesion of the coating to the metal surface when subjected to a high humidity environment is another factor that influences the corrosion performance of any coating.[113]

Coatings are generally formulated from a solvent, resin, pigments, filler, and additives and when applied to the underlying metal, they provide a continuous, homogeneous coating that prevents cracking and structure breakdown during stress, water permeability, and physical aging and are considered a vital part to most organic coating systems. [114]

Paints used for anti-corrosion protection composed of a combination of polymers, resins, additives, solvents, pigments, and extenders. The composition of most high-tech paints are composed of 50-80 % of volatile organic compounds (VOCs) by mass in order to appropriately dissolve the resins and dilute the paint. [115] Degradation of organically-coated metals usually begins when a corrosive species penetrate at the coating-substrate interface through coating defects, where a corrosion induced failure mechanism such as cathodic delamination can occur, whereby the cathodic reaction at the defect, or delamination front, generates hydroxyl ions and creating a highly alkaline environment, driving the coating failure. [116] The coating failure mechanism proposed by Gonzalez *et al.* attributes coating failure to the solubilisation of the metal oxide coating at the coating-metal interface. This oxide dissolution results in the disruption of the metal-coating bonds, and the high pH in the cathodic areas leads to localised attack of the coating at the substrate-coating interface. [100]

In order to prevent these corrosion mechanisms from occurring, corrosion inhibitors are added to organic coatings, for example, Galliano and Landolt investigated the addition of a carboxylic acid based organic inhibitor compared to a phosphate based inorganic corrosion inhibitor added to an epoxy coating on steel. [117] Adhesion testing of each coating showed that both coatings showed a significantly greater substrate-coating bond strength compared to the blank coat with the inorganic coating requiring the greatest pull-off force.

If corrosion inhibitors are not added directly to the organic coating, a conversion coating is applied directly to the steel surface with the organic coating placed on top. On steels, mainly epoxy topcoats deposited onto conversion coatings have been studied. [118–120] Sababi et al investigated the dry and wet adhesion of epoxy coated commercial Zr-based pre-treatments on carbon steel, using EIS to study coating degradation, with SKP and pull off experiments to investigate adhesion strength and delamination kinetics. SKP testing of the epoxy coating shows that the delamination front without pre-treatment is greater than with Zr-treated steel, with a 2mm decrease after 56 hours. EIS experiments showed that the Zr-based treatment has a beneficial effect on the interfacial bonding stability between the epoxy layer and the underlying carbon steel with a secondary time constant in the phase angle not seen in a pre-

treated which is seen in an uncoated substrate which indicates increased stability of the interfacial region upon water molecule diffusion with the Zr-based pre-treatment at the epoxy/carbon steel interface. Adhesion testing showed improved wet and dry adhesion for pre-treated surfaces was higher than untreated steel after 70 days exposure to 0.1M NaCl and is improved under wet conditions and is more durable due to increasing the interfacial bonding stability and influencing the water molecule interaction mechanism at the interface. [121] Further investigation on the effect of Zr-based pre-treatment on the cathodic delamination of epoxy coatings on steel has been conducted by Khun and Frankel. [122] Similarly to the results reported by Sababi et al. the delamination of epoxy coatings in 0.5M Na_2SO_4 solution was much slower for a pre-treated surface compared to an untreated steel surface as a result of the stronger adhesion of the coating on the pre-treated surface, and in acidic solutions the rate of cathodic delamination was still much slower for pre-treated surfaces, with the delamination behaviour attributed to anodic delamination of the coatings induced by the anodic dissolution of the interfaces in addition to the cathodic delamination of the epoxy coating. [121]

On galvanised steels, the corrosion and adhesion of organic lacquers and epoxy topcoats applied onto Zr-based pre-treatment has been studied. The de-adhesion kinetics of an organic lacquer applied to a zirconium oxyhydroxide gradient film was investigated by Stromberg et al using Scanning Kelvin Probe. [123] A conversion coating was applied by dip coating onto the steel surface for varying times, with lower conversion times producing thinner conversion coatings. The de-adhesion kinetics of an organic lacquer is influenced by the conversion time, with lower conversion times impeding oxygen reduction and the Volta potential being close to the zinc defect potential prevents the formation of driving force for cathodic delamination.

The adhesion of an epoxy topcoat on a hexafluorozirconic acid based conversion coating containing nickel was investigated by Asemani et al. [124] Addition of Ni to the coating layer had an adverse effect on the adhesion strength, but deposition of a Ni layer onto the Zr coating improved the adhesion strength of the bonding between the epoxy coating and the Zr layer by improving the surface roughness and enabling mechanical interlocking.

1.7 Electrochemical corrosion testing of organic coatings

As mentioned in the previous section on the use of pre-treatments to protect organic coatings, scanning electrochemical techniques are now commonly used to study the kinetics and thermodynamics of metallic corrosion in aqueous conditions. There are a range of different techniques which all use a reference micro-tip probe to scan close above the corroding metal surface, which measures information such as local potential, potential gradients or current. There are three main variants of scanning electrochemical techniques used for corrosion investigation: scanning reference electrode technique (SRET); Scanning vibrating electrode technique (SVET); and, scanning Kelvin probe (SKP). [125] For example, Grundmeier *et al*. have written a comprehensive review on SKP, SVET and EIS and how these techniques can be utilised in the analysis of how organic coatings protect metallic substrates from corrosion mechanisms like cathodic delamination and filiform corrosion. [126] The proceeding chapters use the SKP technique and so only this technique will be covered for further review.

1.7.1. Organic coating failure mechanisms

Corrosion driven organic coating delamination is the process in which a relatively intact coating becomes physically separated from the underlying substrate and is key failure process which effects organically coated metal products. The two processes of corrosion driven coating delamination that typically occur are cathodic delamination and filiform corrosion (FFC), and both of these phenomena tend to occur due to defects in the organic coating which allows species from an external electrolyte to bypass the organic coating.

Cathodic delamination is a common and economically important mechanism of coating delamination on iron and zinc surfaces and occurs wherever a metallic substrate becomes exposed to scratches or cut edges during manufacturing or through damage. [127–130] Numerous studies have indicated that when iron or zinc substrates are exposed to an aqueous electrolyte, through coating defects, a cathodic delamination cell may be established whereby a thin layer of electrolyte penetrates beneath a delaminated coating and acts to couple anodic metal dissolution occurring at the defect to cathodic oxygen reduction occurring at the site of coating disbondment. At the cathode, an alkaline environment forms, and possible mechanisms for coating disbondment include; dissolution of amphoteric metal oxide film at the metal coating interface, base-catalysed polymer degradation, base-catalysed hydrolysis of interfacial bonds, and, attack on the polymer by hydrogen peroxide and other reactive

intermediates in cathodic oxygen reduction. [131] Koehler showed that cathodic delamination occurred only when group I cations were available to act as counter ions to cathodically generated hydroxide ions because only group I cations possess the hydrolytic stability and solubility at high pH necessary to support the strongly alkaline electrolyte. [128]

Another corrosion phenomenon that will be briefly touched on that also causes coating degradation is filiform corrosion and causes "hair-like" filaments which can be tracked away from the coating defect. FFC is regarded as a type of atmospheric corrosion which typically affects iron and aluminium surfaces which initiates at penetrative coating defects and producing the hair-like corrosion products. On steel (iron) surfaces, the mechanism of FFC is that filament advance is driven by differentia aeration which arises from mass transport of oxygen through the filament tail.[132] Cathodic oxygen reduction is considered to be localised at the droplet trailing edge and anodic metal dissolution located at the leading-edge of the electrolyte filled head. Compared to cathodic disbondment, FFC is considered to have an anodic disbondment mechanism on aluminium substrates, but controversy remains whether this is true for iron substrates due to the location of anodic and cathodic sites for corrosion sites which propagate on iron.

1.7.2 Investigating cathodic delamination using Scanning Kelvin Probe.

The most systematic work which pioneered the SKP technique on zinc surfaces was pioneered by Stratman et al in a series of experiments to investigate the possibility of through coating cation transport.[133–135] Samples were prepared in these studies which were analysed using the SKP apparatus similar to that shown in Figure 1.12. Using this sample preparation, a cathodic delamination cell becomes established and a thin layer of electrolyte ingresses beneath the delaminated coating. A schematic of how delamination occurs on the surface and how this tracks an E_{corr} vs distance profile can be seen in Figure 1.12
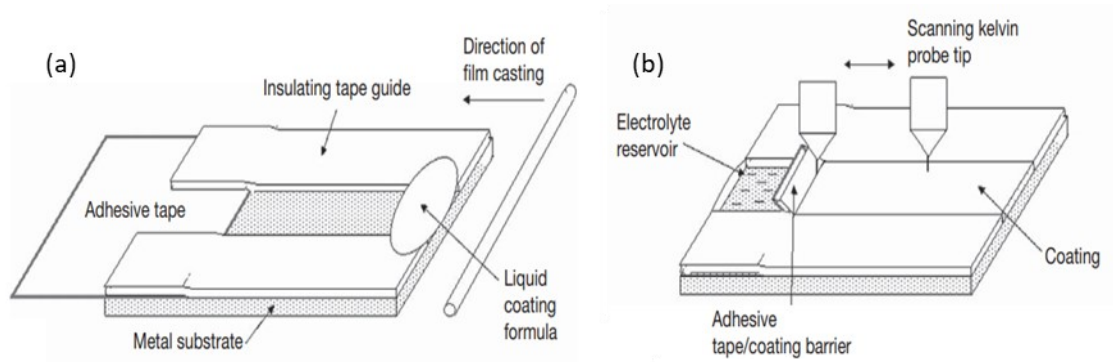
Figure 1.12. Diagram showing (a) sample preparation and (b) experimental procedure for a delamination experiment.
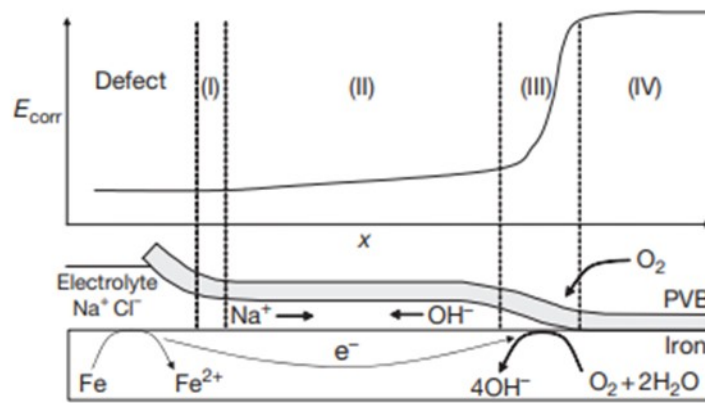
Figure 1.13. Schematic representation of the corrosion driven delamination cell showing correspondence with various regions of the time dependent E_{corr} profile.

As can be seen in Figure 1.13, there are several steps that are involved during the reaction that occurs in a delamination cell:

1. The region immediately next to the defect where E_{corr} is low and is similar to that of the freely corroding metal.

2. A region of E_{corr} gradient linking region (I) with region (III) below and resulting from ohmic resistance to ionic current flow in the thin under-coating electrolyte layer.

3. A region of sharp transition in E_{corr} corresponding to the cathodic delamination front where coating disbondment takes place.

4. A region of as yet undelaminated polymer where oxygen can diffuse to the metal surface, but electrolyte is not present, and metal cannot corrode. Here, E_{corr} (or the intact potential E_{intact}) is high.

The SKP technique has been used to study the effect of corrosion processes that occur underneath organic coatings on metallic substrates and has since been used to research organic coating degradation,[136] pigment inhibition[131,137–139] and understanding corrosion mechanisms that occur on metal surfaces.[140,141] SKP is a non-perturbing technique and does not hinder the corrosion process that occurs on the surface whilst the SKP measures the change in Volta potential associated with the corrosion processes occurring on the metal substrate surface. The SKP technique can measure the corrosion process in atmospheric conditions, which are especially damaging to metallic surfaces as a thin electrolyte layer will develop through adsorption and condensation reactions. Compared to traditional electrochemical techniques such as cyclic voltammetry, the use of SKP in atmospheric conditions is more beneficial as it does not rely on an electrolyte to connect the scanning and reference electrodes and does not require a reference electrode at all which allows the SKP to measure and map under-film corrosion phenomena. An example of how SKP has been used has been shown by Leng *et al.* who determined that the electrochemical reactions that take place at the substrate-electrolyte and substrate-polymer interfaces are responsible for coating delamination occurring on metallic substrates. [142] In this study, SKP was used to detect Volta potential differenced at polymer coating defects. These coating defects allow the diffusion of corrosive species from solution onto the substrate, causing corrosion reactions to occur and subsequent coating delamination. SKP measurements indicates an increase in Volta potential for every incremental increase in pH from 10-14 (starting from pH 9 and moving to a higher pH), which results in an increase of negatively charged species within the polymer coating. However, what was also observed was that Volta potential changes attributed to the change from pH 9 had an average increase of 15 mV/pH, with an overall potential change of 50 – 70 mV and required extreme conditions, compared to the much greater potential change of delamination (500 – 800 mV). Leng *et al.* concluded that the delamination change is due to a change of electrode potential during delamination and this change of potential is affected by the changing potential differences at the electrolyte-polymer interface. Numerous studies using the SKP have been conducted within Swansea University, with the SKP being highly useful in mapping corrosion phenomena occurring on the surface of organic coatings with

various corrosion inhibitors added such as chromates and phosphates in order to further protect steel surfaces. [138,143–145]

The literature analysed in this chapter investigates the various types of conversion coatings used as corrosion protection measures, and the corrosion behaviour of galvanised steel substrates such as hot dip galvanised (HDG) steel and 4.8%-Al steel. However within the literature the influence of alkaline cleaning on Galvalloy is absent, and the influence of alkaline cleaning on HDG steel with a pre-treatment applied has not been investigated in great detail. The aims of the research contained within this thesis is to investigate the corrosion driven cathodic disbondment behaviour of HDG and 4.8%-Al steels that have undergone alkaline cleaning, along with their in-situ corrosion behaviour which has been not been investigated thoroughly in the literature. The influence of these cleaning parameters on the corrosion behaviour of hexaflourotitanate pre-treatment on HDG will also be investigated to see how alkaline cleaning influences the performance of a model organic coating with pre-treatment applied.

1.8. References

1. Great Britain. Committee on Corrosion and Protection., Hoar TP, Great Britain. Department of Trade and Industry. Report of the Committee on Corrosion and Protection : a survey of corrosion and protection in the United Kingdom. 1971:129.

2. Cost of Corrosion Study - NACE. https://www.nace.org/resources/what-is-corrosion/corrosion-reference-library/cost-of-corrosion-study. Accessed November 17, 2021.

3. El-Meligi AA. Corrosion Preventive Strategies as a Crucial Need for Decreasing Environmental Pollution and Saving Economics. *Recent Patents Corros Sci*. 2010;2:22-33.

4. Trethewey KR, Chamberlain J. Corrosion for science and engineering, second edition. December 1995.

5. Catastrophic corrosion failure. https://www.corrosion-doctors.org/Forms-pitting/sewer.htm. Accessed November 17, 2021.

6. Griffiths CM. A Systematic Study of Phosphate Based Pigments to Inhibit the Cathodic Disbondment of Organically Coated Hot Dipped Galvanised Steels. 2019.

7. Pourbaix M. Thermodynamics and Corrosion. 1991:1-30. doi:10.1007/978-94-011-3636-5_1

8. Thompson WT, Kaye MH, Bale CW, Pelton AD. Pourbaix Diagrams for Multielement Systems. *Uhlig's Corros Handb Third Ed*. April 2011:103-109.

doi:10.1002/9780470872864.CH8

9. Perry. S; Gateman. S; Stephens. L; Mauzeroll. J. Pourbaix diagrams as a root for the simulation of polarization curves for corroding metal surfaces. 232rd ECS Meeting. https://www.researchgate.net/publication/320593379_Pourbaix_diagrams_as_a_root_f or_the_simulation_of_polarization_curves_for_corroding_metal_surfaces. Published 2017. Accessed February 13, 2020.

10. Plieth W. Electrochemistry for Materials Science. *Electrochem Mater Sci*. 2008. doi:10.1016/B978-0-444-52792-9.X5001-5

11. Wagner C, Traud W. On the interpretation of corrosion processes through the superposition of electrochemical partial processes and on the potential of mixed electrodes. *Corrosion*. 2006;62(10):843-855. doi:10.5006/1.3279894

12. Shreir, LL; Burstein GJR. *Shreir's Corrosion 4th Ed.* Amsterdam Elsevier Ltd; 1994.

13. Al-Hinai AT, Al-Hinai MH, Dutta J. Application of Eh-pH diagram for room temperature precipitation of zinc stannate microcubes in an aqueous media. *Mater Res Bull*. 2014;49(1):645-650. doi:10.1016/j.materresbull.2013.10.011

14. Mouanga M, Berçot P, Rauch JY. Comparison of corrosion behaviour of zinc in NaCl and in NaOH solutions. Part I: Corrosion layer characterization. *Corros Sci*. 2010;12(52):3984-3992. doi:10.1016/J.CORSCI.2010.08.003

15. Spathis P, Poulios I. The corrosion and photocorrosion of zinc and zinc oxide coatings. *Corros Sci*. 1995;37(5):673-680. doi:10.1016/0010-938X(95)80001-8

16. Mouanga M, Berçot P. Comparison of corrosion behaviour of zinc in NaCl and in NaOH solutions; Part II: Electrochemical analyses. *Corros Sci*. 2010;52(12):3993-4000. doi:10.1016/J.CORSCI.2010.08.018

17. Wint N, Khan K, Sullivan JH, McMurray HN. Concentration Effects on the Spatial Interaction of Corrosion Pits Occurring on Zinc in Dilute Aqueous Sodium Chloride. *J Electrochem Soc*. 2019;166(11):C3028-C3038. doi:10.1149/2.0051911JES/XML

18. Thomas S, Birbilis N, Venkatraman MS, Cole IS. Corrosion of zinc as a function of pH. *Corrosion*. 2012;68(1). doi:10.5006/1.3676630

19. McMurray H., Magill SR, Jeffs BD. Scanning reference electrode technique as tool for investigating localised corrosion phenomena in galvanised steels. *Ironmak Steelmak*. 1996;23. https://cronfa.swan.ac.uk/Record/cronfa29129. Accessed September 26, 2022.

20. Hosking NC, Ström MA, Shipway PH, Rudd CD. Corrosion resistance of zinc-magnesium coated steel. *Corros Sci*. 2007;49(9):3669-3695. doi:10.1016/j.corsci.2007.03.032

21. Volovitch P, Vu TN, Allély C, Abdel Aal A, Ogle K. Understanding corrosion via corrosion product characterization: II. Role of alloying elements in improving the corrosion resistance of Zn-Al-Mg coatings on steel. *Corros Sci*. 2011;53(8):2437-2445. doi:10.1016/j.corsci.2011.03.016

22. Smith WJ, Goodwin FE. Hot Dip Coatings. In: *Reference Module in Materials Science and Materials Engineering*. Elsevier; 2017. doi:10.1016/b978-0-12-803581-8.09214-6

23. Townsend, H. ; Zoccola, J. C.; Borzillo, A. R.; Horton JB. (PDF) Atmospheric Corrosion Behavior of Aluminum-Zinc Alloy-Coated Steel. Atmospheric Factors Affecting the Corrosion of Engineering Metals. https://www.researchgate.net/publication/305993317_Atmospheric_Corrosion_Behavior_of_Aluminum-Zinc_Alloy-Coated_Steel. Published 1978. Accessed February 3, 2020.

24. Sullivan J, Weirman C, Kennedy J, Penney D. Influence of steel gauge on the microstructure and corrosion performance of zinc alloy coated steels. *Corros Sci*. 2010;52(5):1853-1862. doi:10.1016/J.CORSCI.2010.02.032

25. Marder AR. The metallurgy of zinc-coated steel. *Prog Mater Sci*. 2000;45(3):191-271. doi:10.1016/S0079-6425(98)00006-1

26. Chen ZY, Persson D, Leygraf C. Initial NaCl-particle induced atmospheric corrosion of zinc-Effect of CO2 and SO2. *Corros Sci*. 2008;50(1):111-123. doi:10.1016/j.corsci.2007.06.005

27. ASM International. Handbook Committee. *ASM Handbook, Vol. 13B, Corrosion: Materials*.; 2005.

28. Moreira AR, Panossian Z, Camargo PL, Moreira MF, Da Silva IC, Ribeiro De Carvalho JE. Zn/55Al coating microstructure and corrosion mechanism. *Corros Sci*. 2006;48(3):564-576. doi:10.1016/J.CORSCI.2005.02.012

29. Jones DRH, Ashby MF. Wet Corrosion of Materials. In: *Engineering Materials 1*. Elsevier; 2019:431-447. doi:10.1016/b978-0-08-102051-7.00026-9

30. Tang N-Y, Liu Y. Corrosion Performance of Aluminum-containing Zinc Coatings. *ISIJ Int*. 2010;50(3):455-462. doi:10.2355/isijinternational.50.455

31. Persson D, Thierry D, LeBozec N. Corrosion product formation on Zn55Al coated steel upon exposure in a marine atmosphere. *Corros Sci*. 2011;53(2):720-726. doi:10.1016/j.corsci.2010.11.004

32. Li Y. Formation of nano-crystalline corrosion products on Zn-Al alloy coating exposed to seawater. *Corros Sci*. 2001;43(9):1793-1800. doi:10.1016/S0010-938X(00)00169-4

33. Moreira AR, Panossian Z, Camargo PL, Moreira MF, Da Silva IC, Ribeiro De Carvalho JE. Zn/55Al coating microstructure and corrosion mechanism. *Corros Sci*. 2006;48(3):564-576. doi:10.1016/j.corsci.2005.02.012

34. LeBozec N, Thierry D, Persson D, Stoulil J. Atmospheric corrosion of zinc-aluminum alloyed coated steel in depleted carbon dioxide environments. *J Electrochem Soc*. 2018;165(7):C343-C353. doi:10.1149/2.0721807jes

35. Gallagher C. The corrosion of Zn-4.8%Al sacrificial coatings used for the protection of steel. January 2022. doi:10.23889/SUTHESIS.59489

36. Yang L, Zhang Y, Zeng X, Song Z. Corrosion behaviour of superplastic Zn-Al alloys in simulated acid rain. *Corros Sci*. 2012;59:229-237. doi:10.1016/j.corsci.2012.03.013

37. Zhang X, Leygraf C, Odnevall Wallinder I. Atmospheric corrosion of Galfan coatings on steel in chloride-rich environments. *Corros Sci*. 2013;73:62-71. doi:10.1016/j.corsci.2013.03.025

38. Marcus P, Maurice V, Strehblow HH. Localized corrosion (pitting): A model of passivity breakdown including the role of the oxide layer nanostructure. *Corros Sci*. 2008;50(9):2698-2704. doi:10.1016/j.corsci.2008.06.047

39. Odnevall I, Leygraf C. Formation of NaZn4Cl(OH)6SO4 · 6H2O in a marine atmosphere. *Corros Sci*. 1993;34(8):1213-1229. doi:10.1016/0010-938X(93)90082-R

40. Kasperek J, Verchere D, Jacquet D, Phillips N. Analysis of the corrosion products on galvanized steels by FTIR spectroscopy. *Mater Chem Phys*. 1998;56(3):205-213. doi:10.1016/S0254-0584(98)00167-9

41. Leygraf, T; Graedel T. Atmospheric Corrosion. John Wiley & Sons, New York. https://books.google.co.uk/books?hl=en&lr=&id=eOYGCwAAQBAJ&oi=fnd&pg=PP15&ots=DIbGrSj2Vs&sig=IBTgJSGsyY__Y8b8xUFlmQWZ9kk&redir_esc=y#v=onepage&q&f=false. Published 2000. Accessed February 4, 2020.

42. Theiss FL, Sear-Hall MJ, Palmer SJ, Frost RL. *Zinc Aluminium Layered Double Hydroxides for the Removal of Iodine and Iodide from Aqueous Solutions*. Vol 39. http://eprints.qut.edu.au/. Accessed February 4, 2020.

43. Schürz S, Luckeneder GH, Fleischanderl M, et al. Chemistry of corrosion products on Zn-Al-Mg alloy coated steel. *Corros Sci*. 2010;52(10):3271-3279. doi:10.1016/j.corsci.2010.05.044

44. Odnevall I, Publication CL-A special technical, 1995 U. *Reaction Sequences in Atmospheric Corrosion of Zinc*. Philadelphia, PA; 1995. https://books.google.com/books?hl=en&lr=&id=7fyVHJbEwaMC&oi=fnd&pg=PA215&ots=xEvgXJzzHm&sig=4mD3uXCIfmySipI_31DxiuKgrBk. Accessed June 27, 2022.

45. Biber HE. Scanning auger microprobe study of hot-dipped regular-spangle galvanized steel: Part I. surface composition of As-produced sheet. *Metall Trans A*. 1988;19(6):1603-1608. doi:10.1007/BF02674035

46. Rodnyansky A, Warburton YJ, Hanke LD. Segregation in hot-dipped galvanized steel. *Surf Interface Anal*. 2000;29(3):215-220. doi:10.1002/(SICI)1096-9918(200003)29:3<215::AID-SIA703>3.0.CO;2-X

47. Saarimaa V, Markkula A, Juhanoja J, Skrifvars BJ. Novel insight to aluminum compounds in the outermost layers of hot dip galvanized steel and how they affect the reactivity of the zinc surface. *Surf Coatings Technol*. 2016;306:506-511. doi:10.1016/j.surfcoat.2015.11.014

48. Mcdevitt E, Morimoto Y, Meshii M. Characterization of the Fe-Al Interfacial Layer in a Commercial Hot-dip Galvanized Coating. *ISIJ Int*. 1997;37(8):776-782. doi:10.2355/isijinternational.37.776

49. Hörnström SE, Hedlund EG, Klang H, Nilsson J-O, Backlund M, Tegehall P-E. A surface study of the chemical pretreatment before coil coating of hot dip zinc-coated steel. *Surf Interface Anal*. 1992;19(1-12):121-126. doi:10.1002/sia.740190124

50. Adhikari S. *Alkaline Dissolution of Aluminum: Surface Chemistry and Subsurface Interfacial Phenomena Recommended Citation*. https://lib.dr.iastate.edu/rtd. Accessed March 20, 2020.

51. Maeda S. Surface chemistry of galvanized steel sheets relevant to adhesion

performance. *Prog Org Coatings*. 1996;28(4):227-238. doi:10.1016/0300-9440(95)00610-9

52. Schoeman L, Burty M. Cleaning Optimization of Hot-Dip Galvanized Steel Surfaces in Preparation for Paint Application. *Mater Sci Forum*. 2018;941:1772-1777. doi:10.4028/www.scientific.net/MSF.941.1772

53. Berger R, Bexell U, Stavlid N, Grehk TM. The influence of alkali-degreasing on the chemical composition of hot-dip galvanized steel surfaces. *Surf Interface Anal*. 2006;38(7):1130-1138. doi:10.1002/sia.2364

54. Puomi P, Fagerholm HM, Rosenholm JB, Sipilä R. Effect of skin pass rolling on the primer adhesion and corrosion resistance of hot-dip galvanized (HDG) steel. *J Adhes Sci Technol*. 2000;14(4):583-600. doi:10.1163/156856100742753

55. Puomi P, Fagerholm HM. Performance of silane treated primed hot-dip galvanised steel. *Anti-Corrosion Methods Mater*. 2001;48(1):7-17. doi:10.1108/00035590110365273

56. Christian JW, Mahajan S. Deformation twinning. *Prog Mater Sci*. 1995;39(1-2):1-157. doi:10.1016/0079-6425(94)00007-7

57. Saarimaa V, Markkula A, Arstila K, Manni J, Juhanoja J. Effect of Hot Dip Galvanized Steel Surface Chemistry and Morphology on Titanium Hexafluoride Pretreatment. *Adv Mater Phys Chem*. 2017;07(02):28-41. doi:10.4236/ampc.2017.72004

58. Saarimaa V, Lange C, Paunikallio T, et al. Evaluation of surface activity of hot-dip galvanized steel after alkaline cleaning. *J Coatings Technol Res*. 2020;17(1):285-292. doi:10.1007/s11998-019-00272-9

59. Chen XB, Chong K, Abbott TB, Birbilis N, Easton MA. Biocompatible strontium-phosphate and manganese-phosphate conversion coatings for magnesium and its alloys. In: *Surface Modification of Magnesium and Its Alloys for Biomedical Applications*. Vol 2. Elsevier Inc.; 2015:407-432. doi:10.1016/B978-1-78242-078-1.00015-3

60. A New Standard For Facades - Architecture Today. https://architecturetoday.co.uk/new-standard-facades/. Accessed March 20, 2023.

61. Ramezanzadeh B, Attar MM, Farzam M. Corrosion performance of a hot-dip galvanized steel treated by different kinds of conversion coatings. *Surf Coat Technol*. 2010;205(3):874-884. doi:10.1016/J.SURFCOAT.2010.08.028

62. Stankiewicz A. Self-healing nanocoatings for protection against steel corrosion. In: *Nanotechnology in Eco-Efficient Construction*. Elsevier; 2019:303-335. doi:10.1016/b978-0-08-102641-0.00014-1

63. Matin MA, Shaikh MAA, Hossain MA, et al. The Effects of Oxidation States and Spin States of Chromium Interaction with Sargassum Sp.: A Spectroscopic and Density Functional Theoretical Study. *Green Sustain Chem*. 2021;11(4):125-141. doi:10.4236/GSC.2021.114011

64. Weckhuysen BM, Wachs IE, Schoonheydt RA. Surface Chemistry and Spectroscopy of Chromium in Inorganic Oxides. *Chem Rev*. 1996;96:3327-3349. http://pubs.acs.org.openathens-proxy.swan.ac.uk/doi/pdf/10.1021/cr940044o.

Accessed January 16, 2018.

65. Kotasâ J, Stasicka Z. Chromium occurrence in the environment and methods of its speciation. https://ac.els-cdn.com/S0269749199001682/1-s2.0-S0269749199001682-main.pdf?_tid=1e244062-fab9-11e7-8a7c-00000aacb35d&acdnat=1516106044_f2f9f3fa3c41decfb46d672901817d9e. Accessed January 16, 2018.

66. Pourbaix Diagram | Diagram Site. http://www.printablediagram.com/pourbaix-diagram/. Accessed February 23, 2018.

67. Kendig, M W; Buchheit RG. Corrosion inhibition of aluminum and aluminum alloys by soluble chromates, chromate coatings, and chromate-free coatings - ProQuest. Corrosian. https://search-proquest-com.openathens-proxy.swan.ac.uk/docview/223131983?accountid=14680. Published 2003. Accessed February 23, 2018.

68. Thomas S, Birbilis N, Venkatraman MS, Cole IS. Self-repairing oxides to protect zinc: Review, discussion and prospects. *Corros Sci*. 2013;69:11-22. doi:10.1016/J.CORSCI.2013.01.011

69. Lytle FW, Greegor RB, Bibbins GL, Blohowiak KY, Smith RE, Tuss GD. *AN INVESTIGATION OF THE STRUCTURE AND CHEMISTRY OF A CHROMIUM-CONVERSION SURFACE LAYER ON ALUMINUM*. Vol 31.; 1995.

70. Osborne JH. Observations on chromate conversion coatings from a sol-gel perspective. *Prog Org Coatings*. 2001;41(4):280-286. doi:10.1016/S0300-9440(01)00143-6

71. Shen-Yang T, Ke-An L. The distribution of chromium(VI) species in solution as a function of pH and concentration. *Talanta*. 1986;33(9):775-777. doi:10.1016/0039-9140(86)80187-4

72. Kendig M, Addison R, Jeanjaquet S. The Influence of Adsorbed Oxo-Cr(VI) Species on the Zeta Potential in the Porous Oxide of Anodized Aluminum. *J Electrochem Soc*. 1999;146(12):4419. doi:10.1149/1.1392653

73. Xia L, McCreery RL. Chemistry of a Chromate Conversion Coating on Aluminum Alloy AA2024-T3 Probed by Vibrational Spectroscopy. *J Electrochem Soc*. 1998;145(9):3083. doi:10.1149/1.1838768

74. Zhao, J ;Frankel G. Corrosion Protection of Untreated AA-2024-T3 in Chloride Solution by a Chromate Conversion Coating Monitored with Raman Spectroscopy. *J Electrochem Soc*. 1998;145(7):2258. doi:10.1149/1.1838630

75. Schuman TP. Protective Coatings for Aluminum Alloys. In: *Handbook of Environmental Degradation of Materials: Second Edition*. Elsevier Inc.; 2012:503-538. doi:10.1016/B978-1-4377-3455-3.00017-1

76. Sankara Narayanan TSN. SURFACE PRETREATMENT BY PHOSPHATE CONVERSION COATINGS - A REVIEW. *RevAdvMaterSci*. 2005;9:130-177. http://eprints.nmlindia.org/337/1/Surface_pretreatment_by_phosphating_-_A_review_RAMS_paper.pdf. Accessed April 30, 2018.

77. Ferreira MGS, Zheludkevich ML, Tedim J, Yasakau KA. Self-healing nanocoatings for corrosion control. In: *Corrosion Protection and Control Using Nanomaterials*. Elsevier; 2012:213-263. doi:10.1533/9780857095800.2.213

78. Twite RL, Bierwagen GP. Review of alternatives to chromate for corrosion protection of aluminum aerospace alloys. *Prog Org Coatings*. 1998;33(2):91-100. doi:10.1016/S0300-9440(98)00015-0

79. L.Y. Niu; Z.H. Jiang; G.Y. Li; C.D. Gu; J.S. Lian. A study and application of zinc phosphate coating on AZ91D magnesium alloy. *Surf Coat Technol*. 2006;200:3021-3026. https://ac.els-cdn.com/S0257897204011338/1-s2.0-S0257897204011338-main.pdf?_tid=1c62b04e-1ae2-11e8-ab6e-00000aacb35f&acdnat=1519642088_4bc3c92b718709aae8f883fd835ec17c. Accessed February 26, 2018.

80. Nair UB. Calcium as a Phosphating Additive: An Overview. http://infohouse.p2ric.org/ref/25/24150.pdf. Accessed February 27, 2018.

81. Zeng R, Lan Z, Kong L, Huang Y, Cui H. Characterization of calcium-modified zinc phosphate conversion coatings and their influences on corrosion resistance of AZ31 alloy. *Surf Coat Technol*. 2011;205:3347-3355. doi:10.1016/j.surfcoat.2010.11.027

82. Zeng R-C, Zhang F, Lan Z-D, Cui H-Z, Han E-H. Corrosion resistance of calcium-modified zinc phosphate conversion coatings on magnesium-aluminium alloys. *Corros Sci*. 2014;88:452-459. doi:10.1016/j.corsci.2014.08.007

83. Westberg HJ, Nilsson PH, Rosén BG, Stenbom B. Manganese phosphating of gears and surface roughness consequence. *Tribol Ser*. 2000;38:145-153. doi:10.1016/s0167-8922(00)80120-0

84. Fang L, Xie L-B, Hu J, Li Y, Zhang ʾwen-Ting. Study on the growth and corrosion resistance of manganese phosphate coatings on 30CrMnMoTi alloy steel. *Phys Procedia*. 2011;18:227-233. doi:10.1016/j.phpro.2011.06.086

85. Duszczyk J, Siuzdak K, Klimczuk T, Strychalska-nowak J. Manganese Phosphatizing Coatings : The Effects of Preparation Conditions on Surface Properties. 2018;(Iii). doi:10.3390/ma11122585

86. Alvarado-Macías G, Fuentes-Aceituno JC, Salinas-Rodríguez A, Rodríguez-Varela FJ. Understanding the nature of the manganese hot dip phosphatizing process of steel. *J Mex Chem Soc*. 2013;57(4):328-336. doi:10.29356/jmcs.v57i4.197

87. Weng D, Jokiel P, Uebleis A, Boehni H. Corrosion and protection characteristics of zinc and manganese phosphate coatings. *Surf Coatings Technol*. 1997;88(1-3):147-156. doi:10.1016/S0257-8972(96)02860-5

88. Hawke D, Albright DL. A Phosphate-Permanganate Conversion Coating for Magnesium. https://ac.els-cdn.com/0026057696804284/1-s2.0-0026057696804284-main.pdf?_tid=1c73cb8f-77e0-4d7a-add5-7e2c84cb4f55&acdnat=1520326202_217aa1a314418bd64c982338c8b95732. Accessed March 6, 2018.

89. Wang C-M, Liau H-C, Tsai W-T. Effects of temperature and applied potential on the microstructure and electrochemical behavior of manganese phosphate coating. *Surf Coatings Technol*. 2006;201:2994-3001. doi:10.1016/j.surfcoat.2006.06.010

90. Popí J, Jegdí B, Bajat J, Veljoví Đ, Stevanoví S, Mišković c-Stankoví V. The effect of deposition temperature on the surface coverage and morphology of iron-phosphate coatings on low carbon steel. *Appl Surf Sci*. 2011;257:10855-10862.

doi:10.1016/j.apsusc.2011.07.122

91. Popić JP, Jegdić B V, Bajat JB, Mitrić M, Mišković-stanković VB. Determination of surface coverage of iron-phosphate coatings on steel using the voltammetric anodic dissolution technique. *J Serb Chem Soc*. 2013;78(1):101-114. doi:10.2298/JSC120706096P

92. Jegdić BV, Bajat JB, Popić JP, Mišković-Stanković VB. Corrosion stability of polyester coatings on steel pretreated with different iron–phosphate coatings. *Prog Org Coatings*. 2011;70(2-3):127-133. doi:10.1016/J.PORGCOAT.2010.11.004

93. Milošev I, Frankel GS. Review—Conversion Coatings Based on Zirconium and/or Titanium. *J Electrochem Soc*. 2018;165(3):C127-C144. doi:10.1149/2.0371803jes

94. Chidambaram D, Clayton CR, Halada GP. The role of hexafluorozirconate in the formation of chromate conversion coatings on aluminum alloys. *Electrochim Acta*. 2006;51(14):2862-2871. doi:10.1016/j.electacta.2005.08.022

95. George FO, Skeldon P, Thompson GE. Formation of zirconium-based conversion coatings on aluminium and Al-Cu alloys. *Corros Sci*. 2012;65:231-237. doi:10.1016/j.corsci.2012.08.031

96. Stromberg C, Thissen P, Klueppel I, Fink N, Grundmeier G. Synthesis and characterisation of surface gradient thin conversion films on zinc coated steel. *Electrochim Acta*. 2006;52(3):804-815. doi:10.1016/j.electacta.2006.06.014

97. Guan Y, Liu J-G, Yan C-W. *Novel Ti/Zr Based Non-Chromium Chemical Conversion Coating for the Corrosion Protection of Electrogalvanized Steel*. Vol 6.; 2011. www.electrochemsci.org. Accessed June 5, 2020.

98. Lostak T, Krebs S, Maljusch A, et al. Formation and characterization of Fe3+-/Cu2+-modified zirconium oxide conversion layers on zinc alloy coated steel sheets. *Electrochim Acta*. 2013;112:14-23. doi:10.1016/j.electacta.2013.08.161

99. Ogle K, Morel S, Meddahi N. An electrochemical study of the delamination of polymer coatings on galvanized steel. *Corros Sci*. 2005;47(8):2034-2052. doi:10.1016/j.corsci.2004.08.017

100. Gonzalez OD, Josephic PH, Oriani RA. The Undercutting of Organic Lacquers on Steel. *J Electrochem Soc*. 1974;121(1):29. doi:10.1149/1.2396825

101. Chen T, Li W, Cai J. Formation of a chrome-free and coloured conversion coating on AA6063 aluminium alloy. doi:10.1039/c1ra00036e

102. Golru SS, Attar MM, Ramezanzadeh B. Morphological analysis and corrosion performance of zirconium based conversion coating on the aluminum alloy 1050. *J Ind Eng Chem*. 2015;24:233-244. doi:10.1016/j.jiec.2014.09.036

103. Santa Coloma P, Izagirre U, Belaustegi Y, Jorcin JB, Cano FJ, Lapeña N. Chromium-free conversion coatings based on inorganic salts (Zr/Ti/Mn/Mo) for aluminum alloys used in aircraft applications. *Appl Surf Sci*. 2015;345:24-35. doi:10.1016/J.APSUSC.2015.02.179

104. Santa Coloma P, Izagirre U, Belaustegi Y, Jorcin JB, Cano FJ, Lapeña N. Chromium-free conversion coatings based on inorganic salts (Zr/Ti/Mn/Mo) for aluminum alloys used in aircraft applications. *Appl Surf Sci*. 2015;345:24-35.

doi:10.1016/J.APSUSC.2015.02.179

105. Zhu L, Yang F, Ding N. Corrosion resistance of the electro-galvanized steel treated in a titanium conversion solution. 2007. doi:10.1016/j.surfcoat.2007.03.024

106. Bamoulid L, Maurette M-T, De Caro D, et al. An efficient protection of stainless steel against corrosion: Combination of a conversion layer and titanium dioxide deposit. 2008. doi:10.1016/j.surfcoat.2008.05.011

107. Liu Y, Arenas AM, Garcia-Vergara SG, et al. Ageing effects in the growth of chromate conversion coatings on aluminium. *Corros Sci*. 2005;47(1):145-150. doi:10.1016/J.CORSCI.2004.05.012

108. Li L, Swain GM. Effects of aging temperature and time on the corrosion protection provided by trivalent chromium process coatings on AA2024-T3. *ACS Appl Mater Interfaces*. 2013;5(16):7923-7930. doi:10.1021/AM4020023/ASSET/IMAGES/MEDIUM/AM-2013-020023_0009.GIF

109. Thirupathi K, Bárczy P, Vad K, Csik A, Somosvári BM. Effects of vacuum and ageing on Zr4/Cr3 based conversion coatings on aluminium alloys. *Appl Surf Sci*. 2018;441:1043-1047. doi:10.1016/J.APSUSC.2018.02.092

110. Qi J, Hashimoto T, Walton J, Zhou X, Skeldon P, Thompson GE. Formation of a Trivalent Chromium Conversion Coating on AA2024-T351 Alloy. *J Electrochem Soc*. 2016;163(2):C25-C35. doi:10.1149/2.0771602JES/XML

111. Puomi P, Fagerholm HM, Rosenholm JB, Sipilä R. Optimization of commercial zirconic acid based pretreatment on hot-dip galvanized and Galfan coated steel. *Surf Coatings Technol*. 1999;115(1):79-86. doi:10.1016/S0257-8972(99)00171-1

112. Lyon SB, Bingham R, Mills DJ. Advances in corrosion protection by organic coatings: What we know and what we would like to know. *Prog Org Coatings*. 2017;102:2-7. doi:10.1016/J.PORGCOAT.2016.04.030

113. Funke W, Haagen H. Empirical or Scientific Approach to Evaluate the Corrosion Protective Performance of Organic Coatings. *Ind Eng Chem Prod Res Dev*. 1978;17(1):50-53. doi:10.1021/I360065A014/ASSET/I360065A014.FP.PNG_V03

114. de Wit JHW, van der Weijde DH, Ferrari G. Organic coatings. In: *Corrosion Mechanisms in Theory and Practice: Third Edition*. CRC Press; 2011:863-906. doi:10.1016/b978-0-444-62722-3.00013-6

115. Almeida E. New anti-corrosive painting technologies at the beginning of the 21st century. *J Coatings Technol*. 2000;72(911):73-84. doi:10.1007/bf02720528

116. Leidheiser H. Corrosion of Painted Metals—A Review. *CORROSION*. 1982;38(7):374-383. doi:10.5006/1.3581899

117. Galliano F, Landolt D. Evaluation of corrosion protection properties of additives for waterborne epoxy coatings on steel. *Prog Org Coatings*. 2002;44(3):217-225. doi:10.1016/S0300-9440(02)00016-4

118. Mohammad Hosseini R, Sarabi AA, Eivaz Mohammadloo H, Sarayloo M. The performance improvement of Zr conversion coating through Mn incorporation: With and without organic coating. *Surf Coatings Technol*. 2014;258:437-446. doi:10.1016/J.SURFCOAT.2014.08.056

119. Asemani HR, Ahmadi P, Sarabi AA, Eivaz Mohammadloo H. Effect of zirconium conversion coating: Adhesion and anti-corrosion properties of epoxy organic coating containing zinc aluminum polyphosphate (ZAPP) pigment on carbon mild steel. *Prog Org Coatings*. 2016;94:18-27. doi:10.1016/J.PORGCOAT.2016.01.015

120. Eivaz Mohammadloo H, Sarabi AA, Mohammad Hosseini R, Sarayloo M, Sameie H, Salimi R. A comprehensive study of the green hexafluorozirconic acid-based conversion coating. *Prog Org Coatings*. 2014;77(2):322-330. doi:10.1016/J.PORGCOAT.2013.10.006

121. Sababi M, Terryn H, Mol JMC. The influence of a Zr-based conversion treatment on interfacial bonding strength and stability of epoxy coated carbon steel. *Prog Org Coatings*. 2017;105:29-36. doi:10.1016/J.PORGCOAT.2016.11.016

122. Khun NW, Frankel GS. Effect of Hexafluorozirconic Acid Pretreatment on Cathodic Delamination of Epoxy Coatings from Steel Substrates. *Corrosion*. 2015;71(3):277-284. doi:10.5006/1407

123. Stromberg C, Thissen P, Klueppel I, Fink N, Grundmeier G. Synthesis and characterisation of surface gradient thin conversion films on zinc coated steel. *Electrochim Acta*. 2006;52(3):804-815. doi:10.1016/J.ELECTACTA.2006.06.014

124. Asemani HR, Sarabi AA, Mohammadloo HE, Sarayloo M. Electrochemical and morphological properties of zirconium conversion coating in the presence of nickel ions on galvanized steel. *J Coatings Technol Res*. 1998;13. doi:10.1007/s11998-016-9800-x

125. Zhong Q. Corrosion measurements with wire beam electrodes under temporarily protective oil coatings. In: *Techniques for Corrosion Monitoring*. Elsevier Inc.; 2008:638-657. doi:10.1533/9781845694050.4.638

126. Grundmeier G, Schmidt W, Stratmann M. Corrosion protection by organic coatings: electrochemical mechanism and novel methods of investigation. *Electrochim Acta*. 2000;45(15-16):2515-2533. doi:10.1016/S0013-4686(00)00348-0

127. Koehler EL. MECHANISM OF CATHODIC DISBONDMENT OF PROTECTIVE ORGANIC COATINGS - AQUEOUS DISPLACEMENT AT ELEVATED pH. *Corrosion*. 1984;40(1):5-8. doi:10.5006/1.3579295

128. Koehler EL. The Influence of Contaminants on the Failure of Protective Organic Coatings on Steel. *Corrosion*. 1977;33(6):209-217. doi:10.5006/0010-9312-33.6.209

129. Leidheiser H, Kendig MW. The Mechanism of Corrosion of Poly butadiene-Coated Steel in Aerated Sodium Chloride. *Corrosion*. 1976;32(2):69-76. doi:10.5006/0010-9312-32.2.69

130. Leidheiser H, Wang W, Igetoft L. The mechanism for the cathodic delamination of organic coatings from a metal surface. *Prog Org Coatings*. 1983;11(1):19-40. doi:10.1016/0033-0655(83)80002-8

131. McMurray HN, Williams G. Under Film/Coating Corrosion. In: *Reference Module in Materials Science and Materials Engineering*. Elsevier; 2016. doi:10.1016/b978-0-12-803581-8.01601-5

132. Bautista A. Filiform corrosion in polymer-coated metals. *Prog Org Coatings*. 1996;28(1):49-58. doi:10.1016/0300-9440(95)00555-2

133. Fürbeth W, Stratmann M. Delamination of polymeric coatings from electrogalvanized steel - a mechanistic approach. Part 3: Delamination kinetics and influence of CO2. *Corros Sci*. 2001;43(2):243-254. doi:10.1016/S0010-938X(00)00049-4

134. Fürbeth W, Stratmann M. Delamination of polymeric coatings from electrogalvanized steel - a mechanistic approach. Part 2: Delamination from a defect down to steel. *Corros Sci*. 2001;43(2):229-241. doi:10.1016/S0010-938X(00)00048-2

135. Fürbeth W, Stratmann M. Delamination of polymeric coatings from electrogalvanized steel - a mechanistic approach. Part 1: Delamination from a defect with intact zinc layer. *Corros Sci*. 2001;43(2):207-227. doi:10.1016/S0010-938X(00)00047-0

136. Reddy B, Doherty MJ, Sykes JM. Breakdown of organic coatings in corrosive environments examined by scanning kelvin probe and scanning acoustic microscopy. *Electrochim Acta*. 2004;49(17-18):2965-2972. doi:10.1016/J.ELECTACTA.2004.01.055

137. Geraint W, McMurray HN, Williams G, McMurray H. Chromate inhibition of corrosion driven organic coating delamination studied using a scanning Kelvin probe technique. *J Electrochem Soc*. 2001;148(10):B377. doi:10.1149/1.1396336

138. Williams G, McMurray HN, Loveridge MJ. Inhibition of corrosion-driven organic coating disbondment on galvanised steel by smart release group II and Zn(II)-exchanged bentonite pigments. *Electrochim Acta*. 2010;55(5):1740-1748. doi:10.1016/J.ELECTACTA.2009.10.059

139. Geraint W, McMurray HN, Worsley DA, Williams G, McMurray H. Cerium(III) inhibition of corrosion-driven organic coating delamination studied using a scanning Kelvin probe technique. *J Electrochem Soc*. 2002;149(4):B154. doi:10.1149/1.1457983

140. Stratmann M, Feser R, Leng A. Corrosion protection by organic films. *Electrochim Acta*. 1994;39(8-9):1207-1214. doi:10.1016/0013-4686(94)E0038-2

141. Krieg R, Vimalanandan A, Rohwerder M. Corrosion of zinc and Zn-Mg alloys with varying microstructures and magnesium contents. *J Electrochem Soc*. 2014;161(3). doi:10.1149/2.103403jes

142. Leng A, Streckel H, Stratmann M. The delamination of polymeric coatings from steel. Part 1: Calibration of the Kelvinprobe and basic delamination mechanism. *Corros Sci*. 1999;41:547-578. https://ac.els-cdn.com/S0010938X98001668/1-s2.0-S0010938X98001668-main.pdf?_tid=95b21839-005f-461b-bda3-f3ef13deb5f3&acdnat=1526467594_0e90046e0671b4e33b421f8e6943ef9a. Accessed May 16, 2018.

143. Williams G, Geary S, McMurray HN. Smart release corrosion inhibitor pigments based on organic ion-exchange resins. *Corros Sci*. 2012;57:139-147. doi:10.1016/J.CORSCI.2011.12.024

144. Richards CAJ, McMurray HN, Williams G. Smart-release inhibition of corrosion driven organic coating failure on zinc by cationic benzotriazole based pigments. *Corros Sci*. 2019;154:101-110. doi:10.1016/J.CORSCI.2019.04.005

145. Williams G, McMurray HN. Chromate Inhibition of Corrosion-Driven Organic Coating Delamination Studied Using a Scanning Kelvin Probe Technique. *J*

Chapter 2 – Materials and Methodology

2.1 Materials

This thesis focuses on the corrosion and surface analysis of a metal surface coated with a hexaflourotitanate conversion coating and an organic coating. The current section outlines the key materials used to create the necessary samples that were used for experimentation, both metal and coatings. Table 2.1. gives a full list of materials used.

Table 2.1. A table for all materials used for the research presented in this Thesis

Material	Supplier	Purity
Hot dip galvanised steel	Tata Steel UK	-
4.8%-Al galvanised steel	Tata Steel UK	-
Bonderite 1445 M-NT Hexaflourotitanate pre-treatment wipe	Henkel	-
Bonderite U-187	Henkel/Tata Steel UK	-
Ethanol	Sigma-Aldrich	99%+
PVB	Sigma-Aldrich	99%+
Silicon Rubber	RS	Non-Corrosive
PTFE Tape	RS	-
NaCl	Sigma-Aldrich	99%+
Calomel Reference Electrode	Sentek	-
Platinum Counter Electrode	Metrohm	-

2.1.1 Specification of steel samples.

Commercially produced hot dipped galvanised steel (HDG) and 4.8%-Al galvanised steel (Galvalloy/ZA) were used for all experimentation. All HDG and Galvalloy substrates were produced by Tata Steel UK and comprised of 0.7 mm gauge mild steel coated on both sides with a 20 μm zinc layer for HDG and an 18 μm Al-Zn layer for ZA, as collected from a continuous strip galvanising line under production conditions and were received in A4 metal sheets.

2.1.2 Alkaline cleaning solution

HDG and Galfan were cleaned using Novamax U-187 alkaline cleaner. This cleaner is composed of sodium hydroxide and sodium xylene sulfonate. For the cleaning of HDG and Galfan, 2.5% and 2% U-187 v/v concentrations were made respectively with de-ionised water. This solution was then heated to 50°C, 65°C and 80°C and the steels were submerged in solution for the required amount of time.

2.1.3 Conversion coating

Delamination and impedance and surface analysis experiments were conducted in the presence and absence of a hexaflourotitanate (HFT) conversion coating. Bonderite 1445 M-NT pre-treatment was supplied as a wipe, which was applied to steel substrates by applying pressure with the wipe and wiping across the surface and allowing to dry at room temperature.

2.1.4 Model organic coatings

Delamination experiments were done using poly-vinyl butyral-co vinyl alcohol (PVB), MW ~70,000-100,000 supplied by Sigma-Aldrich Co. PVB is a polymer which is soluble in ethanol, allowing for controlled viscosity solutions, is non-toxic and shows good adhesion to metal substrate. Another important factor for using PVB is that it delaminates quickly under delamination experiment conditions; this allows for easy assessment of conversion coating added to the system at inhibiting cathodic disbondment. The standard coating used for delamination experiments used a 15.5% PVB in ethanol solution. This solution is made by adding PVB powder incrementally to ethanol using a high sheer mixer (IKA Ministar 20).

2.2 Standard Alkaline Cleaning

2.2.1 Steel sample preparation

The metal sheets were reduced into square coupons of 5 x 5 cm using a guillotine. The samples were rinsed with ethanol to remove any excess contamination prior to alkaline cleaning. The focus of studies was not the cleaning ability of the chosen alkaline cleaner but the effect the alkaline cleaner may have on the metal surface.

2.2.2 Experimental procedure

Bonderite 187-U alkaline cleaning solution was used to clean steel surfaces. The concentration, temperatures and times for each steel is listed below. After alkaline cleaning, samples were removed from solution using PTFE tweezers to avoid surface contamination on the surface. After removal of the metal substrate from the surface, the sample was immediately rinsed with distilled water to remove any excess cleaning solution from the surface and a squeegee and hairdryer were used to dry the surface.

Table 2.2. Cleaning parameters of HDG and ZA steel alloys.

Steel substrate	Alkaline cleaning concentration / %	Cleaning Time / s	Cleaning Temperature / °C
HDG	2.5	30, 60, 120, 300, 600	50, 65, 80
ZA	2	30, 600	50, 65, 80

The temperatures selected were chosen because 65°C is the temperature used by Tata Steel UK in its cleaning operation. A higher and lower temperature were selected to show comparisons of how temperature can affect the cleaning step. The cleaning times were selected to both attempt to replicate the turbulent conditions that the strip moves through the cleaning bath on the coating line at high speeds (40 m/s to 100 m/s) under static lab conditions, with higher times used to show how long immersion times can influence the surface. The cleaning concentrations used are the same as those used to clean the relevant steels on the coating line. Application of Henkel G1445T M-NT hexafluorotitanic acid conversion coating was applied post-cleaning to the surface of HDG substrates using Henkel pre-treatment wipes.

2.3 Standard methodology for cathodic delamination

2.3.1 Preparation of a delamination cell (Stratmann cell)

A model organic coating based on poly(vinyl butyral-co-vinyl alcohol-co-vinyl acetate) (PVB) was used as a model coating to avoid any uncontrolled variables such as additives that would influence the HDG/ZA alloys. PVB (Mw: 70,000-100,000) was provided by Sigma-Aldrich in the form of a powder and was mixed with ethanol at a fraction of 15.5% w/w. The mixing of the two elements was promoted by stirring using a shear mixer until a clear,

homogenous mixture was produced. The PVB/ethanol solution was moved into a glass bottle to prevent evaporation of ethanol.

This method of sample preparation is taken from a method developed by Stratmann *et al.* for the measurement of cathodic disbondment of a model coating and has been used widely is this field of study. [1–6] A schematic of the Stratmann cell can be found in Figure 2.1. A clear adhesive tape (Scotch™) is used to cover a 15mm x 50mm area adjacent to one edge of the 50 mm x 50 mm HDG/ZA sample. Two strips of electrical adhesive tape (supplied by RS), of thickness 30μm, are placed on the parallel edges normal to the edge with the clear tape. There is now a gap of bare HDG sample at the centre, approximately 35 mm x 20 mm, which acts as the site for the organic coating. The PVB (15.5% w/w) containing the required volume fraction of inhibitor pigment is then applied to the bare site using a glass rod to cast a thin film. The two parallel pieces of adhesive tape act as height guides for the organic coating which allows for an even coating distribution and a dry film thickness of ~20μm. A scalpel is used to apply a cut between the Scotch™ tape and metal substrate. The PVB coating is then left to air dry for 30 minutes allowing for the PVB to completely set. The area of Scotch™ tape which has been cut is then lifted away from the metal substrate into a raised lip leaving an exposed area of 20 mm x 15 mm of bare metal. A well is created around this area of bare metal using a non-corrosive silicon rubber (supplied by RS), also containing the lip.
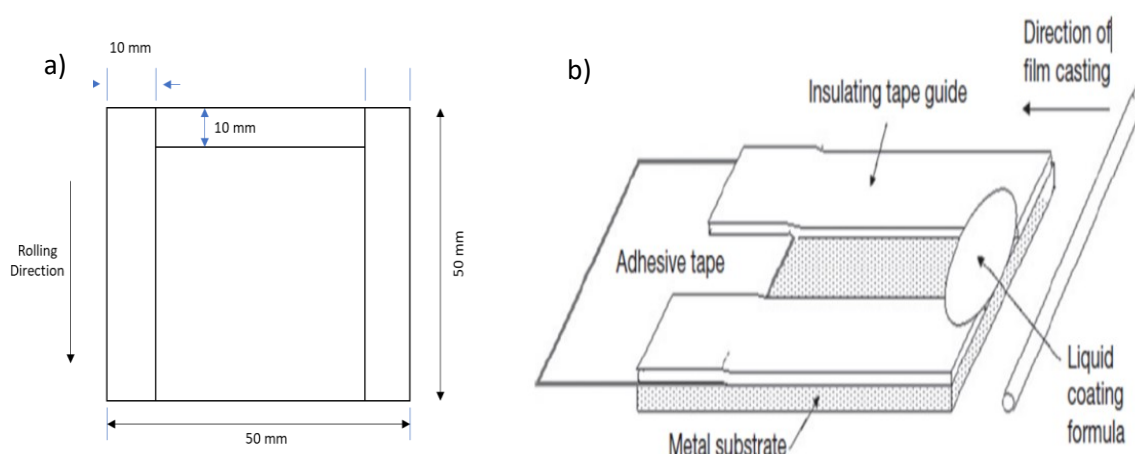
Figure 2.1 A schematic of a delamination cell. a) general schematic of the delamination cell. b) showing the process of applying a PVB coating.

2.3.2 Cathodic Delamination Initiation on HDG

Sodium chloride was selected as the initiative electrolyte for cathodic delamination of HDG and a solution of 5% sodium chloride was prepared for each cathodic delamination experiment. The well created on the Stratmann cells will be used as a source of electrolyte for the duration of cathodic delamination. Approximately 3 ml of 5% NaCl solution was placed into the well to initiate cathodic delamination and the samples were stored in a sealed container at a constant room temperature of 20°C and a relative humidity of 95%.

2.3.3 Cathodic delamination monitoring and image analysis

The total experiment time for cathodic delamination was 24 hours for HDG samples which had been alkaline cleaned but not coated with G1445T M-NT conversion coating. This was extended to 1 week for Galvalloy samples and HDG which had HFT pre-treatment present on the surface. For the duration of the study optical images were taken using a Canon EOS 600d camera and then imported into Windows Video Editor for analysis. The distance at which cathodic delamination occurred was measured using ruler guides next to the samples and measured after images were taken. Four recordings were taken for each experimental condition and the mean and standard deviation value was calculated.

2.3.4 Experimental procedure & apparatus for In-situ Time-Lapse Microscopy

For cathodic disbondment of Stratmann corrosion cells to be recorded in-situ, four Stratmann cells were placed on top of plastic cylinders in a transparent plastic box surrounded by 1 litre of 5% w.v NaCl to create a relative humidity of 95%. Approximately 3 ml of 5% NaCl solution was placed into the well to initiate cathodic delamination. For the duration of the study optical images were taken using a Canon EOS 600d camera and then imported into Windows Video Editor.

2.4 X-ray Photoelectron Spectroscopy

The elemental composition of a solid can be assessed by analysing the electronic structure of the atoms on the surface. X-ray Photoelectron Spectroscopy (XPS) works by using photoemission to provide surface composition data by sampling and quantifying the electrons

which are emitted from the substrate surface.[7] The emission of an electron from the solid surface is a result of the interaction by electron found at the core level of the atoms present, and the photons produced by an exciting photon source (i.e Al anode at 1486.6 eV or Mg anode 1253.6 eV). This produced a transfer in kinetic energy to the electron, resulting in emission. The kinetic energy (KE) of the of the electron is experimentally determined by the XPS analyser and the binding energy (BE) of the electron can be deduced through equation 2.1, whereby the binding energy is a result of the Planks constant (h) and X-ray frequency (v) produces the X-ray energy and ψ is the spectrometer work function of the instrument.[7]

$$BE = hv - KE - \psi \hspace{4cm} \text{Equation 2.1}$$

Auger electron emission can take place within an atom when the atomic number is less than 30, above this atomic number the Auger yield decreases but can still occur. Following the emission of a core electron, a higher energy electron can fill this vacant hole within the atomic core. This electronic decay from a higher-level result in the emission of a third electron whose KE is equal to the difference in the electronic states.
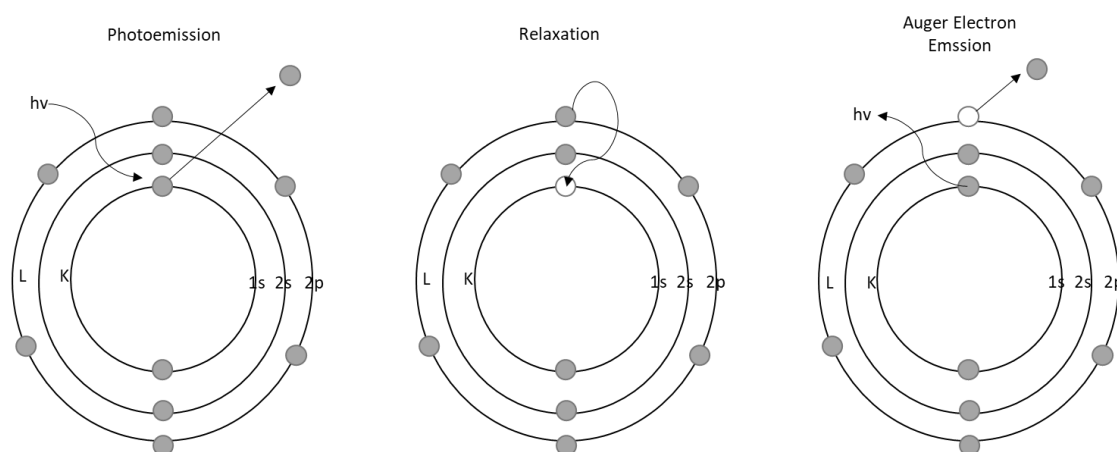
Figure 2.2. Schematic representation of Auger electron emission reproduced from Wagner. [8]

The electrons on the surface can escape from the top ~10 nm without losing energy.[8] Electrons emitted from beneath a 10 nm depth experience inelastic scattering, whereby they lose energy due to the increased wavelength of the interacting electrons. Inelastic scattering is dependent on the inelastic mean free path, λ, of the electron which is defined as the mean distance covered by an electron with specific kinetic energy through the solid before experiencing inelastic scattering. [8] Electrons which have been inelastically scattered during analysis contribute to the background signal of the XPS spectrum.

2.4.1 Sample preparation for XPS

Surface characterisation on the chemical composition of HDG and ZA which had been alkaline cleaned and coated in a pre-treatment was performed using XPS before and after each stage. The samples were alkaline cleaned as 5 x 5 cm coupons at 50°C, 65°C and 80°C for a range of immersion times between 0 and 600 seconds. Following alkaline cleaning, samples were rinsed with deionised water and dried. In the case of pre-treated samples, following alkaline cleaning samples were coated with a conversion coating using pre-treatment wipes. All samples were then cut to 1 x 1 cm coupons. Samples were then mounted using the sample tray using copper holders and polyamide tape to ensure electrical insulation and placed in the vacuum chamber of the XPS instrument (Axis Supra, Kratos Analytical, UK). Spectral analysis of the samples was taken between 1200 – 0 eV and subsequent high resolution elemental scans were conducted on the surface for elemental quantification.

2.4.2. Processing of XPS data

Peak fitting of the produced spectra was conducted using CasaXPS software. Upon collection of high resolution elemental spectra, peaks were fitted using CasaXPS in order to gather atomic composition of each element. Initially all elements are calibrated to the main carbon peak of 284.8eV. A spectral background around the element peaks is created around each peak in order to assist with more accurate peak fittings using a Shirley background in which the background intensity at any given binding energy is proportional to the intensity of the total peak area above the background in the lower binding energy peak range.[9] After the regions are created element components are fitted within the relevant peaks. Quantification of the peaks is then taken from the area of the peak of each element before being processed in Microsoft Excel.

2.5. Electrochemical corrosion testing

Scanning electrochemical techniques are now commonplace in studying the kinetics and thermodynamics of metallic corrosion in aqueous conditions. There are a range of different techniques which use a reference probe that is scanned above the corroding metal surface. The micro-tip probe measures information such as local potential, potential gradient or current. The cathode and anode sites that are active during corrosion can be observed from this data, which can then be visualised using software to deduce corrosion kinetics. The software used to visualise the corroding surface can produce a topographical map of the area

or spatially resolved representations that can be used to measure local differences in surface current density and reactivity.

There are three main variants of scanning electrochemical techniques most used for corrosion investigation: scanning reference electrode technique (SRET), scanning vibrating electrode technique (SVET), and scanning Kelvin probe (SKP). The proceeding Chapters use the SKP technique, so only this technique will be covered.

2.5.1 Scanning Kelvin Probe

The SKP technique is used throughout this thesis and was manufactured in-house at Swansea University. A schematic of the Scanning Kelvin Probe can be seen below in Figure 2.3.
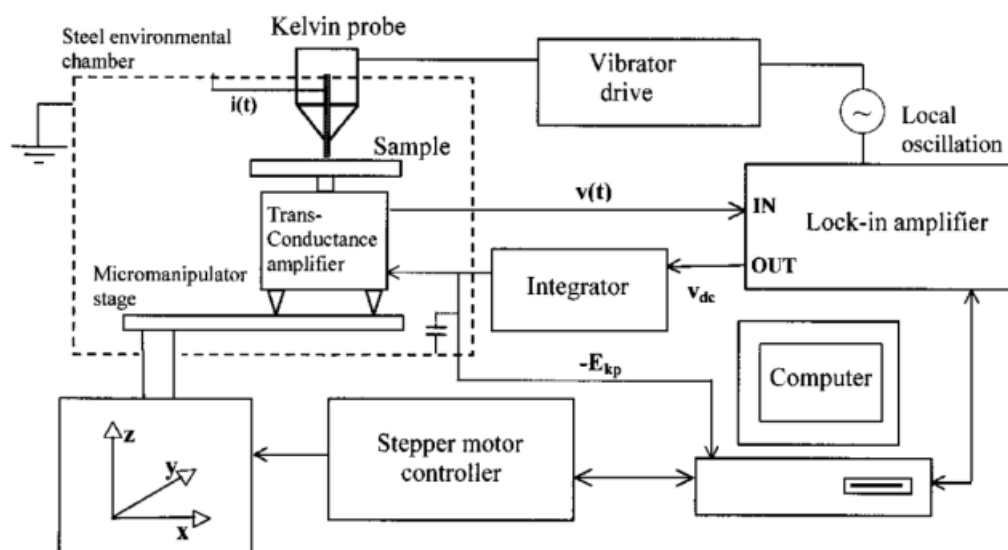
Figure 2.3. A schematic of Scanning Kelvin Probe apparatus at Swansea University.[2]

The dotted line shown in Figure 2.3 is a steel environmental chamber which contains the SKP head and sample stage. This chamber acts as a Faraday cage, reducing the outside electrical noise interfering with the sensitive Kelvin probe. The sample holder is connected to a tri-axial motor stage which allows for spatially resolved maps by moving the sample stage with reference to the SKP probe tip. The system is computer controlled and data is stored on the computer hard drive. The SKP reference probe tip consists of 125μm diameter gold (99,99%) wire which is vibrated in a sinusoidal manner normal to the sample, the sample and reference probe form two plates of a parallel plate capacitor.

The gold wire is attached to a glass rod which is then attached to a speaker which allows the tip to vibrate at an amplitude of 40μm (as measured with a strobe light and microscope). A lock-in amplifier oscillator function controls the vibrator drive which allows the speaker to vibrate at a frequency of 280Hz and an amplitude of ± 20μm. The capacitance between the two plates of the capacitor varies periodically and results in an a.c. current which is initially amplified and converted to an a.c. voltage. A feedback circuit is used to send a corresponding d.c. output from the amplifier to an integrator where it is applied to the sample which nulls the voltage. This nulling of the d.c. voltage is accompanied by finite equalisation by the integrator of the Galvani potentials of the probe and specimen which nullifies the a.c current. Null conditions are created by the integrator altering the d.c. voltage, gradually requiring small and smaller changes until the system is stable. Once the system has become stable, with the currents and potential are null, the integrator sends the reverse bias required to achieve the conditions. This is converted to a digital signal by the lock-in amplifier before being logged on the computer as a point of measurement. The stage can then be moved to repeat the process for other sites that will be scanned, the resultant spatially resolved map of Kelvin potentials can then be converted into a spatially resolved map of Ecorr via the SKP calibration.

2.5.2 Calibrating the scanning Kelvin probe

Typical calibration of the SKP is done using metal/aqueous metal couple such as Ag/Ag^+, Cu/Cu^{2+}, Fe/Fe^{2+} and Zn/Zn^{2+} The calibration cells are made by machining a circular well of ~15mm in diameter and ~5mm deep into disks of the respective metal. An aqueous solution of metal cations (~0.5 mol dm^{-3}) containing the corresponding metal is placed into the metal well. The SKP probe tip is moved into position ~100 μm above the electrolyte meniscus and is vibrated above the centre of the well where the Kelvin Probe potential (E_{KP}) value is logged on the computer. The SKP has been used to carry out experiments on organically coated metal samples for this thesis, the effect of the PVB coating must be taken into consideration with respect to calibration. The effect that the PVB has on E_{KP} values is measured by casting a PVB film over a smooth glass surface, peeling it away from the surface, and placing it over the metal well filled with the aqueous solution containing the metal cation. The electrolyte and PVB film are left to equilibrate for ~6 hours before the E_{KP} values are recorded. The calibration of the PVB film has been carried out elsewhere and found to amount of an offset of -220mV which can then be added to the

calibration to convert the E_{KP} measurement to E_{corr} (mV vs SHE).The standard procedure for experiments involved a calibration of the SKP using a

copper well containing 0.5 mol dm^{-3} $CuSO_4$. The following, simplified, equation is used for calibration:

$$E_{corr} = E_{KP} + constant \qquad\qquad\qquad \text{Equation 2.2}$$

The simplification of the equation arises because of the constant relative humidity, gas composition and temperature inside the steel environmental chamber. The calibration using the Cu/Cu^{2+} redox couple has a known E_{corr} of 298mV which then allows for the constant to be determined. An example of a calibration calculation is given below, where the reading of the Cu/Cu^{2+} redox couple is 250mV. When values are added to Equation 2.2 we get the following vales:

$$298 = -250 + constant \qquad\qquad\qquad \text{Equation 2.3}$$

$$548 = constant \qquad\qquad\qquad \text{Equation 2.4}$$

$$548 – 220 \text{ (the offset for a PVB film)} = 328mV \qquad\qquad \text{Equation 2.5}$$

This value of 328mV can then be used to convert the potential provided by experimental measurements to Ecorr for each measured point produced using the SKP technique.

2.5.3 Operation of the SKP

Once the SKP is calibrated, described in Section 2.5.2, the sample is mounted onto the triaxial stage within the steel chamber. The sample is first levelled manually using a spirit level before being levelled more precisely using the SKP probe. The first step to levelling the sample using the SKP is to position the probe at one end of the sample and reduce the distance between sample and probe by incrementally raising the sample. Once the probe touches the sample surface the lock-in amplifier will read an overload signal, at this point the probe is moved 100μm away from the surface and moved to the opposite end of the sample. This procedure is repeated at this end with the distance required to reach the surface recorded. At this point it is known which side of the sample is lower than the other and so can be carefully moved to compensate. This process is repeated until both edges of the sample are vertically equidistant from the probe. Once the sample is made level the probe is set 100μm above the sample which is the scan height for all SKP experiments and 12mm away from the electrolyte well. Once the sample has been set up within the steel chamber a petri dish of 5% w/w NaCl(aq) is included into the bottom of the chamber to maintain 95% relative humidity.

The steel chamber is closed to allow for the correct humidity to be established and the full hydration of the model coating being tested.

Once ready the cathodic disbondment is initiated using 5% w/w NaCl(aq) in the sample well, described in Section 2.1.5. The spatial resolution of the Volta potential is then achieved by scanning the sample area along four 12mm lines up to the electrolyte well.

Scans are produced immediately after the addition of electrolyte to the sample and then every hour for 24 hours or longer if specified in the relevant Chapter.

Once the experiment is finished the data is retrieved from the computer and extrapolated using Microsoft Excel. Plots of time dependent Ecorr versus distance are produced for each of the four scans.

2.5.4 Sample preparation for SKP

Samples were prepared the same was as in section 2.3 (cathodic delamination preparation). Once the sample is ready, a plastic 7 mm nut is glued to the back of the sample to allow the sample to be placed onto the SKP stage. The SKP tip was dipped in 2M hydrochloric acid for 15 minutes, followed by deionised water for 15 minutes. After this, the probe was calibrated using a copper metal well filled with 0.5M copper sulphate. The probe tip is moved into position ~100 μm above the electrolyte solution and vibrated above the centre of the well where the E_{KP} value is logged on the computer. This is allowed to calibrate for 1 hour with the chamber containing 2 petri dishes containing solutions of 5% NaCl. With respect to calibration, due to the samples being coated with PVB this must be taken into consideration. The effect that PVB has on the E_{KP} values measured by casting a PVB film over a small glass surface, peeling it away from the surface and placing it over the copper well filled with copper electrolyte. This is left to equilibrate for ~6 hours before E_{KP} is recorded. This PVB calibration has been carried out elsewhere and found to amount of an offset of -220 mV, which can then be added to the calibration to convert the E_{KP} measurement to E_{corr} (mV vs SHE).

2.6. Scanning electron microscopy (SEM) and energy dispersive X-ray spectroscopy (EDX)

The samples were alkaline cleaned as 5 x 5 cm coupons at 50°C, 65°C and 80°C for a range of immersion times between 0 and 600 seconds. SEM images were taken using a Hitachi TM

300 microscope. All images were taken using 15kV acceleration voltage and a working distance of 10mm. EDX analysis was done using Quantax 70 software on the Hitachi TM 300 microscope. The EDX scan is run for 15 minutes per sample to allow adequate elemental images to be obtained.

2.7 Potentiodynamic Polarisation

2.7.1 Sample preparation and apparatus for polarisation experiments

The corrosion mechanism and rate of a metal substrate can be determined by polarising the potential of the sample by applying a current through the electrolyte. The potential of the sample, or the working electrode, can be shifted anodically or cathodically, which can give detailed information on the processes occurring when electrons are either pushed into, or removed, from the sample.

A three electrode set up was used to analyse the change in current as the potential of the working electrode was shifted either anodically or cathodically. The working electrode consisted of a 4 x 7 cm piece of steel which had been alkaline cleaned, with further analysis conducted on steel which had been cleaned and pre-treated. A 1 x 1 square of the surface was exposed with the remaining surface covered by PTFE tape, which would act as the reaction site. A 100 cm^3 reaction cylinder was used to cover this area with 5% NaCl and a platinum counter electrode and a calomel (HgCl) reference electrode was immersed into solution. This set-up was connected to a Metrohm Autolab M204 potentiostat with Nova 2.1.4 software. This set up can be seen below in Figure 2.4

For anodic and cathodic polarisation analysis ,the potential was varied shifted $^{+/-}$ 0.5V with respect to the OCP, with the OCP measured for 120 seconds before polarisation was initiated, with steps of 0.001 V being recorded and a scan rate of 0.01V/s for both sets of polarisations. Longer experiments of linear polarisation were also performed over a 3.5 hour timescale. The OCP was measured for 120 seconds before the potential is shifted from -0.01 V to + 0.01 V with respect to the OCP, and then the OCP is recorded for 30 minutes before polarisation is again induced onto the sample. A scan rate of 0.001667 V/s with a step of 0.000244 V was used.
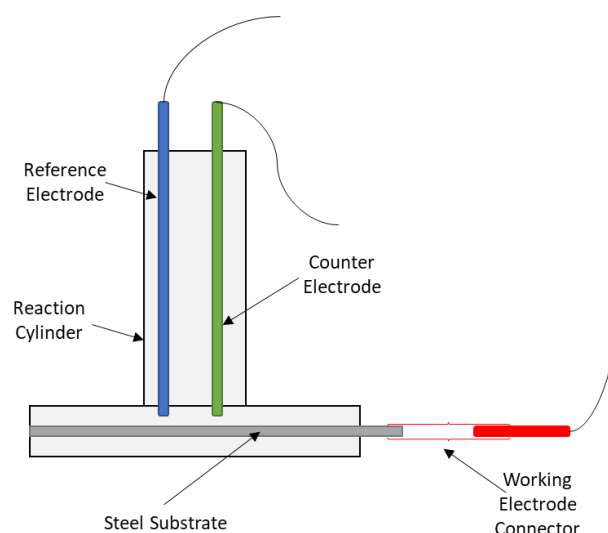
Figure 2.4. Three-electrode set up used during polarisation experiments

2.8. Titanium Deposition Analysis using X-Ray Fluorescence Analysis

X-ray fluorescence (XRF) works via emission of characteristic "secondary" (or fluorescent) X-rays from a material that has been excited by being bombarded with high-energy x-rays. In order to excite the atoms a source of radiation with sufficient energy to expel electrons which are tightly held near the centre of the atom. The fluorescent x-rays emitted by the sample are directed towards a solid-state detector which produces digital information of the detected energies produced.[10] In this case of XRF for Titanium coating weight, the final digital readout is the titanium coating weight (mg/m^2) of the coating.

XRF analysis of pre-treated samples was conducted using Rigaku-NEX QC-XRF which specifically analyses the titanium weighting of the pre-treatment coating with a sampling depth up to 1µm. Samples were prepared in a slightly different fashion to other tests due to the industrial nature of testing. HDG samples were cut to A7 (105 x 74 mm) dimensions, which were subsequently cleaned in 2% U-187 at 50°C, 65°C and 80°C for 30 seconds or 10 minutes, rinsed with deionised water and dried. Bonderite 1445 M-NT was applied with 1 or 10 wipe applications on one side of the panel. For analysis, samples were placed pre-treated side down onto the x-ray sensor, which would then detect the titanium weight in the coating.

2.9. References

1. Geraint W, McMurray HN, Worsley DA, Williams G, McMurray H. Cerium(III) inhibition of corrosion-driven organic coating delamination studied using a scanning Kelvin probe technique. *J Electrochem Soc*. 2002;149(4):B154. doi:10.1149/1.1457983

2. Geraint W, McMurray HN, Williams G, McMurray H. Chromate inhibition of corrosion driven organic coating delamination studied using a scanning Kelvin probe technique. *J Electrochem Soc*. 2001;148(10):B377. doi:10.1149/1.1396336

3. Fürbeth W, Stratmann M. The delamination of polymeric coatings from electrogalvanised steel – a mechanistic approach.: Part 1: delamination from a defect with intact zinc layer. *Corros Sci*. 2001;43(2):207-227. doi:10.1016/S0010-938X(00)00047-0

4. Stratmann M, Leng A, Fürbeth W, Streckel H, Gehmecker H, Große-Brinkhaus KH. The scanning Kelvin probe; a new technique for the in situ analysis of the delamination of organic coatings. *Prog Org Coatings*. 1996;27(1-4):261-267. doi:10.1016/0300-9440(94)00542-7

5. Fürbeth W, Stratmann M. Scanning Kelvin Probe investigations on the delamination of polymeric coatings from metallic surfaces. *Prog Org Coatings*. 2000;39(1):23-29. doi:10.1016/S0300-9440(00)00095-3

6. Stratmann M, Feser R, Leng A. Corrosion protection by organic films. *Electrochim Acta*. 1994;39(8-9):1207-1214. doi:10.1016/0013-4686(94)E0038-2

7. Fadley CS. X-ray photoelectron spectroscopy: Progress and perspectives. *J Electron Spectros Relat Phenomena*. 2010;178-179(C):2-32. doi:10.1016/J.ELSPEC.2010.01.006

8. Wagner C, Traud W. On the interpretation of corrosion processes through the superposition of electrochemical partial processes and on the potential of mixed electrodes. *Corrosion*. 2006;62(10):843-855. doi:10.5006/1.3279894

9. X-ray Photoelectron Spectroscopy (XPS) Reference Pages: Background Selection. https://www.xpsfitting.com/2011/09/background-selection.html. Accessed March 17, 2023.

10. How does XRF work? | Bruker. https://www.bruker.com/en/products-and-solutions/elemental-analyzers/xrf-spectrometers/how-does-xrf-work.html. Accessed March 20, 2023.

Chapter 3 – Investigating the influence of alkaline cleaning parameters on surface chemistry and corrosion driven cathodic disbondment on galvanised steel.

3.1. Introduction

During the production of organically coated steels (OCS) the steel substrate is cleaned in an acidic or alkaline solution before an application of a conversion coating and subsequent paint coating. The chemical cleaning procedure is used to chemically etch the substrate surface which modifies the surface chemistry prior to the application of corrosion resistant coatings to improve performance by providing a more suitable surface for bonding by increasing surface roughness.[1] Chemical cleaning of aluminium substrates uses both alkaline and acid cleaning in step order, with alkaline degreasing typically used first to remove contamination by dissolving away the native alumina layer and acid de-smutting then used to remove any remaining particulates left on the surface prior to deposition of plasma polymers. [2] Chemical cleaning of metallic substrates results in alteration of the native oxides present and changes the concentrations of metal ions on the surface resulting in a change in substrate microstructure. [3] Chemical cleaning of a metallic surface is conducted in order to prepare the surface prior to the application of an anti-corrosive layer such as a conversion coating, in order to increase corrosion resistance of the metal. [4]

The conditions used for chemical cleaning of a surface prior to any coating application are key to controlling the surface conditions for a coating to adhere to with cleaning playing a role in varying the surface chemistry such as influencing intermetallic and hydroxyl formation on the surface. [5, 6 7 8, 9, 10] Cleaning conditions also influence the physical properties of the surface such as surface roughness, oxide thickness and adhesion strength of deposited coatings.[11, 12, 13]

This chapter is related to the study of how alkaline cleaning influences the corrosion resistance of zinc-based HDG substrates, however, in contrast to the depth of work conducted on alkaline cleaning on aluminium alloys, relatively little work has been devoted to the

subject of surface cleaning of zinc based substrates. Studies investigating the effect of alkaline cleaning on HDG has been studied by various researchers, which can be seen in Section 1.5.

A significant amount of work in the past 20 years has been dedicated to understanding the film formation of zirconium or titanium based conversion coatings of various metal alloys. The basic film formation mechanism of a Zr/Ti coating is as follows: i) Chemical etching of the surface using an appropriate chemical agent,[14] ii) fluoride activation of the surface oxide layer, iii) onset of anodic hydrogen evolution on the surface as a result of increasing surface pH and iv) subsequent precipitation of oxyhydroxides as oxide precursors . [15, 16] This chapter will focus mainly on step i), the chemical activation of the surface prior to application of a Zr/Ti conversion coating in order to investigate the influence that chemical etching has on the performance of the conversion layer. Subsequent steps will be investigated in subsequent chapters. The work in this chapter builds on some of the work conducted in the literature, relating the alkaline cleaning time and temperature to both the surface chemistry of HDG steel surfaces and the corrosion resistance of activated surfaces. The former will be quantified through XPS analysis of the surface pre and post activation, and the latter quantified by electrochemical testing of the zinc surface, and by determining the kinetics of organic coating failure via a cathodic delamination mechanism when over-coated with a model PVB film.

Work has been conducted in depth into the cathodic disbondment behaviour of galvanised steel. The use of a Scanning Kelvin Probe (SKP) can be used to study the delamination of polymer coated steel and was pioneered by Stratmann et al to study the effect of corrosion processes that occur underneath organic coatings on metallic substrates, in particular steel and zinc substrates.[17–24] The work conducted by Stratmann et al allowed for further advances in the study of organic coating degradation. A significant body of work has been completed within Swansea University, investigating organic coating degradation, pigment inhibition and corrosion mechanisms.[25–29] For example, Richards et al used a SKP to study the delamination of a cationic benzotriazole pigment on HDG steel as a potential replacement for strontium chromate, with the SKP being used to study the delamination of the inhibitor-containing coating.[30] Changes in the corrosion potential measured by the SKP over a 24 hours showed that inhibited coatings on HDG steel are slower than that on uninhibited coatings.

3.2. Experimental details

3.2.1. Materials

Bonderite U-187 alkaline cleaner was provided by Henkel. This is a sodium hydroxide based cleaning agent containing surfactants to help remove organic contamination on the steel surface. Bonderite U-187 alkaline cleaning solution was provided by Tata Steel UK and was diluted to 2.5% v/v concentration with deionised water. Hot dip galvanized steel was provided by Tata Steel UK, with a gauge of 0.7mm mild steel and a zinc layer of 20µm thick, containing 0.15% aluminium. Polyvinyl butryal-co-vinyl alcohol-co-vinyl acetate (PVB), molecular weight 70,000-100,000, was obtained from Sigma Aldrich Chemical Co. and was at an analytical grade purity. The PVB solution was prepared in ethanol to 15.5% w/w with the required amount of inhibitor added using a high shear mixer.

3.2.2. Experimental Methodology

The full description of the instrumentation, calibration, experimental set-up and analysis of the XPS, SKP, time-lapse photography and potentiodynamic polarisation can be found in Chapter 2. Description of sample preparation and alkaline cleaning parameters can also be found in Chapter 2 under the relevant section.

3.3. Results and Discussion

3.3.1. Surface characterisation of alkaline cleaned hot dipped galvanised steel

Prior to investigations of the influence of alkaline cleaning on the corrosion-driven cathodic delamination of HDG, XPS was utilised to identify and quantify the elemental composition of the surface oxides found on the HDG surface prior to and after chemical treatment. Figure 3.1 displays a typical "survey" spectrum over a wide binding energy range for untreated HDG, demonstrating the surface consists of Zn, C, O and Al. In some instances, the X-ray photon used to generate spectra creates a vacant electron hole at the stationary electronic state closest to the nuclei of the atoms. This vacancy is filled by a more energetic electron decaying from a higher stationary state and an electron is emitted with an energy equal to the difference between the two states. This phenomenon is seen in the spectra as Auger KLL and LMM peaks.
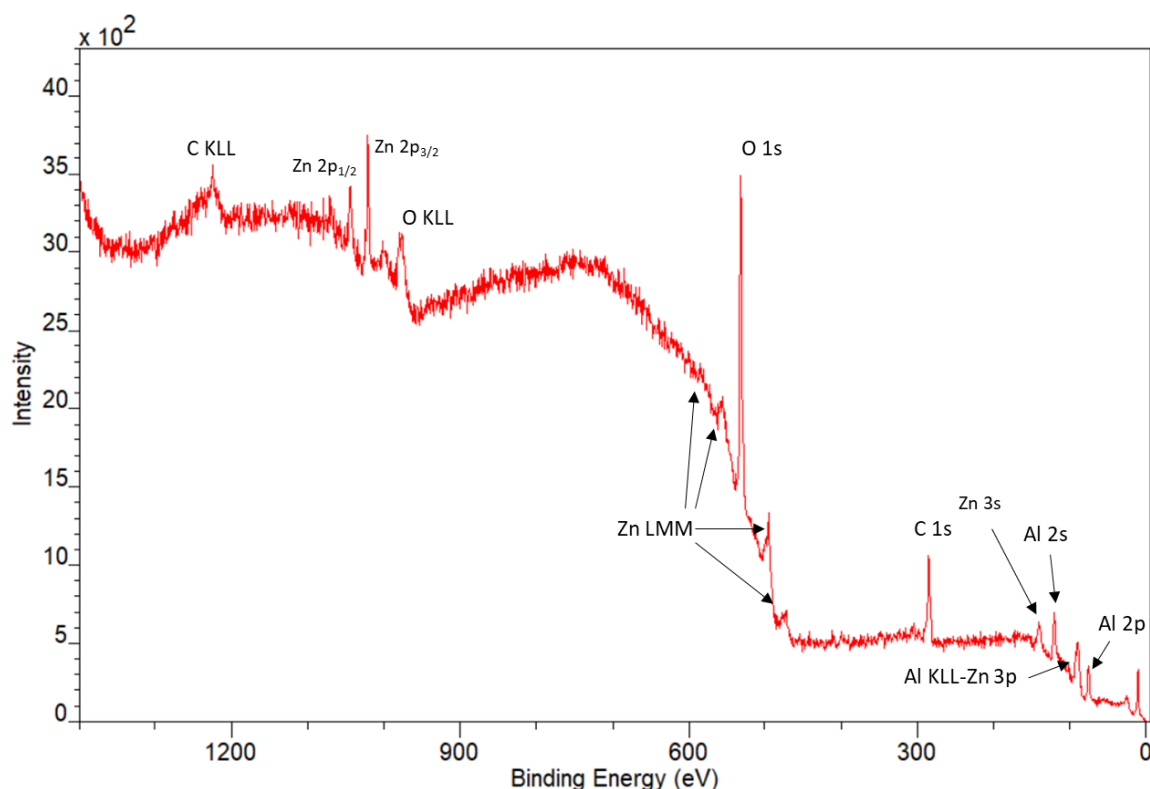
Figure 3.1. XPS spectral survey scan of HDG steel

The typical peak for each corresponding element has been identified and are shown individually in greater detail in Figure 3.2 The main C 1s peak is centred at 284.8eV, identified as C-C, and is accompanied by two smaller peaks identified as C-O-C located at 286.82 eV and result from surface contamination. The peaks generated by Zn 2p and Al 2p exhibit spin orbit splitting and are resolved into doublets of peak area ratio constrained at 1:2. Splitting occurs when the angular momentum quantum number is non-zero, which is true for all orbital levels except the s orbital.[31] Regarding Zn 2p, two peaks arise of distinct energies having a peak separation (Δ_{metal}) equal to 23 eV. Metallic zinc is centred at 1021.7 eV and 1044.7 eV and Zn(II) is located at 1022.5 eV and 1045.5 eV.[32] Al 2p also resolves into two doublet peaks equal to 0.44 eV which are identified as two different chemical states attributed to metallic aluminium at 73 eV and Al(III) at 75.5 eV.[33]
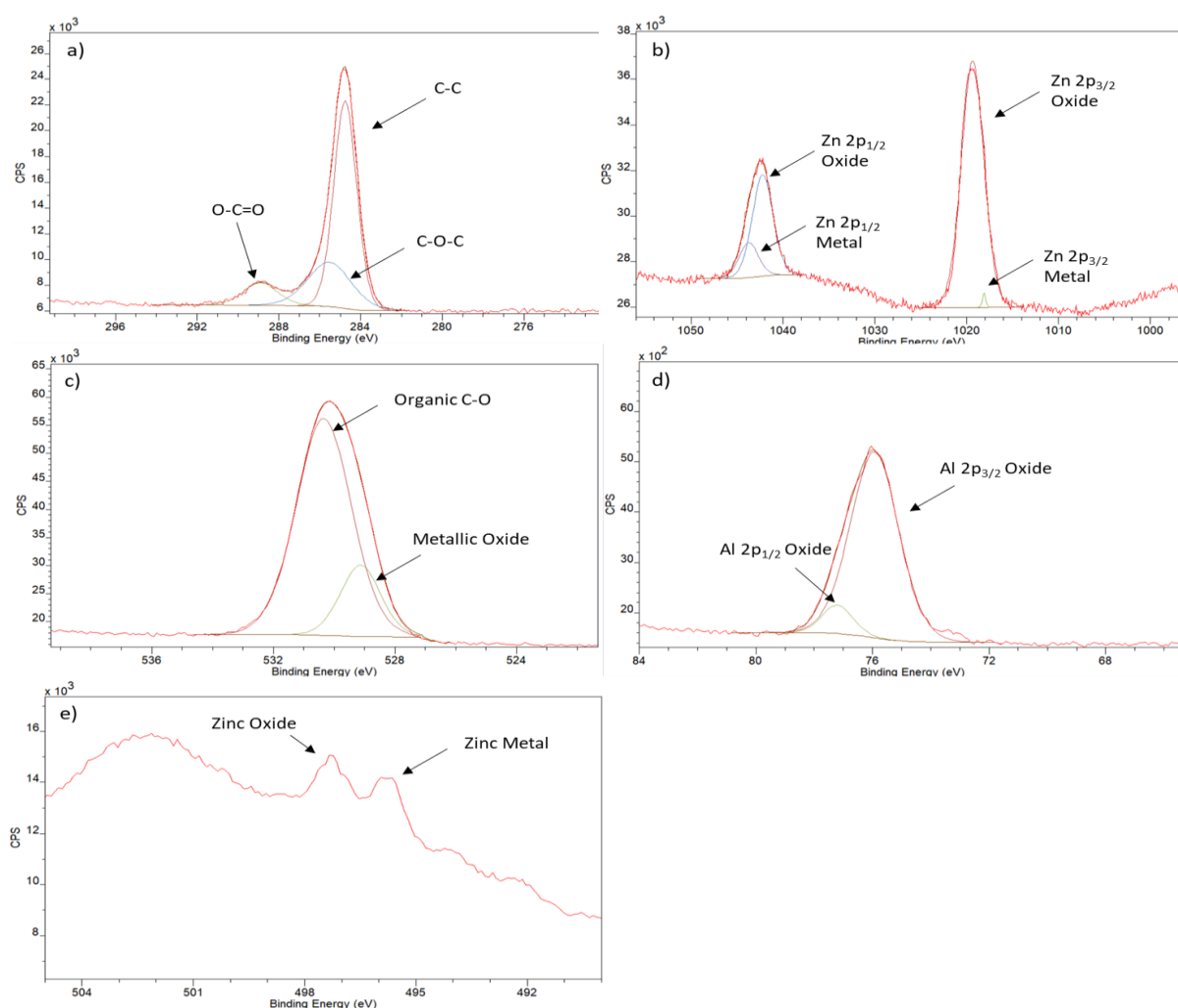
Figure 3.2. X-ray photolectron spectroscopy analysis of unconditoned HDG. (a) carbon analysis; (b) zinc analysis; (c) oxygen analysis; (d) aluminium analysis; (e) zinc Auger analysis

XPS-derived spectra were recorded and quantified over five HDG samples to assess consistency between the data. Small differences were observed in the background signal resulting from electron inelastic scattering arising from an electron losing energy to its surrounding whilst still remaining within the bulk solid.[34] In all cases, the element peaks remain close to their previously defined binding energies suggeting the precision and accuracy of the data.

The XPS-derived spectra of the surface HDG steel cleaned at 50°C, 65°C, and 80°C for 30, 120, 300, and 600 seconds was conducted to illustrate how the surface is influences by variation in surface conditioning.

 Samples immersed in cleaning solution at 50°C, 65°C and 80°C for varying times illustrate slight variation in the elemental composition, with the main C 1s peak being centred around 284.8 eV, with the C=O peak being situated around 287.8 eV, with some very small (~0.3eV) fluctuations and the C-O peak present at 289.1 eV . The O 1s peak is composed of a metal oxide peak at 529.9 eV and a C-O peak present at 531.8 eV. With regards to the Zn 2p peaks, the Zn $2p_{1/2}$ and $2p_{3/2}$ peaks are generated at 1044.8 eV and 1021.8 eV respectively. The Zn LMM peaks produced alongside the Zn 2p peaks produce a single Auger peak at 493.8 eV which indicates only the presence of zinc metal. The Al 2p peak present in an unwashed HDG sample is absent in these washed samples. The wide survey scans and elemental scans, with the washing times of relevant spectra, can be seen below in Figure 3.3.
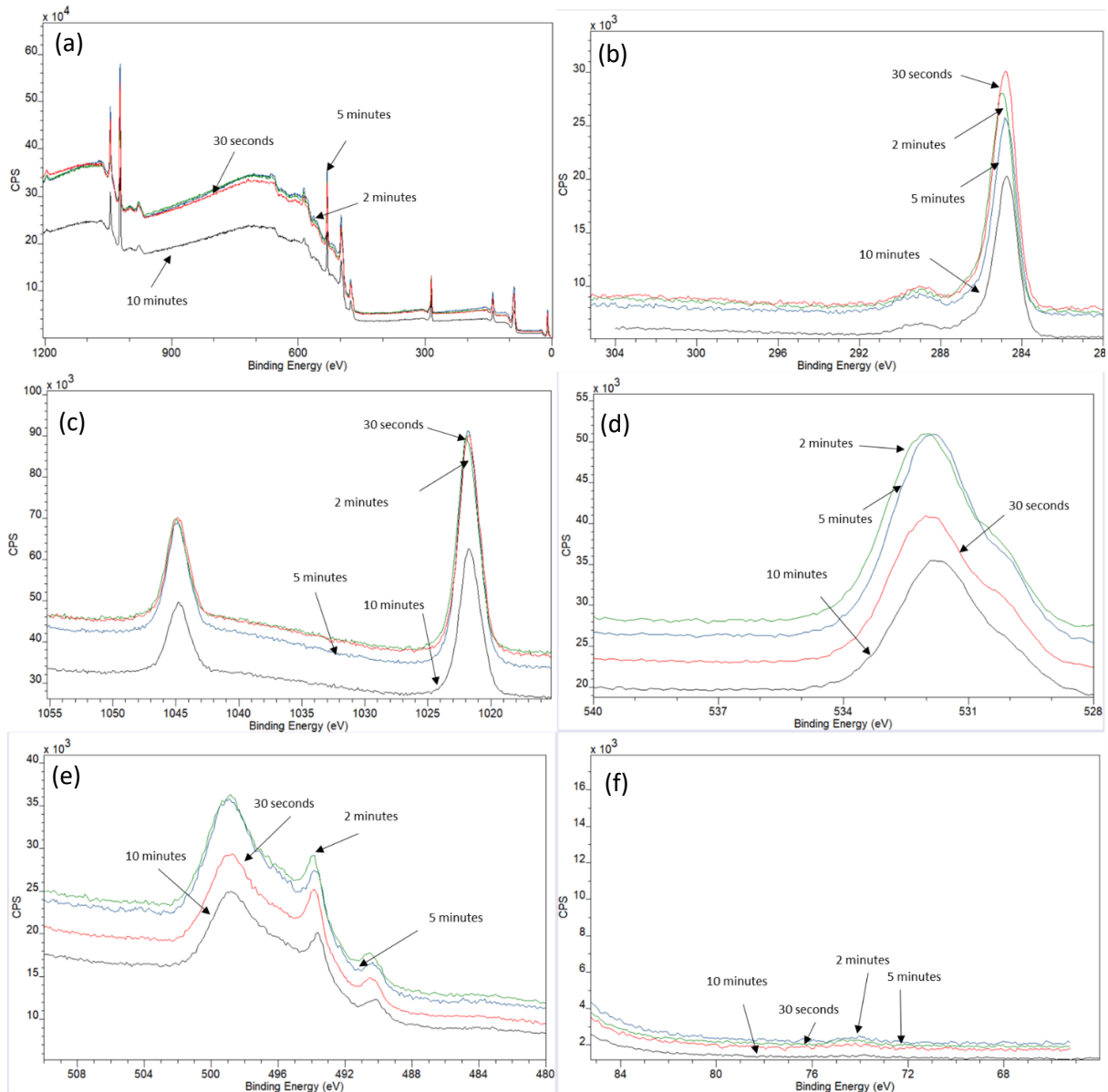
Figure 3.3. X-ray photolectron spectroscopy analysis of HDG alkaline cleaned at 50°C for varying times. (a) wide spectral analysis (b) carbon analysis; (c) zinc analysis; (d) oxygen analysis; (e) zinc Auger analysis; (f) aluminium analysis

In all cases, regardless of cleaning parameters, the element peaks produced remain close to their previously located binding energies, and, the average atomic concentrations in percentage have also been derived from each corresponding peak and are summaries below.

Table 3.1. XPS quantification of elemental components of alkaline cleaned HDG surface.

Sample	C-O (Atomic %)	C-C (Atomic %)	C=O (Atomic %)	O (Atomic %)	Zn (II) (Atomic %)	Zn(0) (Atomic %)	Al_2O_3 (Atomic %)
HDG Uncleaned	4.080	24.700	10.250	36.800	8.850	2.940	12.380
HDG 50°C 30s	5.250	33.320	9.933	33.267	4.727	13.507	0.000
HDG 50°C 2m	4.480	33.963	10.057	32.983	4.923	13.590	0.000
HDG 50°C 5m	5.270	31.483	8.197	34.000	5.470	15.580	0.000
HDG 50°C 10m	5.163	36.430	10.190	31.043	5.497	11.677	0.000
HDG 65°C 30s	4.905	37.945	11.740	24.945	5.790	14.670	0.000
HDG 65°C 2m	4.623	36.223	10.660	30.400	5.813	12.287	0.000
HDG 65°C 5m	5.403	31.893	9.343	33.000	5.497	14.860	0.000
HDG 65°C 10m	4.727	35.293	9.730	33.353	3.720	13.187	0.000
HDG 80°C 30s	4.620	35.593	11.893	31.823	4.653	11.413	0.000
HDG 80°C 2m	5.100	35.200	11.920	32.577	4.590	10.617	0.000
HDG 80°C 5m	5.500	35.057	11.417	36.113	2.813	9.107	0.000
HDG 80°C 10m	4.660	35.330	12.727	32.497	3.973	10.823	0.000
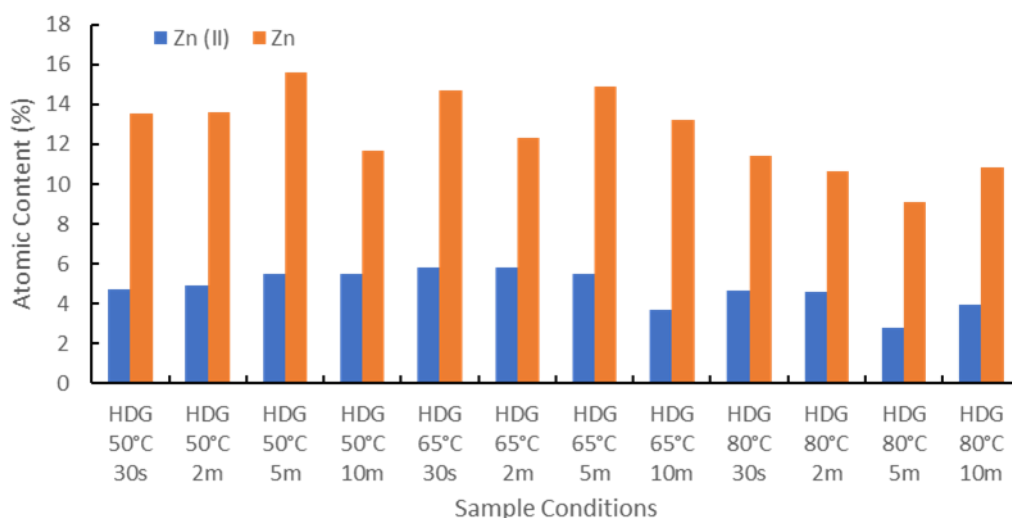
Figure 3.4. XPS quantification of Zinc and Zinc(II) of alkaline cleaned HDG surfaces.
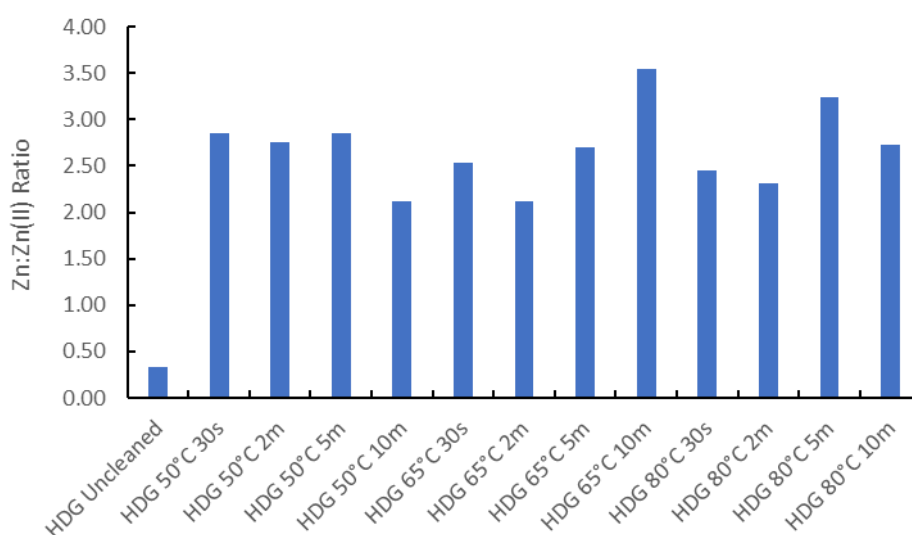
Figure 3.5. Ratio of zinc to zinc(II) of HDG steel surfaces calculated from XPS quantification

In terms of the alkaline cleaning influences the surface chemistry of HDG, the surface content generated by XPS analysis shows the surface is largely made up of carbon and oxygen, with consistent carbon contamination on the surface of all cleaned samples, with contents of 50.437 +/– 2.680 %., for an unwashed sample, this is measures at 39.030 %. This carbon content is extremely high for what should be a "cleaned" sample, and so there are clearly issues with sample handling and contamination prior to analysis. The oxygen content of the alkaline cleaned samples is calculated at 36.956 +/– 2.131% whereas an uncleaned samples has an oxygen content of 45.650 %, which is likely to be large due to a much larger

concentration of Al_2O_3 contributing to the oxygen peak. The contribution of oxygen from metal oxides drops by 35-65% after alkaline cleaning which illustrates the drop in metal oxide after cleaning. The peak produced for Zn $2p_{3/2}$ show a shift from 1022 eV to 1021.7 eV after alkaline cleaning, indicating a shift from zinc oxide to zinc metal, this can be corroborated by the production of the metallic zinc Auger peak produced at ~494 eV. This Zn LMMa peak is present in an uncleaned HDG XPS spectra but is accompanied by a zinc oxide LMMa peak at 497 eV, which is absent in all alkaline cleaned HDG spectra and would indicate complete removal of the protective surface aluminium oxide. The total Zn content can be calculated and for alkaline cleaned substrates, tends to stay around 12.610 $^{+/-}$ 3.236 %. This is much higher than the Zn content of the uncleaned HDG substrate which is calculated as 2.940 %, however the Al content is 12.380% greater as it is absent after alkaline cleaning. What is also noticeable is the increase in the Zn:Zn(II) ratio after alkaline cleaning, with uncleaned HDG steel showing a very low Zn:Zn(II), with the HDG after alkaline cleaning showing ratios of 2-3.5 Zn for every Zn(II) detected on the surface. It is likely that this much larger Al content for an unwashed sample contributes to its greater resistance to cathodic disbondment compared to alkaline washed HDG due to aluminium oxide possessing greater corrosion resistance compared to zinc oxide. As shown above in Table 3.1 and Figure 3.4 there is an increase in the metallic zinc content and a decrease in the atomic content of zinc oxide when any alkaline cleaning is performed compared to uncleaned HDG. On cleaned surfaces, there is a steady decrease in the metallic and oxidic zinc content on the surface as the cleaning intensity is increased, indicating increasing dissolution of the zinc on the surface.

3.3.2. Influence of alkaline cleaning parameters on electrochemical response using anodic, cathodic, and linear polarisation.

Polarisation experiments were performed as described in Chapter 2 to test the behaviour of HDG cleaned in alkaline solution at 50 °C, 65 °C and 80 °C for 30 seconds or 10 minutes and immersed in 5wt.% NaCl pH 7.

3.3.2.1. Anodic polarisation of alkaline cleaned HDG

Anodic Polarisation curves of alkaline cleaned HDG substrates were conducted to see how the influence of surface conditioning influences the metal oxidation reaction that occurs on the surface when in 5wt.% NaCl solution. The Open Circuit Potential (OCP) of samples were taken before anodic-going polarisation of the sample from the OCP to +0.5 V of the OCP. The anodic polarisation curve of an unconditioned HDG sample shows an OCP of the metal surface to be -0.786 V, compared to measured OCPs of -0.732 V seen in literature. The anodic curves of alkaline cleaned samples to compare with an unconditioned control can be seen in Figure 3.6.
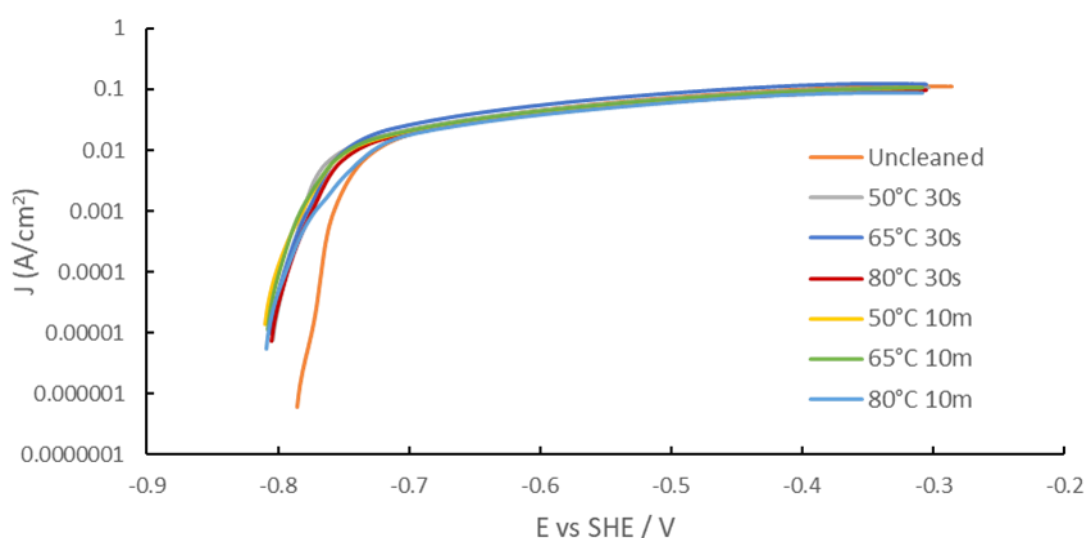
Figure 3.6. Anodic polarisation curve of HDG alkaline cleaned at all conditions in 5wt.% NaCl solution.

The OCP of a HDG sample alkaline washed at 50°C for 30 seconds is shown to be -0.8035 V, with the active region of the sample beginning at -0.7415 V, by comparison the HDG that has been washed at 50°C for 10 minutes shows an OCP of -0.8094, with the active region of the sample beginning at -0.7496 V.

The OCP of a HDG sample alkaline washed at 65°C for 30 seconds is shown to be -0.8058 V, with the active region of the sample beginning at -0.7459 V. By comparison the HDG that has been washed at 65°C for 10 minutes shows an OCP of -0.8080, with the active region of the sample beginning at -0.7461 V.

The OCP of a HDG sample alkaline washed at 80°C for 30 seconds is shown to be -0.8051 V, with the active region of the sample beginning at -0.7431 V. By comparison the HDG that has been washed at 80°C for 10 minutes shows an OCP of -0.8090, with the active region of the sample beginning at -0.7480 V.

The anodic polarisation curves generated for all alkaline washed HDG substrates indicate very little difference in the anodic response of the substrate, with all samples readily undergoing anodic metal dissolution. What can be seen when all the polarisation curves are compared to each other, there is no evidence of any samples showing any passive characteristics and readily undergo anodic metal dissolution. Any indication of a passive region is only ~7 mV, which is too small a potential change to indicate any passivity shown by the surface.

3.3.2.2. Cathodic polarisation of alkaline cleaned HDG

Cathodic Polarisation curves of alkaline cleaned HDG substrates were conducted to see how the influence of surface conditioning influences the cathodic oxygen reduction reaction that occurs on the surface when in 5wt.% NaCl solution. The Open Circuit Potential (OCP) of samples were taken before cathodic-going polarisation of the sample from the OCP to -0.5 V of the OCP. An unconditioned HDG sample undergoing cathodic polarisation shows an immediate increase in the current across a narrow potential range. Much like the alkaline cleaned samples shown below in Figure 3.7, this increase in current occurs for all samples and illustrates that a transition occurs that means the oxygen reduction reaction stops becoming an activation-controlled process and becomes a diffusion limited process, resulting a much slower increase in the measured current as the applied potential becomes more negative, with this behaviour also being shown in in samples washed at all conditions.

 The region at which the oxygen reduction occurs before diffusion begins to limit the reaction is measured as 1.88×10^{-6} A across a potential range of 0.01 V. What is also notable is the increase in the current which can be shown as a bump in the polarisation curve that occurs at ~1.04 V, which can be attributed to reduction of the zinc surface. This additional reduction reaction has a current increase of ~1.79×10^{-5} A before the current continues to increase as the potential moves further away from the OCP.
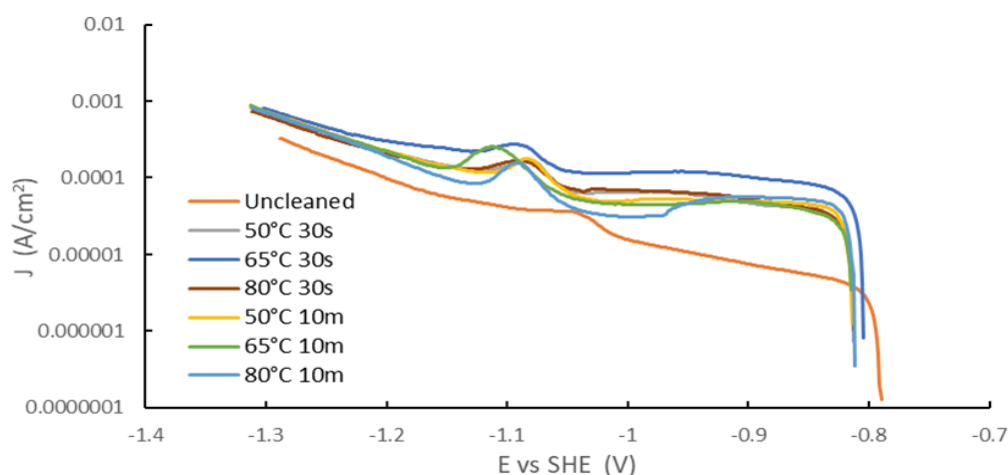
Figure 3.7. Cathodic polarisation curve of HDG alkaline cleaned at all conditions in 5wt.% NaCl solution.

The cathodic branch of HDG cleaned at 50°C shows similar behaviour to that of an unconditioned HDG substrate, however, there are some differences in the currents produced in the activation-controlled regions and the additional reduction reaction that occurs. For HDG washed at 50°C for 30 seconds, the activation-controlled reduction region has a current increase of 3.256×10^{-5} A over a 0.02 V potential range. The secondary reduction reaction is also more apparent in the cathodic branch, showing an increase of 9.09×10^{-5} A at a measured potential of -1.07 V. Very similar behaviour is also shown for washing conditions of 50°C for 10 minutes, with the initial spike in current to be measured as a 3.774×10^{-5} A increase over a 0.02 V potential range. The additional reduction reaction again occurs at -1.08 V, with a corresponding current increase of 1.128×10^{-4} A.

Much like the polarisation curves for a 50°C alkaline wash, a 65°C cleaning temperature shows very similar behaviour across the potential range for both immersion times shown. For HDG washed at 65°C for 30 seconds, the activation-controlled reduction region has a current increase of 5.479×10^{-5} A over a 0.02 V potential range. The secondary reduction reaction is also more apparent in the cathodic branch, showing an increase of 1.4×10^{-4} A at a measured potential of -1.09 V. Very similar behaviour is also shown for washing conditions of 50°C for 10 minutes, with the initial spike in current to be measured as a 2.569×10^{-5} A increase over a 0.02 V potential range. The additional reduction reaction occurs at -1.10 V, with a corresponding current increase of 1.844×10^{-4} A.

For HDG washed at 80°C for 30 seconds, the activation-controlled reduction region has a current increase of 3.423×10^{-5} A over a 0.02 V potential range. The secondary reduction reaction is also more apparent in the cathodic branch, showing an increase of 8.7×10^{-5} A at a measured potential of -1.09 V. Very similar behaviour is also shown for washing conditions of 80°C for 10 minutes, with the initial spike in current to be measured as a 4.345×10^{-5} A increase over a 0.02 V potential range. The additional reduction reaction occurs at -1.10 V, with a corresponding current increase of 1.062×10^{-4} A. The current density at different measured potentials, denoted point A (-0.9 V) and point B (-1.2 V) can be seen below and a summary of the measured potentials and currents of the cathodic reactions involved can be seen below in Table 3.2. The changes in current density during initial cathodic-going polarisation, and measured currents and plots of the measured current densities for the cleaning times used at the different temperatures in Figure 3.8.

Table 3.2. Comparison of potentiodynamic parameters across HDG cleaning regimes.

Cleaning Conditions	OCP (V)	Primary reduction region ΔJ (A/cm^{-2})	Measured Current at point A (A/cm^{-2})	Measured Current at point B (A/cm^{-2})
Uncleaned	-0.788	1.88×10^{-6}	7.56×10^{-6}	1.00×10^{-4}
50°C 30s	-0.812	3.256×10^{-5}	4.69×10^{-5}	2.24×10^{-4}
50°C 10m	-0.814	3.774×10^{-5}	4.97×10^{-5}	2.25×10^{-4}
65°C 30s	-0.803	5.479×10^{-5}	1.02×10^{-4}	3.02×10^{-4}
65°C 10m	-0.812	2.569×10^{-5}	4.90×10^{-5}	2.24×10^{-4}
80°C 30s	-0.811	4.423×10^{-5}	5.27×10^{-5}	2.08×10^{-4}
80°C 10m	-0.811	4.345×10^{-5}	5.59×10^{-5}	1.95×10^{-4}
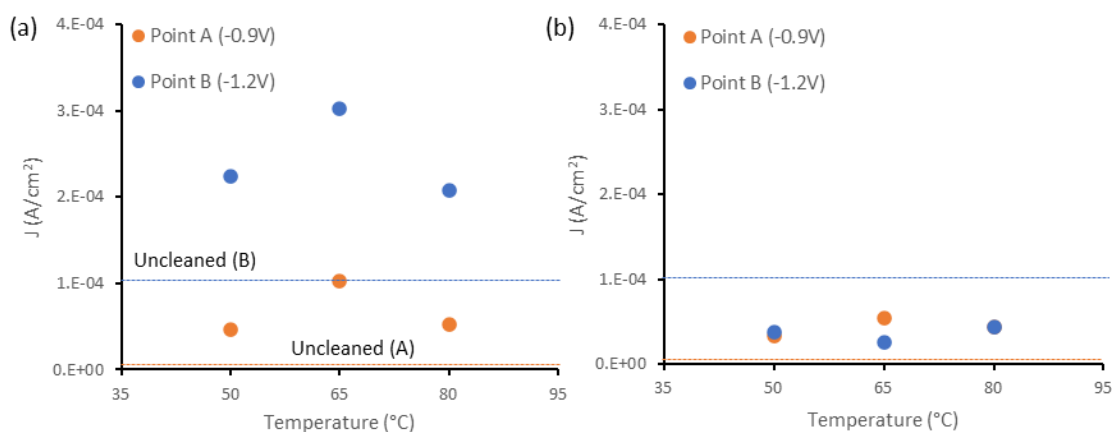
Figure 3.8. Measured current changes at point A and point B for HDG alkaline cleaned for: (a) 30 seconds; (b) 10 minutes

The cathodic polarisation curves do, however, show slight differences in how alkaline cleaning influences the cathodically driven oxygen reduction (ORR) reaction on the surfaces of chemically etched surfaces. The initial change in current as the cathodic oxygen reduction is a result of the initial cathodic oxygen reduction, as shown in equation 3.1.

$$O_2 + H_2O + 2e^- \rightarrow HO_2^- + OH^- \hspace{4cm} \text{Equation 3.1}$$

The reaction curve that is formed is the result of the initial oxygen reduction reaction being an activation controlled process whereby there is plenty of oxygen available at the surface and alkaline cleaning appears to increase the amount the current changes as the reaction proceeds. This initial burst in current then subsides and the current struggles to increase as the reaction is polarised more negatively, changing from an activation controlled process to a diffusion controlled process, as oxygen is no longer readily available to the surface due to mass transport being limited.[35, 36] However, there is a second increase in the current which can be attributed to a four electron reduction reaction occurring.[37] This additional reaction results in the current increasing due to an additional four electron reduction reaction occurring and alkaline cleaning appears to also influence this, with greater cleaning intensity promoting greater increases in current and is shown in equation 3.2.

$$O_2 + 2H_2O + 4e^- \rightarrow 4OH^- \hspace{4cm} \text{Equation 3.2}$$

This reaction also occurs at more cathodic potentials at more intense cleaning times, these changes are marginal, but there is a 30mV cathodic shift from an uncleaned HDG substrate to HDG cleaned at 50°C for 30 seconds, and a further 20 to 30 mV cathodic shift for samples

cleaned at 65°C and 80°C. This would appear to show that as alkaline cleaning intensity increases, the surface is becoming a more active oxygen cathode, producing the increased current changes before the current plateaus, and increasing the current further after the additional reduction reaction.

3.3.2.3. Linear polarisation of alkaline cleaned HDG

Linear Polarisation of alkaline cleaned HDG substrates were conducted to see how the influence of surface conditioning influences the metal oxidation and oxygen reduction reactions that occurs on the surface when in 5wt.% NaCl solution. The Open Circuit Potential (OCP) of samples were taken before polarisation of the sample, with the potential shifting from -0.01 V below the OCP to +0.01 greater than the OCP. After polarisation, samples were held at the OCP for 30 minutes before polarisation was conducted again. This was done every 30 minutes for 210 minutes to ascertain the corrosion properties of the different substrates over time. From the linear polarisation curves, the polarisation resistance of the substrate can be gathered from the change in current and potential, which subsequently allows for calculation of the corrosion rate, which allows for direct comparisons in the performance and behaviour of tested samples. A selection of linear polarisation curves can be seen below in Figures 3.9-3.12 with a summary of polarisation resistances seen in Figures 3.13 and 3.14.
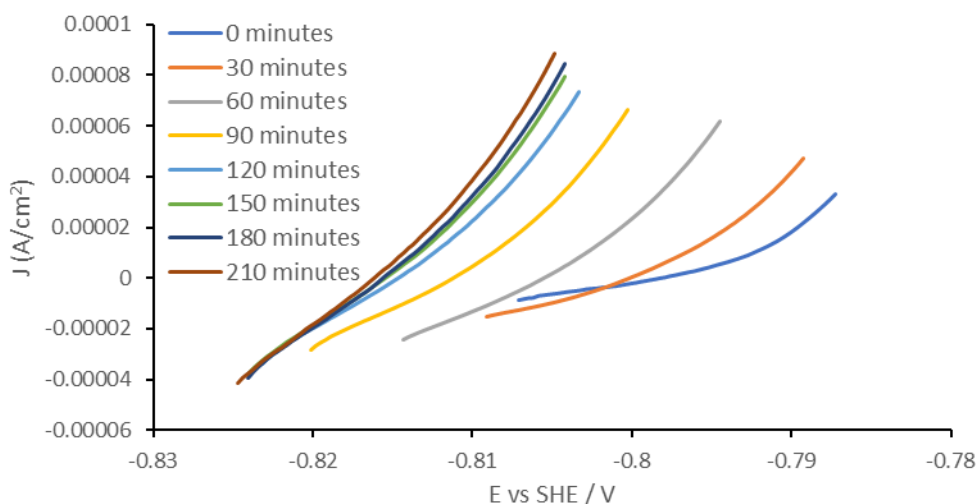
Figure 3.9. Linear Polarisation curved of unconditioned HDG. Polarisation was conducted every 30 minutes for 210 minutes.
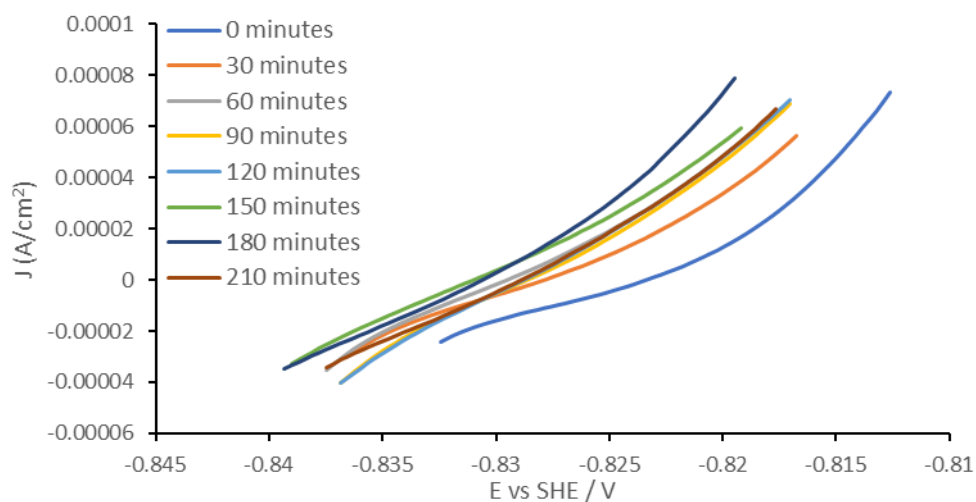
Figure 3.10. Linear Polarisation curve of HDG alkaline cleaned at 50°C for 30 seconds. Polarisation was conducted every 30 minutes for 210 minutes.
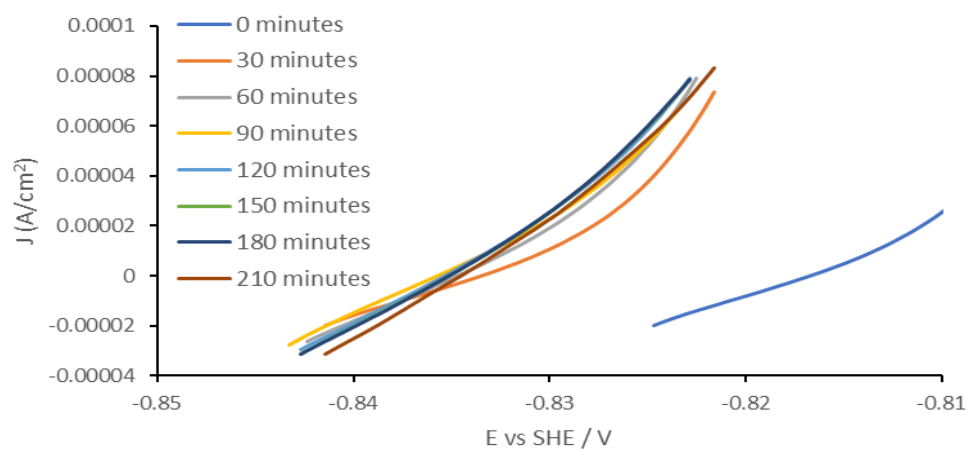
Figure 3.11. Linear Polarisation curve of HDG alkaline cleaned at 65°C for 30 seconds. Polarisation was conducted every 30 minutes for 210 minutes.
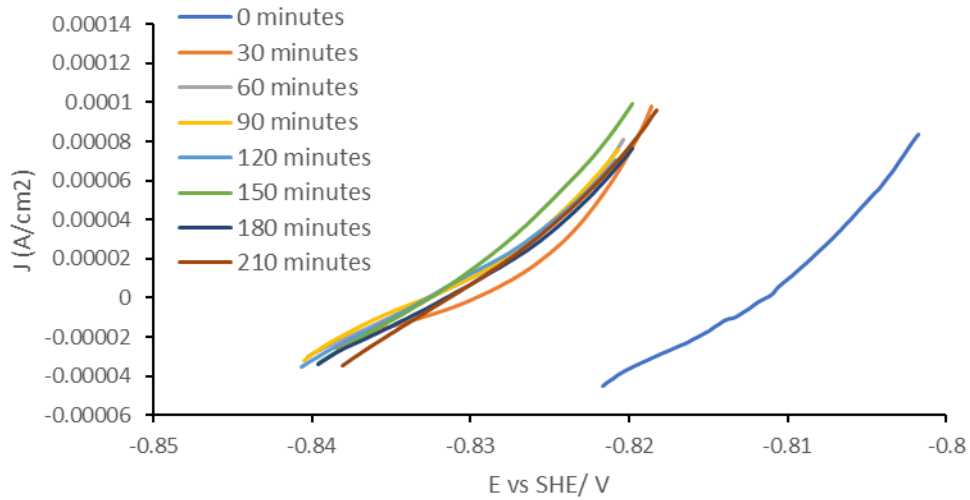
Figure 3.12. Linear Polarisation curved of HDG alkaline cleaned at 80°C for 30 seconds. Polarisation was conducted every 30 minutes for 210 minutes.

As shown above, the polarisation curves show that as the time immersed in 5% NaCl increases, the OCP and subsequent linear polarisation curves shift to more cathodic potentials, before stabilising at lower potentials. The initial polarisation curve produced can be attributed to the OCP still stabilising before the surface is polarised, subsequent curves indicate the OCP has stabilised after 30 minutes in solution.

From the linear polarisation curves produced, the polarisation resistance can be obtained from equation 3.3.

$R_{pol} = \Delta E \, / \, \Delta I$ Equation 3.3

Where ΔE is the change in the applied potential from the free corrosion potential and ΔI is change in polarisation current. The polarisation resistance of HDG cleaned at different conditions can be seen below in Figures 3.13 and 3.14
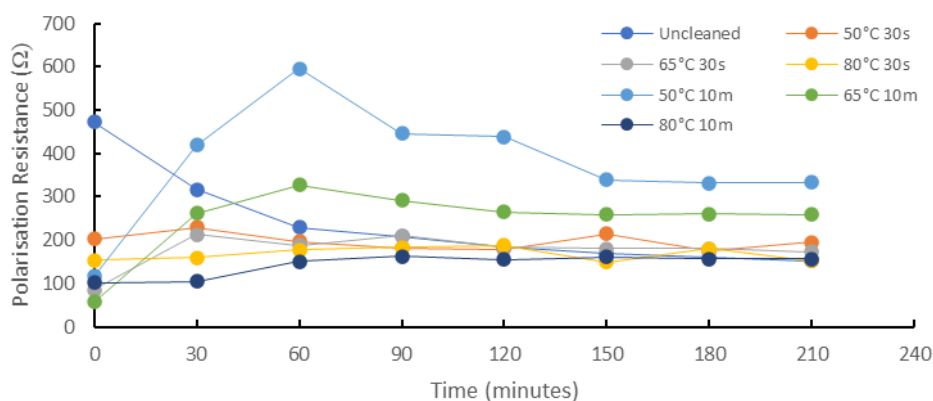
Figure 3.13. Polarisation resistance of HDG at varying cleaning conditions
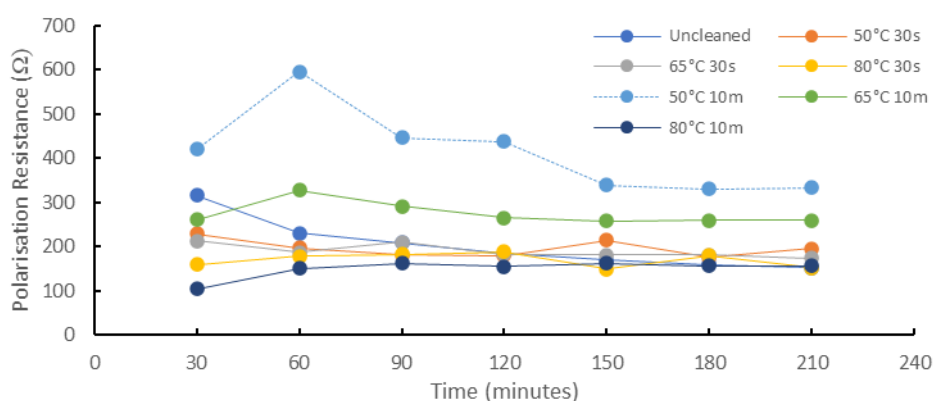
Figure 3.14. Polarisation resistance of HDG at varying cleaning conditions from 30 to 210 minutes.

The polarisation resistances calculated show that HDG washed for 30 seconds have polarisation resistances that drop over time whereas HDG washed for 10 minutes at 50°C, 65°C and 80°C all show very similar polarisation resistances. The polarisation resistances shown typically remain reasonably constant over the experiment time, with no real increase or decrease in the calculated R_{pol} values. The intensity of the cleaning parameters also do not relate to the R_{pol} of the surface, with a surface cleaned at 50°C for 10 minutes showing the greatest R_{pol} values from 30 to 210 minutes, with resistances measured between 330 - 600Ω. The remaining samples typically show R_{pol} values between 104 - 328Ω.

The corrosion current density of the system can be related to the polarisation resistance by the Stern-Geary Equation: [38,39]

$$icorr = \frac{B}{Rpol}$$ Equation 3.4

$$B = \frac{ba.bc}{2.303\,(ba+bc)}$$

Equation 3.5

B is the Stern-Geary coefficient which is calculated using the anodic and cathodic Tafel slopes (ba and bc).

$$Icorr = \frac{1}{Rpol}\,x\,\frac{ba.bc}{2.303(ba+bc)}$$

Equation 3.6

From the Stern-Geary equation, the corrosion rate can be calculated using Faraday's corrosion equation: [40]

Corrosion rate (μmyear^{-1}) = $K\frac{icorr}{d}EW$

Equation 3.7

Where K is a conversion factor (3.27×10^6 μm.g.A^{-1}.cm^{-1}.yr^{-1}), I$_{corr}$ is the corrosion current density, EW is the equivalent weight and d is the density of the polarised sample. An outline of the calculated coefficients, I$_{corr}$ and the calculated corrosion rates for uncleaned HDG and HDG cleaned for 30 seconds and 10 minutes at all temperatures can be seen below in Table 3.3.

Table 3.3. Tafel coefficients, I$_{corr}$ and corrosion rate values for alkaline cleaned HDG.

Sample	Bc (V/decade)	Ba (V/decade)	I$_{corr}$ (A/cm^2)	Corrosion rate (μm/year)
Uncleaned	0.004	0.2477	8.28×10^{-6}	124.14
50°C 30s	0.0028	0.2387	5.00×10^{-6}	75.83
65°C 30s	0.0011	0.278	2.83×10^{-6}	42.43
80°C 30s	0.001	0.2147	1.74×10^{-6}	26.15
50°C 10m	0.0011	0.233	1.15×10^{-6}	17.17
65°C 10m	0.0011	0.2389	1.73×10^{-6}	25.92
80°C 10m	0.001	0.2032	2.88×10^{-6}	43.21

The corrosion rate and polarisation resistance are inversely proportional to one another with higher polarisation resistances resulting in lower corrosion rates and vice versa. [41] Through use of the Stern-Geary equation and using average polarisation resistances to calculate I$_{corr}$, the calculated corrosion rate for a selection of samples can be seen above, and interestingly as cleaning temperature increases and the time is kept constant the corrosion rate drops. When cleaning time is increased at a constant temperature the corrosion rate is variable, with a

decreases in corrosion rate at 50°C and 65°C, and an increase in the corrosion rate at 80°C. However, as the corrosion rate is measured in microns per year, the calculated difference over the course of a year is negligible.

3.3.3. Investigation of corrosion driven cathodic disbondment kinetics using time-lapse photography and Scanning Kelvin Probe

Time-lapse photography and Scanning Kelvin Probe (SKP) were used to investigate the kinetics of corrosion driven cathodic disbondment of polyvinyl-butyral coatings applied to alkaline cleaned HDG steel substrates. Stratmann cells were created to create a defect region to allow for the initiation of cathodic disbondment and samples were exposed to a 95% relative humidity atmosphere and disbondment was initiated using 5% sodium chloride solution. This Stratmann cell set-up creates an artificial defect on the coating which when exposed to corrosive electrolyte undergoes corrosion driven cathodic disbondment, causing delamination of the coating. The anodic site for metal dissolution occurs at the exposed metal site in the electrolyte well, and the cathodic area of the electrochemical cell is set up at the cathodic front at the metal-coating interface. Time-lapse images and SKP potentials were measured every hour for 24 hours and the kinetics of coating failure were analysed as alkaline cleaning time and temperature are varied.

3.3.3.1. Use of time-lapse photography to analyse kinetics of corrosion driven cathodic disbondment

The delamination rate, initiation time and delamination distance of failed PVB coatings were calculated from measuring the distance covered by coating failure over 24 hours. The kinetic information gathered from cathodic disbondment can be seen below from a set of time-lapse sequence images. Diagrams of the Stratmann cell set up used in time-lapse and SKP studies and time-lapse images of how information was gathered can be seen in Figure 3.15 and an example of a 24 hour delamination study in Figure 3.16.
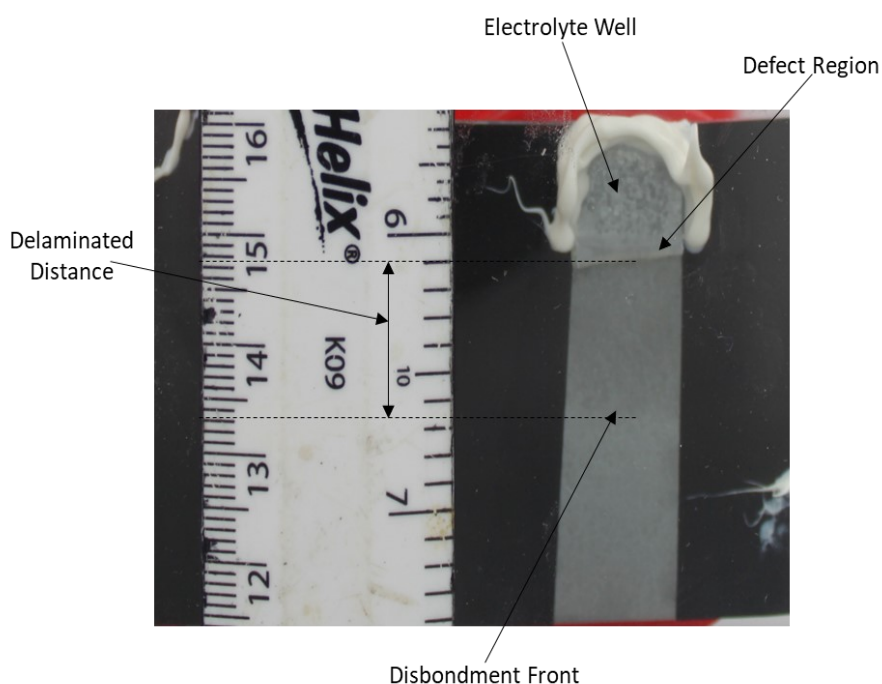
Figure 3.15. A Stratmann cell set up used in timelapse and SKP studies.
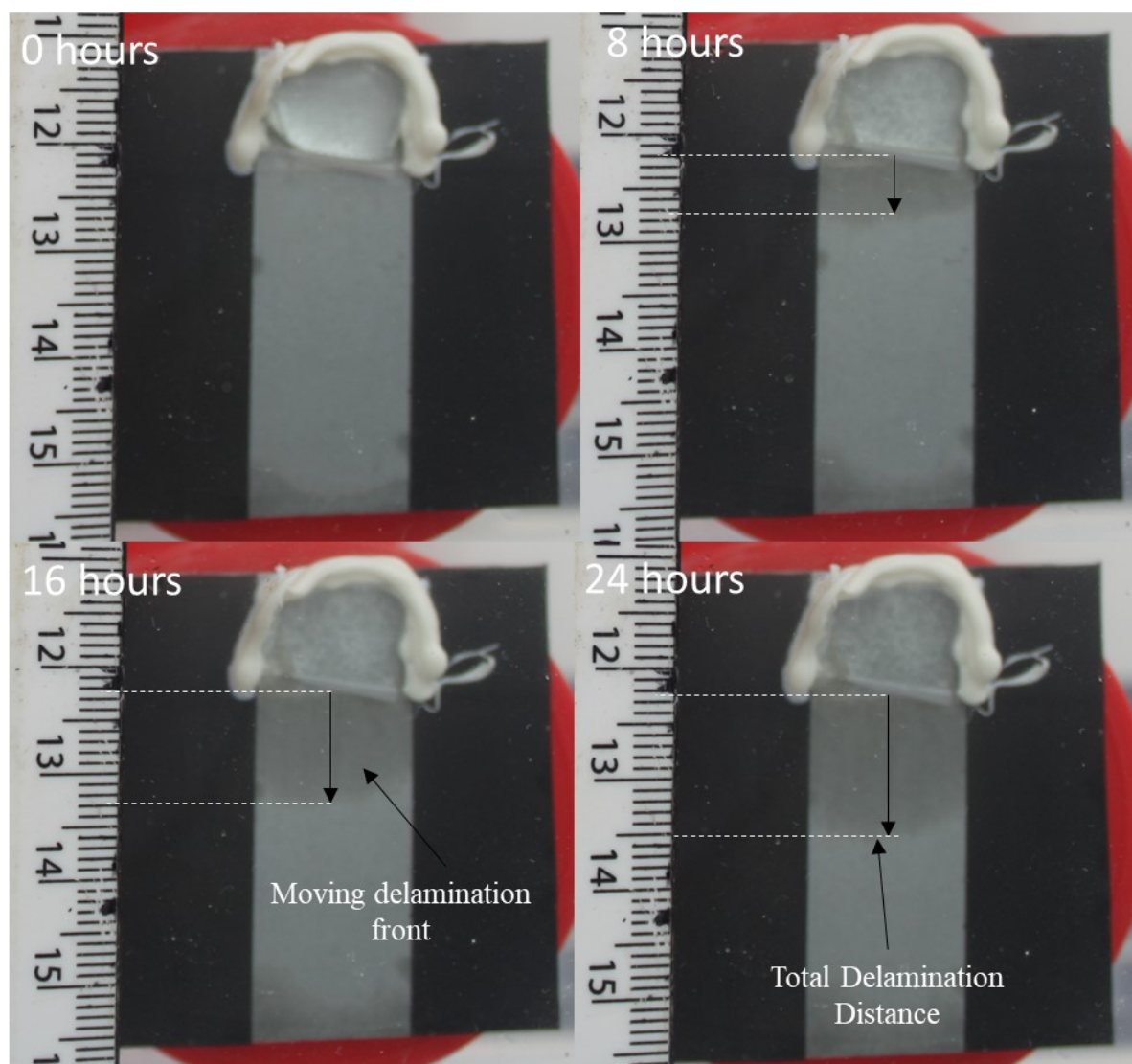
Figure 3.16. Time-lapse images of uncleaned HDG steel and HDG steel alkaline cleaned for 10 minutes at 80°C.

From Figures 3.15 and 3.16, the delamination of PVB from the steel surface can be visually seen via tarnishing of the surface caused by generation of an alkaline under-film region. This results in the solubilisation of amphoteric ZnO and Zn on the surface in alkaline conditions and forms zincate ions which can be seen in equations 3.8 and 3.9:

$$ZnO + H_2O + 2NaOH \rightarrow Na_2Zn(OH)_4 \qquad \text{Equation 3.8}$$

$$Zn + 2H_2O + 2NaOH \rightarrow Na_2Zn(OH)_4 + H_2 \qquad \text{Equation 3.9}$$
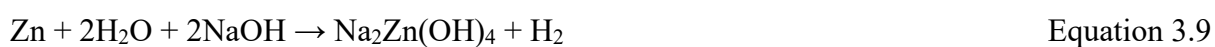
The influence of variation in the time and temperature of alkaline cleaning of HDG steel on the performance of PVB coatings can be seen below. The delamination distance of cathodic

disbondment of PVB on HDG which has been washed in 50°C, 65°C and 80°C for varying amounts of time and compared to HDG which has not been cleaned can be seen below in Figures 3.17- 3.20.
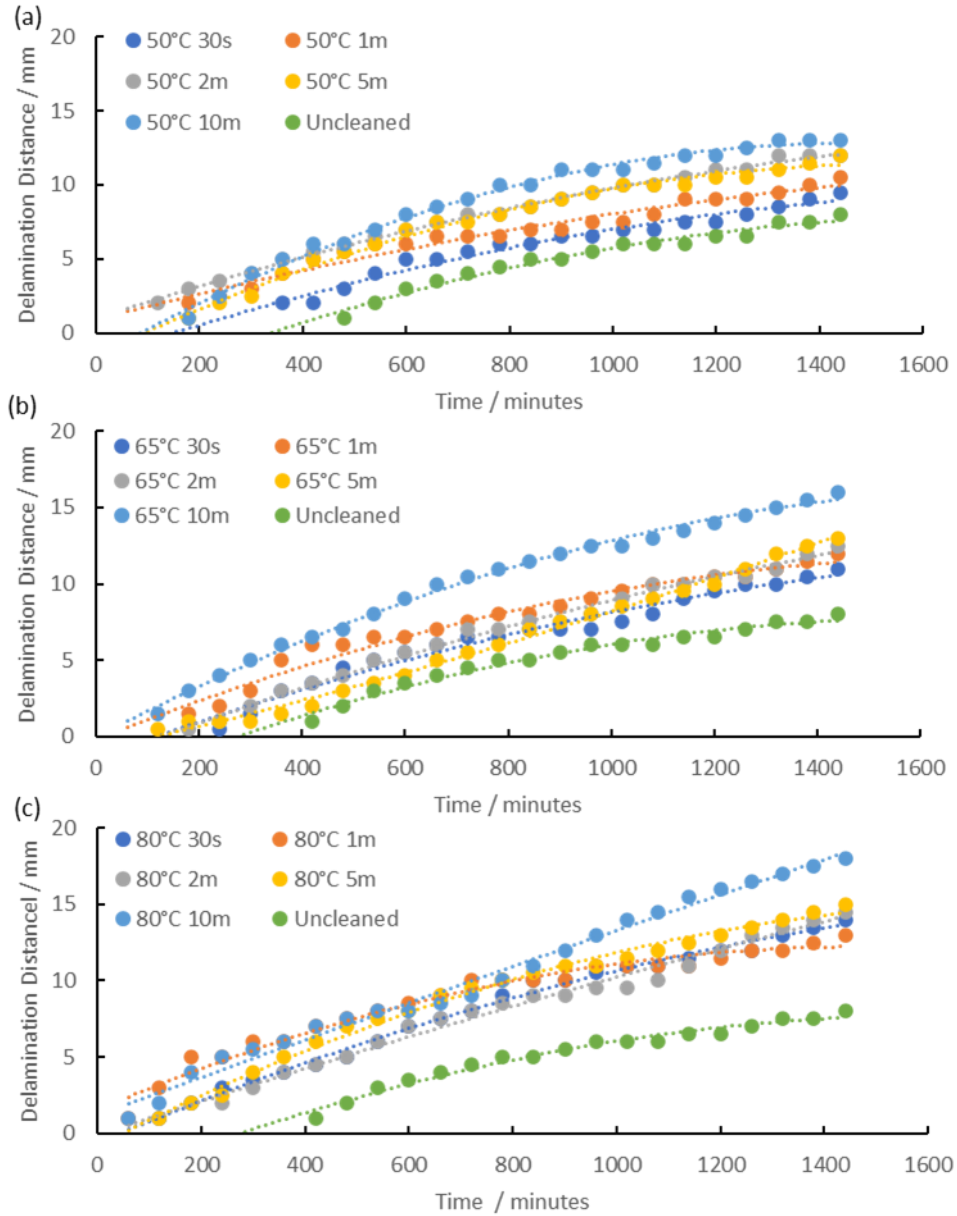
Figure 3.17. Delamination distance versus time plots obtained for PVB coated-HDG steel which had previously been alkaline cleaned at 9a) 50°C for varying times; (b) 65°C for varying times; (c) 80°C for varying times.
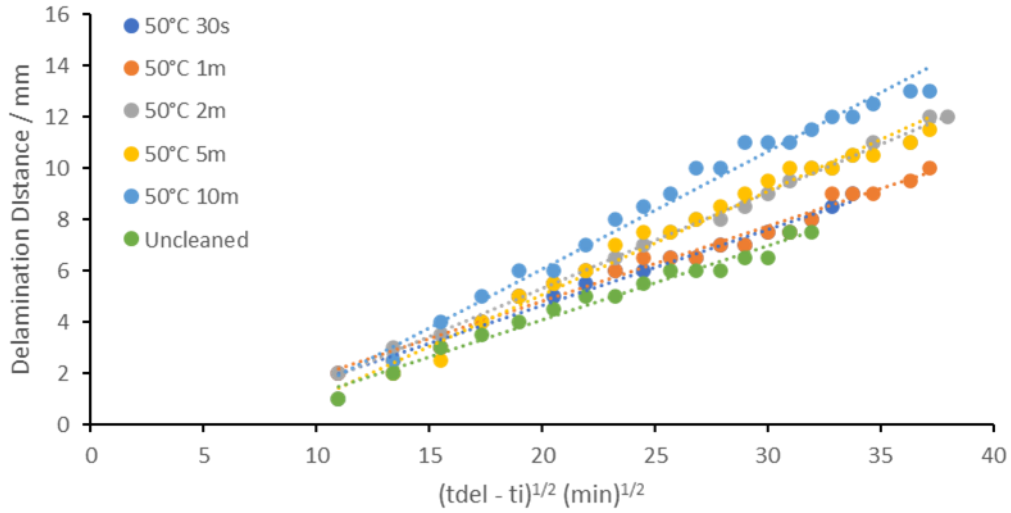
Figure 3.18. Delamination distance versus time plots obtained for PVB coated-HDG steel which had previously been alkaline cleaned at 50°C for varying times.
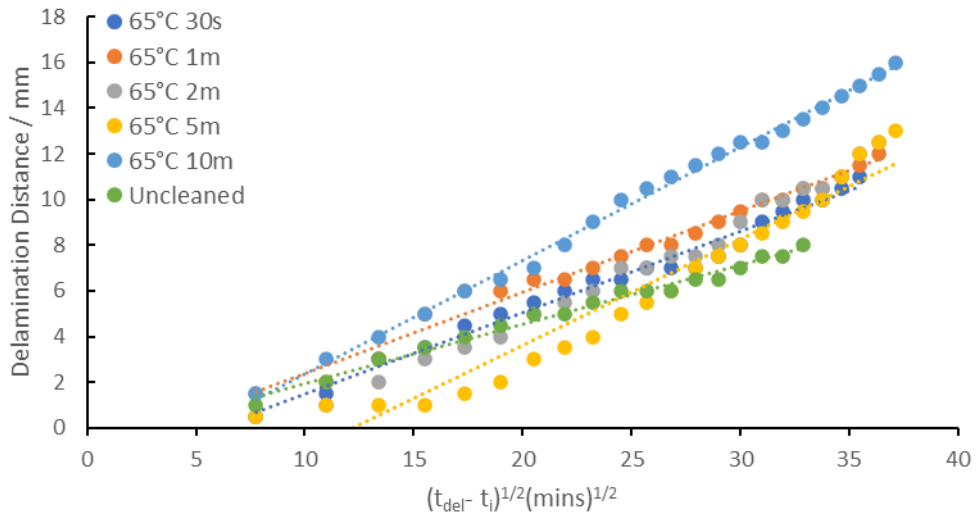
Figure 3.19. Delamination distance versus time plots obtained for PVB coated-HDG steel which had previously been alkaline cleaning at 65°C for varying times
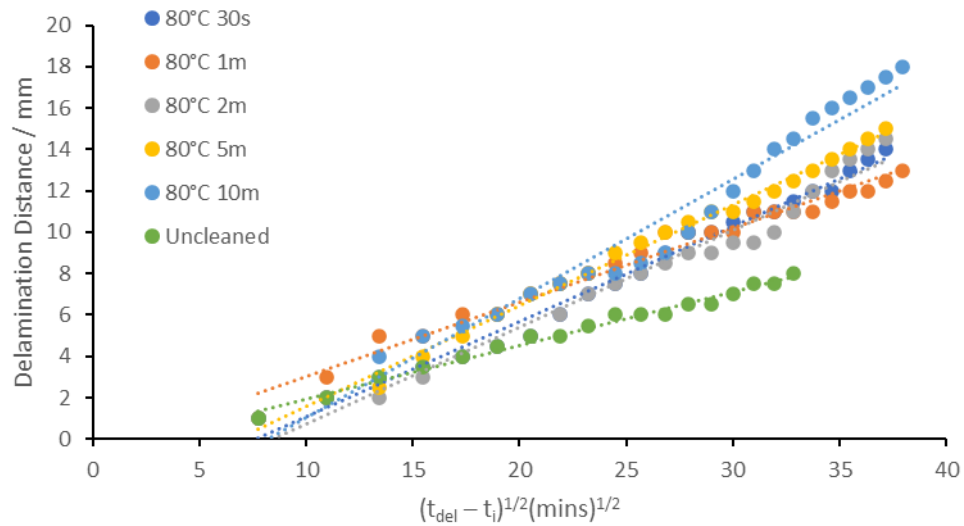
Figure 3.20. Delamination distance versus time plots obtained for PVB coated-HDG steel which had previously been alkaline cleaning at 80°C for varying times

As shown in Figures 3.17-3.20, the time of the alkaline cleaning step has an influence on the delamination of PVB that occurs when the cleaning temperature is maintained. An uncleaned HDG substrate shows the lowest delamination distance compared to all cleaned surfaces. A 10 minute cleaning time shows the greatest distance travelled over the 24 hours, with the other washing times showing similar delamination behaviour. A comparison of how variation of time and temperature of the alkaline wash influences the final delamination distance achieved after 24 hours can be seen below in Figure 3.21.
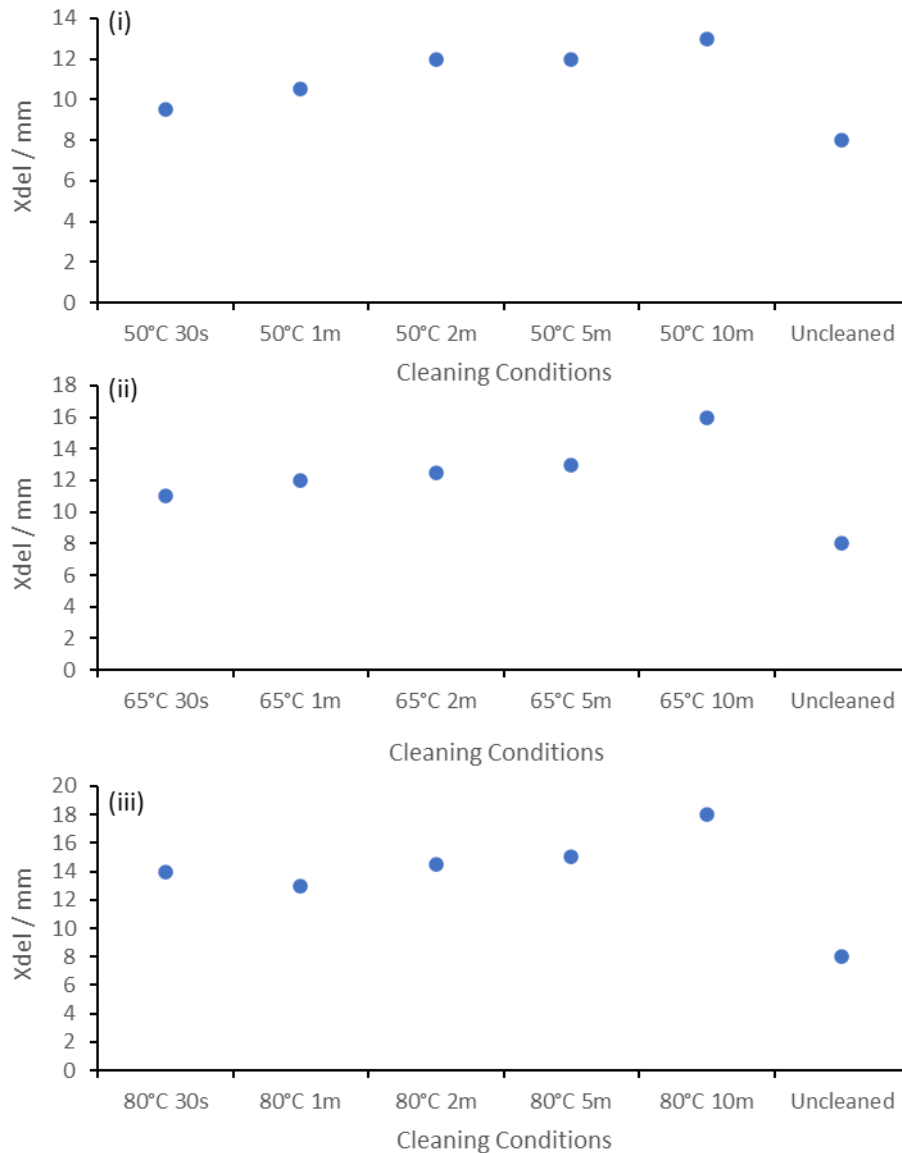
Figure 3.21. Delamination distance from defect of PVB on alkaline cleaned HDG; (i) HDG cleaned at 50°C, (ii) HDG cleaned at 65°C, (iii) HDG cleaned at 80°C.

As seen in Figure 3.21 there is a clear trend in how the intensity of the alkaline wash influences the final delamination distance. At a set temperature, as the cleaning time increases, there is a steady increase in the delamination distance achieved, for example, a wash that occurs at 50°C for 30 seconds has a delamination distance of 9.5 mm, whereas a 10 minute was at 50 °C has a delamination distance of 13 mm. Also, if the time is kept constant and the temperature is varied there is also an increase in the delamination. From the total delamination distance which occurs over 24 hours, the delamination rate of the delaminated coating can also be calculated and can be seen below in Figure 3.22 for each of the cleaning

temperatures and this follows the same trend as that seen in the delamination distance charts seen above.
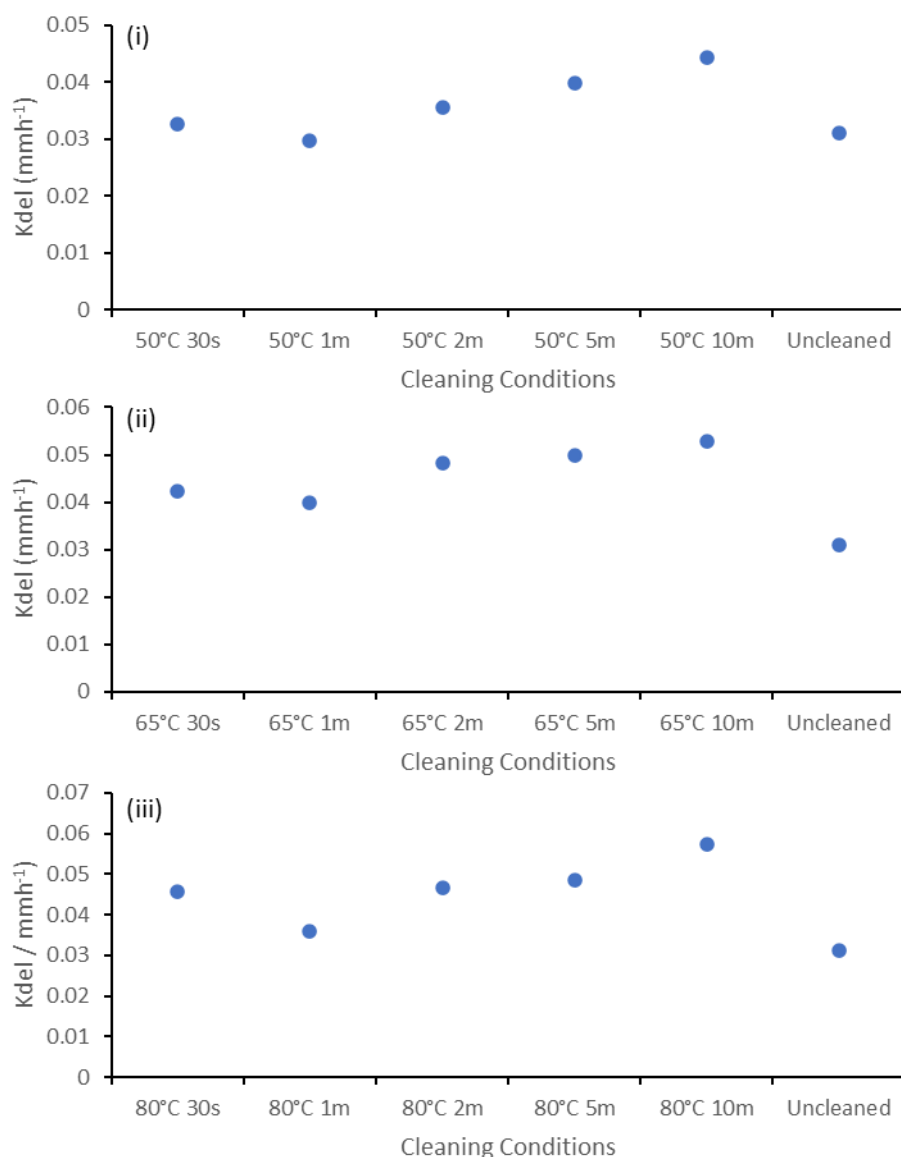
Figure 3.22. Delamination rate of PVB on alkaline cleaned HDG. (i) HDG cleaned at 50°C, (ii) HDG cleaned at 65°C, (iii) HDG cleaned at 80°C.

Although there are clear trends in how the alkaline cleaning influences the delamination rate and the maximum distance achieved, there is a slight negative trend in how the cleaning conditions influence the initiation of cathodic disbondment. At temperatures of 50°C and 65°C, there is a tendency for the initiation time to decrease as the cleaning time increases, with the longest initiation time being present for 30 second washing times, and the initiation times being similar at times of 1 minute or greater. At a cleaning temperature of 80°C, there

is no overall trend in how cleaning times influences the initiation time of coating failure, with initiation time fluctuating between 60 and 120 minutes. Alkaline cleaning does however cause coating failure to occur faster than that of an uncleaned HDG surface, which takes 420 minutes for coating failure to start. The time taken for 5% NaCl to initiate coating failure was also measured and can be seen in Figure 3.23.
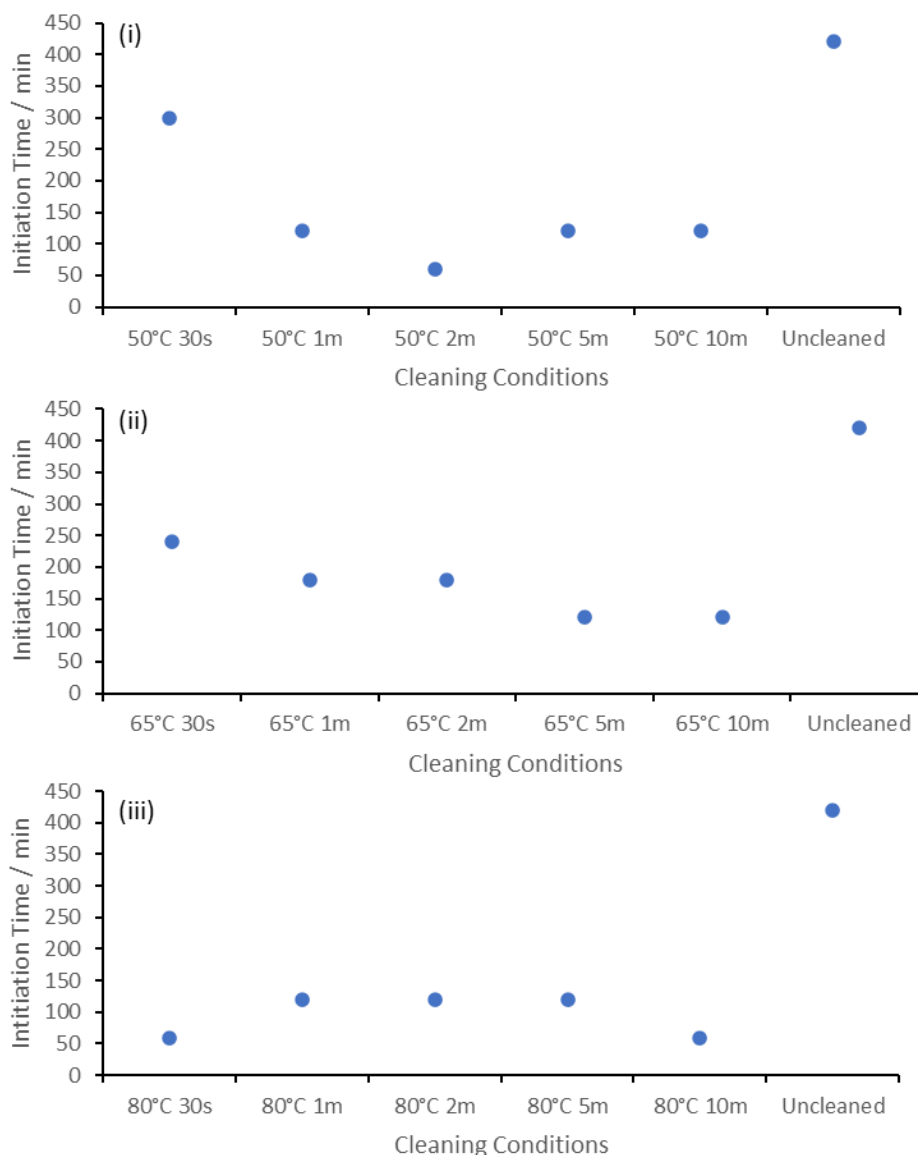
Figure 3.23. Initiation time of alkaline cleaned HDG. (i) HDG cleaned at 50°C, (ii) HDG cleaned at 65°C, (iii) HDG cleaned at 80°C.

The time-lapse data of cleaned HDG samples shows that as the cleaning time increases withing a set temperature, the delamination rate and delamination distance increases, with

there being a ~1-2 mm increase in the delamination achieved over 24 hours as the cleaning temperature is increased and a consistent increase in the delamination rate. What is also notable is how an unconditioned HDG sample undergoes cathodic delamination compared to a sample which has undergone alkaline cleaning. An uncleaned sample only delaminates 8 mm over 24 hours, compared to a minimum delamination of 9.5 mm shown by HDG washed at 50°C for 30 seconds and is also much lower than the 18 mm of delamination shown by HDG washed at 80°C for 10 minutes.

3.3.3.2. Use of Scanning Kelvin Probe to analyse kinetics of corrosion driven cathodic disbondment

The use of scanning Kelvin probe is to analyse not only the kinetics of the cathodic disbondment of the alkaline cleaned samples but also how the surface potential changes with delamination of the organic coating and whether the surface conditioning changes the measured potentials. Measurements were taken using 30 second and 10 minute washing times used at the temperatures used previously. The E_{corr} versus distance (X) for the case of a control HDG sample which did not undergo alkaline surface conditioning prior to PVB application is given in Figure 3.24 which allows for determination of baseline kinetics for a HDG system with a model PVB coating applied. As shown below, an unconditioned HDG sample begins to undergo cathodic disbondment after 2 hours and after 24 hours had only delaminated 7 mm from the defect region.
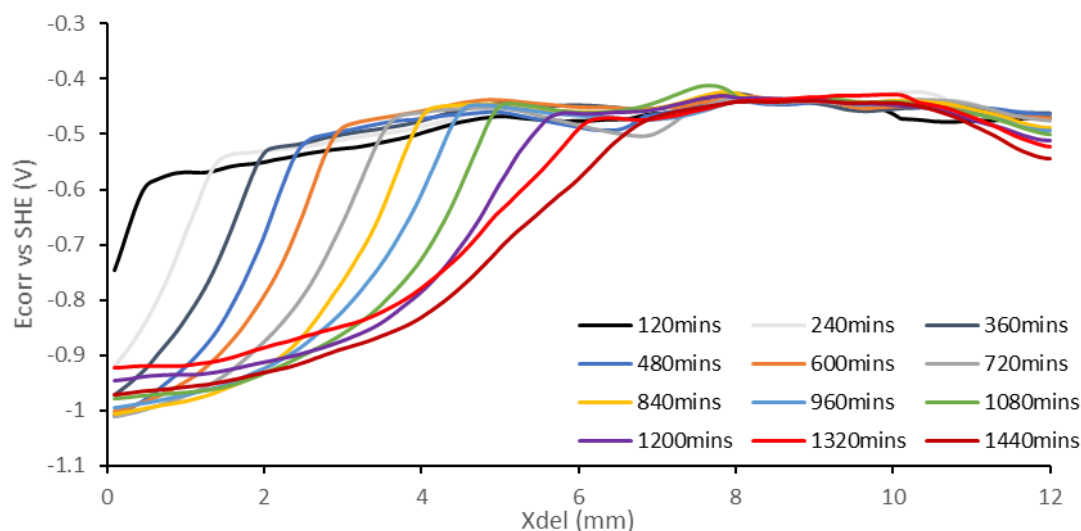
Figure 3.24. An SKP profile showing the time dependent E_{corr} measurements against distance from defect (X) for PVB coating from an unconditioned HDG sample. E_{corr} measurements were taken every hour for 24 hours with measurements shown every 2 hours.

A selection of SKP profiles illustrating E_{corr} versus distance (X) for the case of HDG alkaline washed at 50°C, 65°C, and 80°C for 10 minutes prior to PVB application is given in Figures 3.25 – 3.27, with the remaining SKP profiles shown in the appendix.
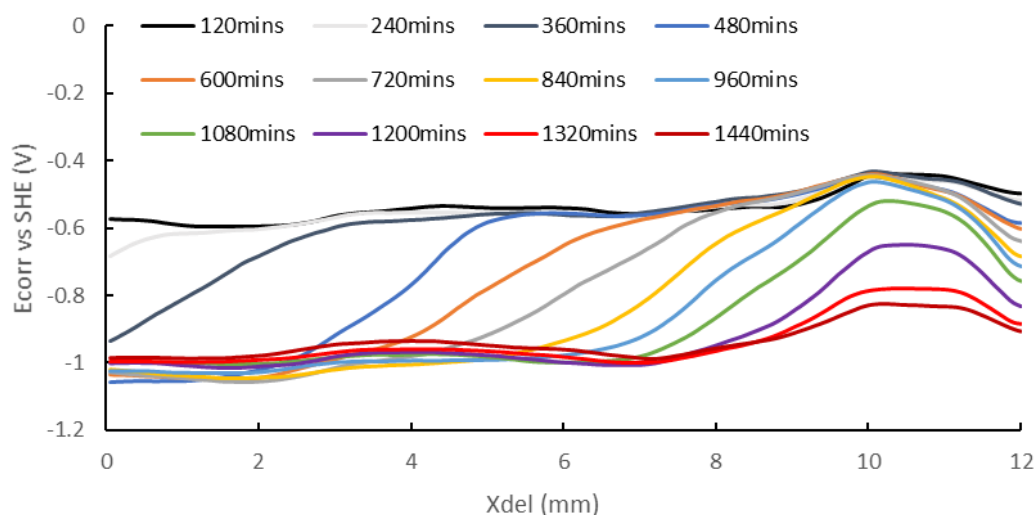
Figure 3.25. A graph showing the time dependent E_{corr} measurements against distance from defect (X) for 50°C, 10-minute alkaline cleaned surface with PVB coating from a HDG sample. E_{corr} measurements were taken every hour for 24 hours, with measurements shown every 2 hours.
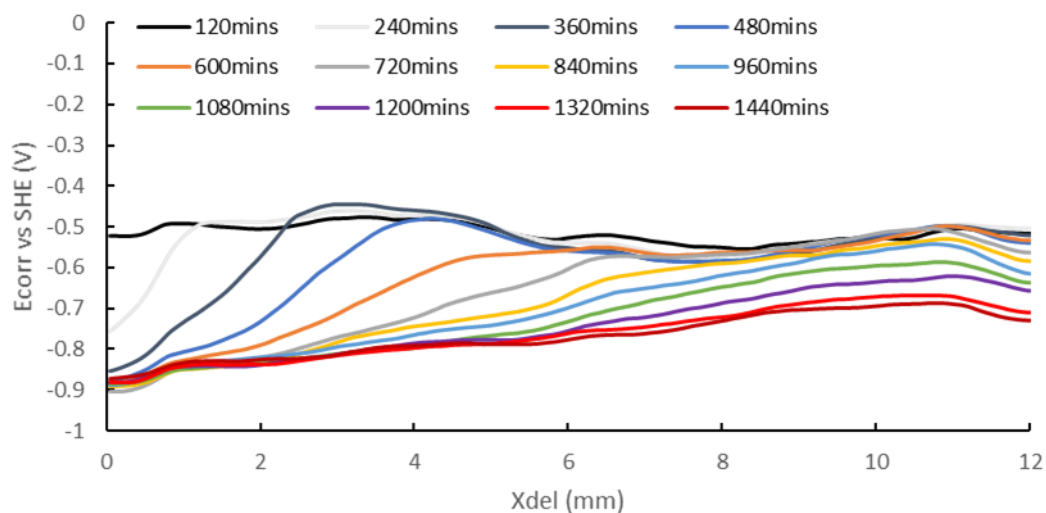
Figure 3.26. A graph showing the time dependent E$_{corr}$ measurements against distance from defect (X) for 65°C, 10-minute alkaline cleaned surface with PVB coating from a HDG sample. E$_{corr}$ measurements were taken every hour for 24 hours¸ with measurements shown every 2 hours.
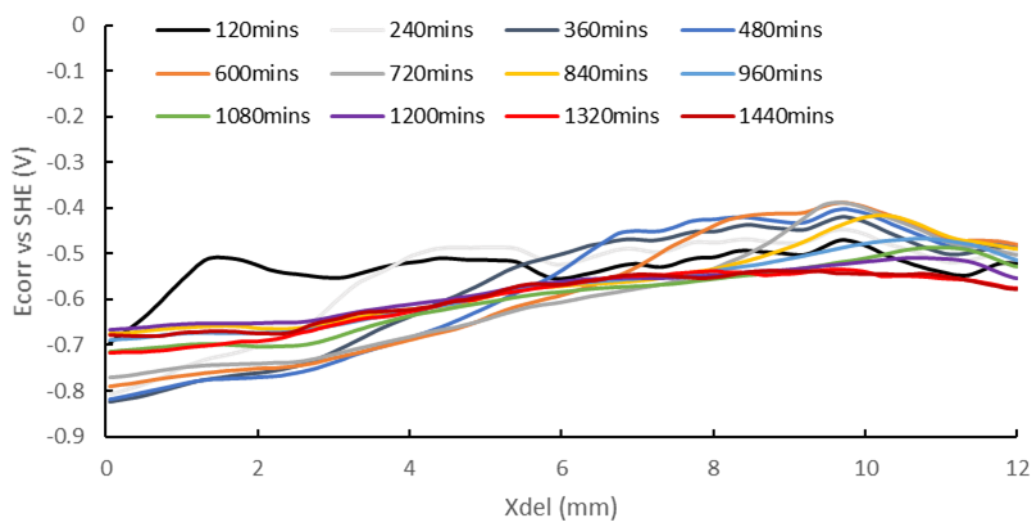
Figure 3.27. A graph showing the time dependent E$_{corr}$ measurements against distance from defect (X) for 80°C, 10-minute alkaline cleaned surface with PVB coating from a HDG sample. E$_{corr}$ measurements were taken every hour for 24 hours, with measurements shown every 2 hours.
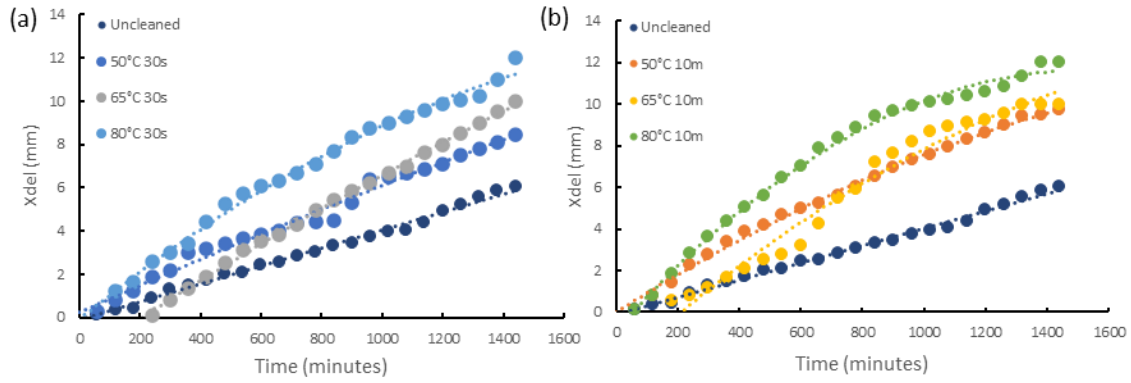
Figure 3.28. Delamination distance versus time plots obtained for PVB coated-HDG steel which had previously been alkaline cleaned at a) 30 seconds at varying temperatures; (b) 10 minutes at varying temperatures

The SKP derived delamination distance and initiation times for all measured PVB-coated alkaline cleaned HDG can be seen below in Figure 3.29 as a function of cleaning temperature, with each cleaning time being plotted systematically to view changes in how alkaline cleaning temperature influences cathodic disbondment behaviour.
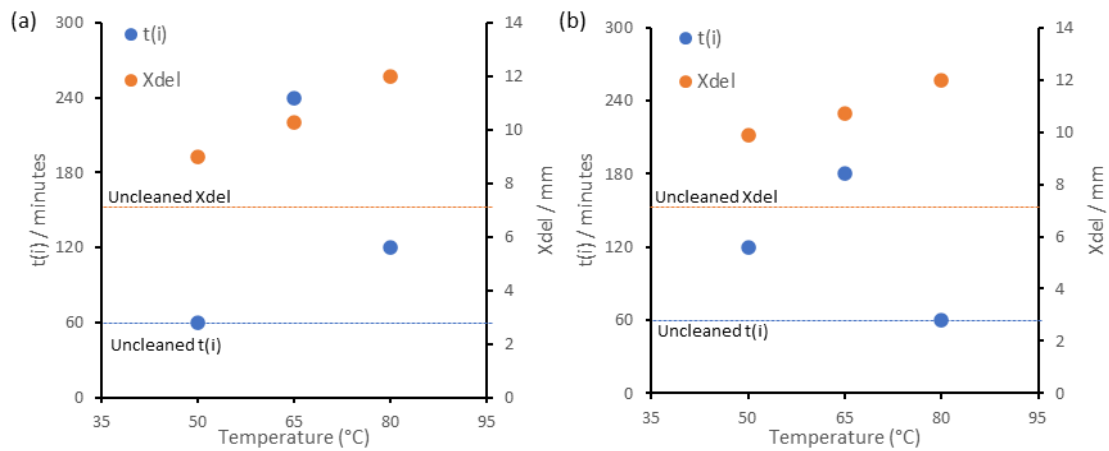
Figure 3.29. Delamination distance from defect and Initiation time of PVB of alkaline cleaned HDG as determined by scanning Kelvin probe; (a) Alkaline cleaned for 30 seconds, (b) Alkaline cleaned for 10 minutes.

As shown in Figure 3.29 (i) and (ii), the delamination distance increases as temperature increases. At a 30 second washing time, X_{del} is measured as 9mm, 10.33mm, and 12mm, for 50°C, 65°C, and 80°C respectively. When HDG is washed for 10 minutes, X_{del} is measured as 9.9mm, 10.7mm, and 12mm for 50°C, 65°C, and 80°C respectively. These measured X_{del}

values are all greater than the 7mm X_{del} measured for uncleaned HDG. The X_{del} values shown also show how variation in cleaning time also influences X_{del} values, with 10-minute washes showing greater delamination distances when the surface is cleaned at identical temperatures. The time taken to initiate cathodic disbondment of the PVB coating also appears to be correlated to the alkaline cleaning temperature. At a 30 second cleaning time, initiation time is measured at 60 minutes, 240 minutes, and 120 minutes for 50°C, 65°C, and 80°C respectively. At a 10-minute cleaning time, initiation time is measured at 120 minutes, 180 minutes and, 60 minutes for 50°C, 65°C, and 80°C respectively. Delamination of PVB on uncleaned HDG takes 60 minutes, which is identical to some alkaline cleaned substrates.

The maximum slop of the time dependent E_{corr} profile can be used as a semi empirical way of locating the delamination front for each specimen. The distance separating the E_{corr} profiles gives an indication of how fast the rate of corrosion is for a given substrate. The E_{corr} profiles for all substrates have very similar separation distances at each time interval, indicating similar delamination rates and the delamination rate can be determined from using the midpoint of the increase in the E_{corr} indicating the distance that coating delamination has travelled, before reaching the intact potential of the PVB coating. Evidence of how alkaline cleaning influences the rate of cathodic disbondment can be seen in Figure 3.30 which shows plots of the time-dependent distance (from defect edge) over which delamination (X_{del}) has occurred delamination time minus the initiation time ($t_{(del)}$-$t_{(i)}$) which allows comparison of delamination kinetics. This data is gathered through plotting the distance travelled by coating delamination as a function of the square root of time and are plotted below to show how cleaning temperature influences the delamination kinetics. The delamination rates calculated from the X_{del} versus $(t_{del} - t_i)^{1/2}(mins)^{1/2}$ plots can be seen in Figure 3.30.
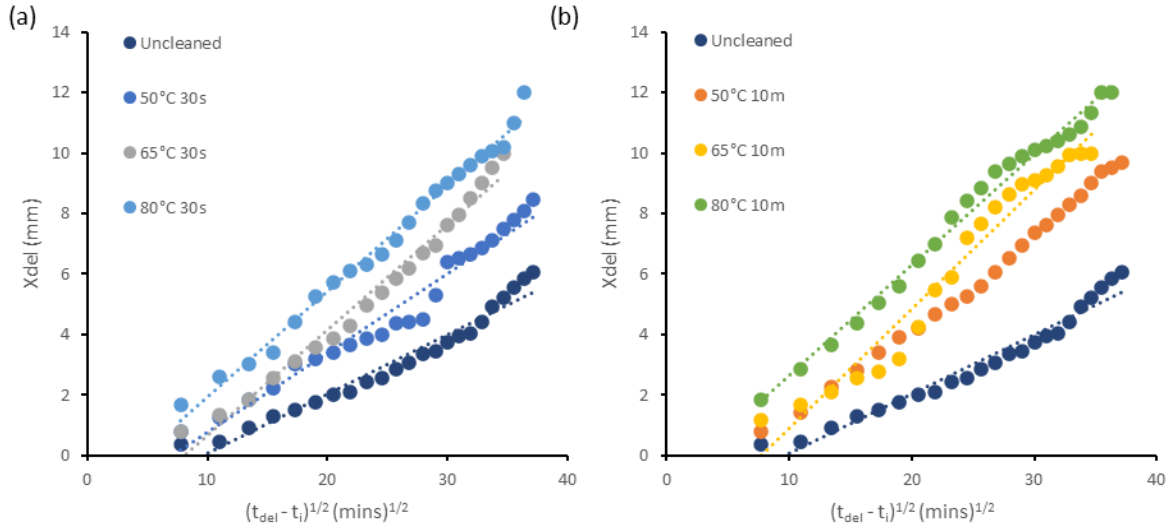
Figure 3.30. Plots of X_{del} versus $(t_{del} - t_i)^{1/2}(mins)^{1/2}$ showing the effect of alkaline cleaning on cathodic delamination kinetics on HDG steel; (a) HDG cleaned for 30 seconds; (b) HDG cleaned for 10 minutes
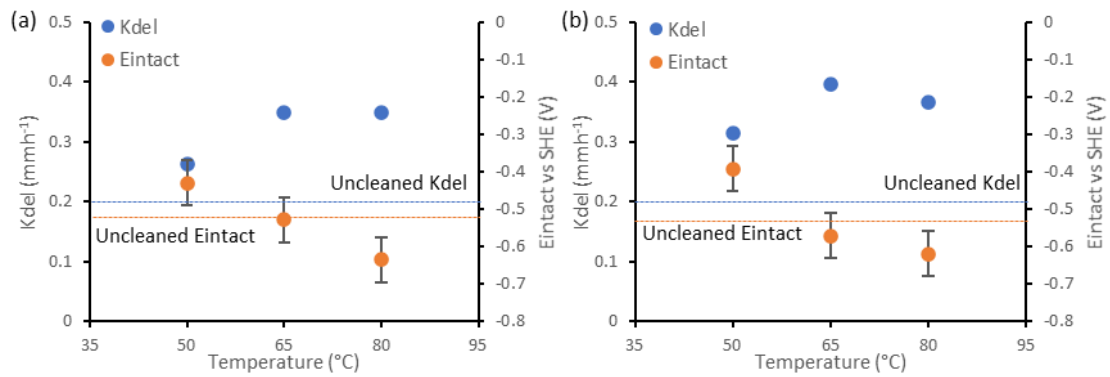
Figure 3.31. Delamination rates (K_{del}) and intact potential (E_{intact}) of PVB on alkaline cleaned HDG. (a) Alkaline cleaned for 30 seconds; (b) Alkaline cleaned for 10 minutes.

What can be seen by the rates determined through SKP data manipulation is the rate increases as the cleaning intensity increases and this is mirrored by the intact potential becoming more cathodic as cleaning intensity increases. At each cleaning time, there is a trend in the calculated K_{del} and E_{intact}. Uncleaned HDG shows the slowest rate, with an increase in temperature resulting in an increased rate. When the temperature increases from 65°C to 80°C the rate either stabilises (30 seconds) or decreases (10 minutes), indicating similar rate determining behaviour. The E_{intact} also appears to mirror the changes in K_{del}, with a progressive depression of the intact potential as temperature increases. This K_{del} and E_{intact}

behaviour could potentially be linked to the XPS results produced from the cleaned surfaces, with decreasing zinc oxide and zinc metal quantities being produced at increasing cleaning intensities. This thinner oxide produced from more intense cleaning would dissolve more rapidly producing OH⁻ as a reduction product.

The determination of the rate kinetics of the alkaline cleaned vs uncleaned HDG also shows a difference in how the delamination kinetics occur. When delamination distance is plotted against time, both uncleaned and alkaline cleaned HDG surfaces exhibit parabolic kinetics which is exhibited as a curve on X_{del} vs time plots. This is exhibited as a straight line when plotted as a function of the square root of time. This would illustrate that the rate determining step is the migration of cations to the delamination front via Fichian diffusion. [27,29]

The scanning Kelvin probe work conducted alongside the time-lapse work shows similar cathodic disbondment behaviour, however, there is some variation between the delamination distance, rate and initiation time between the two techniques. Compared to using time-lapse, the time taken to initiate cathodic disbondment using SKP is still erratic, with the cleaned HDG samples initiating cathodic disbondment within 4 hours. The largest difference in time taken for coating delamination to occur is shown in the uncleaned HDG sample. Uncleaned HDG takes 60 minutes for the PVB to begin delaminating under SKP conditions, whereas it takes much longer to initiate using time-lapse photography, taking 6 hours to begin delamination.

 The difference between the results shown in the data gathered between the time-lapse photography and the SKP techniques is the experimental conditions under which the data is gathered. Time-lapse photography is conducted in a plastic humidity chamber with ~2L of 5% NaCl solution and under warm lightbulbs, which creates a warm and humid atmosphere within the box. The SKP is run at ambient conditions with ~300ml of 5% NaCl solution in a metal box with no additional fixtures that can generate heat. The temperatures measured within the humidity chamber and SKP chamber were measured as 35°C and 24°C respectively, which would indicate experimental conditions result in differing results obtained regarding the performance of model organic coatings. What also needs to be considered is the sensitivity of the SKP compared to time-lapse measurements. The SKP may be more sensitive in detecting the onset of delamination due to a measurable change in potential, whereas the time-lapse technique relies on visual evidence of delamination

occurring, which would visualise as under-film tarnish of the surface which may lag behind the actual cathodic disbondment phenomenon occurring.

The corrosion driven cathodic disbondment of PVB on alkaline cleaned HDG steel can be linked to the cathodic polarisation behaviour seen in Section 3.3.2. As cleaning conditions become more intense the surface of the cleaned steel becomes a more active oxygen cathode, producing increased current when cathodically polarised. It appears that the increase in current from the initial $2e^-$ reaction and subsequent $4e^-$ reactions act as a driving force for the cathodic disbondment of PVB. The measured current density of the cathodic ORR increases as the cleaning intensity increases and the delamination performance also decreases. According the XPS data showing that alkaline cleaning results in metallic zinc being dominant on the surface, this results in the $4e^-$ process dominating at the initiation of cathodic disbondment, whereas zinc oxide/hydroxide is dominant on uncleaned HDG, resulting in the $2e^-$ process dominating at initiation. This can also be shown as a function of Zn:Zn(II). An uncleaned substrate shows a Zn:Zn(II) ratio of 0.33:1, illustrating how Zn oxide is prevalent on the surface whereas cleaned surfaces show ratios of 2.12-3.54:1, which effects the number of electrons involved in the cathodic reduction process.

3.4. Conclusions

In conclusion the alkaline cleaning has a direct influence of the surface chemistry of zinc based HDG surfaces, removing the Al present on uncleaned surfaces completely and increasing the amount of metallic zinc accompanied by a decrease in oxidic zinc on the surface. Study of the corrosion driven cathodic disbondment using time-lapse and SKP techniques shows that time and temperature of alkaline cleaning have a direct effect on the performance of the delamination of PVB coating, with increasing time and temperature resulting in increased delamination rates and decreased coating performance. The rate kinetics shown by cleaned substrates are parabolic in nature, indicating that the delamination rate is limited by the migration of ions to and from the delamination front. Anodic polarisation of substrates shows very similar behaviour of HDG cleaned at varying parameters with a negligible passive region present. Cathodic polarisation appears to show that more intense cleaning conditions produce a surface that is a more active oxygen cathode, with cleaned surfaces showing a greater current increase when polarised compared to uncleaned HDG, and further promotes corrosion driven cathodic disbondment. Polarisation

studies of cleaned HDG shows a drop in the polarisation resistance of substrates over time and increasing the cleaning intensity results in a drop in the initial and average polarisation resistance.

3.5. References

1.   Forsgren A, Knudsen OØ. Corrosion Control through Organic Coatings, 2nd Edition. 2nd Editio. CRC Press

2.   Moffitt CE, Wieliczka DM, Yasuda HK. An XPS study of the elemental enrichment on aluminum alloy surfaces from chemical cleaning. Surf Coatings Technol. 2001. doi:10.1016/S0257-8972(00)01121-X

3.   Mol JMC, De Wit JHW, Van Der Zwaag S. The Effect of Mechanical Surface Patterning on Filiform Growth Characteristics. https://link.springer.com/content/pdf/10.1023%2FA%3A1015881403065.pdf. Accessed September 9, 2019.

4.   Milošev I, Frankel GS. Review—Conversion Coatings Based on Zirconium and/or Titanium. J Electrochem Soc. 2018;165(3):127-144. doi:10.1149/2.0371803jes

5.   Laha P, Schram T, Terryn H. Use of spectroscopic ellipsometry to study Zr/Ti films on Al. Surf Interface Anal. 2002;34(1):677-680. doi:10.1002/sia.1386

6.   Sarfraz A, Posner R, Lange MM, Lill K, Erbe A. Role of Intermetallics and Copper in the Deposition of ZrO_2 Conversion Coatings on AA6014. J Electrochem Soc. 2014;161(12):C509-C516. doi:10.1149/2.0121412jes

7.   Cerezo J, Vandendael I, Posner R, de Wit JHW, Mol JMC, Terryn H. The effect of surface pre-conditioning treatments on the local composition of Zr-based conversion coatings formed on aluminium alloys. Appl Surf Sci. 2016;366:339-347. doi:10.1016/j.apsusc.2016.01.106

8.   BUCHHEIT RG. Copper removal during formation of corrosion resistant alkaline oxide coatings on Al–Cu–Mg alloys. J Appl Electrochem. 1998;28(5):503-510. doi:10.1023/A:1003217211727

9.   Dimitrov N, Mann JA, Vukmirovic M, Sieradzki K. Dealloying of Al[sub 2]CuMg in Alkaline Media. J Electrochem Soc. 2000;147(9):3283. doi:10.1149/1.1393896

10.   Liu WB, Zhang SC, Li N, Zheng J, Xing Y. Dealloying Behavior of Dual-Phase Al 40 atom % Cu Alloy in an Alkaline Solution. J Electrochem Soc. 2011;158(2):D91. doi:10.1149/1.3511771

11.   Lunder O, Olsen B, Nisancioglu K. Pre-treatment of AA6060 aluminium alloy for adhesive bonding. Int J Adhes Adhes. 2002;22(2):143-150. doi:10.1016/S0143-7496(01)00049-5

12.   Molitor P, Barron V, Young T. Surface treatment of titanium for adhesive bonding to polymer composites: a review. Int J Adhes Adhes. 2001;21(2):129-136. doi:10.1016/S0143-7496(00)00044-0

13. Joshi S, Fahrenholtz WG, O'Keefe MJ. Effect of alkaline cleaning and activation on aluminum alloy 7075-T6. Appl Surf Sci. 2011;257(6):1859-1863. doi:10.1016/j.apsusc.2010.08.126

14. Joshi S, Fahrenholtz WG, O'Keefe MJ. Electrochemical Characterization of Al 7075-T6 Surface Oxide After Alkaline Treatments. J Electrochem Soc. 2011;158(9):C296. doi:10.1149/1.3610404

15. Adhikari S, Unocic KA, Zhai Y, Frankel GS, Zimmerman J, Fristad W. Hexafluorozirconic acid based surface pretreatments: Characterization and performance assessment. Electrochim Acta. 2011;56(4):1912-1924. doi:10.1016/J.ELECTACTA.2010.07.037

16. Yi A, Li W, Du J, Mu S. Preparation and properties of chrome-free colored Ti/Zr based conversion coating on aluminum alloy. Appl Surf Sci. 2012;258(16):5960-5964. doi:10.1016/J.APSUSC.2011.12.045

17. Fürbeth W, Stratmann M. Delamination of polymeric coatings from electrogalvanized steel - a mechanistic approach. Part 1: Delamination from a defect with intact zinc layer. Corros Sci. 2001;43(2):207-227. doi:10.1016/S0010-938X(00)00047-0

18. Fürbeth W, Stratmann M. Delamination of polymeric coatings from electrogalvanized steel - a mechanistic approach. Part 2: Delamination from a defect down to steel. Corros Sci. 2001;43(2):229-241. doi:10.1016/S0010-938X(00)00048-2

19. Fürbeth W, Stratmann M. Delamination of polymeric coatings from electrogalvanized steel - a mechanistic approach. Part 3: Delamination kinetics and influence of CO_2. Corros Sci. 2001;43(2):243-254. doi:10.1016/S0010-938X(00)00049-4

20. Leng A, Streckel H, Stratmann M. The delamination of polymeric coatings from steel. Part 1: Calibration of the Kelvinprobe and basic delamination mechanism. Corros Sci. 1999;41:547-578. https://ac.els-cdn.com/S0010938X98001668/1-s2.0-S0010938X98001668-main.pdf?_tid=95b21839-005f-461b-bda3-f3ef13deb5f3&acdnat=1526467594_0e90046e0671b4e33b421f8e6943ef9a. Accessed May 16, 2018.

21. Grundmeier G, Schmidt W, Stratmann M. Corrosion protection by organic coatings: electrochemical mechanism and novel methods of investigation. Electrochim Acta. 2000;45(15-16):2515-2533. doi:10.1016/S0013-4686(00)00348-0

22. Stratmann M, Leng A, Fürbeth W, Streckel H, Gehmecker H, Große-Brinkhaus KH. The scanning Kelvin probe; a new technique for the in situ analysis of the delamination of organic coatings. Prog Org Coatings. 1996;27(1-4):261-267. doi:10.1016/0300-9440(94)00542-7

23. Fürbeth W, Stratmann M. Scanning Kelvin Probe investigations on the delamination of polymeric coatings from metallic surfaces. Prog Org Coatings. 2000;39(1):23-29. doi:10.1016/S0300-9440(00)00095-3

24. Schmidt W, Stratmann M. Scanning Kelvinprobe investigations of filiform corrosion on aluminium alloy 2024-T3. Corros Sci. 1998;40(8):1441-1443. doi:10.1016/S0010-938X(98)00044-4

25. Williams G, Neil McMurray H. Localized corrosion of magnesium in chloride-containing electrolyte studied by a scanning vibrating electrode technique. J

Electrochem Soc. 2008;155(7). doi:10.1149/1.2918900

26.   Williams G, Grace R. Chloride-induced filiform corrosion of organic-coated magnesium. In: Electrochimica Acta. Vol 56. Pergamon; 2011:1894-1903. doi:10.1016/j.electacta.2010.09.005

27.   Geraint W, McMurray HN, Williams G, McMurray H. Chromate inhibition of corrosion driven organic coating delamination studied using a scanning Kelvin probe technique. J Electrochem Soc. 2001;148(10):B377. doi:10.1149/1.1396336

28.   Williams G, McMurray HN. The mechanism of group (I) chloride initiated filiform corrosion on iron. Electrochem commun. 2003;5(10):871-877. doi:10.1016/j.elecom.2003.08.008

29.   Geraint W, McMurray HN, Worsley DA, Williams G, McMurray H. Cerium(III) inhibition of corrosion-driven organic coating delamination studied using a scanning Kelvin probe technique. J Electrochem Soc. 2002;149(4):B154. doi:10.1149/1.1457983

30.   Richards CAJ, McMurray HN, Williams G. Smart-release inhibition of corrosion driven organic coating failure on zinc by cationic benzotriazole based pigments. Corros Sci. 2019;154:101-110. doi:10.1016/J.CORSCI.2019.04.005

31.   Van der Heide P. X-ray photoelectron spectroscopy : an introduction to principles and practices. 2012. https://www.perlego.com/book/1014648/xray-photoelectron-spectroscopy-an-introduction-to-principles-and-practices-pdf. Accessed November 18, 2021.

32.   Goodhew PJ, Humphreys J, Humphreys J. Electron Microscopy and Analysis. Electron Microsc Anal. November 2000. doi:10.1201/9781482289343

33.   Khursheed A. Scanning Electron Microscope Optics and Spectrometers. Singapore ;;London: World Scientific Publising Co Pte Ltd; 2014.

34.   Michailidou E. Corrosion Studies on Magnesium and Magnesium Containing Alloys. 2018.

35.   Le Bozec N, Compère C, L'Her M, Laouenan A, Costa D, Marcus P. Influence of stainless steel surface treatment on the oxygen reduction reaction in seawater. Corros Sci. 2001;43(4):765-786. doi:10.1016/S0010-938X(00)00113-X

36.   Babić R, Metikoš-Huković M. Oxygen reduction on stainless steel. J Appl Electrochem. 1993;23(4):352-357. doi:10.1007/BF00296691

37.   Dafydd H, Worsley DA, McMurray HN. The kinetics and mechanism of cathodic oxygen reduction on zinc and zinc-aluminium alloy galvanized coatings. Corros Sci. 2005;47(12):3006-3018. doi:10.1016/J.CORSCI.2005.05.036

38.   Mansfeld F. Fundamental aspects of the polarization resistance technique-the early days. doi:10.1007/s10008-008-0652-x

39.   Stern M, Geary AL. Electrochemical Polarization: I . A Theoretical Analysis of the Shape of Polarization Curves. J Electrochem Soc. 1957;104(1):56. doi:10.1149/1.2428496

40.   Wong LL, Martin SI, Rebak RB. Methods to calculate corrosion rates for alloy 22

from polarization resistance experiments. Am Soc Mech Eng Press Vessel Pip Div PVP. 2006;2006. doi:10.1115/PVP2006-ICPVT-11-93421

41. Toshev Y, Mandova V, Boshkov N, et al. Protective coating of zinc and zinc alloys for industrial applications. 4M 2006 - Second Int Conf Multi-Material Micro Manuf. January 2006:323-326. doi:10.1016/B978-008045263-0/50073-8

Chapter 4- Investigating the influence of alkaline cleaning parameters on surface chemistry, electrochemical, and corrosion behaviour of Zn-Al(4.8%) alloy coated steel.

4.1. Introduction

The addition of aluminium to zinc coated galvanised steels have long been used as a coating system to reduced corrosion of galvanised steels and do show better corrosion performance compared to hot-dip galvanised steels and have been developed for continuous galvanised sheet steels. [1] Zinc coatings usually corrode as a result of a slow dissolution of zinc from the surface, however, zinc possesses the ability to "self-heal", whereby protective layers of Zn-based carbonates, oxides or hydrated sulphides are formed, depending on the environment.[2] The addition of aluminium to a zinc coating is highly beneficial, with a surface layer combining Zn and Al to form a mixed-compound surface. When zinc-based coating are exposed to corrosive environments, the corrosion products formed help slow the rate of corrosion. How the addition of Al influence Zn-base coatings has been reviewed and can be seen in Section 1.4.

The work in this chapter builds on some of the work conducted from Chapter 3, relating the alkaline cleaning time and temperature to both the surface chemistry of Galvalloy (4.8%-Al) steel surfaces and the corrosion resistance of activated surfaces in comparison to HDG steel. Alkaline cleaning of zinc and aluminium based substrates has been covered in the scientific literature, however, very little if any work has been conducted on Zn-Al (4.8%) alloy surfaces and so the work in this chapter can be considered as novel. The surface of Galvalloy can be quantified through XPS analysis of the surface pre and post activation, and the corrosion resistance quantified by electrochemical testing of the zinc-aluminium surface, and by determining the kinetics of organic coating failure via a cathodic delamination mechanism when over-coated with a model PVB film.

4.2. Experimental details

4.2.1. Materials

Bonderite U-187 alkaline cleaner was provided by Henkel. 4.8% Al-Zn (Galvalloy) was provided by Tata Steel UK, with a gauge of 0.7mm mild steel and a galvanised zinc-aluminium layer of 20μm. Bonderite U-187 alkaline cleaning solution was provided by Tata Steel UK and was diluted to 2% v/v concentration with deionised water. Polyvinyl butyral-co-vinyl alcohol-co-vinyl acetate (PVB), molecular weight 70,000-100,000, was obtained from Sigma Aldrich Chemical Co. and was at an analytical grade purity. The PVB solution was prepared in ethanol to 15.5% w/w with the required amount of inhibitor added using a high shear mixer. .

4.2.2. Experimental Methodology

The full description of the instrumentation, calibration, experimental set-up and analysis of the XPS, SKP, time-lapse photography and potentiodynamic polarisation can be found in Chapter 2. Description of sample preparation and alkaline cleaning parameters of Galvalloy can also be found in Chapter 2 under the relevant section.

4.3. Results and Discussion

4.3.1. Surface characterisation of alkaline cleaned Galvalloy

To investigate how the alkaline cleaning of Galvalloy affects the corrosion driven cathodic delamination behaviour, XPS was utilised to identify and quantify the elemental composition of the surface oxides found on the Galvalloy surface prior to and after chemical treatment. Figure 4.1 displays a typical survey spectrum over a wide binding energy range for untreated Galvalloy, demonstrating the surface consists of Zn, C, O and Al.
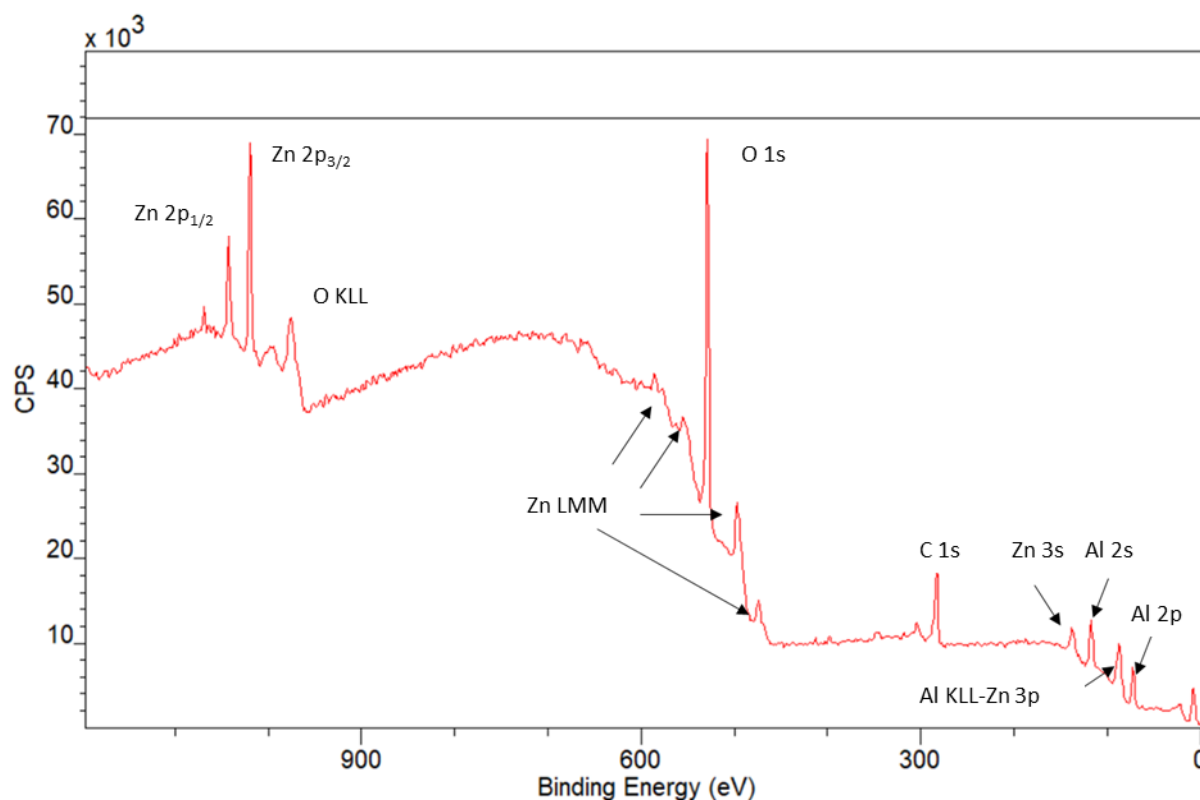
Figure 4.1. XPS spectral survey scan of Galvalloy

A typical peak for each corresponding element have been identified and is shown in Figure 4.2, which shows highly resolved elemental peak which has been processed through CasaXPS software. The main C 1s peak is centred at 284.8eV, identified as C-C, and is accompanied by two smaller peaks identified as C-O and C=O located at 286.3 eV and 289.1 eV respectively which result from surface contamination. Metallic zinc is centred at 1021.7 eV and 1044.7 eV and Zn(II) is located at 1022.5 eV and 1045.5 eV. Al 2p also resolves into two doublet peaks which are identified as two different chemical states attributed to metallic aluminium at 73 eV and Al(III) at 75.5 eV. However, only the doublet splitting of Al_2O_3 is present.
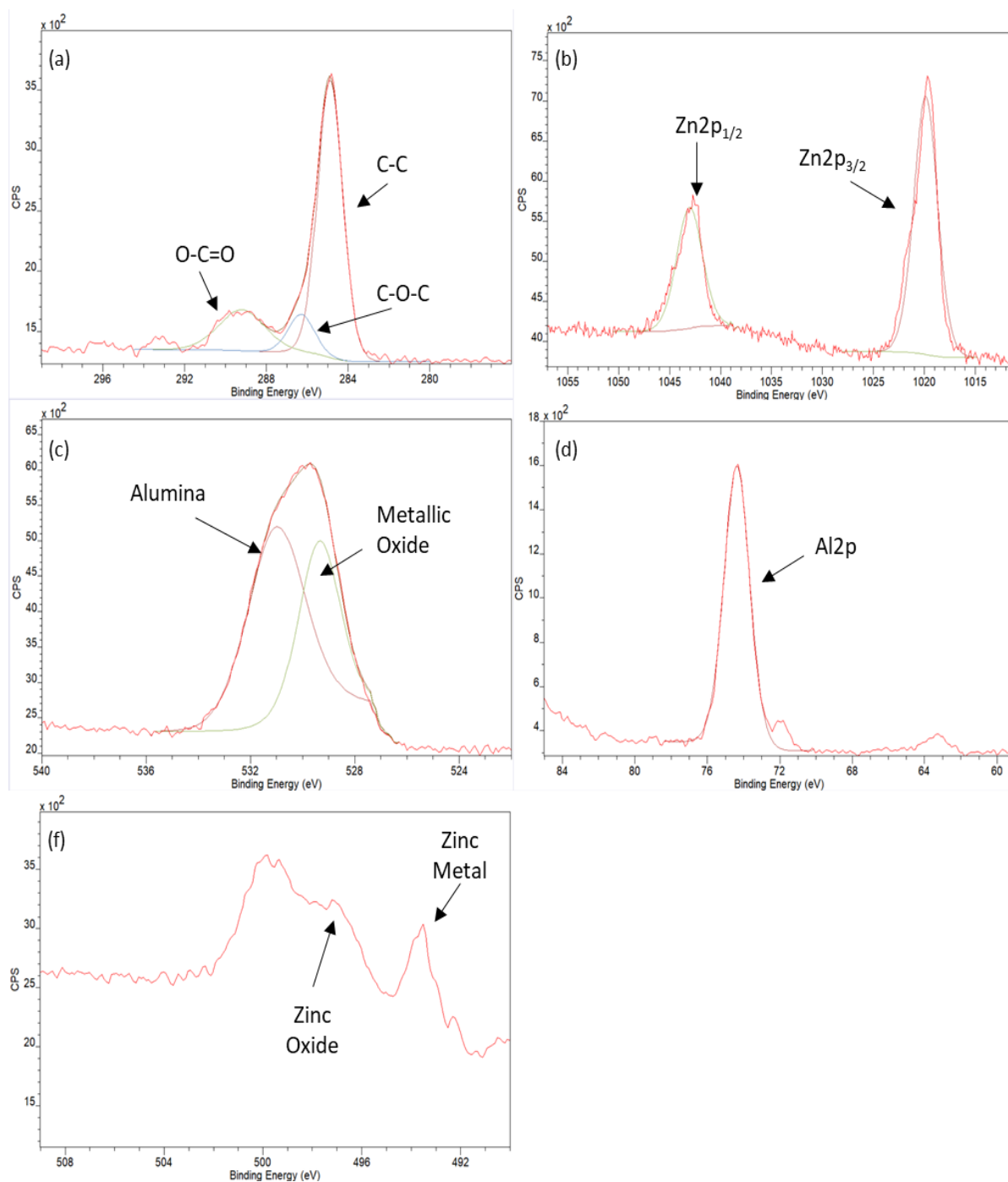
Figure 4.2. X-ray photoelectron spectroscopy analysis of Galvalloy. (a) carbon analysis; (b) zinc analysis; (c) oxygen analysis; (d) aluminium analysis; (e) zinc Auger analysis

XPS-derived spectra were recorded and quantified over five Galvalloy samples to assess consitency between the data. Small differences were observed in the background signal resulting from electron inelastic scattering arising from an electron losing energy to its surrounding whilst still remaining within the bulk solid, much like that seen for HDG samples.

The XPS-derived spectra of the surface Galvalloy steel cleaned at 50°C, 65°C, and 80°C for 30, 120, 300, and 600 seconds was conducted to illustrate how the surface is influenced by variation in surface conditioning. An unconditioned Galvalloy sample shows an elemental composition consisting of carbon, oxygen, zinc and aluminium. The main carbon 1s peak illustrating C-C contamination is centred around 284.8 eV, with component peaks of C-O and C=O positioned at 286.3 eV and 289.1 eV respectively. The O 1s peak is composed of two oxide peaks at 531.8 eV and at 530.1 eV which are generated from alumina and metallic oxide contributions. The metallic oxide peak present is indicative of Al(III) oxide present on the surface, which is not is prevalent on the surface of HDG due to its decreased Al-content.[3] The peak present at 530.8 eV can be attributed to ZnO present on the surface. There is also likely to be oxygen related carbon contamination on the surface due to the peak width. The Zn 2p peaks generated are from the Zn $2p_{1/2}$ and Zn $2p_{3/2}$ orbital splitting and are positioned at 1045.2 eV and 1022.1 eV. Zinc also produces Auger peaks that allows for the determination of the chemical state of the zinc 2p peaks generated.. The Zn Auger peaks produced for uncleaned Galvalloy generate Zn LMM peaks at 498.1 eV and 494.5 eV which indicates the presence of both zinc oxide and metallic zinc. There is also the production of an Al 2p peak at 76.2 eV produced by Al_2O_3 due to the presence of 4.8% Al in the Galvalloy structure.

Samples washed at 50°C, 65°C and 80°C for the different times illustrate slight variation in the elemental composition, and the element peaks all centred at similar binding energy. The main C 1s peak being centred at 284.8 eV, with the C=O peak being situated around 286.3 eV, and the C-O peak present at 289.1 eV . The O 1s peak is composed of a metal oxide peak at 530.3 eV and a C-O peak present at 531.9 eV. With regards to the Zn 2p peaks, the Zn $2p_{1/2}$ and $2p_{3/2}$ peaks are generated at 1044.9 eV and 1021.8 eV respectively. The Zn LMM peaks produced alongside the Zn 2p peaks produce a single Auger peak at 493.9 eV which indicates only the presence of zinc metal. The Al 2p peak present in an unwashed Galvalloy sample is absent in these washed samples indicating alumina dissolution from the surface during cleaning. Figure 4.3 below shows the wide survey and high resolution spectra of the elemental composition of Galvalloy cleaned at 65°C at the varying times.
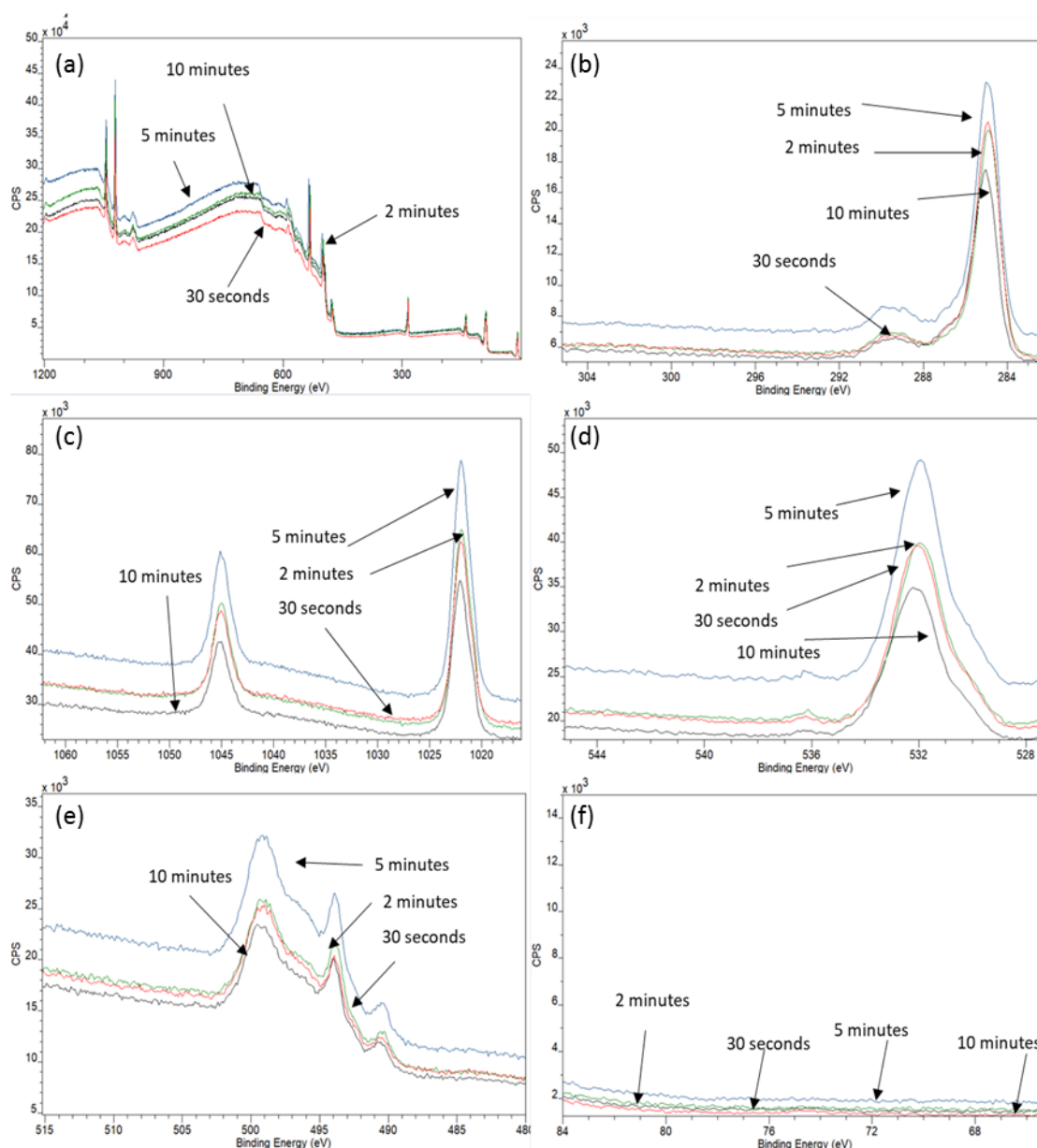
Figure 4.3. X-ray photoelectron spectroscopy analysis of Galvalloy alkaline cleaned at 65°C for varying times. (a) wide spectral analysis (b) carbon analysis; (c) zinc analysis; (d) oxygen analysis; (e) zinc Auger analysis; (f) aluminium analysis

In all cases, regardless of cleaning parameters, the element peaks produced remain close to their previously defined binding energies, with average atomic concentrations in percentage have been derived from each corresponding peak area and are summarised below in Table 4.1, Figure 4.4 shows the change in zinc oxide and metal concentrations, and Figure 4.5 shows how the Zn:Zn(II) ratio changes as cleaning conditions are changed.

Table 4.1. Atomic composition of uncleaned and cleaned Galvalloy surfaces.

Sample	C-O (atomic %)	C-C (atomic %)	C=O (atomic %)	O (atomic %)	Zn (II) (atomic %)	Zn (0) (atomic %)	Al (atomic %
ZA Uncleaned	8.3	16.51	4.91	17.39	10.25	5.18	37.45
ZA 50°C 30s	2.89	44.08	4.32	27.7	8.05	12.97	0
ZA 50°C 2m	3.02	44.47	4.41	28.82	5.1	14.19	0
ZA 50°C 5m	10.29	35.95	5.68	31.71	3.81	12.59	0
ZA 50°C 10m	9.97	33.59	6.46	34.46	3.19	12.33	0
ZA 65°C 30s	10.62	36.59	6.46	32.51	3.09	10.72	0
ZA 65°C 2m	8.93	35.96	5.61	34.18	2.91	12.41	0
ZA 65°C 5m	9.56	32.54	5.78	34.4	3.04	14.68	0
ZA 65°C 10m	11.86	34.33	6.72	33.41	2.3	11.37	0
ZA 80°C 30s	7.63	27.24	6.29	38.64	4.49	15.72	0
ZA 80°C 2m	7.48	29.78	7.48	38.63	2.61	14.24	0
ZA 80°C 5m	7.55	27.42	7.55	38.13	2.88	14.73	0
ZA 80°C 10m	8.01	27.41	8.01	37.44	2.46	15.31	0
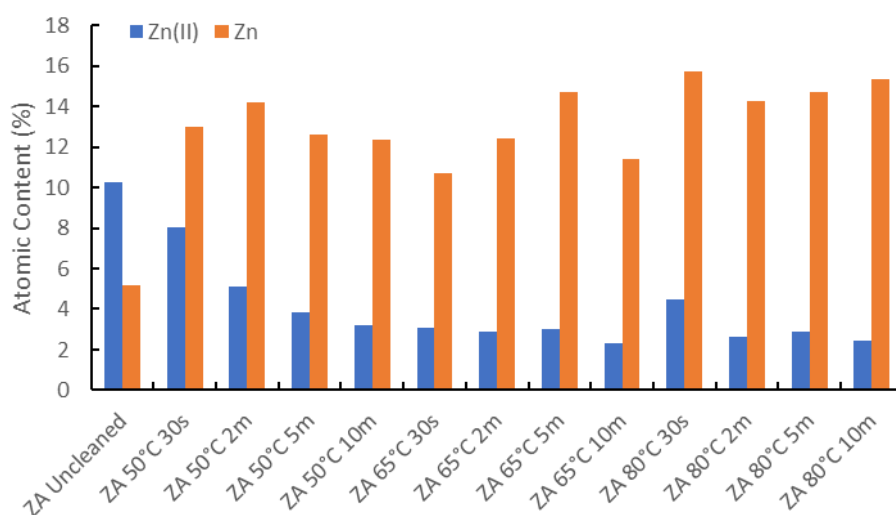
Figure 4.4. Atomic composition metallic and oxidic zinc on uncleaned and cleaned Galvalloy surfaces.
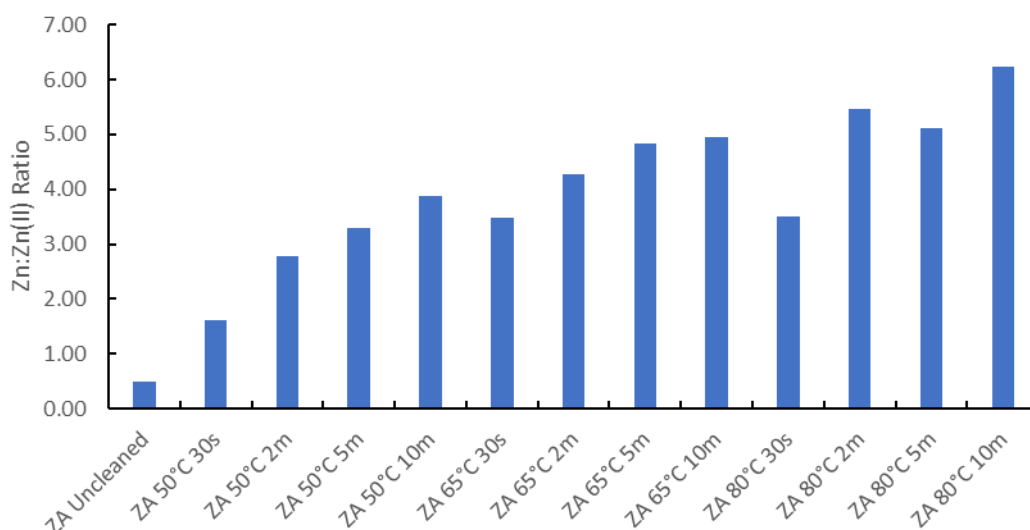
Figure 4.5. Ratio of zinc to zinc(II) of Galvalloy surfaces calculated from XPS quantification

XPS analysis of uncleaned Galvalloy shows that carbon, oxygen, zinc and aluminium are present on the surface. The content of aluminium is particularly high, making up 37.45% of the surface chemistry, which is ~3 times greater than the calculated aluminium content of a HDG substrate. Carbon and oxygen make up the bulk of the surface chemistry, with 29.72% of the surface consisting of various carbon chemistries and 27.64% of the surface consisting of organic oxygen and oxide species. Zinc makes up the remaining 5.18% of the surface.

In terms of the alkaline cleaning influences the surface chemistry of Galvalloy the surface content generated by XPS analysis shows the surface is largely made up of carbon and oxygen, with consistent carbon contamination on the surface of all cleaned samples, with contents of 48.73 $^+/_-$ 3.9 %. Much like that seen on HDG surfaces, the carbon content on Galvalloy surfaces is extremely high for what should be a "cleaned" sample, and so there are clearly issues with sample handling and contamination prior to analysis which is contributing to a high carbon content on the surface. The oxygen content of the alkaline cleaned samples is calculated at 37.83 $^+/_-$ 2.73 % whereas an uncleaned samples has an oxygen content of 27.64 %. The contribution of oxygen from metal oxides drops significantly as alkaline cleaning becomes more intense, with drops of 21-75 % measured. The aluminium also drops from 37.45 % to 0% after minimal alkaline cleaning, which can be tied to aluminium's amphoteric nature, and so would readily dissolve into alkaline solution. It is the appearance of this metallic zinc peak that would give an indication into the cathodic delamination behaviour of the alkaline cleaning of HDG at different temperatures and times and in

comparison, to unconditioned HDG. The peak produced for Zn 2p$_{3/2}$ show a shift from 1022 eV to 1021.7 eV after alkaline cleaning, indicating a shift from zinc oxide to zinc metal, this can be corroborated by the production of the metallic zinc Auger peak produced at ~494 eV. This Zn LMMa peak is present in an uncleaned Galvalloy XPS spectra but is accompanied by a zinc oxide LMMa peak at 497 eV, which is absent in all alkaline cleaned Galvalloy spectra and would indicate complete removal of the protective surface oxide. It is the appearance of these metallic zinc peak that would give an indication into the cathodic delamination behaviour of the alkaline cleaning of Galvalloy at different temperatures and times and in comparison, to unconditioned Galvalloy. The total Zn content can be calculated and for alkaline cleaned substrates, tends to stay around 13.44 $^+/_-$ 1.53%. This is much higher than the Zn content of the uncleaned Galvalloy substrate which is calculated as 5.18%. However the Al content of uncleaned Galvalloy is much greater at 37.45% which decreases the detected zinc content, which is then removed by alkaline cleaning. The zinc content after alkaline cleaning if very similar to the 12.610 $^+/_-$ 3.236% shown by quantification of HDG Zn 2p XPS spectra. The content of oxidic zinc on the surface drops as cleaning intensity increases, and appears to stabilise (whilst still decreasing) at cleaning temperatures of 65°C and 80°C indicating that oxide dissolution slows after a certain point. The metallic zinc generally increases as cleaning intensity increases, with the Zn:Zn(II) ratio being much higher in alkaline cleaned Galvalloy, with 1.5-6.5 Zn for every Zn(II) detected on the surface with the ratio generally increasing with increased cleaning intensity, which is much higher than the 0.5:1 ratio seen in uncleaned Galvalloy.

4.3.2 Influence of alkaline cleaning parameters on electrochemical response of Galvalloy using anodic, cathodic and linear polarisation.

Polarisation experiments were performed as described in Section 2.7 to test the behaviour of Galvalloy cleaned in alkaline solution at 50°C, 65°C and 80°C for 30 seconds or 10 minutes and immersed in 5wt.% NaCl pH 7 as seen in Chapter 2.

4.3.2.1. Anodic polarisation of alkaline cleaned Galvalloy

Anodic polarisation curves of alkaline cleaned Galvalloy substrates were conducted to see how the influence of surface conditioning influences the metal oxidation reaction that occurs on the surface when in 5wt.% NaCl solution. The Open Circuit Potential (OCP) of samples were taken before anodic-going polarisation of the sample from the OCP to +0.5 V of the OCP.

The anodic polarisation curve of an unconditioned Galvalloy sample shows an OCP of the metal surface to be -0.7867 V. The anodic curves of alkaline cleaned samples to compare with an unconditioned sample can be seen in Figure 4.6.
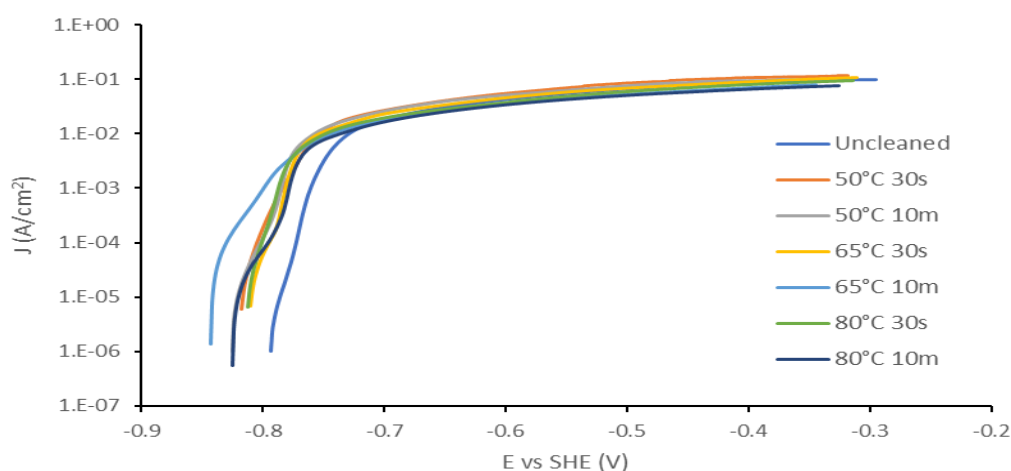
Figure 4.6. Anodic polarisation curve of Galvalloy alkaline cleaned at varying conditions in 5% wt.v NaCl solution

The OCP of a Galvalloy sample alkaline washed at 50°C for 30 seconds is shown to be -0.82 V, with the active region of the sample beginning at -0.7383V. By comparison the Galvalloy that has been washed at 50°C for 10 minutes shows an OCP of -0.83, with the active region of the sample beginning at -0.76 V. The OCP of a Galvalloy sample alkaline washed at 65°C for 30 seconds is shown to be -0.81 V, with the active region of the sample beginning at -0.7405 V. By comparison the Galvalloy that has been washed at 65°C for 10 minutes shows an OCP of -0.84, with the active region of the sample beginning at -0.76 V. The OCP of Galvalloy alkaline washed at 80°C for 30 seconds is shown to be -0.81 V, with the active region of the sample beginning at -0.75 V. comparison the Galvalloy that has been washed at 80°C for 10 minutes shows an OCP of -0.82, with the active region of the sample beginning at -0.76 V.

The anodic polarisation curves generated for all alkaline washed Galvalloy substrates indicate very little difference in the anodic response of the substrate, with all samples readily undergoing anodic metal dissolution. There is some variation in the passive region that is produced after alkaline washing, but all tend to show an inflection of between 0.05 – 0.085 V, however this is a very small potential range indicating a readiness of the surface to undergo anodic metal dissolution.

4.3.2.2. Cathodic polarisation of alkaline cleaned Galvalloy

Cathodic Polarisation curves of alkaline cleaned HDG substrates were conducted to see how the influence of surface conditioning influences the cathodic oxygen reduction reaction that occurs on the surface when in 5wt.% NaCl solution. The Open Circuit Potential (OCP) of samples were taken before cathodic-going polarisation of the sample from the OCP to -0.5 V more negative of the OCP. The cathodic polarisation curve for a control Galvalloy sample can be seen in Figure 4.7.

An unconditioned Galvalloy sample undergoing cathodic polarisation shows an immediate increase in the current across a narrow potential range and the current continues to increase as the potential is pushed to more cathodic voltages. This increase in current occurs for all samples and illustrates that there is abundant oxygen available for the oxygen reduction reaction to occur.

Unlike the secondary reduction region that occurs in Galvalloy substrates, this region is absent in an unconditioned Galvalloy sample, likely a result of the increased aluminium content preventing an additional reduction reaction from occurring.
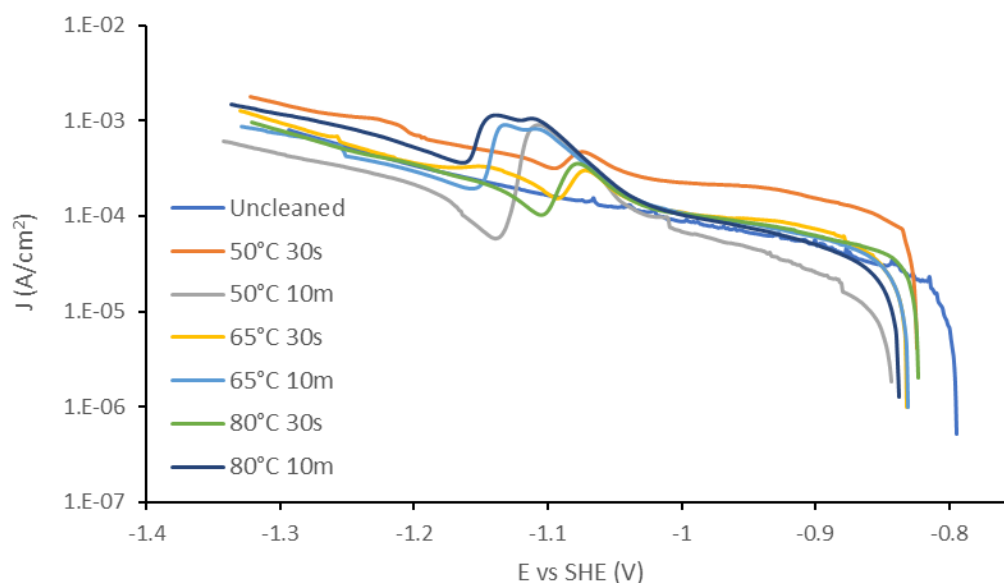
Figure 4.7. Cathodic polarisation curve of Galvalloy alkaline cleaned various conditions in 5wt.% NaCl solution.

The cathodic branches of cleaned Galvalloy substrates all show similar polarisation curves, exhibiting a rapid initial increase in the measured current followed by a slower increase in current as the potential is cathodically shifted. All cleaned Galvalloy show a reduction peak that occurs around -1.1 V. The current density at different measured potentials, denoted point A (measured at -0.9 V) and point B (measured at -1.2 V) can be seen below and a summary of the measured potentials and currents of the cathodic reactions involved can be seen below in Table 4.2. The changes in current densities when the samples are cathodically polarised, and measured currents and plots of the measured current densities for the cleaning times used at the different temperatures in Figure 4.8. What can be shown by measured currents at points -0.9V and -1.2V for Galvalloy cleaned for 30 seconds and 10 minutes is the measured current is greater at more negative potentials. The cleaning time does show a difference in measured currents at -0.9V and -1.2V at the differing cleaning temperature. At a cleaning time of 30 seconds, there is a larger difference in the current change between points -0.9V and -1.2V at 50°C, with similar changes in currents at greater cleaning temperatures. At a cleaning time of 10 minutes, the current change between -0.9V and -1.2V increases at the cleaning temperature increases. These measurements would indicate that the greater the cleaning intensity, the greater the change in current that occurs when ZnO reduction occurs.

Table 4.2. Comparison of potentiodynamic parameters across Galvalloy cleaning regimes

Cleaning Conditions	OCP (V)	Primary reduction region ΔJ (A/cm^2)	Measured Current at point A (A/cm^2)	Measured Current at point B (A/cm^2)
Uncleaned	-0.795	1.040×10^{-6}	4.95×10^{-5}	3.43×10^{-4}
50°C 30s	-0.824	1.070×10^{-4}	1.54×10^{-4}	7.16×10^{-4}
50°C 10m	-0.843	1.199×10^{-5}	2.53×10^{-5}	2.15×10^{-4}
65°C 30s	-0.831	4.499×10^{-5}	7.45×10^{-5}	3.66×10^{-4}
65°C 10m	-0.830	3.537×10^{-5}	6.14×10^{-5}	3.00×10^{-4}
80°C 30s	-0.823	3.704×10^{-5}	6.33×10^{-5}	3.50×10^{-4}
80°C 10m	-0.837	2.938×10^{-5}	5.02×10^{-5}	5.24×10^{-4}
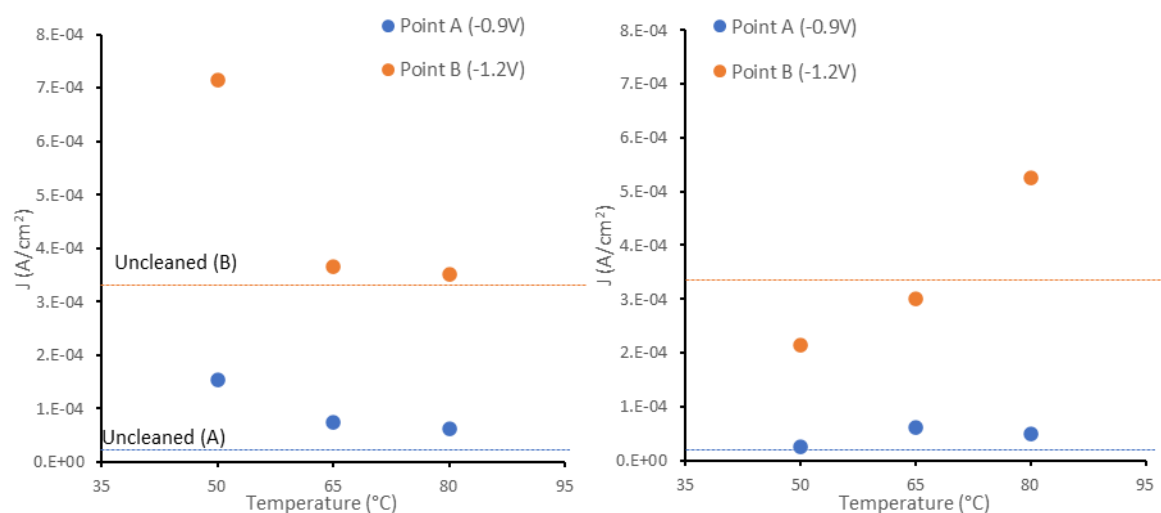
Figure 4.8. Measured current changes at point A and point B for Galvalloy alkaline cleaned for: (a) 30 seconds; (b) 10 minutes

The cathodic polarisation curves of Galvalloy show slight differences in how alkaline cleaning influences the cathodically driven oxygen reduction (ORR) reaction on the surfaces of the chemically etched surface. The initial change in current as the cathodic oxygen reduction is a result of the initial cathodic oxygen reduction, as shown in Equation 4.1.

$$O_2 + H_2O + 2e^- \rightarrow HO_2^- + OH^- \qquad \text{Equation 4.1}$$

The reaction curve that is formed is the result of the initial oxygen reduction reaction being an activation controlled process whereby there is plenty of oxygen available at the surface and alkaline cleaning appears to increase the amount the current changes as the reaction proceeds.

For cleaned Galvalloy substrates, this initial oxygen reduction reaction has a current density change of 10-100 µA, compared to a current change of 1 µA for unconditioned Galvalloy and the change in current for the 2e⁻ oxygen reduction reaction stays relatively stable for as the cleaning intensity increases. HDG substrates comparison also have a current density change in the 25-50 µA and unconditioned HDG having a current change of 1.8 µA, which is very similar to that of Galvalloy. The differences between Galvalloy in HDG in relation to cathodic polarisation is the 4e⁻ reduction process that occurs as the potential becomes more cathodic. .[4] This additional reaction has a greater current increase compared to HDG due to the reformation of the aluminium oxide film on the surface which occurs in aqueous solution according Equation 4.2.[5]

$$2Al_{(m)} + 3H_2O \rightarrow Al_2O_3 + 6H^+_{(aq)} + 6e^- \hspace{3cm} \text{Equation 4.2}$$

As a result of the oxide reformation on the surface of the more reactive Galvalloy surface because of the cleaning regimes, the additional reaction results in the current increasing with 10 minute washing times resulting in large current increases, and 30 second washes having greater current increases compared to the same regimes for HDG and is shown in Equation 4.3.

$$O_2 + 2H_2O + 4e^- \rightarrow 4OH^- \hspace{3cm} \text{Equation 4.3}$$

The change in corrosion current of this secondary reduction reaction is greater for Galvalloy substrates than HDG substrates. An unconditioned Galvalloy substrate does not show this secondary reduction region whereas HDG does, showing a current change of 17 µA, due to the alumina film being present on the surface . For 30 second wash times, Galvalloy shows a current change in this region of 140-240 µA, compared to a 90-140 µA current change for HDG. For longer cleaning times the current change is much more apparent for Galvalloy, showing current changes of 720-940 µA, compared to 30-180 µA differences for HDG washed at 10 minutes. All surfaces show a potential of roughly -1.07 to -1.12 V when this reaction occurs, with 10 minute washing times showing more cathodic potentials at which the reaction occurs. illustrating that Galvalloy washed at longer times becomes a more active oxygen cathode. This reaction also occurs at more cathodic potentials at more intense

cleaning times, these changes are marginal, but there is a 30mv cathodic shift from an uncleaned HDG substrate to HDG cleaned at 50°C for 30 seconds, and a further 20 to 30 mv cathodic shift for samples cleaned at 65°C and 80°C. This would appear to show that as alkaline cleaning intensity increases, the surface is becoming a more active oxygen cathode, producing the increased current changes before the current plateaus, and increasing the current further after the additional reduction reaction.

The cathodic polarisation behaviour can be linked to the corrosion driven cathodic disbondment of PVB on alkaline cleaned Galvalloy substrates. The surface of alkaline cleaned steel becomes a more active oxygen cathode as the cleaning conditions become more intense, producing the two different reduction processes on the surface and the current plateau that occurs as potential becomes more negative. The delamination rate and delamination distance increases as the cleaning intensity increases, however delamination from Galvalloy occurs more slowly compared to HDG. For uncleaned Galvalloy, delamination only reaches 0.85mm, compared to a minimum of 2.35mm for a cleaned sample. The cathodic polarisation curve of uncleaned Galvalloy does not show a $4e^-$ reduction related current increase, which could account for its much lower delamination rate, higher initiation time, and lower delamination distance compared to cleaned Galvalloy, as there is no additional driving force to cause delamination to occur. The measured current density of the cathodic ORR increases as the cleaning intensity increases and the delamination performance also decreases.

4.3.2.3. Linear polarisation of alkaline cleaned Galvalloy

Linear Polarisation of alkaline cleaned Galvalloy substrates were conducted to see how the influence of surface conditioning influences the metal oxidation and oxygen reduction reactions that occurs on the surface when in 5wt.% NaCl solution. The Open Circuit Potential (OCP) of samples were taken before polarisation of the sample, with potential sweeps starting from -0.1 V more negative than the OCP to +0.1 more positive than the OCP. After polarisation, samples were held at the OCP for 30 minutes before polarisation was conducted again. This was done every 30 minutes for 210 minutes to ascertain the corrosion properties of the different substrates over time. From the linear polarisation curves, the polarisation resistance of the substrate can be calculated from the slope of the linear voltage vs current plot, which subsequently allows for calculation of the corrosion rate, which allows for direct

comparisons in the performance and behaviour of tested samples. Linear polarisation curves of a control Galvalloy substrate with no alkaline surface conditioning and a selection of polarisation curves for Galvalloy alkaline cleaned for 10 minutes at 50°C, 65°C, and 80°C can be seen in Figures 4.9 – 4.12.
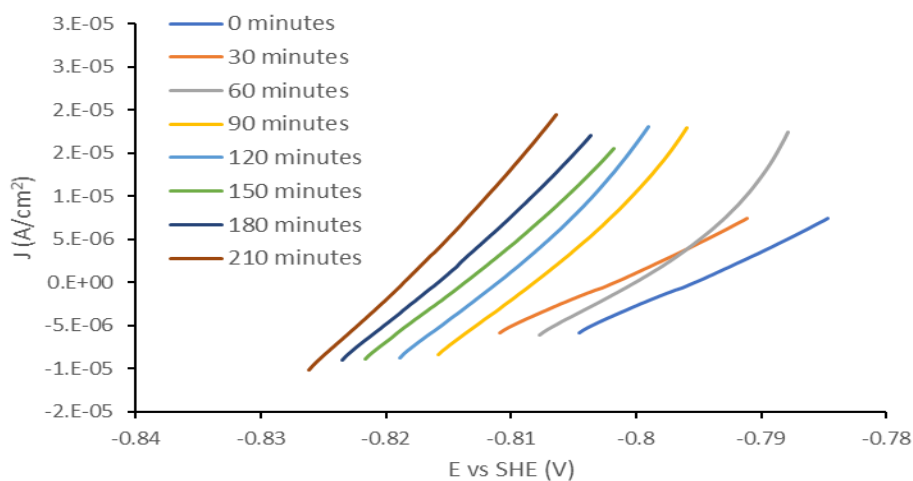
Figure 4.9. Linear Polarisation curved of unconditioned Galvalloy. Polarisation was conducted every 30 minutes for 210 minutes.
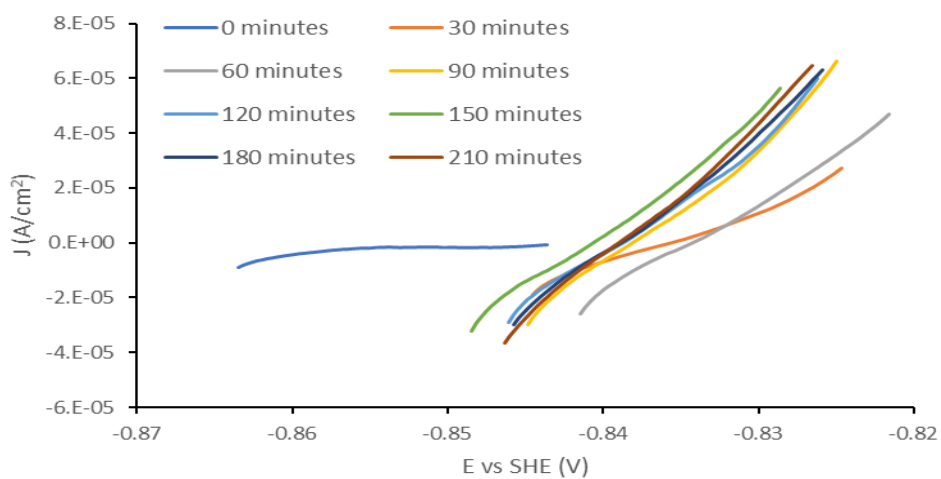
Figure 4.10. Linear Polarisation curved of Galvalloy alkaline cleaned at 50°C for 10 minutes. Polarisation was conducted every 30 minutes for 210 minutes.
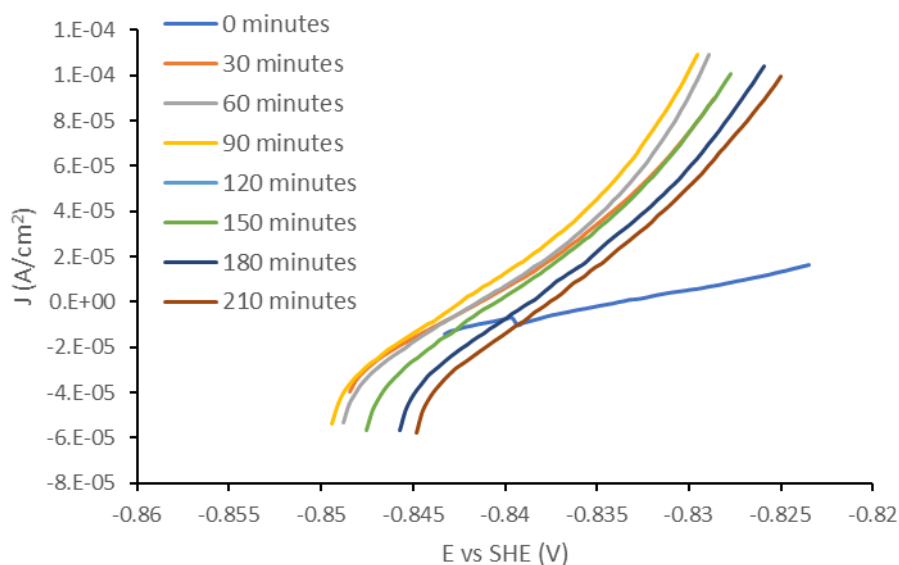
Figure 4.11. Linear Polarisation curved of Galvalloy alkaline cleaned at 65°C for 10 minutes. Polarisation was conducted every 30 minutes for 210 minutes.
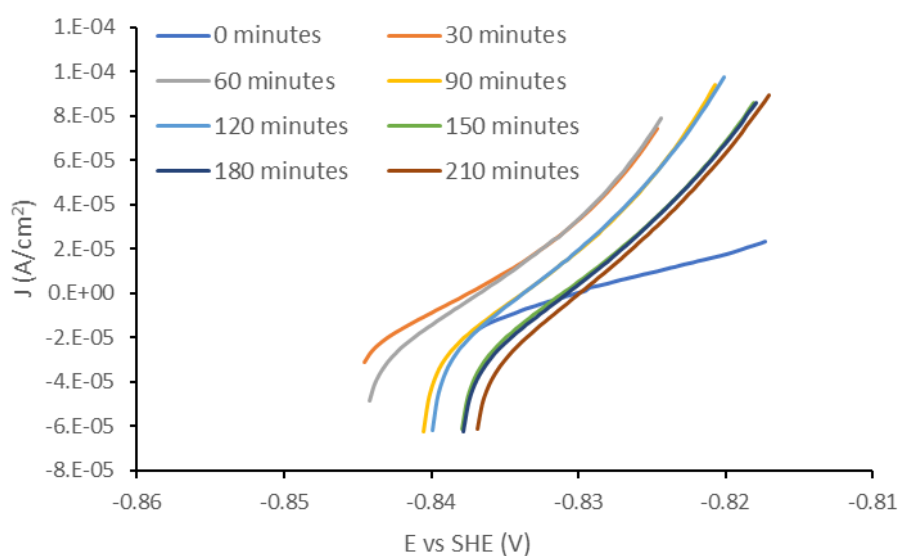
Figure 4.12. Linear Polarisation curved of Galvalloy alkaline cleaned at 80°C for 10 minutes. Polarisation was conducted every 30 minutes for 210 minutes.

As shown above, the polarisation curves show that as the time immersed in 5% NaCl increases, the OCP and subsequent linear polarisation curves shift to more cathodic potentials, before stabilising at lower potentials. The initial polarisation curve produced can be attributed to the OCP still stabilising before the surface is polarised, subsequent curves indicate the OCP has stabilised after 30 minutes in solution.

From the linear polarisation curves produced, the polarisation resistance can be obtained from equation 4.4.

$$R_{pol} = \Delta E / \Delta I \hspace{4cm} \text{Equation 4.4}$$

Where ΔE is the change in the applied potential from the free corrosion potential and ΔI is change in polarisation current. The polarisation resistance of HDG cleaned at different conditions can be seen below in Figure 4.13.
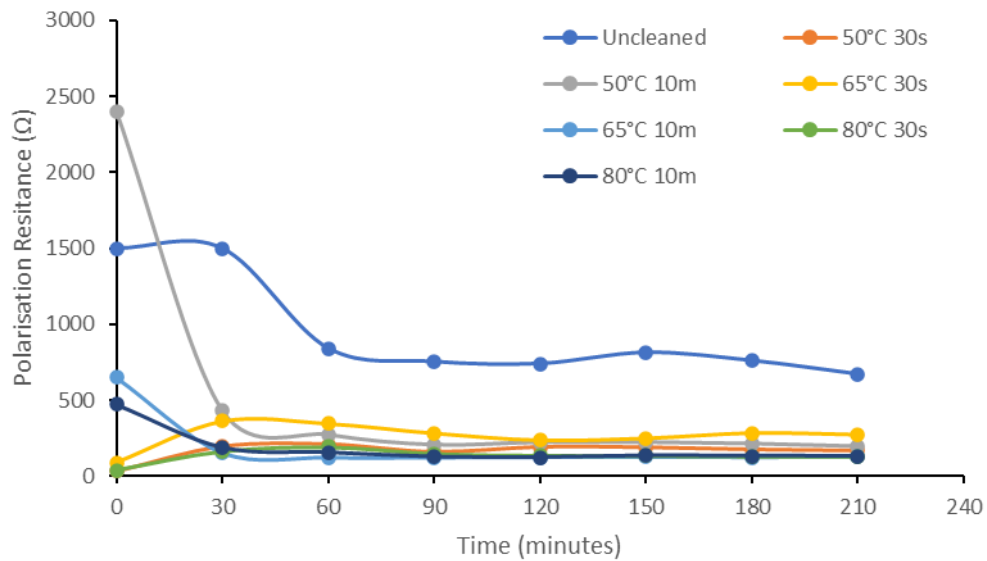
Figure 4.13. Polarisation resistance of Galvalloy at varying cleaning conditions

The polarisation resistances calculated for Galvalloy substrates shows that uncleaned Galvalloy has a significantly higher polarisation resistance than alkaline cleaned Galvalloy. The average polarisation resistance of an alkaline clean at 50°C for 10 minutes is higher than the other cleaning conditions but only due to an erroneous resistance of 2400.82 Ω for the first polarisation scan likely caused by system instability during the first OCP measurement before polarisation. The average resistance would be a more comparable 252.05 Ω if the first scan was discounted. The polarisation resistance calculated from the first current vs potential plot at time = zero, and time = 30 minutes has been removed to illustrate how the polarisation resistance of the substrates remain relatively constant from 60 minutes to 210 minutes.
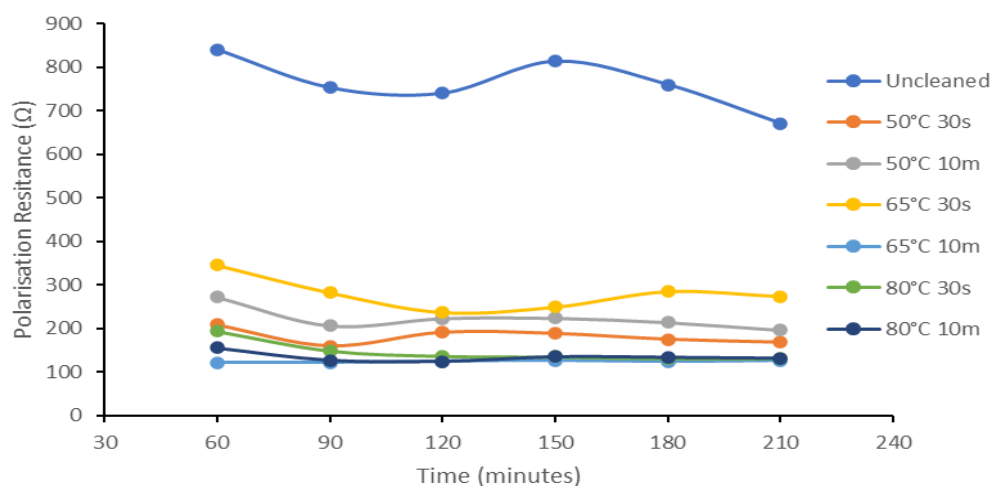
Figure 4.14. Polarisation resistance of Galvalloy at varying cleaning conditions

Through the use of the Stern-Geary equation shown in chapter 3 the corrosion rate can be linked to the polarisation resistance. [6,7] The corrosion rate and polarisation resistance are inversely proportional to one another with higher polarisation resistances resulting in lower corrosion rates and vice versa. [8] Measured polarisation resistances for alkaline cleaned Galvalloy would indicate similar corrosion rates regardless of cleaning parameters, with an unconditioned Galvalloy showing the lowest corrosion rate. Through use of the Stern-Geary equation, the corrosion rate has been calculated for alkaline cleaned Galvalloy substrates, and the calculated values, along with the I_{corr} and Tafel constants can be seen below in Table 4.3.

Table 4.3. Tafel coefficients, I_{corr} and corrosion rate values for alkaline cleaned Galvalloy.

Sample	Bc (V/decade)	Ba (V/decade)	I_{corr} (A/cm^2)	Corrosion rate (µm/year)
Uncleaned	0.0012	0.2232	5.97×10^{-7}	8.94
50°C 30s	0.0028	0.2597	6.55×10^{-6}	98.18
65°C 30s	0.0018	0.2216	3.08×10^{-6}	46.10
80°C 30s	0.0014	0.1971	2.07×10^{-6}	31.10
50°C 10m	0.001	0.2254	3.38×10^{-6}	50.63
65°C 10m	0.0015	0.1667	4.34×10^{-6}	64.99
80°C 10m	0.0027	0.1635	$8.12 \times 10{-6}$	121.74

What is unusual about calculated corrosion rates is the change in rate at the different cleaning times. When the cleaning temperature is increased at a 30 second wash time, the corrosion rate drops at each 15°C temperature increase, whereas when the temperature is increased at a 10 minute cleaning time the corrosion rate increases.

The corrosion driven cathodic disbondment behaviour of Galvalloy substrates can also be indicated by the linear polarisation curves produced for the different substrates. As the alkaline cleaning time increases and the temperature remains constant the average polarisation resistance decreases. The polarisation resistance of Galvalloy washed for 10 minutes at all temperatures remains relatively stable, however Galvalloy washed for 30 seconds at all temperatures has a tendency to drop over time. This can be attributed to the zinc on the surface, with there being a reduced zinc content at 10 minute washes compared to 30 second washes as illustrated by XPS measurements. This difference in polarisation resistance as a result produces greater corrosion rates for Galvalloy washed for 10 minutes compared to those washed for 30 seconds, which is seen in the delamination rates and distances shown by time-lapse and SKP techniques.

4.3.3. Investigation of corrosion driven cathodic disbondment kinetics using time-lapse photography and Scanning Kelvin Probe

Time-lapse photography and Scanning Kelvin Probe (SKP) were used to investigate the kinetics of corrosion driven cathodic disbondment of polyvinyl-butyral (PVB) coatings applied to alkaline cleaned Galvalloy substrates. Stratmann cells were created to create a defect region to allow for the initiation of cathodic disbondment and samples were exposed to a 95% relative humidity atmosphere and disbondment was initiated using 5% sodium chloride solution. Time-lapse images and SKP potentials were measured every hour for 24 hours and the kinetics of coating failure was analysed.

4.3.3.1. Use of time-lapse photography to analyse kinetics of corrosion driven cathodic disbondment

Compared to HDG, Galvalloy under time-lapse photography conditions appears to not readily undergo corrosion driven cathodic disbondment even after 5 days. One reason for this would

be the surface finish of Galvalloy being too reflective for images of cathodic delamination to be taken compared to the duller finish of HDG. An image of Galvalloy in a time-lapse light-box over 120 hours can be seen in Figure 4.15. However, when the images are zoomed in and resolved, delamination does appear to have occurred after 24 hours A highly resolved image of Galvalloy cleaned at 80°C for 10 minutes can be seen in Figure 4.16, and shows darkening of the surface measuring around 2mm from the coating defect, indicating that cathodic disbondment has occurred. However, it is difficult to resolve when delamination begins to occur and how far the delamination front has travelled over 24 hours due to the slow nature at which delamination occurs. In order to further study the cathodic delamination of organically coated Galvalloy, a Scanning Kelvin probe was used to measure the potential over the surface and gain far more detailed information.
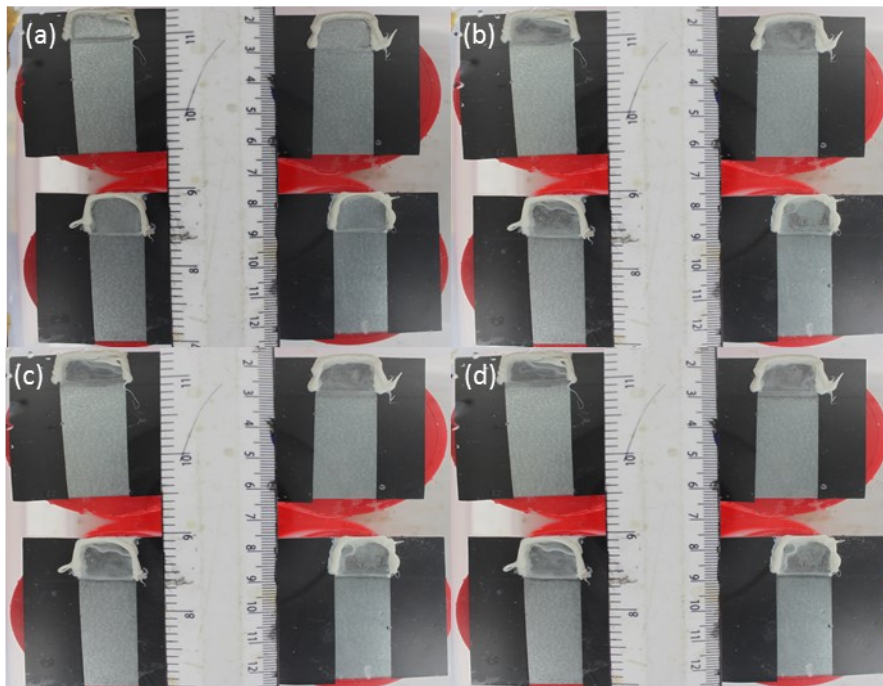
Figure 4.15. Time-lapse images of Galvalloy undergoing cathodic disbondment; (a) 0 hours; (b) 40 hours; (c) 80 hours; (d) 120 hours.

Figure 4.16. Time-lapse images of Galvalloy washed at 80°C for 10 minutes, 120 hours after initiation of cathodic disbondment.

4.3.3.2. Use of Scanning Kelvin Probe to analyse kinetics of corrosion driven cathodic disbondment

The use of scanning Kelvin probe is to analyse not only the kinetics of the cathodic disbondment of the alkaline cleaned samples but also how the surface potential changes with delamination of the organic coating and whether the surface conditioning changes the measured potentials. Measurements were taken using the extremes of the cleaning conditions, with 30 second and 10 minute washing times used at the temperatures used previously. The E_{corr} versus distance (X) for the case of a control Galvalloy sample which had no surface conditioning prior to PVB application is given in Figure 4.16. which allows for determination of baseline kinetics for a Galvalloy system with a model PVB coating applied. As shown below, an unconditioned Galvalloy sample shows no indication of delamination occurring in the 24 hour period. A selection of SKP plots for Galvalloy washed for 30 seconds at 50°C, 65°C, and 80°C can be seen in Figures 4.18 – 4.20. From the SKP profile of the uncleaned Galvalloy sample, the intact potential is pushed more anodically with time, indicating an increased driving force of cathodic disbondment, and would likely begin to undergo delamination within 48 hours.
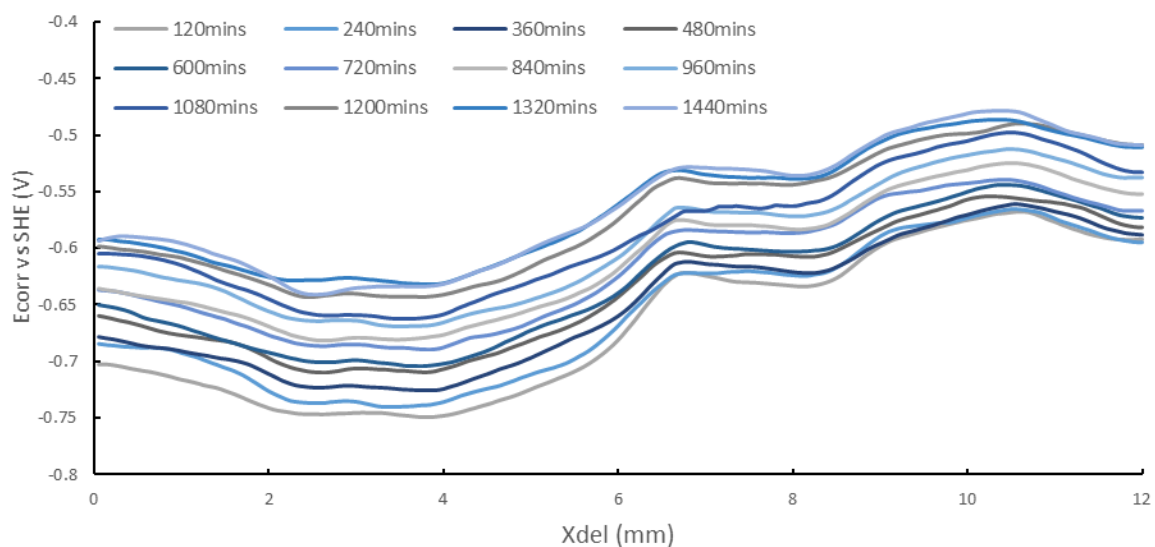
Figure 4.17. A SKP profile showing the time dependent E$_{corr}$ measurements against distance from defect (X) for PVB coating from an unconditioned Galvalloy sample. E$_{corr}$ measurements were taken every hour for 24 hours and data presented every 2 hours.
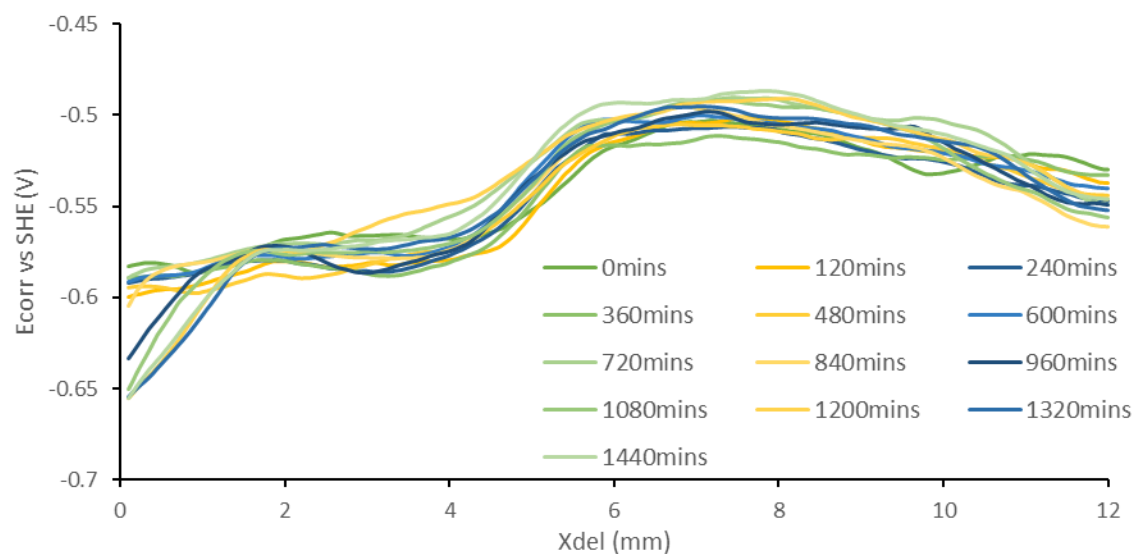
Figure 4.18. A SKP profile showing the time dependent E$_{corr}$ measurements against distance from defect (X) for 50°C, 30 second alkaline cleaned surface with PVB coating from a Galvalloy sample. E$_{corr}$ measurements were taken every hour for 24 hours.
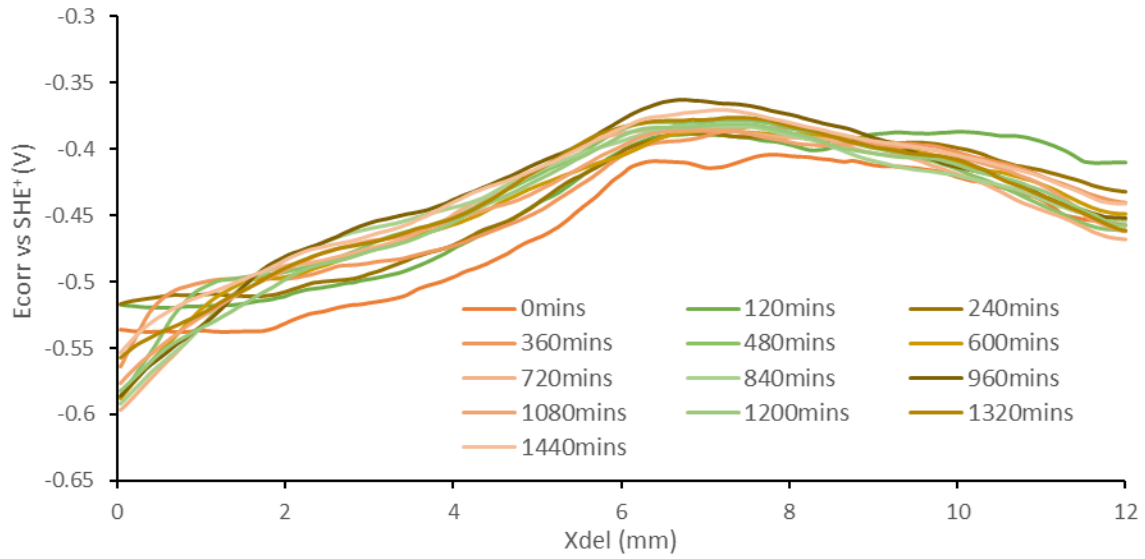
Figure 4.19. A SKP profile showing the time dependent E_{corr} measurements against distance from defect (X) for 65°C, 30 seconds alkaline cleaned surface with PVB coating from a Galvalloy sample. E_{corr} measurements were taken every hour for 24 hours.
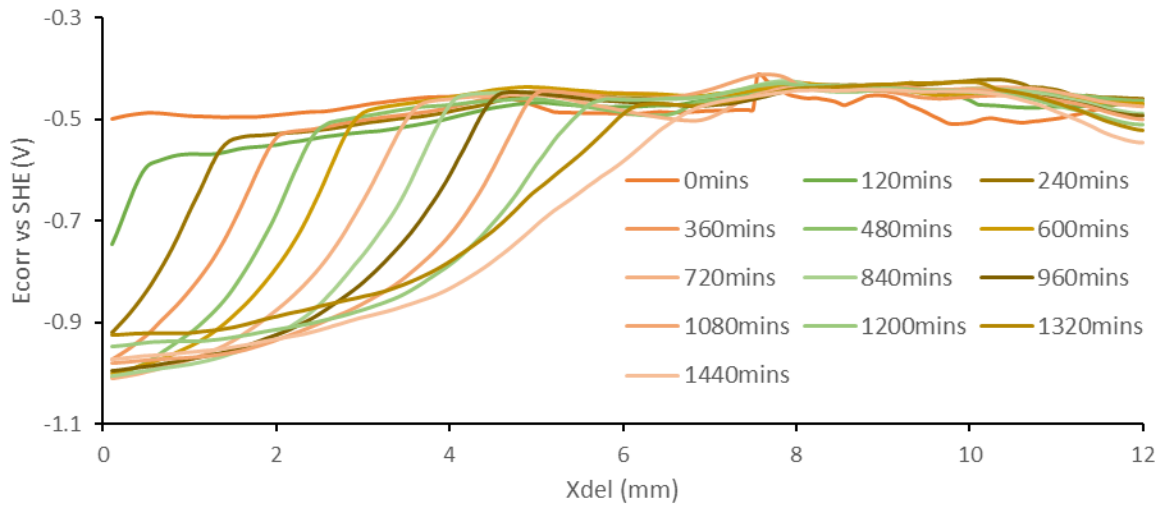
Figure 4.20. A SKP profile showing the time dependent E_{corr} measurements against distance from defect (X) for 80°C, 30 second alkaline cleaned surface with PVB coating from Galvalloy. E_{corr} measurements were taken every hour for 24 hours.

From the SKP profiles the distance of delamination can be taken and plotted which can illustrate how delamination occurs as a function of cleaning conditions with time. This can be seen in Figure 4.21, with X_{del} measured from the point at which E_{corr} becomes more positive i.e. becomes E_{intact}.
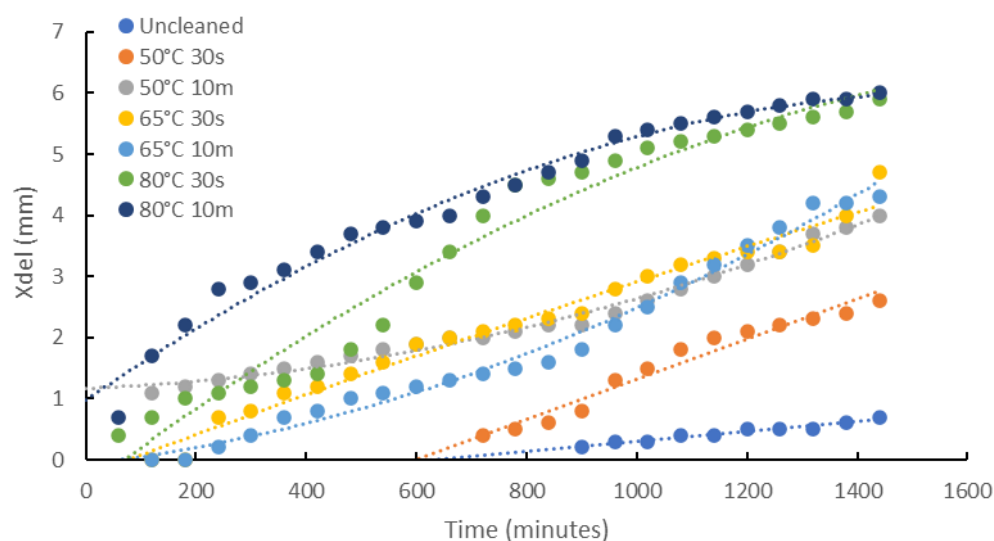
Figure 4.21. Plot of X$_{del}$ versus time showing the effect of alkaline cleaning on cathodic delamination on Galvalloy steel

The determination of the rate kinetics of the alkaline cleaned vs uncleaned Galvalloy also shows a difference in how the delamination kinetics occur. Both unconditioned and Galvalloy cleaned at 50°C and 65°C exhibit linear kinetics. In comparison to alkaline cleaned HDG substrates, in which all alkaline cleaned substrate exhibit parabolic kinetics as a result of uninhibited delamination whereas unconditioned Galvalloy exhibits linear kinetics as a result of the surface oxide inhibiting coating failure. This indicates that cathodic disbondment on Galvalloy substrates is rate-limited by electron transfer from the formed anode to the formed cathode.

From the SKP plots generated for all PVB coated alkaline cleaned samples, a plot of initiation time and delamination distance (X$_{del}$) versus time was plotted to show how cleaning temperature influenced coating performance at 30 second and 10 minute cleaning times and can be seen below in Figure 4.22.
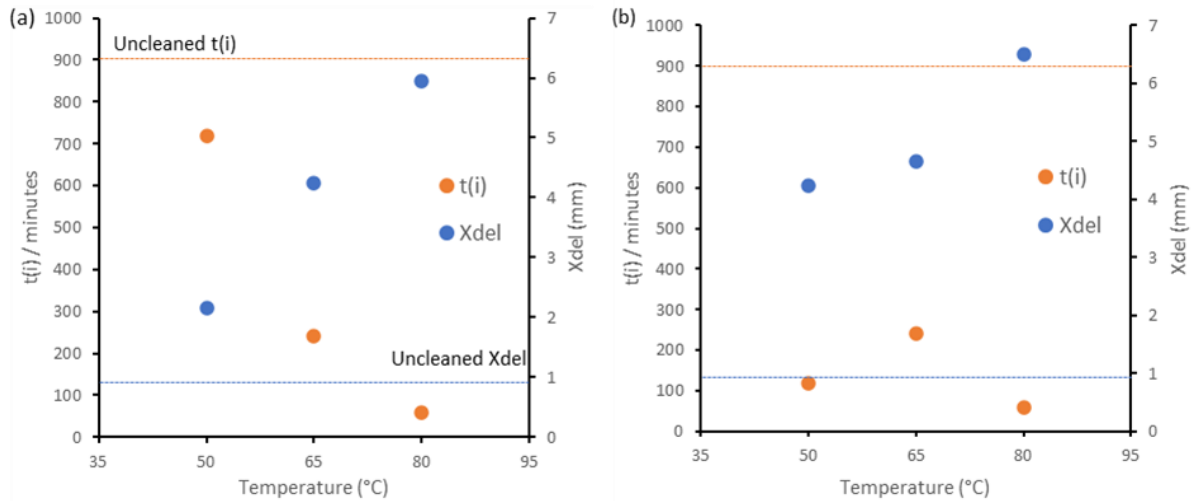
Figure 4.22. Delamination of distance from defect and Initiation time of PVB of alkaline cleaned Galvalloy as determined by scanning Kelvin probe; (a) Alkaline cleaned for 30 seconds; (b) Alkaline cleaned for 10 minutes.

When the cleaning time is fixed at 30 seconds, the initiation times measured are 720 minutes, 240 minutes, and 60 minutes with measured delamination distances of 2.15mm, 4.25mm, and 5.95mm for 50°C, 65°C, and 80°C respectively. When the cleaning time is increased to 10 minutes, the times taken for delamination to initiate for each temperature are 120 minutes, 240 minutes, and 60 minutes, with measured delamination distances of 4.25mm, 4.65mm, and 6.5mm for 50°C, 65°C, and 80°C respectively. From the determination of the initiation time and delamination from the defect of model PVB coating an uncleaned Galvalloy, where the oxide layer remains intact, shows the least delamination distance and the longest amount of time for coating failure to initiate, whereas the delamination travelled from the defect increases with increasing cleaning intensity and initiation time drops. The initiation time is also shortest for uncleaned and Galvalloy washed for 80°C for 30 seconds and 10 minutes, with delamination taking 60 minutes to initiate. Galvalloy which has been unconditioned does not undergo delamination at all, with the delamination time dropping to 720 minutes for a 50°C 30 second wash. The remaining washing conditions result in delaminating initiating withing 120 – 240 minutes. The measured X_{del} also increases when (i) cleaning temperature is fixed and cleaning time is increased, and (ii) when cleaning time is fixed and temperature is increased, indicating coating failure can be tied to cleaning parameters.

The maximum slop of the time dependent E_{corr} profile can be used as a semi empirical way of locating the delamination front for each specimen, as seen in Chapter 3 with HDG steel

substrates. This data is gathered through plotting the distance travelled by coating delamination as a function of the square root of time and are plotted below to show the rate kinetics of coating failure in Figure 4.23. The E_{corr} profiles for all substrates have very similar separation distances at each time interval, indicating similar delamination rates. From the SKP E_{corr} against distance from defect charts shown above, the delamination rate can be determined from using the midpoint of the increase in the E_{corr} indicating the distance that coating delamination has travelled, before reaching the intact potential of the PVB coating, which can be seen in Figure 4.24.
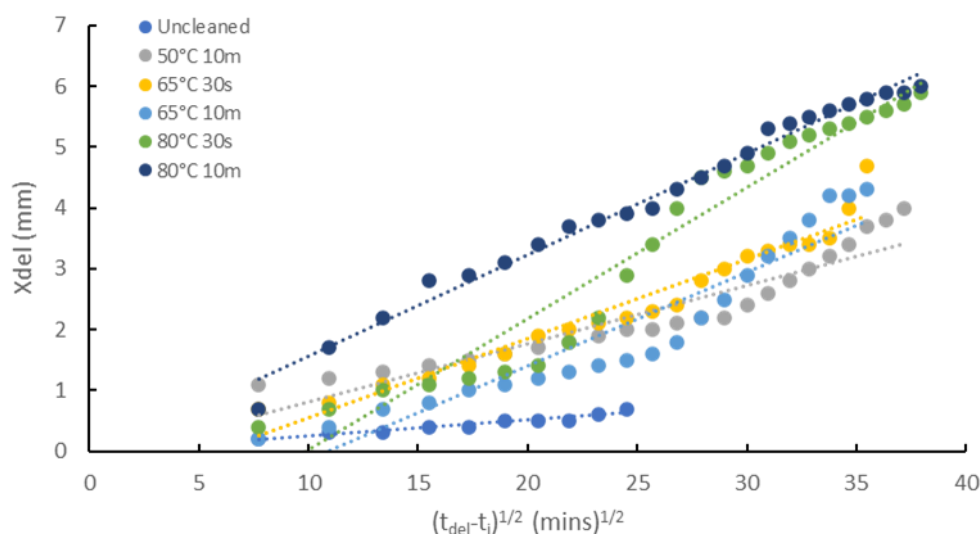
Figure 4.23. Delamination distance $(t_{del}-t_i)^{1/2}(min)^{1/2}$ plot of Galvalloy over 24 hours derived from SKP profiles.
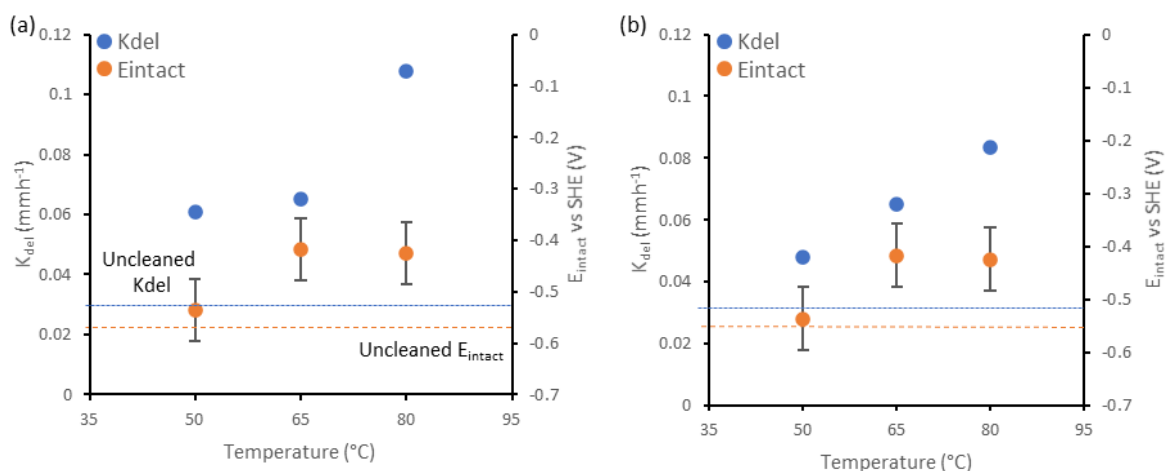
Figure 4.24. Delamination rates and intact potential of PVB on alkaline cleaned Galvalloy; (a) Alkaline cleaned for 30 seconds, (b) Alkaline cleaned for 10 minutes.

What can be seen by the rates determined through SKP data manipulation is the rate generally increases as the cleaning intensity increases and this is mirrored by the intact potential becoming more anodic as cleaning intensity increases compared to an uncleaned Galvalloy surface.

In comparison to HDG, the intact potential (E_{intact}) of Galvalloy shows different behaviour. On HDG substrates, the intact potential becomes more cathodic as cleaning intensity is increased, whereas Galvalloy substrates become more anodic as cleaning intensity is increased. The E_{intact} for unconditioned and Galvalloy cleaned at 50°C is between 50-120 mV more cathodic compared to E_{intact} of HDG at the same conditions, whereas the E_{intact} for the remaining cleaning conditions for Galvalloy is 100-210 mV more anodic compared to HDG. Galvalloy is more resistant than HDG as a result of alloyed aluminium which a poorer oxygen cathode compared to zinc which would indicate the difference in the measured delamination distances between the two substrates. Increasing alkaline cleaning intensity appears to create a greater driving force for cathodic disbondment, which results in a greater driving force for passing current from the defect to the under-film cathode resulting in electron transfer not being supressed as much, which provides more anodic intact potential. When X_{del} is plotted against time, Galvalloy cleaned at 80°C produce parabolic curves, with the remaining cleaning conditions producing linear curves indicating that the rate determining step shifts electron transfer from the anode to the cathode to ion migration in the underfilm electrolyte. This can be seen when all curves become linear when X_{del} is plotted against $(t_{del} - t_i)^{1/2}(mins)^{1/2}$. As the E_{intact} becomes steadily more anodic the driving force for cathodic disbondment becomes greater, increasing the delamination rate.

4.4. Conclusions

In conclusion, the alkaline cleaning has an influence of the surface chemistry of Zn-Al(4.8%) based steel surfaces, removing the Al_2O_3 present on uncleaned surfaces completely and increasing the amount of metallic zinc, and decreasing the content of oxidic zinc present on the surface as measured by XPS. Anodic polarisation of substrates shows very similar behaviour of Galvalloy cleaned at varying parameters and is very similar to the behaviour of HDG steel with a limited passive region present. Cathodic polarisation appears to show that more intense cleaning conditions produce a surface that is a more active oxygen cathode much like that seen for HDG steel, and further promotes corrosion driven cathodic

disbondment. Polarisation studies of cleaned Galvalloy shows a drop in the polarisation resistance of substrates over time and increasing the cleaning intensity results in a drop in the initial and average polarisation resistance. Calculation of the corrosion rate from polarisation resistances also shows that cleaning the surface of Galvalloy increases the corrosion rate, with uncleaned Galvalloy producing a very low corrosion rate of 8.20 µm/year, which is much lower than that seen for cleaned Galvalloy and much lower than the 124 µm/year for uncleaned HDG.

Study of the corrosion driven cathodic disbondment using time-lapse and SKP techniques shows that time and temperature of alkaline cleaning have a direct effect on the performance of the delamination of PVB coating, with increasing time and temperature resulting in increased delamination rates and decreased coating performance. Corrosion rate kinetics appears to change as cleaning intensity increases, with samples cleaned at 80°C exhibiting parabolic kinetics and lower temperature cleans exhibiting linear kinetics. This illustrates that the rate limiting step changes from electron transfer occurring in surface reactions to cation migration in the under-film electrolyte. However, performance of Galvalloy metallic substrates is improved compared to that of HDG, showing at least a 45% reduction in the coating delamination seen at identical cleaning times and temperatures. As shown in the work conducted in this chapter it would not be recommended to apply an organic coating to a cleaned Galvalloy surface as cleaning negatively impacts the performance of the coating on the surface.

4.5. References

1. Hosking NC, Ström MA, Shipway PH, Rudd CD. Corrosion resistance of zinc-magnesium coated steel. *Corros Sci*. 2007;49(9):3669-3695. doi:10.1016/j.corsci.2007.03.032

2. Volovitch P, Vu TN, Allély C, Abdel Aal A, Ogle K. Understanding corrosion via corrosion product characterization: II. Role of alloying elements in improving the corrosion resistance of Zn-Al-Mg coatings on steel. *Corros Sci*. 2011;53(8):2437-2445. doi:10.1016/j.corsci.2011.03.016

3. Strohmeier BR. Characterization of an Activated Alumina Claus Catalyst by XPS. *Surf Sci Spectra*. 2021;3(2):141. doi:10.1116/1.1247775

4. Dafydd H, Worsley DA, McMurray HN. The kinetics and mechanism of cathodic oxygen reduction on zinc and zinc-aluminium alloy galvanized coatings. *Corros Sci*. 2005;47(12):3006-3018. doi:10.1016/J.CORSCI.2005.05.036

5.   Moon SM, Pyun SI. The corrosion of pure aluminium during cathodic polarization in aqueous solutions. *Corros Sci*. 1997;39(2):399-408. doi:10.1016/S0010-938X(97)83354-9

6.   Mansfeld F. Fundamental aspects of the polarization resistance technique-the early days. doi:10.1007/s10008-008-0652-x

7.   Stern M, Geary AL. Electrochemical Polarization: I . A Theoretical Analysis of the Shape of Polarization Curves. *J Electrochem Soc*. 1957;104(1):56. doi:10.1149/1.2428496

8.   Toshev Y, Mandova V, Boshkov N, et al. Protective coating of zinc and zinc alloys for industrial applications. *4M 2006 - Second Int Conf Multi-Material Micro Manuf*. January 2006:323-326. doi:10.1016/B978-008045263-0/50073-8

Chapter 5– Investigation the influence of Titanium-based pre-treatment addition on surface chemistry and corrosion driven cathodic disbondment on galvanised steel.

5.1. Introduction

A conversion coating involves altering the chemistry of a metal surface via a chemical reaction between the metal surface and the ionic species dissolved in the pre-treatment solution. The reaction of a conversion solution with a metal surface generates a layer covering the surface. The conversion coating allows for greater adhesion of subsequent organic coatings due to the presence of chemical bonds and an intermediate layer between the coating and the underlying metal.[1] The addition of a pre-treatment to the surface decreases the surface free energy of the substrate and allows greater adhesion of organic coatings placed on top. [2] This type of coating system is used in contemporary organically coated steel products such as the Colorcoat Prisma system produced by TATA steel which can be seen in Figure 5.1.
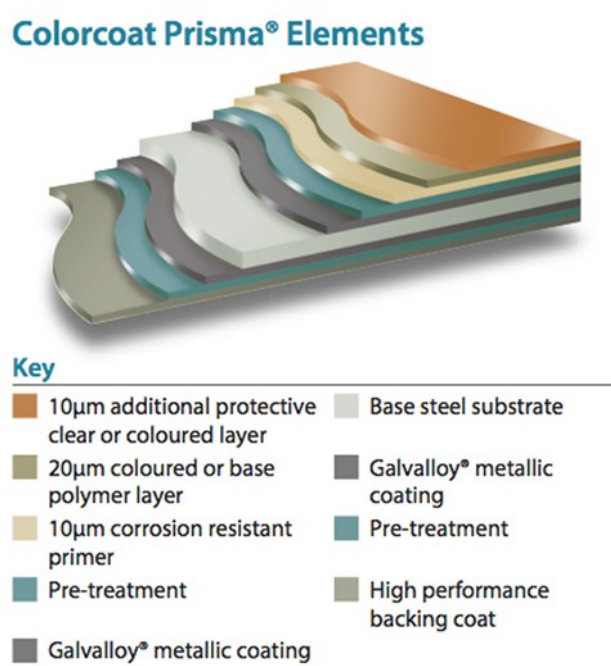
Figure 5.1. Diagram of Tata Steel Colorcoat Prisma coating layers. [3]

Generally an increase in corrosion performance has been attributed to the use of a conversion coating compared to an uncoated sample on Al alloys, galvanised steel and steel. The conversion coating, when applied, reacts with the metal surface which precipitates as a thin film coating the metal surface, inhibiting corrosion from occurring by acting as a barrier to the environment. This is done through providing a physical barrier which prevents access to the metal surface more effectively than the original oxide, neutralising the potential of local anodic and cathodic galvanic corrosion sites and rendering the surface electrochemically inert.[4] These films also acts as an absorption base for improving the adhesion of subsequent of organic layers applied on top.

Hexafluorotitanic acid (HFT) based pre-treatments have been used since the 1980s, with patents being published describing the deposition of HFT which have subsequently led to commercial products. [5,6] The corrosion resistant coatings that are the subject of this thesis for use on colour-coated steel is based on metal oxides, such as zirconia and titania. These coatings are environmentally benign and produce sufficient corrosion resistance. The coating baths normally used to form these conversion coatings are aqueous solutions of hexafluorotitanic acid or hexafluorozirconic acid. The chemical reactions and background literature for the deposition of hexafluorotitanic acid on galvanised steel can be seen in Sections 1.5 and 1.6.

A significant amount of work in the past 20 years has been dedicated to understanding the film formation of zirconium or titanium based conversion coatings of various metal alloys and has been of much interest in recent years to industry due to the phasing out of carcinogenic pre-treatments that are typically used due to new legislation. The work in this chapter builds on some of the work conducted in the literature, which has already investigated electrochemical behaviour of titania based pre-treatments by building an understanding of how alkaline cleaning parameters influence the electrochemical behaviour and performance of the pre-treatment coating. The chemical nature of the surface is quantified through XPS and XRF analysis and the electrochemical behaviour characterised by electrochemical polarisation of the pre-treatment surface. In addition, the pre-treatment performance is also investigated by determining the kinetics of organic coating failure via a cathodic delamination mechanism when over-coated with a model PVB film.

5.2. Experimental details

5.2.1. Materials

Bonderite U-187 alkaline cleaner was provided by Henkel. Hot dip galvanized steel was provided by Tata Steel UK, with a gauge of 0.7mm mild steel and a zinc layer of 20μm. Bonderite 1445 M-NT hexaflourotitante (HFT) pre-treatment wipes manufactured by Henkel were purchased online. Samples were created by cutting the HDG into coupons of 50 x 50mm. Polyvinyl butyral-co-vinyl alcohol-co-vinyl acetate (PVB), molecular weight 70,000-100,000, was obtained from Sigma Aldrich Chemical Co. and was at an analytical grade purity. The PVB solution was prepared in ethanol to 15.5% w/w with the required amount of inhibitor added using a high shear mixer.

5.2.2. Experimental Methodology

Samples of pre-treated HDG were prepared for experimentation by being cut into coupons of the relevant size necessary for analysis. Samples a were degreased with ethanol before using Bonderite U-187 alkaline washing solution which was heated at 50°C, 66°C, and 80°C for between 30 seconds and 10 minutes. Samples were rinsed with de-ionised water to remove any residual cleaning solution and dried with a hairdryer. Pre-treatment was then applied using a Henkel pre-treatment wipe to apply pre-treatment to the surface, this was done by applying with either one or 10 applications by wiping across the surface with minimal pressure and left to air cure for 15 minutes before testing or coating application. The full description of the instrumentation, calibration, experimental set-up and analysis of XRF XPS, SKP, time-lapse photography and potentiodynamic polarisation can be found in Chapter 2.

5.3. Results and Discussion

5.3.1. Surface characterisation of alkaline cleaned hot dipped galvanised steel coated with hexaflourotitanate

5.3.1.1 Titanium quantification of hexaflourotitanate coated hot dipped galvanised steel.

In industry, the titanium weighting of the HFT pre-treatment is quantified to ensure quality control of the pre-treatment layer deposited on any metallic alloy surface. This is done using X-ray fluorescence to quantify the titanium deposited. Results of how variation of the alkaline cleaning of HDG and the variation in the number of wipes used to deposit HFT on HDG can be seen in Figures 5.2 and 5.3.
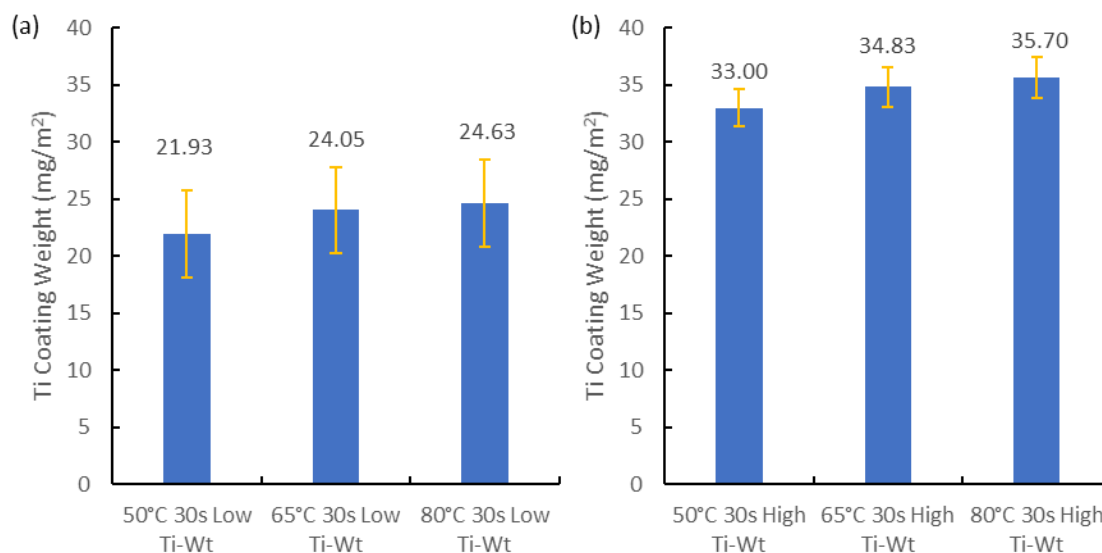
Figure 5.2. Titanium weighting of HFT on HDG steel alkaline cleaned for 30 seconds at varying temperatures; (a) Low Ti-Wt; (b) High Ti-Wt
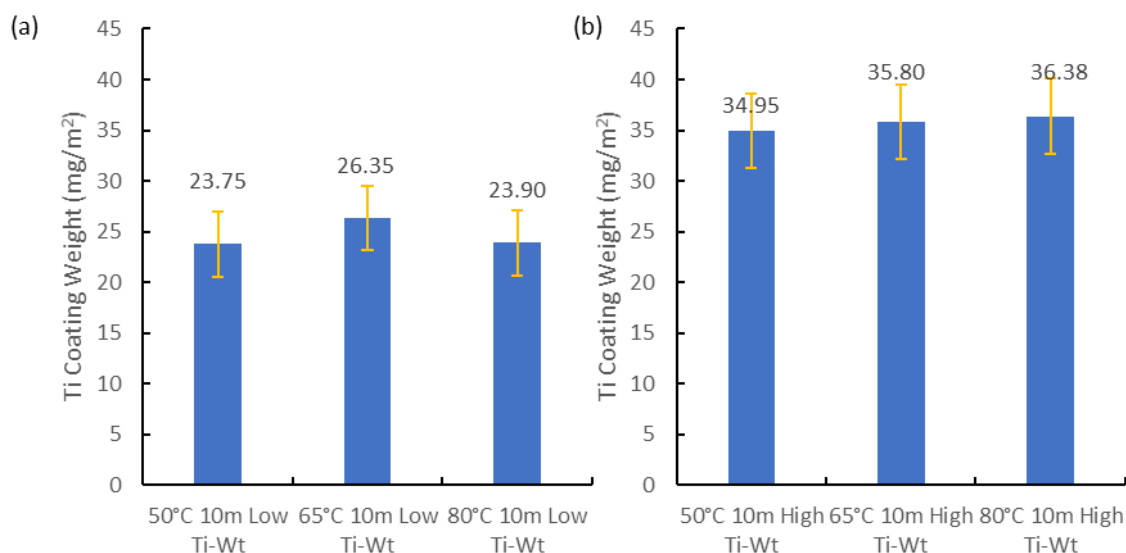
Figure 5.3. Titanium weighting of HFT on HDG steel alkaline cleaned for 10 minutes at varying temperatures; (a) Low Ti-Wt; (b) High Ti-Wt

As shown in Figures 5.2 and 5.3 the Ti-weighting produced by one application (low Ti-Wt) is between 21-27 mg/m^2, whereas ten applications (high Ti-Wt) produces a Ti weighting of 33-37 mg/m^2. The average increase in the Ti content between 1 and applications is 11.01 mg/m^2. There is also a minor relationship between the Ti-weight and the cleaning regime. What can be seen from low Ti-Wt applications seen in Figure 5.2a and 5.2b, increasing the cleaning temperature and keeping the cleaning time at 30 seconds results in an increase in the Ti coating weight, when the cleaning time is increased to 10 minutes, there is an increase in the coating weight when the temperature is increased from 50°C to 65°C, before coating weight drops at an 80°C wash. At 50°C and 65°C, when cleaning time is increased the coating weight increases, and at 80°C the coating weight decreases when cleaning time increases. For high Ti-Wt coatings as shown in Figure 5.3a and 5.3b the coating weight increases when cleaning temperature is increased at a constant time, and when cleaning time is increased, and the temperature is kept constant. The cleaning intensity appears to have an influence on the deposition, with better deposition occurring as cleaning intensity increases. As shown in chapter 3 increasing the cleaning intensity produces a more active surface and it is likely that this increased surface activity of the steel surface allows better deposition at both pre-treatment wipe depositions and so results in typically increased coating weights at greater cleaning intensities. This increase in the Ti-weight as the cleaning intensity and wipe

Much like that of zinc, peaks generated by Mn 2p, Ti 2p and P 2p should also exhibit spin orbit splitting and form $2p_{1/2}$ and $2p_{3/2}$ doublets of peak area ratios constrained at 1:2. Zinc peaks generated are centred around 1022.1 eV and 1045.2 eV, with the zinc Auger peak generated at 499.6 eV. A Fluoride 1s peak is generated at 684.5 eV, indicating the presence of a metal fluoride, combined with the zinc Auger peak this is shown that zinc fluoride is present on the surface. Phosphorous 2p generates a peak at 133.6 eV, and Mn 2p generates peaks centred around 642 eV, both of which illustrate the existence of manganese phosphate and manganese oxides on the surface. The presence of the metallic phosphorus and fluoride peaks could also indicate the existence of manganese fluoride and zinc phosphate on the surface.   Oxygen 1s generates an oxide based peak at 530.9 eV and a carbon-based oxygen peak at 532.5 eV. Titanium 2p generates a peak at 458.3, indicating the presence of TiO_2. The influence in alkaline cleaning on the elemental composition of HFT which had been applied with 1 wipe or 10 wipes can be seen in Figure 5.5 and Figure 5.6.
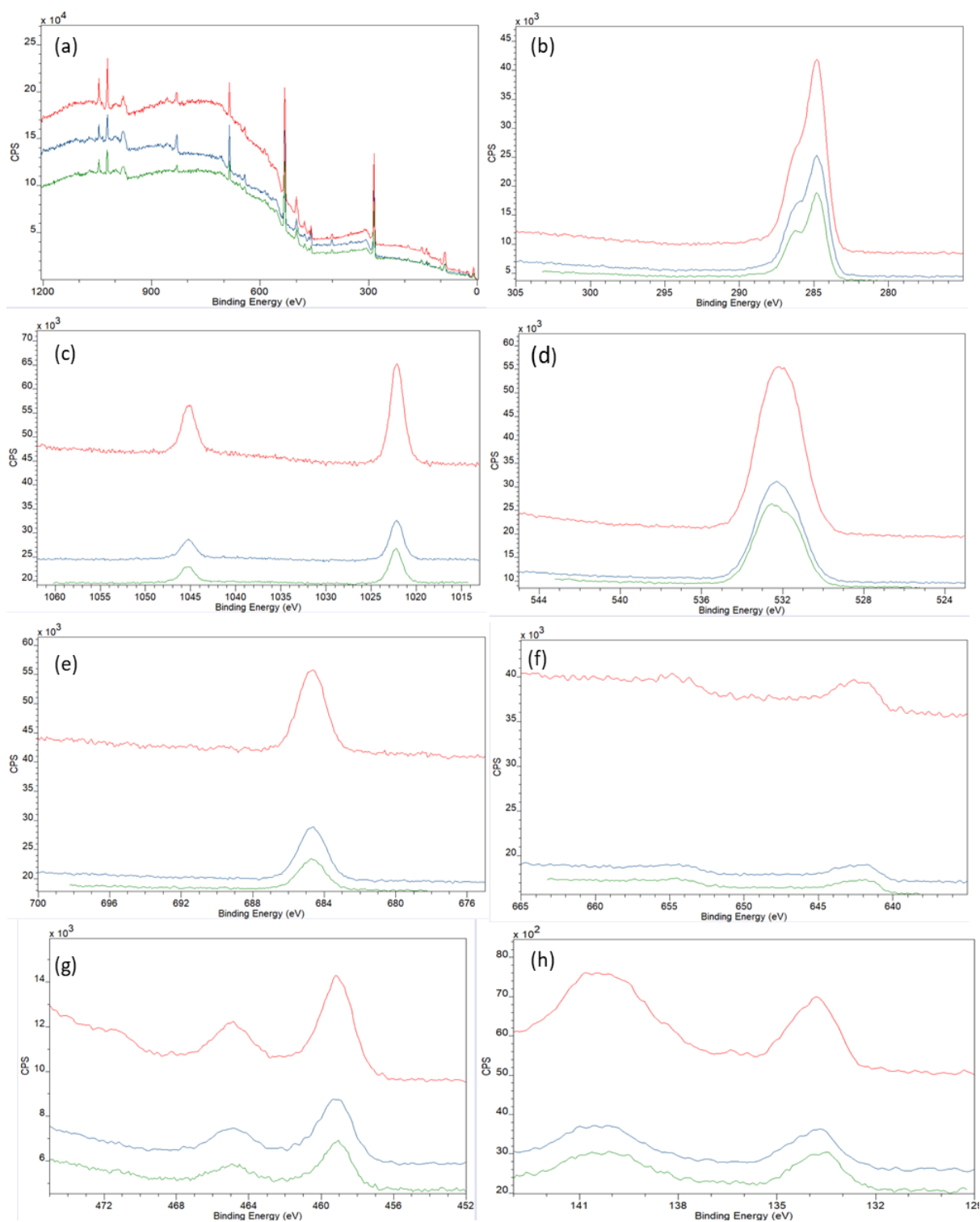
Figure 5.5 Quantifiable. X-ray photolectron spectroscopy analysis of HDG alkaline washed for 50°C, 65°C and 80°C for 30 seconds coated with one HFT application (a) wide spectral analysis (b) carbon analysis; (c) zinc analysis; (d) oxygen analysis; (e) fluorine analysis; (f) manganese analysis; (g) titanium analysis; (h) phosphorus analysis. Key; Red – 50°C, 30 seconds; green - 65°C 30 seconds; blue - 80°C 30 seconds.
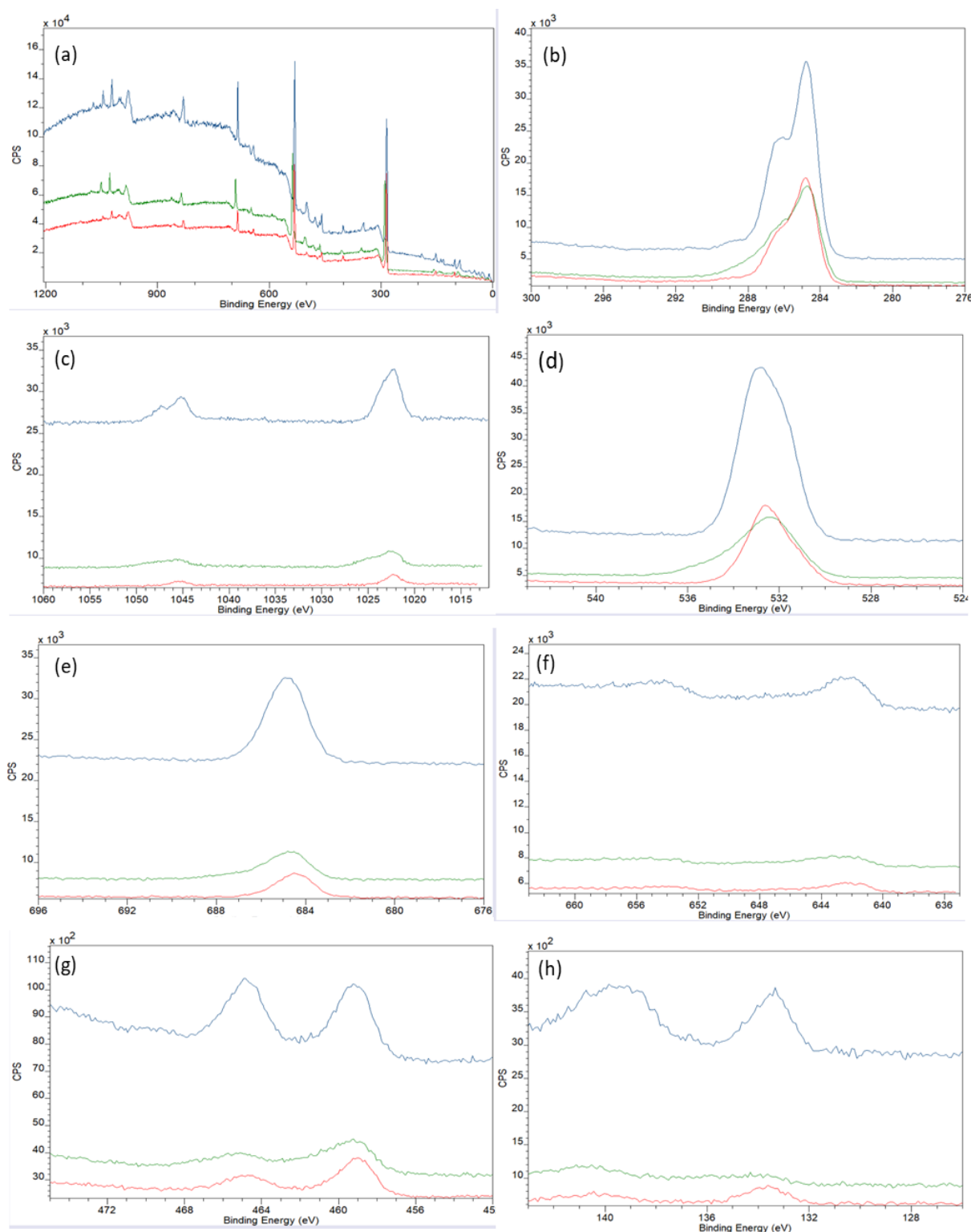
Figure 5.6. Quanifiable X-ray photolectron spectroscopy analysis of HDG alkaline washed for 50°C, 65°C and 80°C for 30 seconds coated with ten HFT applications (a) wide spectral analysis (b) carbon analysis; (c) zinc analysis; (d) oxygen analysis; (e) fluorine analysis; (f) manganese analysis; (g) titanium analysis; (h) phosphorus analysis. Key; Red – 50°C, 30 seconds; green 65°C 30 seconds; blue 80°C 30 seconds.

The XPS-derived spectra of HFT on HDG prepared with various cleaning parameters was conducted to illustrate how the surface is influenced by variation in surface conditioning and varying application of HFT. The temperature of alkaline cleaning used before HFT application appears to have little influence on the peaks generated by XPS. The amount of HFT applied also shows little influence in the peaks generated. The main C 1s peak is centred at 284.8 eV, identified as C-C, and is accompanied by two smaller peaks identified as C-O-C located at 286.82 eV and likely result from surface contamination. Zinc 2p orbital peaks generated are centred around 1022.1 eV and 1045.2 eV, with the zinc Auger peak generated at 499.6 eV. A Fluoride 1s peak is generated at 684.5 eV, indicating the presence of a metal fluoride, combined with the zinc Auger peak this is shown to be zinc fluoride. Phosphorous 2p generates a peak at 133.6 eV, and Mn 2p generates peaks centred around 642 eV, both of which illustrate the existence of manganese phosphate and manganese oxides on the surface, both of which are soluble whilst in the acidic pre-treatment solution but likely form on the surface when the layer dries on the steel surface. Although zinc phosphate also shows similar behaviour, the existence of this metal phosphate can be discounted as the zinc Auger binding energy only indicates the existence of zinc fluoride species on the surface. Oxygen 1s generates an oxide based peak at 530.9 eV and a carbon-based oxygen peak at 532.5 eV. Titanium 2p generates a peak at 458.3, indicating the presence of TiO_2. The components listed above are shown in resolved spectral form in Figure 5.7.
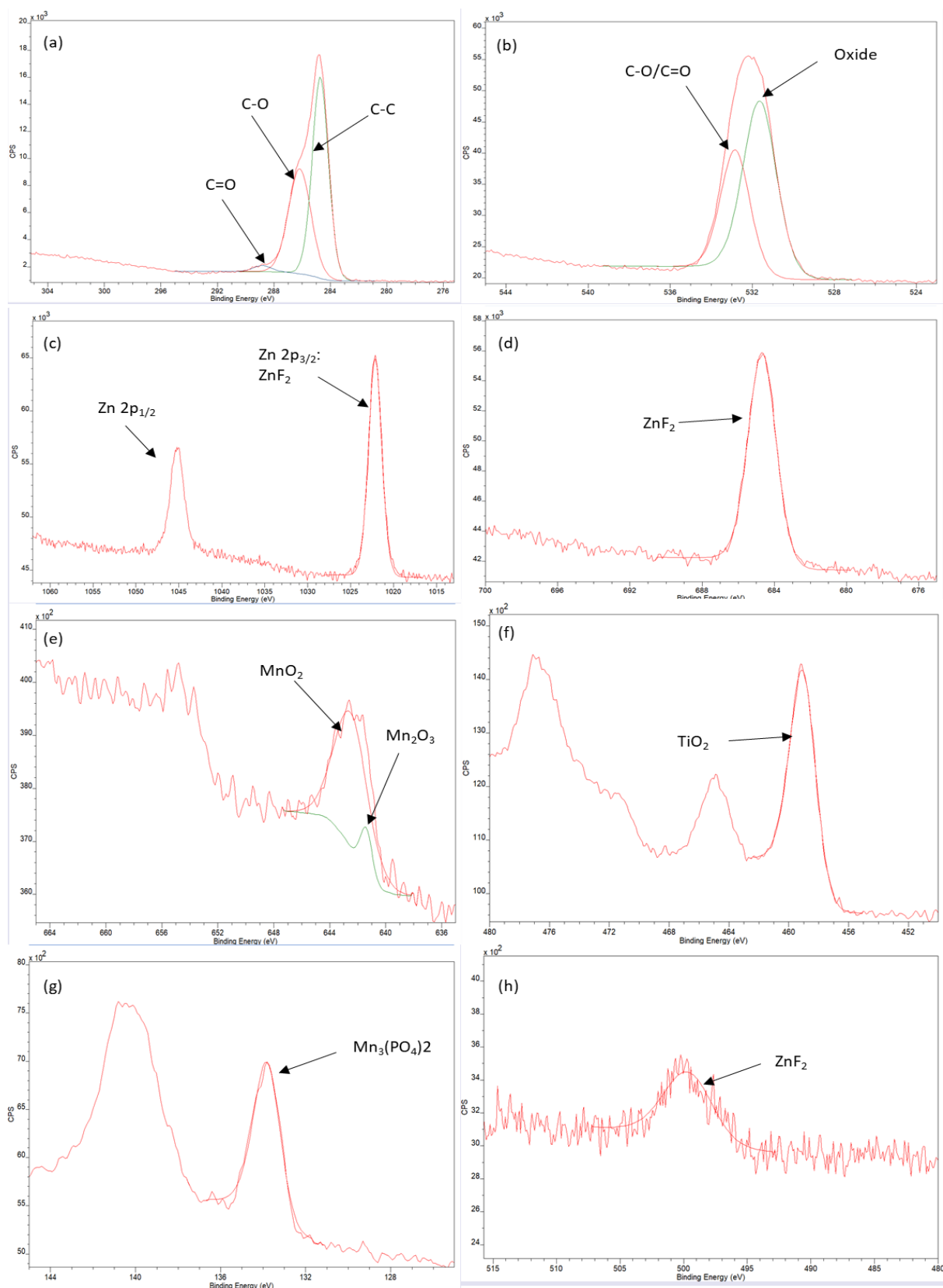
Figure 5.7. X-ray photolectron spectroscopy analysis of HDG alkaline cleaned at 80°C for varying times. (a) wide spectral analysis (b) carbon analysis; (c) zinc analysis; (d) oxygen analysis; (e) zinc Auger analysis; (f) aluminium analysis

In all cases regardless of cleaning parameters and amount of HFT applied, the element peaks produced remain close to their previously defined locations. The average atomic concentrations in percentage have also been derived from each corresponding peak and are summarised below.

Table 5.1. Elemental composition of HFT coated alkaline cleaned HDG steel.

Conditions	C (atomic %)	O (atomic %)	P (atomic %)	Mn (atomic %)	Ti (atomic %)	Zn (atomic %)	F (atomic %)
Uncleaned	39.03	36.800	/	/	/	2.94	/
50°C 30s	48.50	33.267	/	/	/	18.23	/
50°C 30s 1w	66.44	23.44	0.56	0.85	1.79	0.80	6.14
50°C 30s 10w	65.72	21.48	0.35	0.90	1.91	1.22	8.42
65°C 30s	54.59	24.945	/	/	/	20.46	/
65°C 30s 1w	70.49	19.64	0.58	0.63	1.57	0.66	6.45
65°C 30s 10w	67.26	21.73	0.45	0.83	2.11	0.69	6.93
80°C 30s	52.11	31.823	/	/	/	16.07	/
80°C 30s 1w	67.14	22.83	0.64	0.72	1.89	0.59	6.19
80°C 30s 10w	70.62	20.78	0.42	0.77	1.78	0.69	4.96
50°C 10m	51.78	31.043	/	/	/	17.17	/
50°C 10m 1w	65.30	24.61	0.37	1.03	1.60	2.60	4.49
50°C 10m 10w	67.05	23.90	0.42	1.03	2.00	1.32	4.27
65°C 10m	49.75	33.353	/	/	/	16.91	/
65°C 10m 1w	69.90	21.93	0.49	0.78	1.62	1.48	3.81
65°C 10m 10w	68.94	23.66	0.52	0.73	1.63	0.79	3.74
80°C 10m	52.72	32.497	/	/	/	14.80	/
80°C 10m 1w	67.21	22.94	0.39	1.04	1.97	1.20	5.26
80°C 10m 10w	70.20	24.00	0.92	0.56	1.20	0.60	2.52

The surface content generated by XPS analysis shows the surface is largely made up of carbon and oxygen, with the addition of manganese, phosphorus, fluorine, and zinc. The carbon content of all HFT coated HDG steel is 68.01 +/- 2.72% The oxygen content is calculated at 22.58 +/- 2.93%. The contribution to the oxygen content is largely consisting of polymeric oxygen species with concentration of 10-20% and metal oxide contribution of 1-

10%. Titanium contributes 1.75 $^{+/-}$ 2.11%, which consists entirely of TiO_2. The contribution of inhibitor species such as Mn, P, Zn and F contributes between 5.80 – 12.81 %. The LMMa peak generated for Zn is positioned at 499.2 eV which indicates all the Zn present on the surface is present as ZnF_2. Due to Zn only forming ZnF_2, it can be deduced that the only phosphate present is in the form of manganese phosphate, formed as a result of the reaction between manganese and phosphate ions, and remains on the surface due its insolubility in water. The amount of oxygen, phosphorus, manganese and titanium on the surface stays relatively constant with variation of the cleaning conditions and pre-treatment, some trends can be seen in the concentration of carbon and fluorine seen on the surface. When 1 pre-treatment wipe is applied, the carbon concentration drops or stays relatively constant when the cleaning time is increased at identical temperatures. When 10 pre-treatment wipes are applied, the carbon concentration increases when both cleaning temperature is increased for a set time, and when the cleaning time is increased at a set temperature. The fluorine concentration shows a decreasing trend at both pre-treatment wipe applications as the cleaning temperature and time is increased. The drop in fluorine concentration is more obvious when 10 wipes of HFT is applied and drops as the cleaning temperature and time is increased, the decrease in fluorine content can be attributed to fluorine degrading when an x-ray beam is applied.

5.3.1.3 Scanning Electron Microscopy and Energy Dispersive X-Ray analysis of HFT deposited on HDG.

Surface images of HDG coated with 1 wipe and 10 wipes of HFT pre-treatment using Scanning Electron Microscopy (SEM) and Energy Dispersive X-Ray (EDX) were taken to gather information of how the elements detected using XPS were dispersed across the coating surface and how the topology of the surface changes with pre-treatment addition. Seen in Figures 5.8 – 5.13 are SEM and EDX images along with EDX spectra of uncleaned and alkaline cleaned HDG steel, and alkaline cleaned steel with pre-treatment applied to the surface.
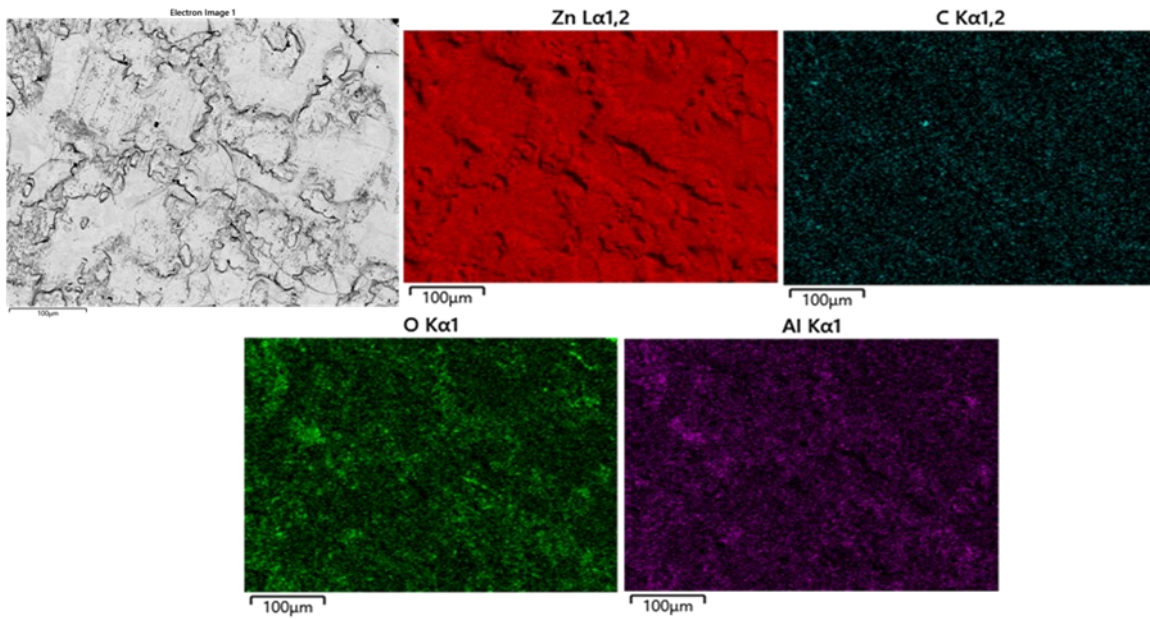
Figure 5.8. SEM image of control HDG steel and EDX maps of zinc, oxygen, carbon and aluminium.
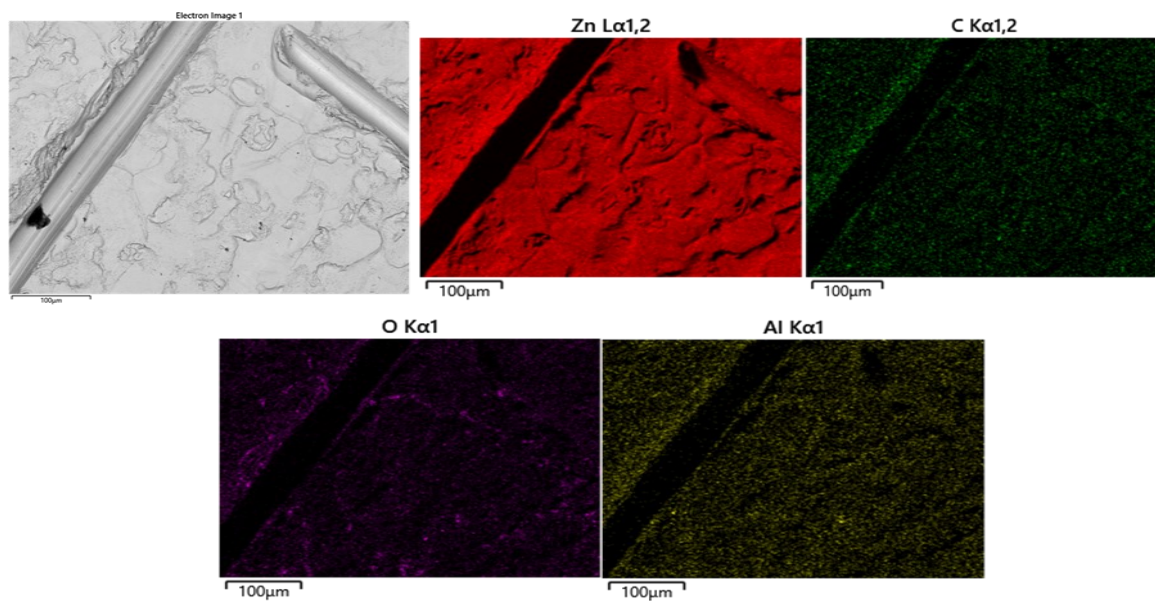
Figure 5.9. SEM image of HDG steel alkaline cleaned at 65°C for 30 seconds and EDX maps of zinc, oxygen, carbon and aluminium.
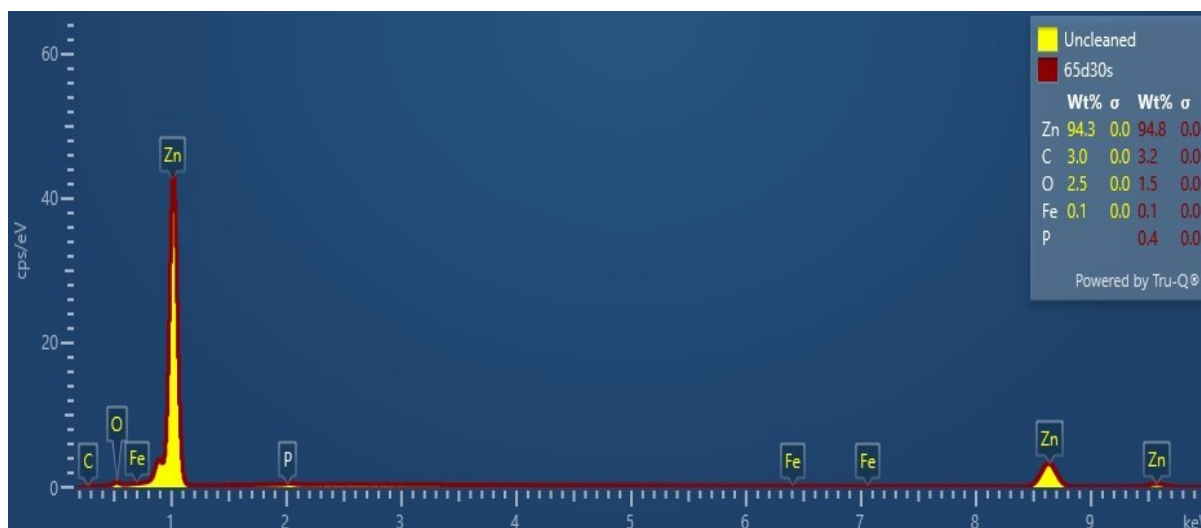
Figure 5.10. EDX spectra of uncleaned HDG steel compared to HDG steel alklaine cleaned at 65°C for 30 seconds.

EDX images of the surface of HDG steel alkaline cleaned at 65°C for 30 seconds primary consists of zinc, which produces a high intensity element map. There is also the presence of oxygen and aluminium on ths surface, likely present as residual oxide on the surface which is not detected by XPS. Carbon is also present, likey due to surface contamination.
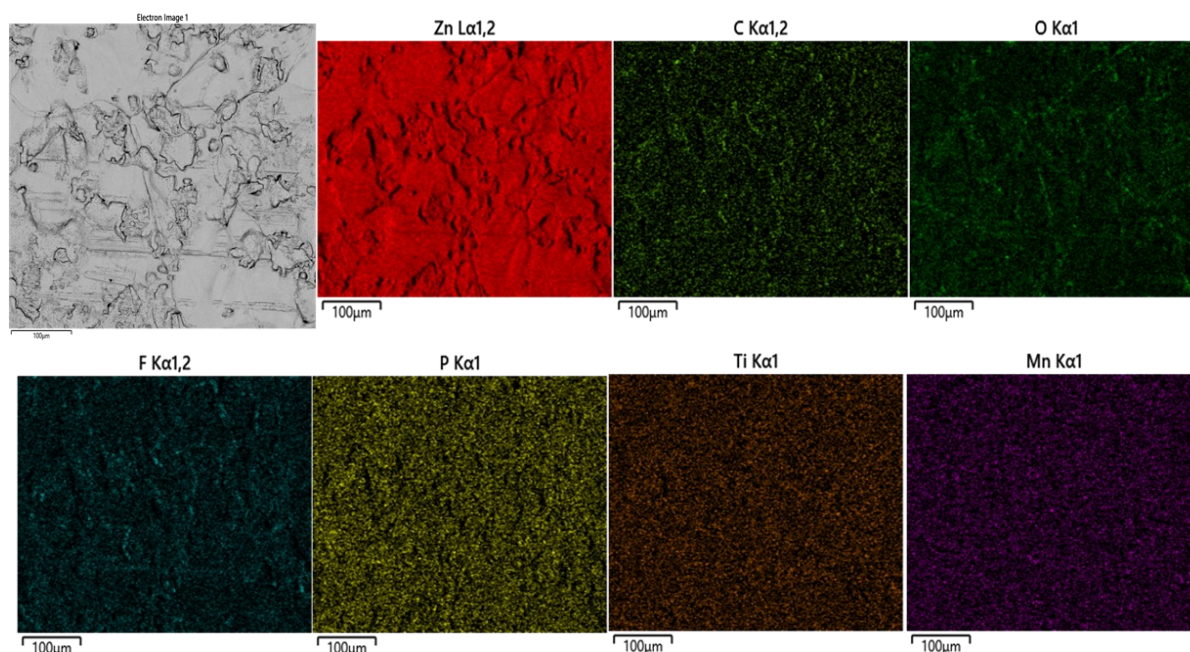
Figure 5.11. SEM image of HDG steel alkaline cleaned at 65°C for 30 seconds with 1 wipe of pre-treatment applied and EDX maps of zinc, oxygen, carbon, flourine, phosphorus, titanium, and manganese.
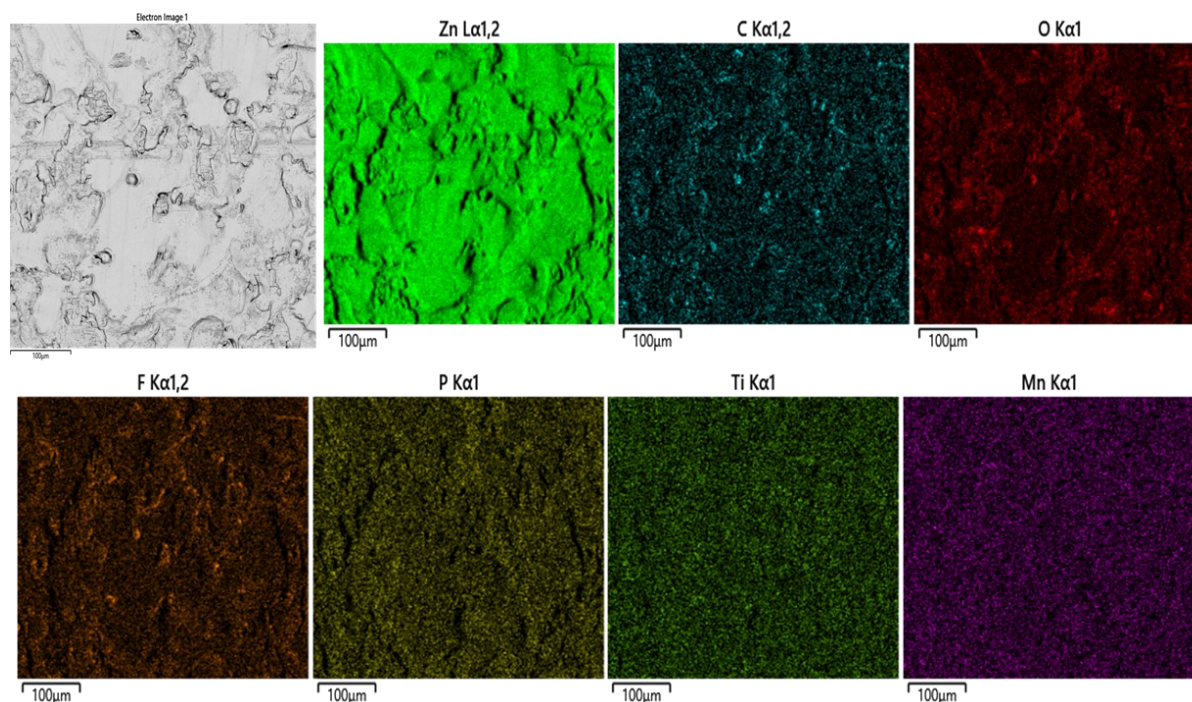
Figure 5.12. SEM image of HDG steel alkaline cleaned at 65°C for 30 seconds with 10 wipes of pre-treatment applied and EDX maps of zinc, oxygen, carbon, flourine, phosphorus, titanium, and manganese.
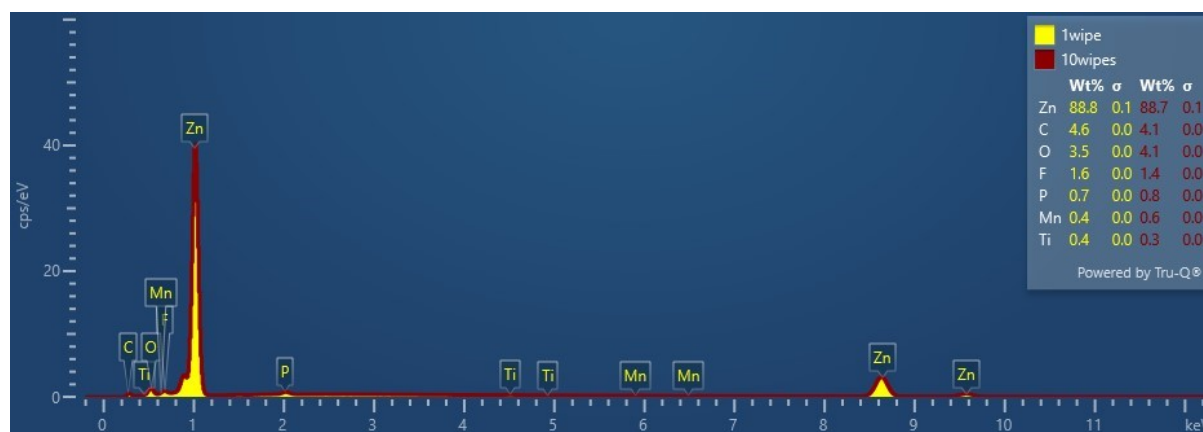
Figure 5.13. EDX spectra of alkaline cleaned HDG steel with 1 wipe of HFT and 10 wipes of HFT

When pre-treatment is applied to the surface of cleaned HDG the elements detected change, with the addition of titanium, fluorine, phosphorus, and manganese also detected on the surface which are also detected by XPS analysis. The presence of oxygen and carbon is detected due to oxide on the surface and carbon from the polymer component of the pre-treatment. Zinc appears to be heavily detected by EDX analysis, which could be partly a

contribution from zinc species on the surface, but also the detector picking up the zinc on the HDG surface through the thin pre-treatment coating.

5.3.2. Influence of Ti-based pre-treatment deposited on HDG on electrochemical response using anodic, cathodic and linear polarisation.

Polarisation experiments were performed as described in section 5.3.3 to study the influence of the presence of the thin film pre-treatment layer deposited on HDG cleaned in alkaline solution at 50°C, 65°C and 80°C for 30 seconds or 10 minutes and immersed in 5wt.% NaCl pH 7.

5.3.2.1. Anodic polarisation of Ti-based pre-treatment on HDG

Anodic Polarisation curves of alkaline cleaned HDG substrates coated with HFT were conducted to see how the influence of surface conditioning influences the metal oxidation reaction that occurs on the surface when in 5wt.% NaCl solution. The Open Circuit Potential (OCP) of samples were taken before anodic-going polarisation of the sample from the OCP to +0.5 V of the OCP. The curves have been displayed to a measured potential of -0.5V vs SHE in order to better resolve any differences between substrates immediately after polarising. Anodic polarisation curves of alkaline cleaned and HFT coated HDG substrates can been seen in Figures 5.14 - 5.16.

Figure 5.14. Anodic polarisation curve of HDG alkaline cleaned at 50°C with HFT applied in 5wt.% NaCl solution; (a) Low Ti-Wt; (b) High Ti-Wt

Figure 5.15. Anodic polarisation curve of HDG alkaline cleaned at 65°C with HFT applied in 5wt.% NaCl solution; (a) Low Ti-Wt; (b) High Ti-Wt.

Figure 5.16. Anodic polarisation curve of HDG alkaline cleaned at 80°C with HFT applied in 5wt.% NaCl solution; (a) Low Ti-Wt; (b) High Ti-Wt.

HDG steel alkaline cleaned at all temperatures show no passive region in the anodic branch, and OCP's measured around -0.81V. When HFT is applied to the surface the OCP shifts to -0.82 $^{+}/_{-}$ 0.02 V, showing a slight cathodic shift and causing a decrease in anodic current, meaning the pre-treated surface is less anodically active. After the application of HFT to the surface the anodic polarisation curves produced illustrate different behaviour, with the curves showing development of a narrow passive region which can be seen through infection of the curves. This occurs along with the increase in current being slowed slightly as the potential is shifted as opposed to bare HDG steel which shows a constant increase in the current before the current levels off. However, when this passivity is measured the passive region only covers a potential range of 100 – 150 mV which is not a significant passive effect. A

comparison of how the passive region varies as a function of cleaning parameters and the titanium weighting of the HFT application can be seen in Table 5.2.

What can be seen when all the polarisation curves are compared to each other, there is variation in the passive regions within a temperature set, but some variability between different temperatures for the same amount of time, however differences are negligible. The anodic polarisation curves generated for all pre-treated HDG substrates indicate very little difference in the anodic response when there is variation of alkaline cleaning and HFT application, however the response is different compared to HDG with no HFT.

Table 5.2. Comparison of cleaning parameters of HDG prior to HFT application, HFT Ti-weight and the anodic passive region generated.

Cleaning Parameters	HFT Ti-Weight (g/m^2)	Passive Region (ΔV)
50°C 30s	21.93 (Low-Wt)	0.11
50°C 30s	33.00 (High-Wt)	0.10
65°C 30s	24.05 (Low-Wt)	0.11
65°C 30s	35.70 (High-Wt)	0.14
80°C 30s	24.63 (Low-Wt)	0.11
80°C 30s	35.70 (High-Wt)	0.13
50°C 10m	23.75 (Low-Wt)	0.11
50°C 10m	34.95 (High-Wt)	0.11
65°C 10m	26.35 (Low-Wt)	0.10
65°C 10m	35.80 (High-Wt)	0.13
80°C 10m	23.90 (Low-Wt)	0.11
80°C 10m	36.38 (High-Wt)	0.12

5.3.2.2. Cathodic polarisation of Ti-based pre-treatment on HDG

Cathodic Polarisation curves of alkaline cleaned HDG substrates were conducted to see how the influence of surface conditioning influences the cathodic oxygen reduction reaction that occurs on the surface when in 5wt.% NaCl solution. The Open Circuit Potential (OCP) of samples were taken before cathodic-going polarisation of the sample from the OCP to -0.5 V of the OCP.
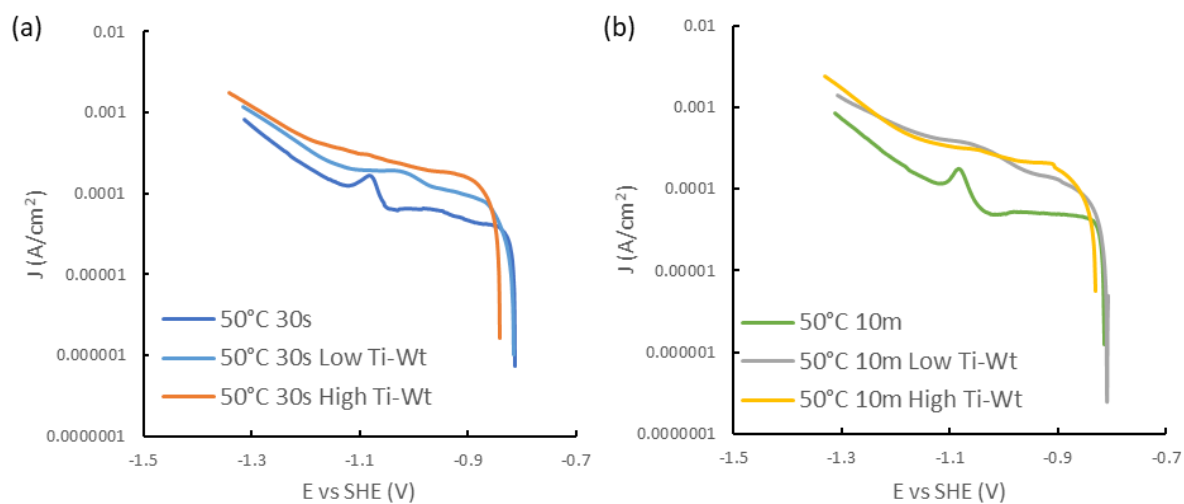
Figure 5.17. Cathodic polarisation curve of HDG alkaline cleaned at 50°C with HFT applied in 5wt.% NaCl solution; (a) Low Ti-Wt; (b) High Ti-Wt
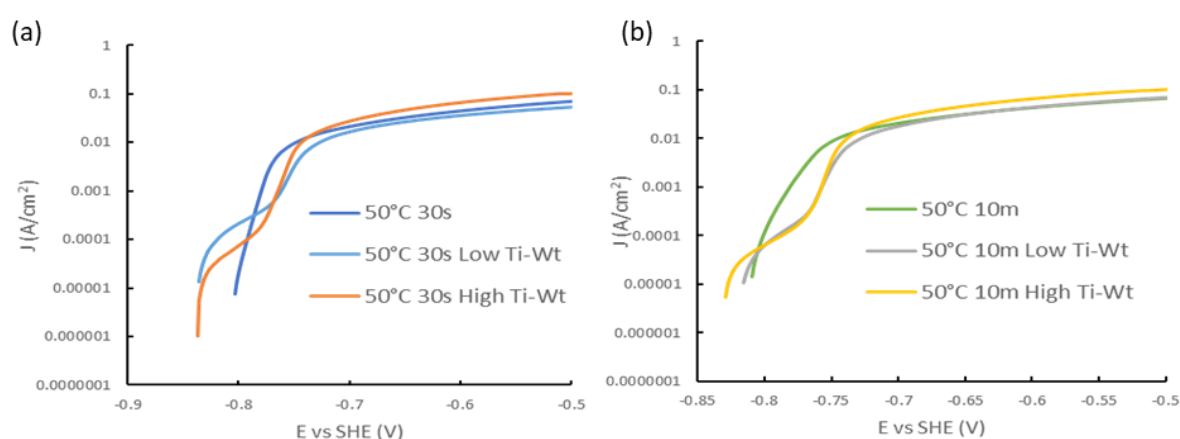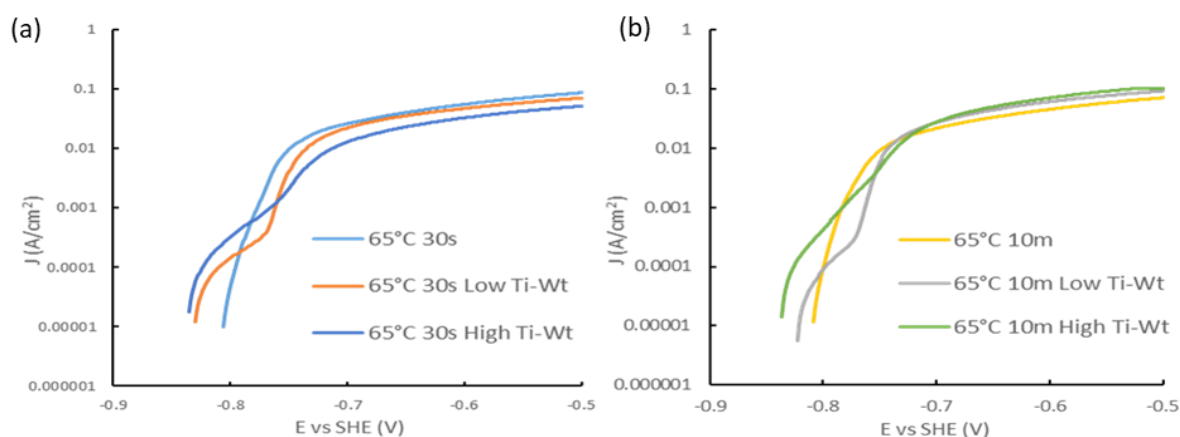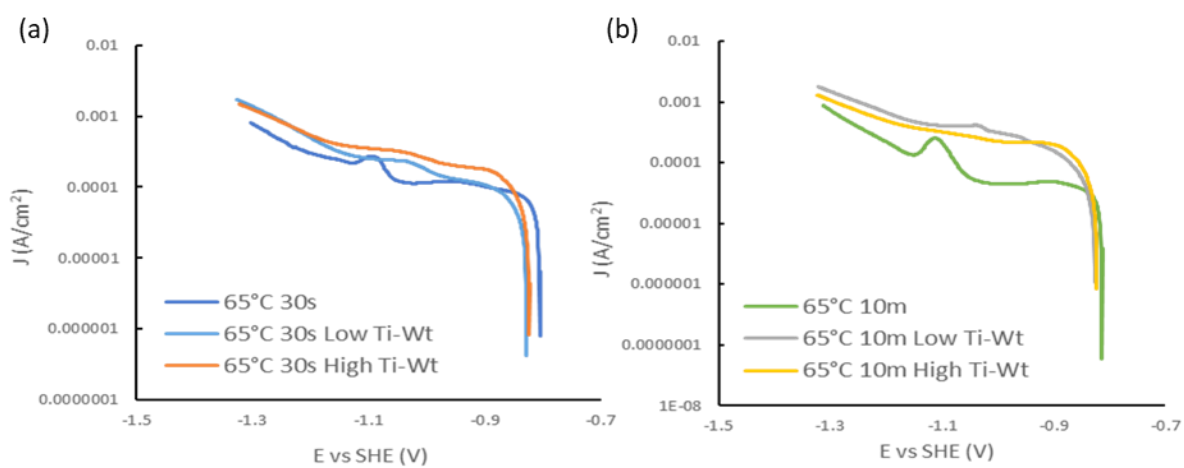

Figure 5.18. Cathodic polarisation curve of HDG alkaline cleaned at 65°C with HFT applied in 5wt.% NaCl solution; (a) Low Ti-Wt; (b) High Ti-Wt
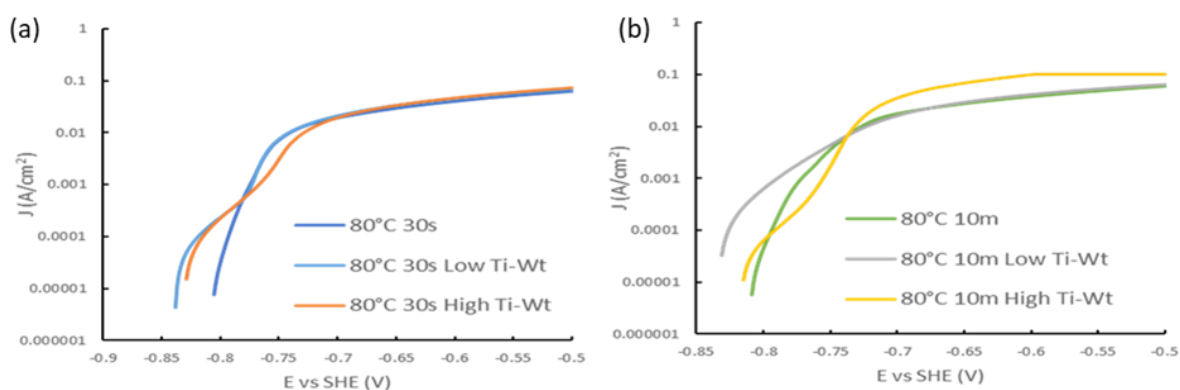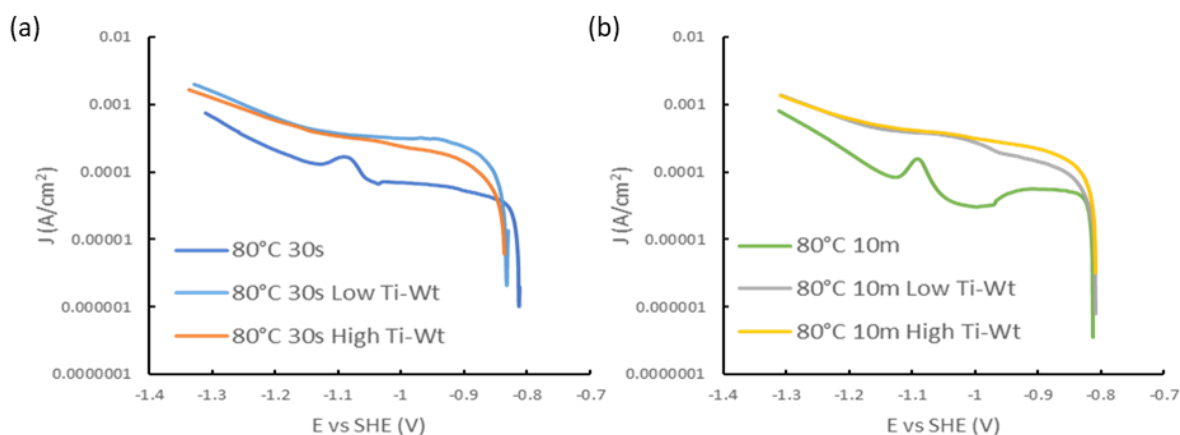
Figure 5.19. Cathodic polarisation curve of HDG alkaline cleaned at 80°C with HFT applied in 5wt.% NaCl solution; (a) Low Ti-Wt; (b) High Ti-Wt

What can be noted from Figures 5.17– 5.19 is that application of HFT results in the suppression of the secondary cathodic reduction that occurs on HDG with identical cleaning parameters. HFT application also shifts the OCP to more cathodic potentials much like that seen in the anodic branch, and also influences the oxygen reduction reaction that occurs at more positive potentials. The initial change in current for alkaline cleaned and pre-treated HDG can be seen in Figure 5.20. What can be seen is that pre-treated surfaces have a higher initial current spike compared to uncoated HDG, with high titanium weight coatings showing a greater increase than low titanium weight coatings, with the exception of samples cleaned at 50°C for 10 minutes, however pre-treated samples cleaned at this condition show similar current increases.
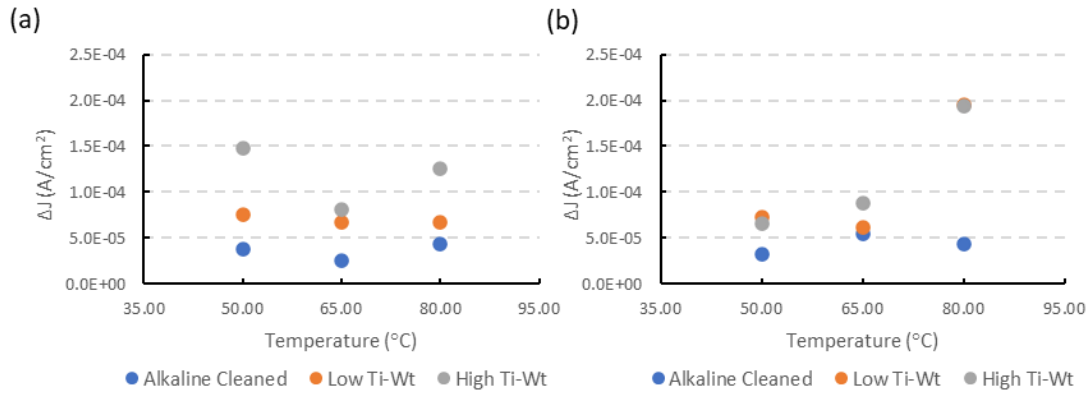
Figure 5.20. Measured change in current density of oxygen reduction reaction when cathodically polarised and OCP of HFT coated HDG cleaned for 30 seconds at varying temperatures; (a) Measured currents of surfaces cleaned for 30 seconds; (b) Measured current of surfaces cleaned for 10 minutes.

The current at two different potentials after this initial current spike was also measured, with currents measured at -0.9V and -1.2V, shown in Figures 5.18 and 5.19. Much like the trend shown in Figure 5.17, the presence of a titania layer shows increased measured currents at the two different potentials, with the current differences more distinct at -1.2V. At 0.9V pre-treated surfaces typically show increased currents but are similar to currents measured for uncoated HDG surfaces, when the current is measured at -1.2V, the measured currents become greater. The cleaning parameters used before application of HFT does not appear to have a great influence on the measured current, with the differences in the current measured in the region of ~100 mA.
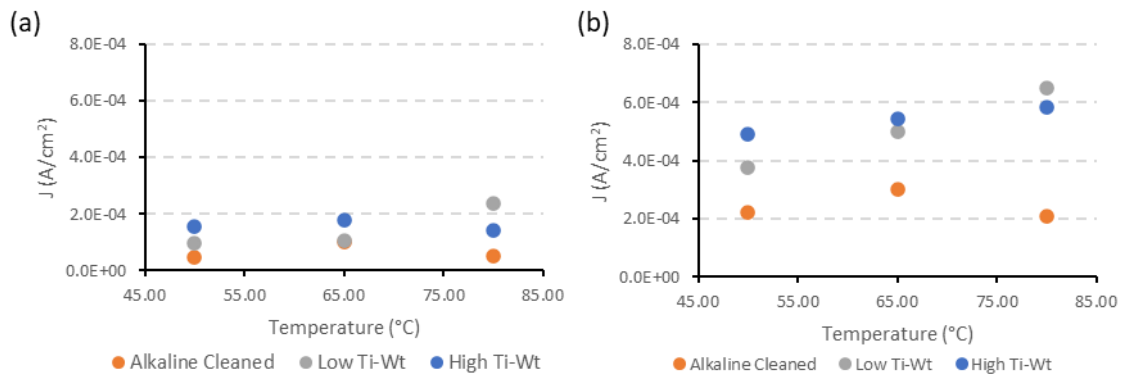
Figure 5.21. Measured current changes at -0.9V and -1.2V of HDG alkaline cleaned for 30 seconds in the presence and absence of HFT; (a) Measured currents at -0.9V; (b) Measured currents at -1.2V.
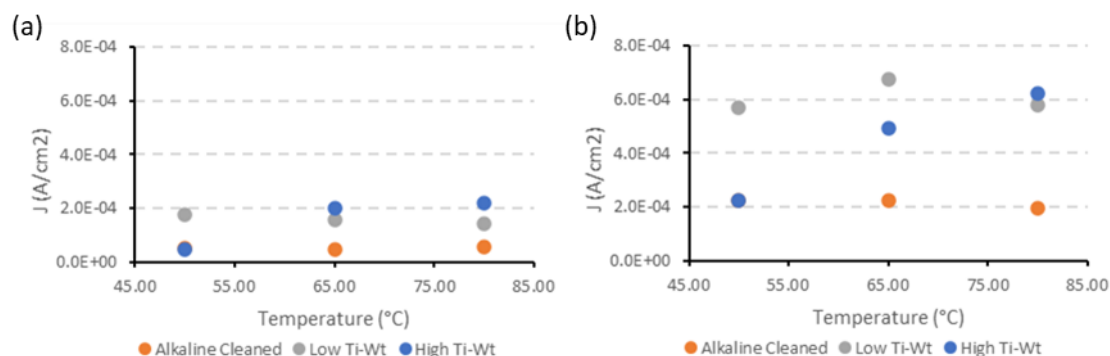
Figure 5.22. Measured current changes at -0.9V HDG alkaline cleaned for 10 minutes in the presence and absence of HFT. (a) Low Ti-Wt; (b) High Ti-Wt.

What can be seen from the comparison of HFT coated HDG steel and uncoated HDG is the greater increase in the current and the higher currents achieved when HDG is coated with HFT. This would indicate that the pre-treated surface is a more active oxygen cathode and rapidly depletes the oxygen at the surface. The initial increase in current is measured as between 0.06 – 0.19 mA compared to the uncoated HDG showing initial current changes of 0.00 – 0.05 mA. The addition of HFT also suppresses the secondary increase in the current that occurs in uncoated HDG steel. As mentioned in Chapter 3, this initial increase in the current is due there being an abundance of oxygen available at the surface, and the larger current increases that occur in HFT in the initial stages of polarisation would indicate suppression of the cathodic oxygen reduction reaction. The suppression of the additional reduction reaction also indicates that only a 2-electron reduction reaction occurs on HFT coated steel and the HFT prevents further reduction reactions from occurring. [7, 8, 9]

Compared to how untreated HDG steel reacts under cathodic conditions (more intense cleans occur at more cathodic potentials), HDG steel coated with HFT has no trend in where the OCP lies, with all reactions starting at -0.82 +/- 0.02 V. When the cleaning intensity is increased before HFT is applied, and when additional HFT is applied to the surface, the cathodic disbondment is suppressed to greater extents. This is likely due to the cleaning regime removing increasing amounts of surface oxide which allows better adhesion of the HFT to the surface, which suppresses the corrosion reactions on the surface.

5.3.2.3. Linear polarisation of Ti-based pre-treatment on HDG

Like in Chapters 3 and 4, linear polarisation of HFT coated HDG was conducted to see how the influence of surface conditioning influences the metal oxidation and oxygen reduction reactions that occurs on the surface when in 5wt.% NaCl solution. The experimental parameters were the same as the preceding chapters. Linear polarisation curves of HDG cleaned at 65°C for 30 seconds and 10 minutes with 1 or 10 HFT applications can be seen in Figures 5.23 and 5.24.
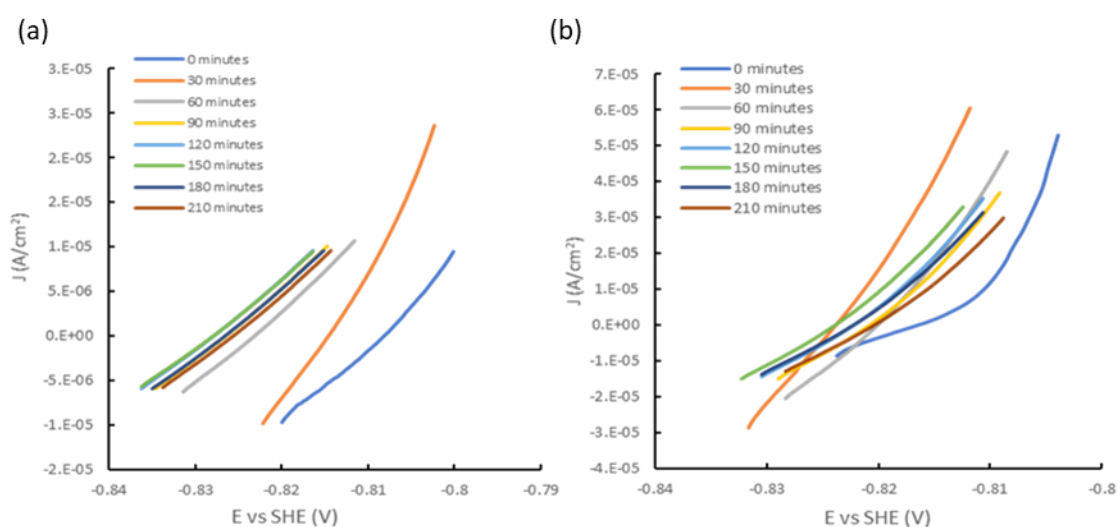
Figure 5.23. Linear Polarisation curved of HDG alkaline cleaned at 65°C for 30 seconds with; (a) Low Ti-Wt; (b) High Ti-Wt. Polarisation was conducted every 30 minutes for 210 minutes.
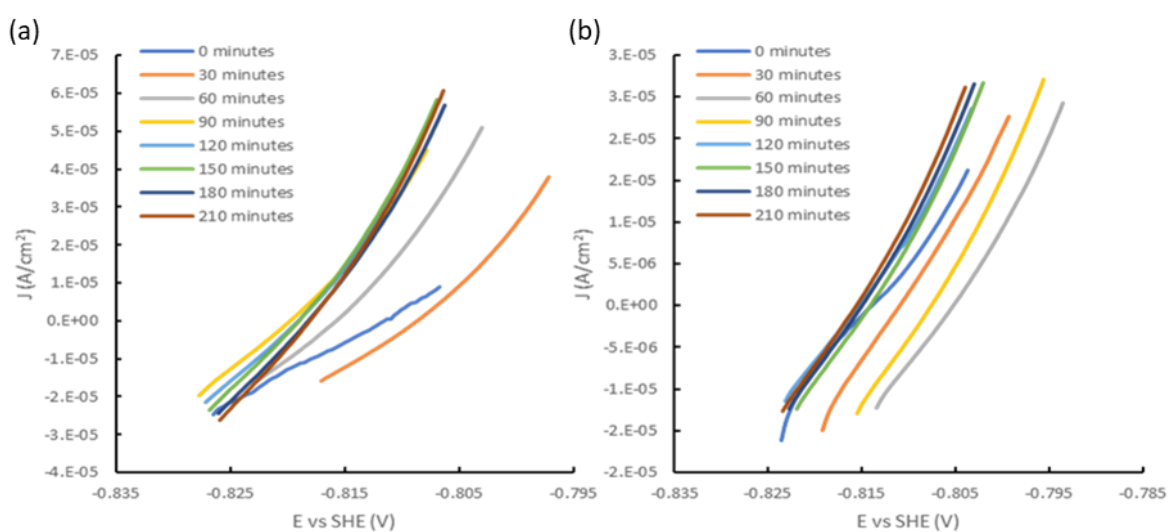
Figure 5.24. Linear Polarisation curved of HDG alkaline cleaned at 65°C for 10 minutes with; (a) Low Ti-Wt; (b) High Ti-Wt. Polarisation was conducted every 30 minutes for 210 minutes.

Polarisation curves show that as the time immersed in 5% NaCl increases, the OCP and subsequent linear polarisation curves shift initially shift to more anodic potentials for the first 30-90 minutes, before shifting to more cathodic potentials and stabilising. From the linear polarisation curves, the polarisation resistance of the HFT coated surface can be calculated by measuring the change in current density and potential. Table 5.3 and Figure 5.25 show the change in polarisation resistance over time for HFT applied on HDG which had been alkaline cleaned for 30 seconds, and Table 5.4 and Figure 5.26 shows the change in polarisation resistance over time for HFT applied on HDG which had been alkaline cleaned for 10 minutes.

Table 5.3. Polarisation resistance of HFT applied on HDG alkaline cleaned for 30 seconds at varying temperatures.

Time (minutes)	50°C 30s Low Ti-Wt (Ω)	50°C 30s High Ti-Wt (Ω)	65°C 30s Low Ti-Wt (Ω)	65°C 30s High Ti-Wt (Ω)	80°C 30s Low Ti-Wt (Ω)	80°C 30s High Ti-Wt (Ω)
0	322	445	1096	1035	1312	1561
30	222	667	757	592	1312	1216
60	287	840	721	1170	1172	1164
90	381	882	657	1239	842	1219
120	397	872	605	1282	760	1218
150	411	842	542	1304	825	1115
180	437	793	546	1280	921	950
210	450	750	498	1262	797	789
Average	364	761	678	1146	993	1154

(a)

(b)

● 50°C 30s Low Ti-Wt ● 65°C 30s Low Ti-Wt ● 80°C 30s Low Ti-Wt   ● 50°C 30s High Ti-Wt ● 65°C 30s High Ti-Wt ● 80°C 30s High Ti-Wt
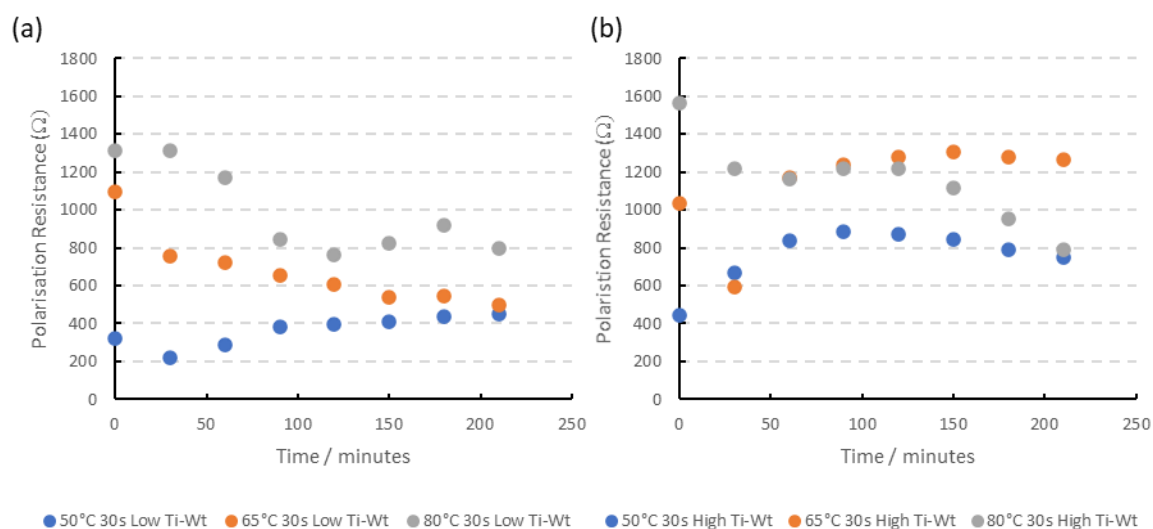
Figure 5.25 Polarisation resistance of HFT applied on HDG alkaline cleaned for 30 seconds at varying temperatures; (a) Low Ti-Wt; (b) high Ti-Wt.

Table 5.4. Polarisation resistance of HFT applied on HDG alkaline cleaned for 10 minutes at varying temperatures

Time (minutes)	50°C 10m Low Ti-Wt (Ω)	50°C 10m High Ti-Wt (Ω)	65°C 10m Low Ti-Wt (Ω)	65°C 10m High Ti-Wt (Ω)	80°C 10m Low Ti-Wt (Ω)	80°C 10m High Ti-Wt (Ω)
0	337	484	587	613	351	1052
30	288	420	370	527	499	500
60	473	370	294	542	672	315
90	556	412	305	495	615	319
120	629	446	259	564	518	411
150	700	646	243	508	479	350
180	735	675	244	509	455	364
210	745	632	219	490	434	336
Average	558	511	315	531	503	456
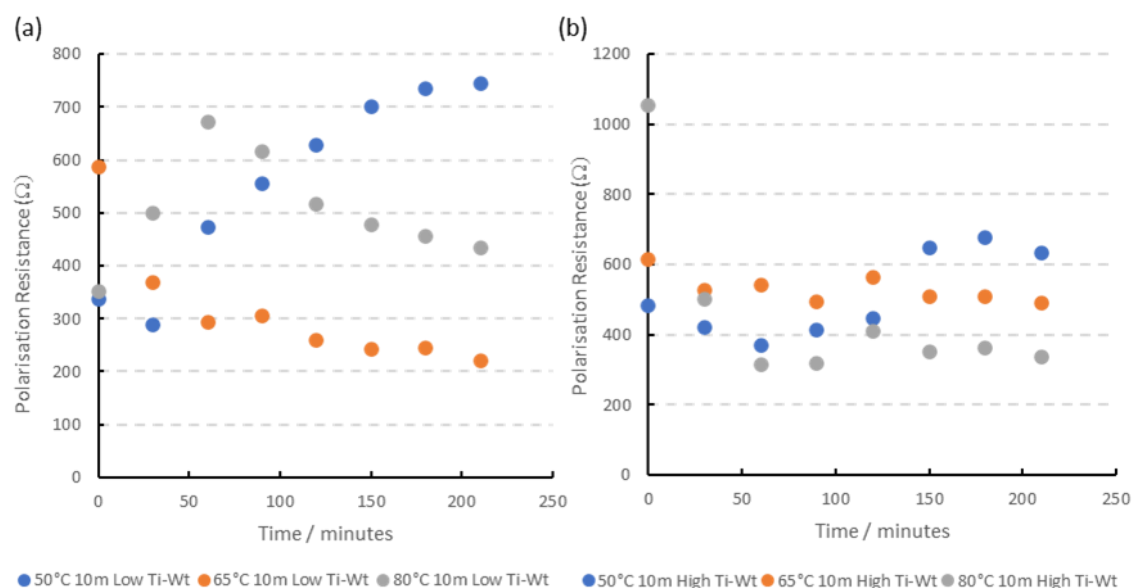
Figure 5.26. Polarisation resistance of HFT applied on HDG alkaline cleaned for 10 minutes at varying temperature; (a) Low Ti-Wt; (b) high Ti-Wt.

When cleaned for 30 seconds and 10 minutes at all temperatures, the polarisation resistance of coated HDG shows R_{pol} values 2-5 times greater than without HFT. At 30 second cleaning time increasing the amount of HFT also shows an increase in the average R_{pol} values shown and values tend to be reasonably stable over the immersion period whereas at 10 minutes additional pre-treatment shows variable R_{pol} values.

From the linear polarisation curves and the acquired polarisation resistances, along with the anodic and cathodic Tafel constants derived from the anodic and cathodic polarisation scans the I_{corr} can be calculated through the Stern-Geary equation. This then allows calculation of the corrosion rate using Faraday's corrosion equation, which are shown in Chapter 3.

Table 5.5 Tafel coefficients, I_{corr} and corrosion rate values for alkaline cleaned HDG steel with HFT coating applied.

Sample	Bc (V/decade)	Ba (V/decade)	I_{corr} (A/cm^2)	Corrosion rate (μm/year)
50°C 30s Low-Ti	0.00017	0.1795	2.01×10^{-6}	30.11
50°C 30s High-Ti	0.00025	0.2179	1.41×10^{-6}	21.11
65°C 30s Low-Ti	0.0026	0.2345	1.64×10^{-6}	24.67
65°C 30s High-Ti	0.0022	0.1879	8.23×10^{-7}	12.35
80°C 30s Low-Ti	0.0028	0.2341	1.20×10^{-7}	18.13
80°C 30s High-Ti	0.0025	0.2468	9.30×10^{-7}	13.95
50°C 10m Low-Ti	0.0023	0.2349	1.47×10^{-8}	26.58
50°C 10m High-Ti	0.0032	0.1987	1.27×10^{-8}	40.14
65°C 10m Low-Ti	0.0027	0.2236	2.59×10^{-8}	55.09
65°C 10m High-Ti	0.0018	0.2346	1.04×10^{-8}	21.89
80°C 10m Low-Ti	0.002	0.2133	1.47×10^{-8}	25.66
80°C 10m High-Ti	0.0019	0.2315	1.03×10^{-8}	26.91

How the corrosion resistance of alkaline cleaned and pre-treated surfaces compare, with surface cleaning time set at 30 seconds can be seen in Figure 5.24. There is an obvious decrease in the corrosion rate when pre-treatment is present on the surface with the corrosion rate being calculated between 13.95 – 55.09 μm/year.
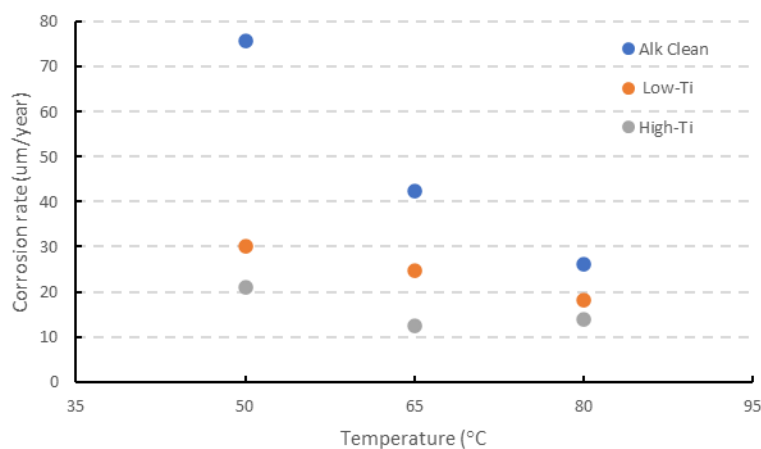
Figure 5.27. Corrosion rates of alkaline cleaned and pre-treated HDG at varying temperatures, with a surface cleaning time of 30 seconds.

The corrosion rate of HFT coated HDG decreases when the Ti-Wt increases. As Ti-XRF shows there is an ~11 g/m^2 increase in the Ti-Wt when the amount of HFT increases from 1 wipe to 10 wipe with this increase in Ti-Wt resulting in a 1.35-2.5 times decrease in corrosion rate. What is most noticeable is the large decrease in the corrosion rate when alkaline cleaning increases from 30 seconds to 10 minutes, with HFT coated samples showing up to 139 times lower corrosion resistance when the HDG is cleaned for 10 minutes compared to samples cleaned for 30 seconds prior to HFT application.

5.3.3. Investigation of corrosion driven cathodic disbondment kinetics using time-lapse photography and Scanning Kelvin Probe

Time-lapse photography and Scanning Kelvin Probe (SKP) were used to investigate the kinetics of corrosion driven cathodic disbondment of polyvinyl-butyral coatings applied to alkaline cleaned and pre-treated HDG steel substrates. Stratmann cells were created to create a defect region to allow for the initiation of cathodic disbondment and samples were exposed to a 95% relative humidity atmosphere and disbondment was initiated using 5% wt.v sodium chloride solution. Time-lapse images were taken every hour for 120 hours and SKP potentials were measured every hour for 24 hours and the kinetics of coating failure was analysed.

5.3.3.1. Use of time-lapse photography to analyse kinetics of corrosion driven cathodic disbondment

The delamination rate, initiation time and delamination distance of failed PVB coatings were calculated from measuring the distance covered by coating failure over 120 hours. The influence of variation in the time and temperature of alkaline cleaning of HDG steel and the application of one or ten applications, denoted low Ti-Wt and high Ti-Wt, on the performance of PVB coatings can be seen below. Measurement of the delamination front was the same as shown in previous chapters can be seen in Figure 5.25 with time-lapse images of delamination of the PVB coating on top of pre-treated HDG substrates can be seen in Figure 5.26.
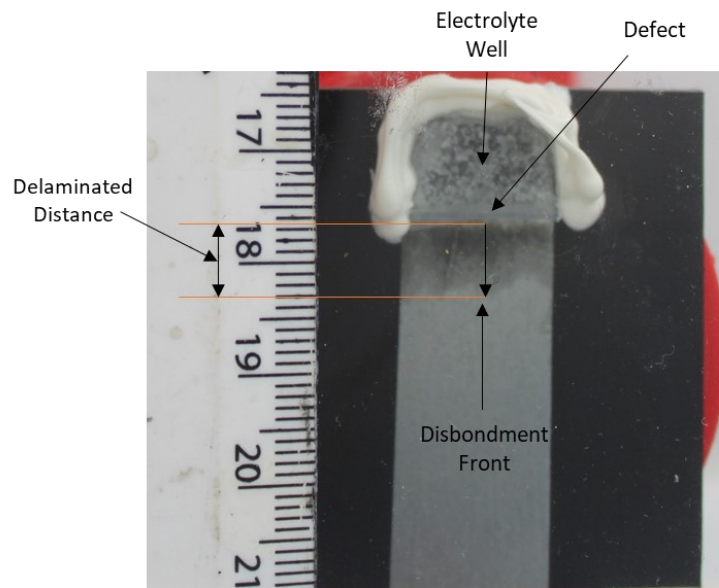
Figure 5.28. A Stratmann cell set up used in timelapse and SKP studies.
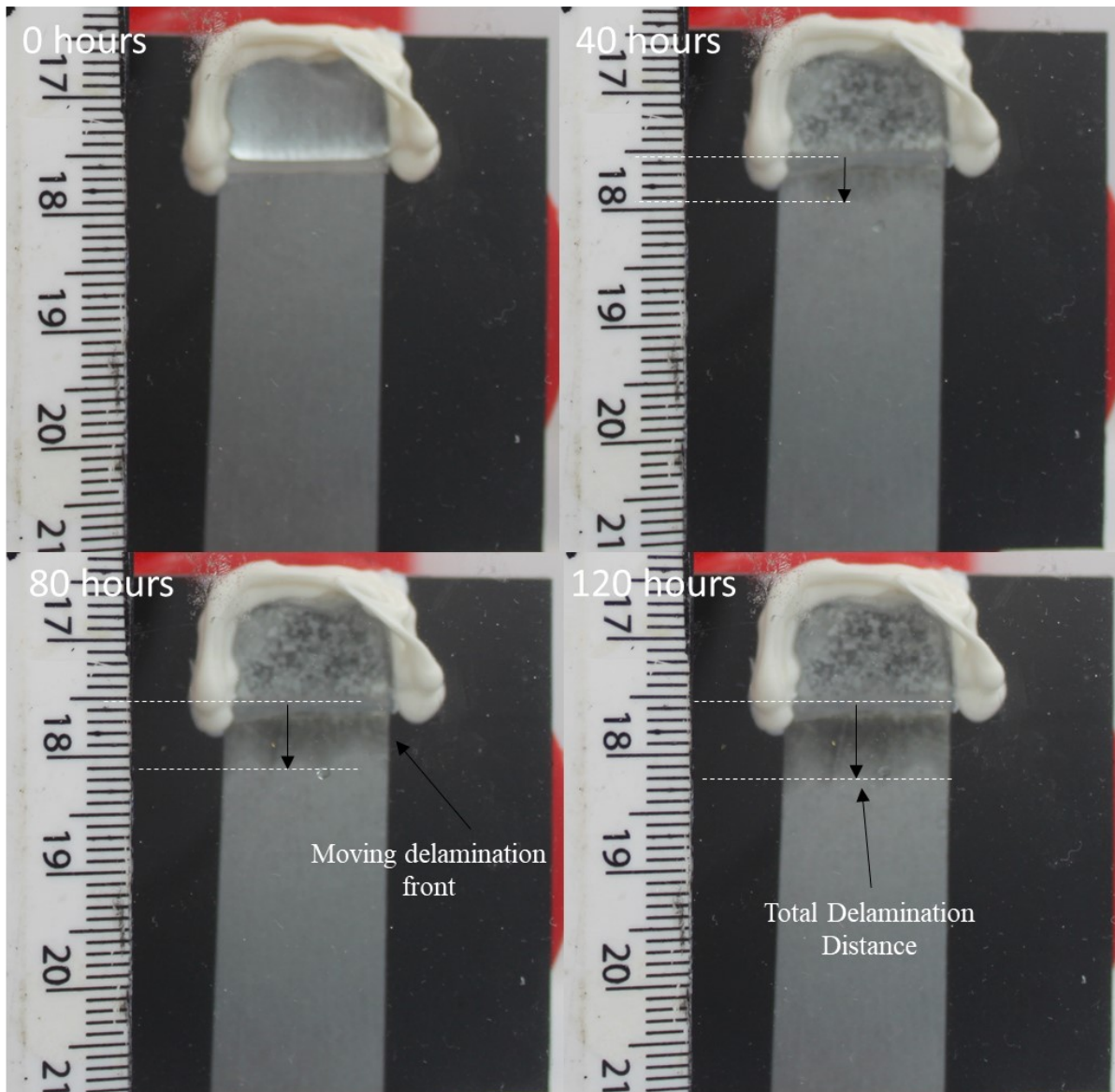
Figure 5.29. Time-lapse images of HDG steel cleaned at 80°C for 30 seconds, coated with 1 pre-treatment wipe application and PVB undergoing delamination..

What can be seen from the time-lapse images above is in the case of HDG steel cleaned for 30 seconds with 1 pre-treatment application, delamination does occur over the 120 hour time period even when pre-treatment is applied to the steel surface before PVB is applied to the surface. How delamination various as a function of cleaning time and temperature, and the number of pre-treatment applications can be seen in Figures 5.27 and 5.28 and a comparison of how pre-treatment influences the delamination of PVB compared to uncoated HDG is seen in Figure 5.29.
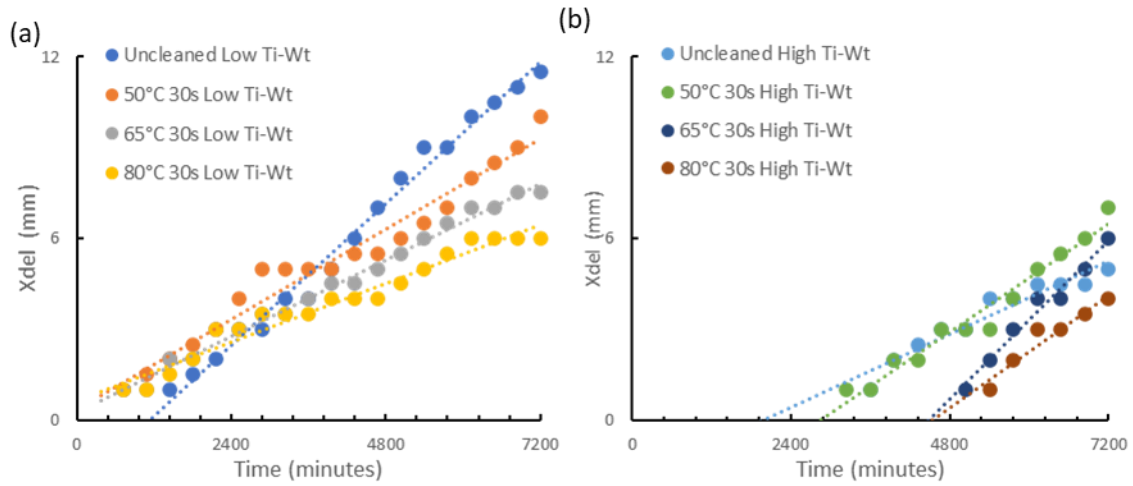
Figure 5.30 Delamination distance versus time plots obtained for HFT and PVB coated-HDG steel which had previously been alkaline cleaned at for 30 seconds at varying temperatures; (a) Low Ti-Wt; (b) High Ti-Wt

Figure 5.31 Delamination distance versus time plots obtained for HFT and PVB coated-HDG steel which had previously been alkaline cleaned at for 10 minutes at varying temperature; (a) Low Ti-Wt; (b) High Ti-Wt
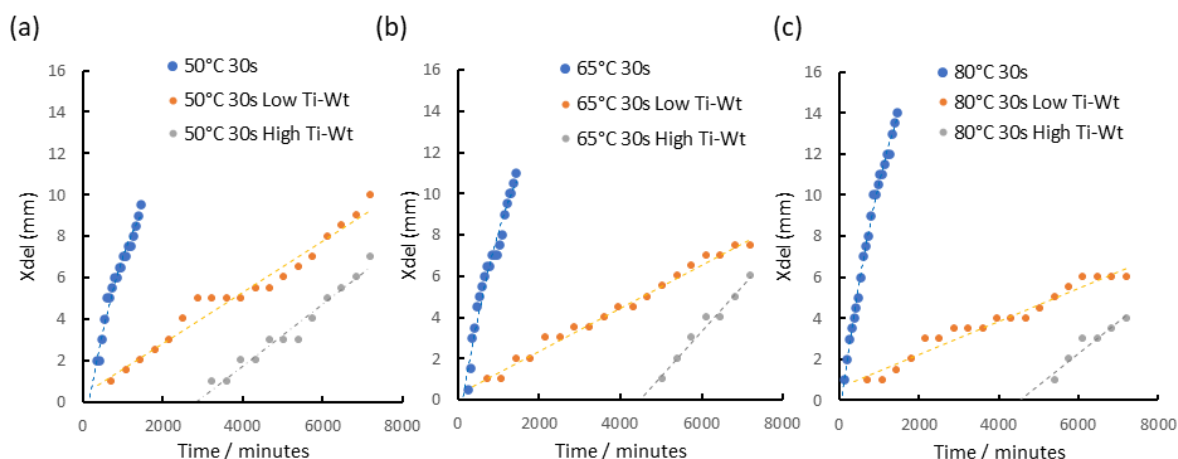
Figure 5.32. Delamination distance versus time plots obtained for HFT and PVB coated-HDG steel which had previously been alkaline cleaned at for varying temperatures for 30 seconds; (a) 50°C, 30 seconds; (b) 65°C, 30 seconds; (c) 80°C, 30 seconds.

It can be seen through measurement of the cathodic disbondment under time-lapse conditions is that increasing the amount of HFT applied to the surface delays the onset of cathodic disbondment and the distance coating failure travels, for example samples washed for 30 seconds with 1 HFT application take between 720 – 1440 minutes to undergo delamination, compared to 3240 – 5400 minutes with 10 HFT applications. What can also be noted is the influence cleaning has on the barrier protection HFT provides. When HDG is cleaned for 10 minutes, time taken for delamination to initiate was measured between 1440 – 2160 minutes for 1 HFT application, and 3240 – 3600 minutes for 10 HFT applications. Although initiation time is increased when there is less HFT on the surface, initiation time is identical (or decreased) with more HFT on the surface (when same temperature and HFT conditions are equal). What cleaning does is decrease the delamination distance that occurs. There is a decrease in the maximum delamination distance when (i) cleaning temperature is increased, and (ii) cleaning time is increased indicating the increased removal of the surface oxide provides a better surface for improved adherence of the pre-treatment layer.

The determination of the rate kinetics of pre-treated HDG was calculated by plotting the delamination distance against the square root of time and gives an indication of how cleaning and amount of HFT applied can influence the delamination kinetics. Figures 5.30 and 5.31 show the delamination kinetics of samples cleaned for 30 seconds and 10 minutes respectively, at the various chosen temperatures, with varying amounts of HFT applied to the surface. What can be seen through the kinetics plot is all samples regardless of cleaning

conditions and HFT application show linear delamination kinetics. This would indicate that the application of HFT on the surface slows the electrochemical reactions that typically occur on the surface, so the electron transfer that occurs between anodic and cathodic sites at the delamination front.
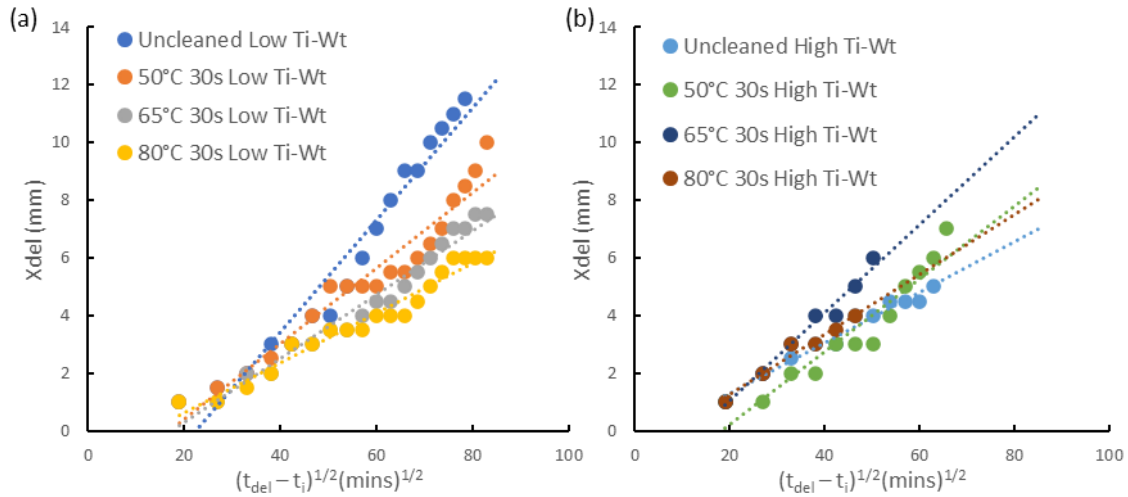
Figure 5.33. Plot of Xdel vs $(t_{del} - t_i)^{1/2}(mins)^{1/2}$ for HFT and PVB coated HDG which had been alkaline cleaned for 30 seconds at varying temperatures; (a) Low Ti-Wt; (b) High Ti-Wt
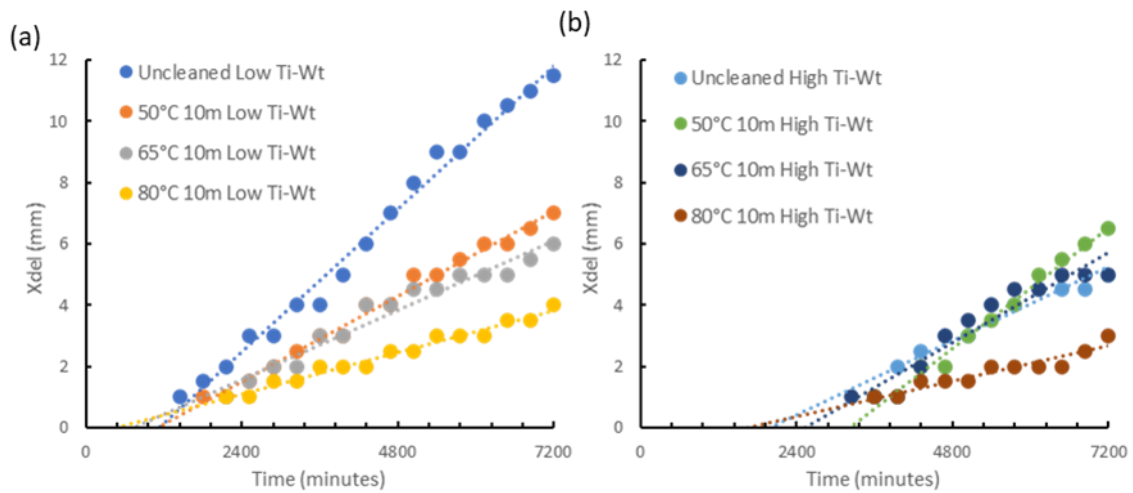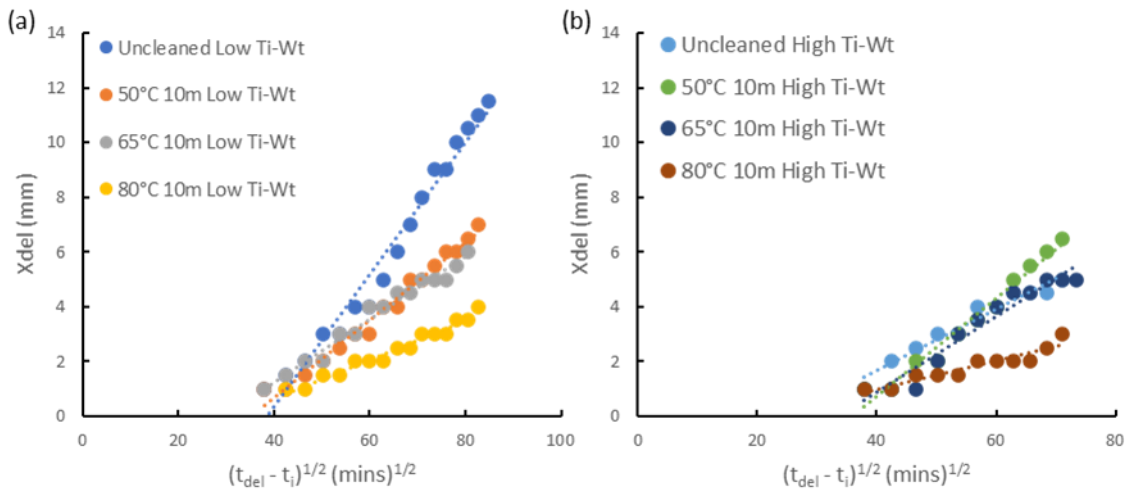

Figure 5.34. Plot of Xdel vs $(t_{del} - t_i)^{1/2}(mins)^{1/2}$ for HFT and PVB coated HDG steel which had been alkaline cleaned for 10 minutes at varying temperatures; (a) Low Ti-Wt; (b) High Ti-Wt

A comparison of how variation of time and temperature of the alkaline wash influences the final delamination distance achieved after 120 hours for pre-treated substrates compared to alkaline cleaned HDG after 24 hours can be seen in Figure 5.32.
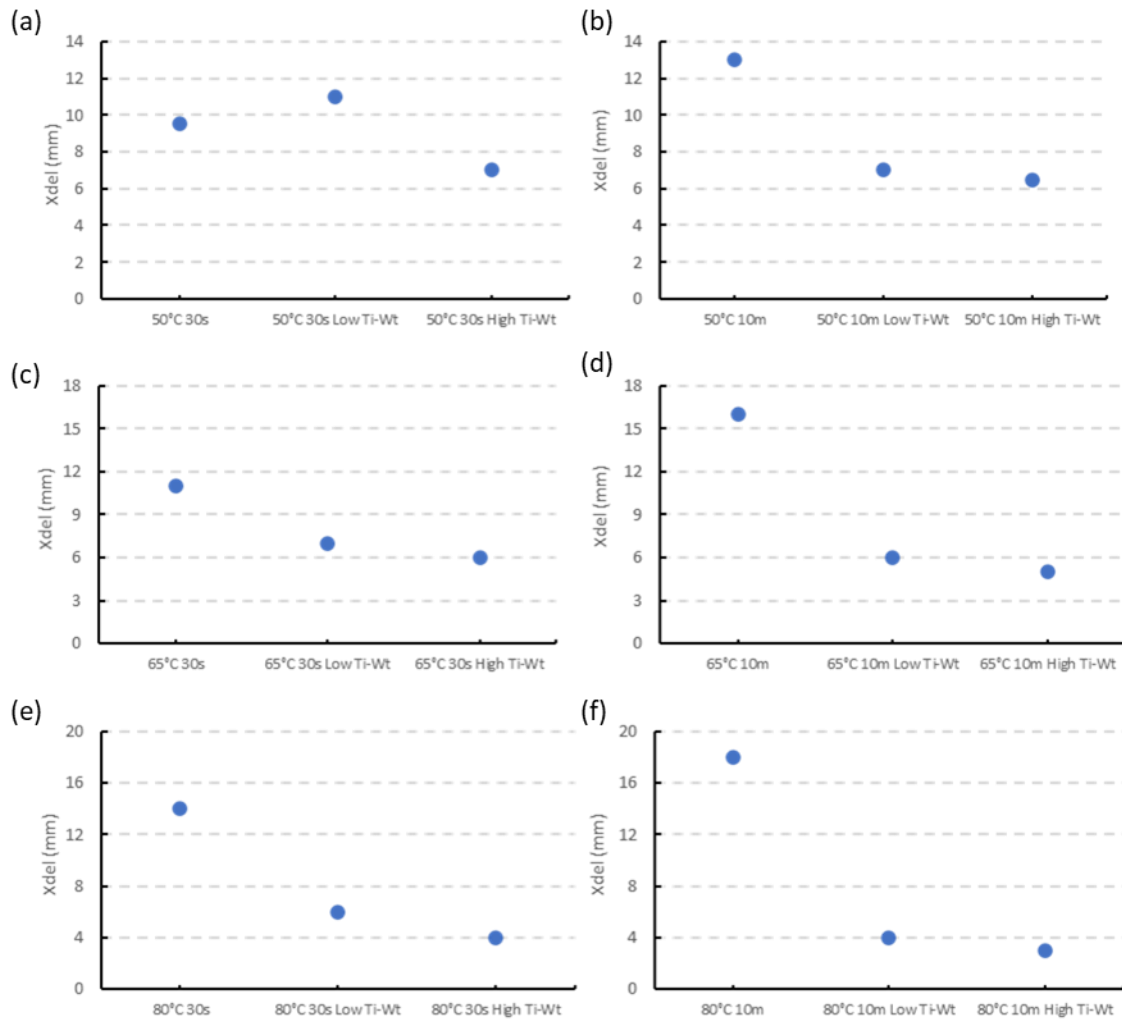
Figure 5.35. Delamination distance from defect of PVB on the surface of alkaline cleaned HDG with and without HFT applied; (a) Surface cleaned at 50°C for 30 seconds; (b) Surface cleaned at 50°C for 10 minutes; (c) Surface cleaned at 65°C for 30 seconds; (d) Surface cleaned at 65°C for 10 minutes; (e) Surface cleaned at 80°C for 30 seconds; (f) Surface cleaned at 80°C for 10 minutes.

As seen in Figure 5.32 there is a clear trend in how the intensity of the alkaline wash and the amount of HFT applied influences the final delamination distance. When the time is kept constant (30 seconds or 10 minutes), the temperature is increased and the amount of HFT applied is kept constant (1 wipe of 10 wipes) there is a decrease in the distance reached when delamination is allowed to occur for 120 hours, for example, a sample of HDG washed for 50°C, 65°C, and 80°C for 10 minutes and 1 wipe of HFT applied will show delamination fronts measuring 7mm, 6mm and 4mm respectively. This trend is applicable for all experiments within an experimental dataset.
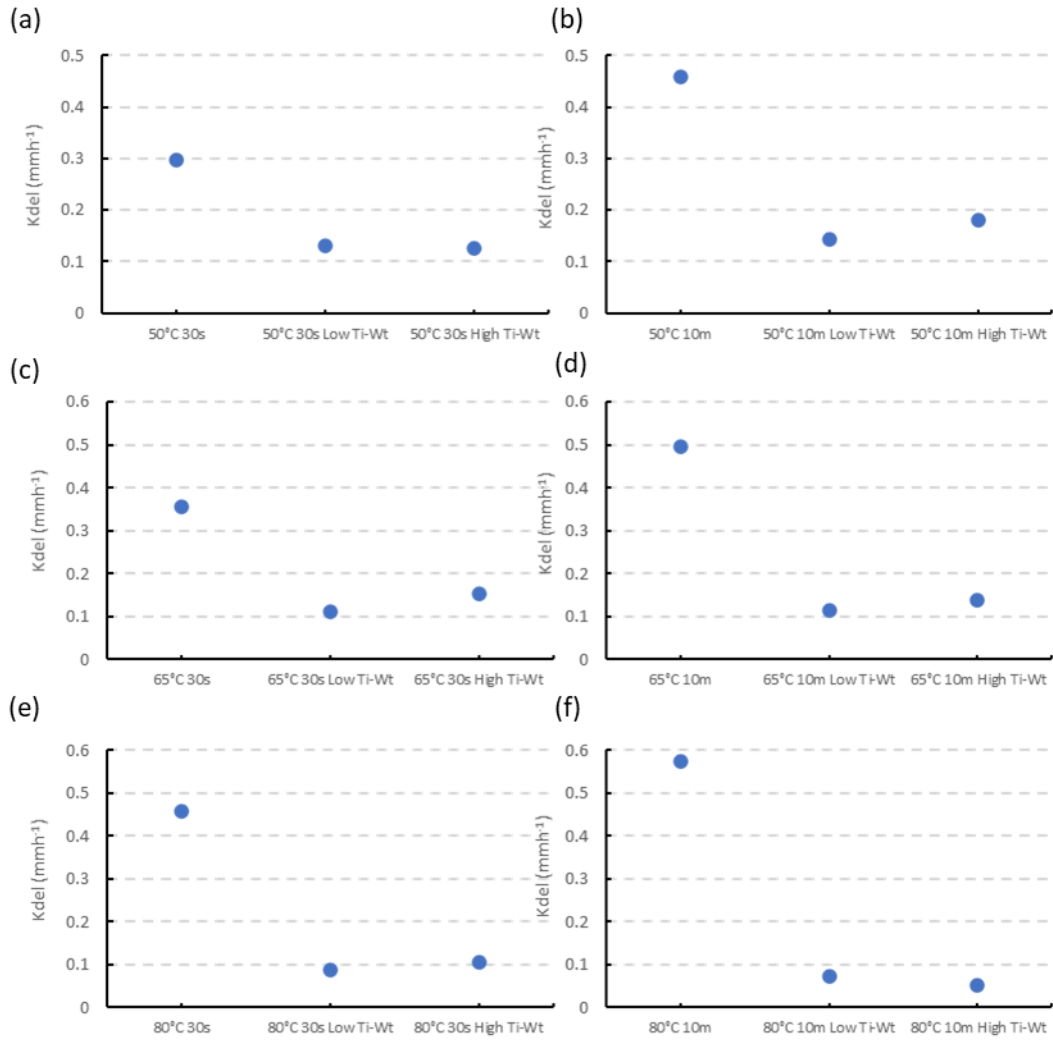
Figure 5.36. Delamination rate of PVB on the surface of alkaline cleaned HDG with and without HFT applied; (a) Surface cleaned at 50°C for 30 seconds; (b) Surface cleaned at 50°C for 10 minutes; (c) Surface cleaned at 65°C for 30 seconds; (d) Surface cleaned at 65°C for 10 minutes; (e) Surface cleaned at 80°C for 30 seconds; (f) Surface cleaned at 80°C for 10 minutes.

The delamination rate of HFT coated alkaline cleaned HDG has a very similar trend to the measured delamination distance of the same samples. Higher temperatures and increased cleaning times with the same amount of HFT wipes applied decreases the delamination rate, with increased application of HFT reducing the delamination rate further. Compared to uncoated alkaline cleaned HDG steel, the rate of delamination is at least a factor of two slower, with the rate of HFT coated surfaces cleaned at 80°C showing the slowest delamination rate and the largest differences between a coated and uncoated surface.
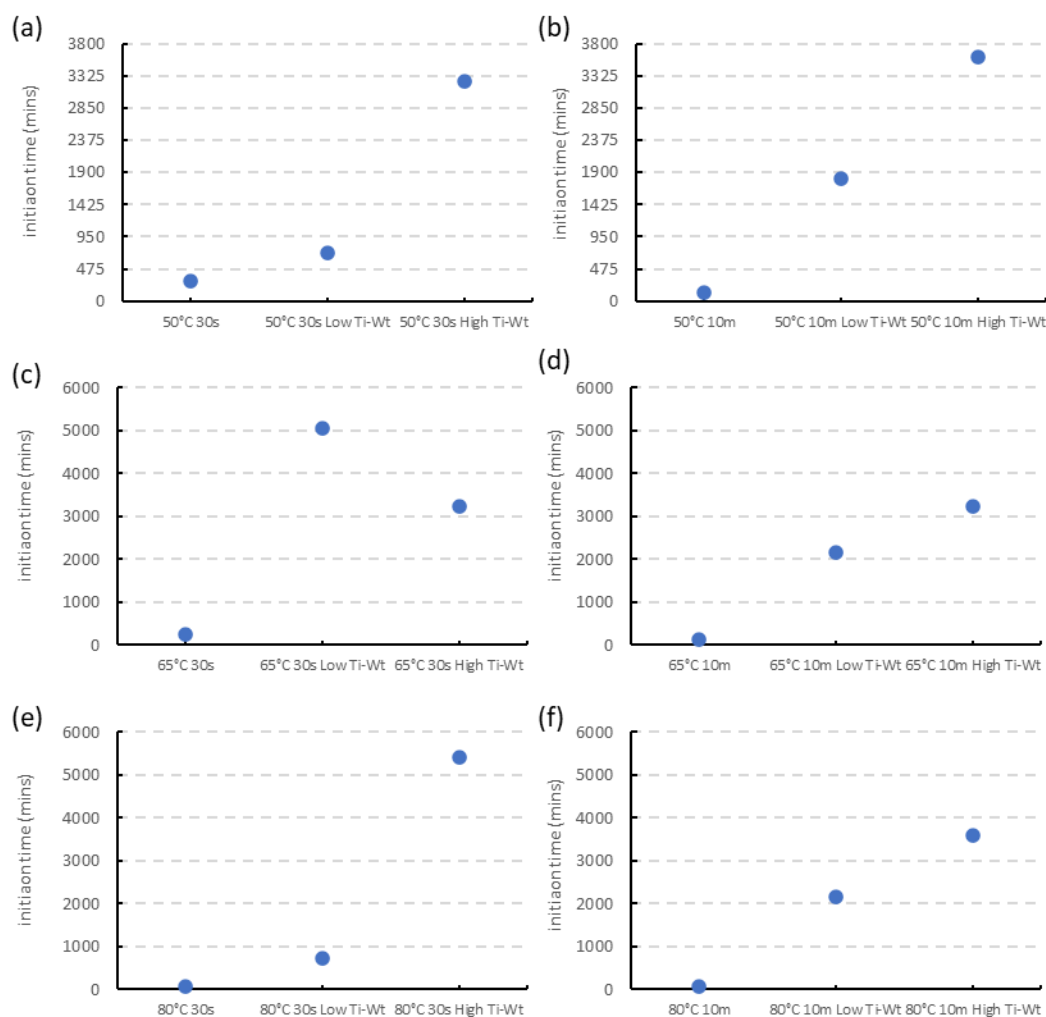
Figure 5.37. Initiation time of alkaline cleaned HDG with and without HFT applied; (a) Surface cleaned at 50°C for 30 seconds; (b) Surface cleaned at 50°C for 10 minutes; (c) Surface cleaned at 65°C for 30 seconds; (d) Surface cleaned at 65°C for 10 minutes; (e) Surface cleaned at 80°C for 30 seconds; (f) Surface cleaned at 80°C for 10 minutes.

The initiation time of HFT coated HDG varies significantly depending on the alkaline cleaning parameters and HFT application and shows no trend in how variation in parameters influence how quickly initiation occurs. For context, HDG cleaned for 80°C and 30 seconds with 10 wipes shows an initiation time of 2160 minutes, whereas a sample cleaned for HDG 65°C for 30 seconds with 1 wipe of HFT shows an initiation time of 5040 minutes.

The time-lapse data of an uncleaned HDG sample delaminates 8 mm over 24 hours, compared to 0 mm for pre-treated samples over the initial 24 hours. Pre-treated HDG does not begin to delaminate for at least 960 minutes and can take up to 5040 minutes for delamination to occur. When the number of HFT wipes applied is kept constant (one or ten

wipes) and the cleaning parameters of the HDG is varied, behavioural differences are observed. When either the cleaning time (30 seconds or 10 minutes) or the cleaning temperature (50°C, 65°C, or 80°C) is increased the delamination distance reached after 120 hours decreases. This behaviour is also matched by a decrease in the delamination rate that occurs at a given HFT application when the cleaning intensity is increased. The application of HFT also plays a role in the delamination performance, when the number of HFT wipes applied is increased and the cleaning intensity is kept constant, the delamination distance and delamination rate also decreases.

The determination of the rate kinetics of the pre-treated HDG also shows a difference in how the delamination kinetics occur. The alkaline cleaned HDG substrates have a curved line when delamination distance is plotted against time, whereas pre-treated HDG exhibits a straight line throughout. These curves indicate that cleaning HDG would appear to result in parabolic kinetics and the pre-treated HDG would appear to exhibit linear kinetics as a result of the pre-treatment acting as a corrosion inhibitor illustrating the pre-treatment changes the rate-determine step from ion migration in the underfilm electrolyte to electron transfer between anodic and cathodic sites. [10,11]An interesting point to note is the apparent difference in behaviour in the behaviour of HFT coated surfaces under cathodic disbondment and cathodic polarisation conditions. Cathodic polarisation appears to indicate that a pre-treated surface is a more active oxygen cathode compared to a cleaned HDG surface whereas cathodic disbondment shows that a pre-treated surface inhibits corrosion driven cathodic disbondment. One possible explanation for this is the concentration and quantity of electrolyte in contact with the coating during these tests. In cathodic polarisation a large volume of 5% wt/v. NaCl solution is in constant contact with the surface, whereas in cathodic disbondment a much more diluted solution is in contact with the pre-treatment through the defect, with even more diluted hydroxide ions causing the delamination to occur. This difference in how the surface interacts with electrolyte in the different tests could be a reason for the opposing behaviour of the pre-treated surface.

5.3.3.2. Use of Scanning Kelvin Probe to analyse kinetics of corrosion driven cathodic disbondment

The use of scanning Kelvin probe is to analyse not only the kinetics of the cathodic disbondment of the alkaline cleaned samples but also how the surface potential changes with delamination of the organic coating and whether the surface conditioning changes the measured potentials. Measurements were taken using the extremes of the cleaning conditions, with 30 second and 10 minute washing times used at the temperatures used previously with the addition of HFT on the cleaned surface before the addition of the modal PVB coating. Over a 24 hour time period, no delamination occurs over on any HFT coated HDG steel, regardless of amount of HFT applied and cleaning conditions used prior to HFT application. Two SKP profiles are shown in Figures 5.35 and 5.36 to show how the coating remains intact over the test time period, and the intact potential of the PVB coating. Delamination of HDG coated with HFT does not occur within 24 hours, a scan lasting 72 hours using HDG steel which had been cleaned for 65°C, 30 seconds with 1 wipe of HFT applied was also taken to test if the SKP could detect delamination occurring on the surface and can be seen in Figure 5.37. A comparison of how HFT influences the SKP profile compared to a purely alkaline cleaned surface is also illustrated in Figure 5.38.

Figure 5.38. A graph showing the time dependent E_{corr} measurements against distance from defect (χ) for 65°C, 30 seconds alkaline cleaned surface with 1 wipe of HFT and PVB coating from a HDG sample. E_{corr} measurements were taken every hour for 24 hours and presented every 2 hours.
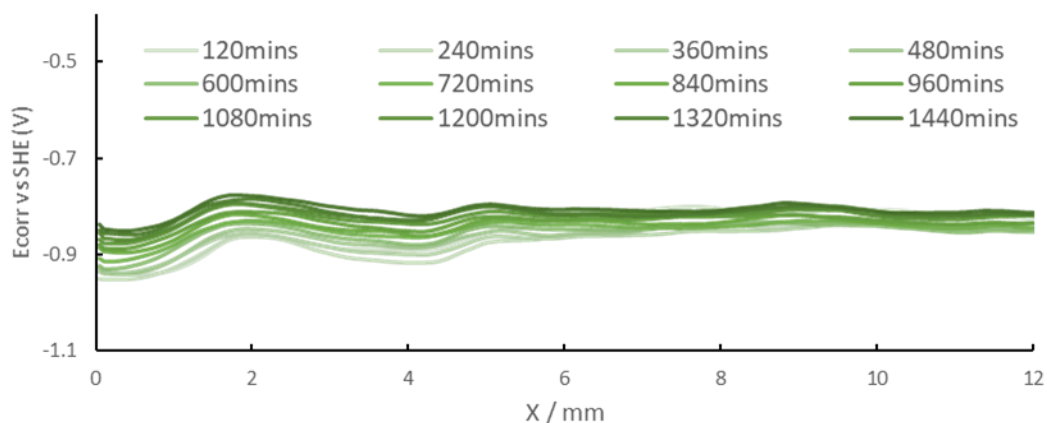
Figure 5.39. A graph showing the time dependent E$_{corr}$ measurements against distance from defect (χ) for 65°C, 30 seconds alkaline cleaned surface with 10 wipes of HFT and PVB coating from a HDG sample. E$_{corr}$ measurements were taken every hour for 24 hours.
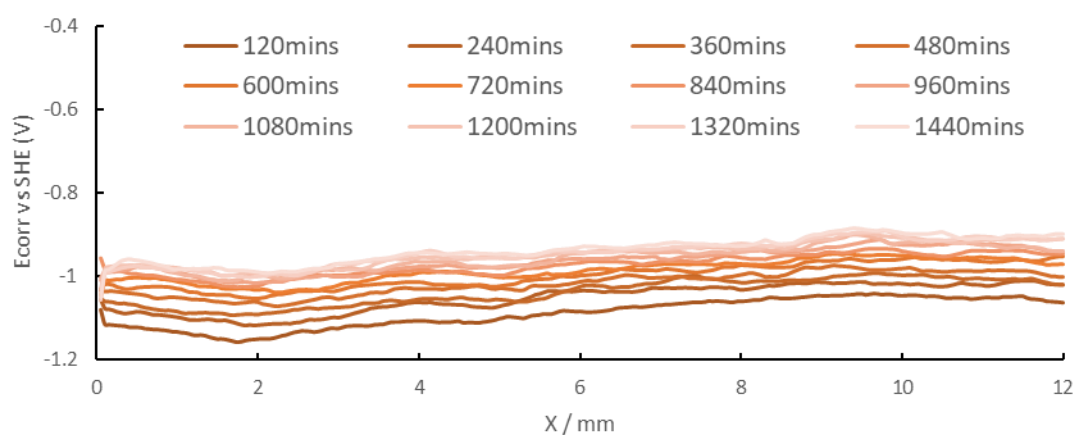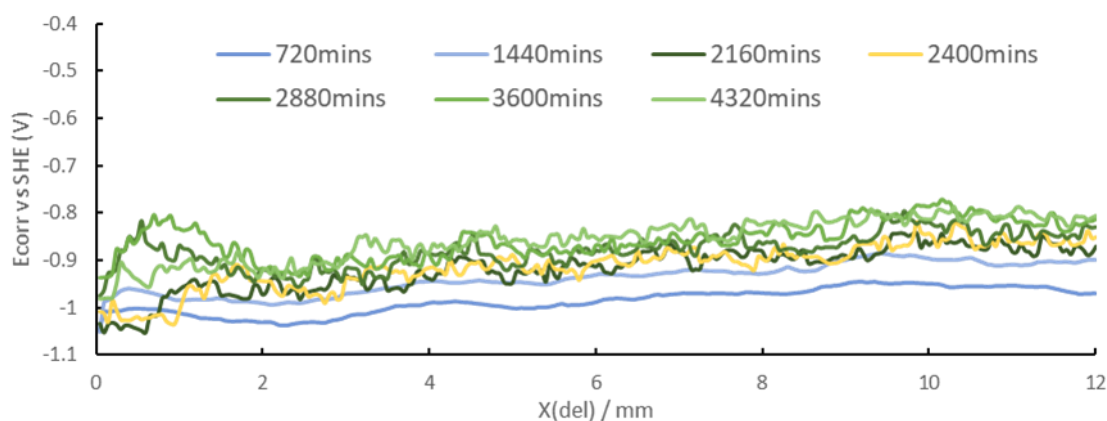

Figure 5.40. A graph showing the time dependent E$_{corr}$ measurements against distance from defect (χ) for 65°C, 30 seconds alkaline cleaned surface with 1 wipe of HFT and PVB coating from a HDG sample. E$_{corr}$ measurements were taken every 12 hours for 72 hours.
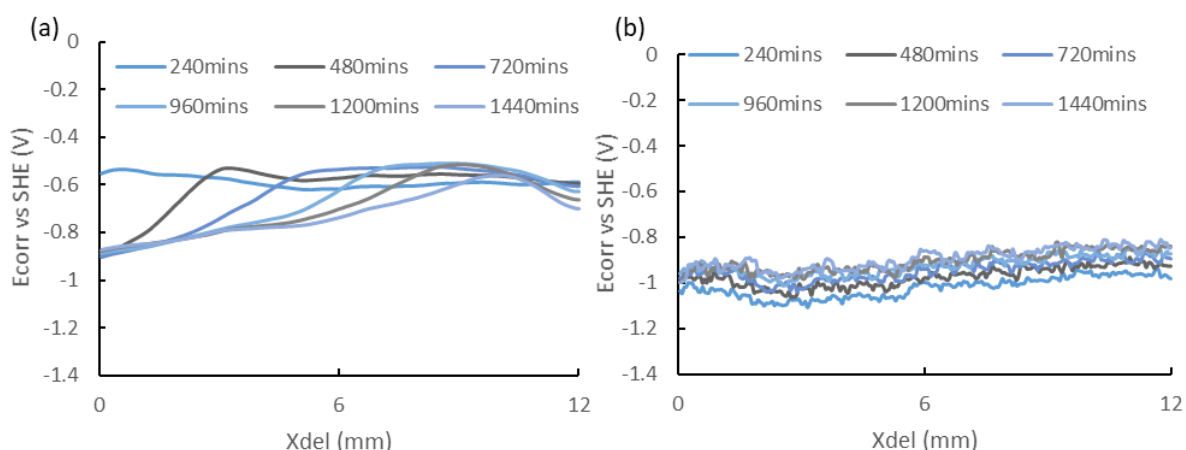
Figure 5.41. SKP profile comparison between (a) HDG steel alkaline cleaned at 65°C for 30 seconds, and (b) HDG steel alkaline cleaned at 65°C for 30 seconds with 1 wipe of HFT.

What can be seen from a 72 hour scan is that delamination is extremely slow to initiate, taking approximately 2160 minutes for the E_{corr} voltage to increase, and even then the uptake may not be copper probe detecting cathodic delamination and could be a natural increase in the E_{corr} of the surface. However, there is a noticeable increase in the E_{corr} that can be seen at times equal to and greater than 2880 minutes, however the E_{corr} increase is only ~0.08V for a distance of 0.5mm. The calculated change in E_{corr} for HDG steel without HFT is 0.2-0.4V, so the suppression in the E_{corr} could be a result of HFT on the surface supressing the measured potential on the surface.

As delamination of PVB does not occur when HFT is applied to cleaned HDG prior to the application of the organic coating, the delamination rate is not determined. However, the intact potential of the coating can be measured over the 24 hour period. The intact potential of HDG cleaned at all temperatures for 30 seconds and 10 minutes with varying HFT application can be seen in Figures 5.39 showing how the average E_{intact} varies with each sample, with Figures 5.40 and 5.41 showing how the average E_{intact} of the pre-treated surface changes over 24 hours.
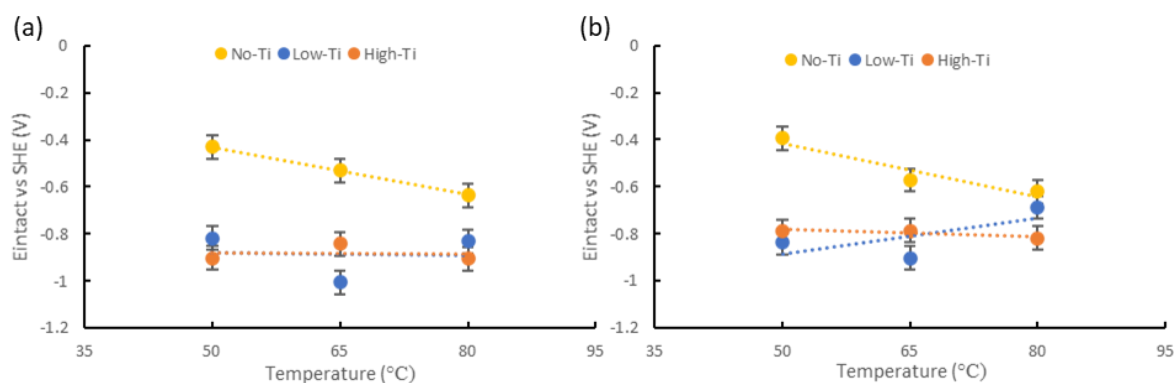
Figure 5.42. Average Intact potential of PVB on HFT coated HDG steel alkaline cleaned at; (a) 30 seconds, and; (b) 10 minutes at varying temperatures.
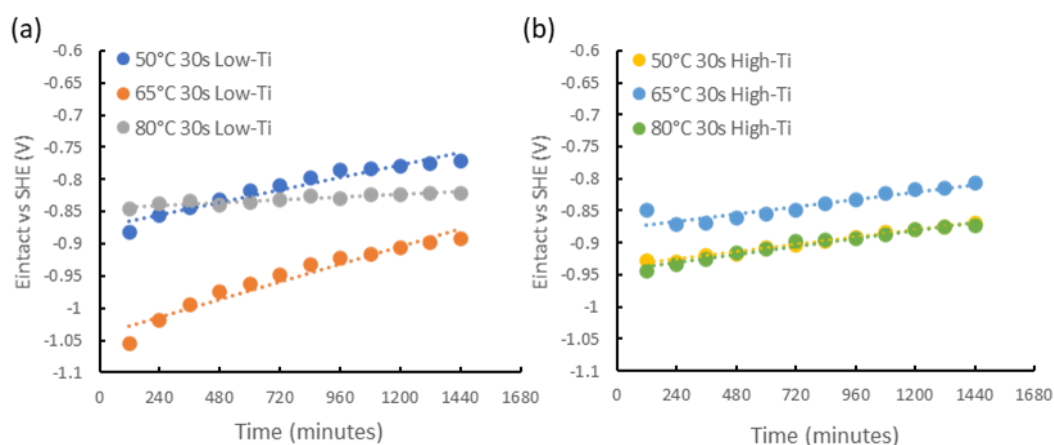
Figure 5.43. Average Intact potential of PVB on HFT coated HDG steel alkaline cleaned for 30 seconds over 24 hours (a)Low Ti-Wt, and; (b) High Ti-Wt.

Figure 5.44. Average Intact potential of PVB on HFT coated HDG steel alkaline cleaned for 10 minutes over 24 hours (a)Low Ti-Wt, and; (b) High Ti-Wt.

From the determination of the initiation time and delamination from the defect of model PVB coating. An uncleaned HDG substrate shows the least delamination distance, whereas the delamination travelled from the defect increases with increasing cleaning intensity. The initiation time is also shortest for uncleaned and HDG washed for 50°C for 30 seconds, with delamination ta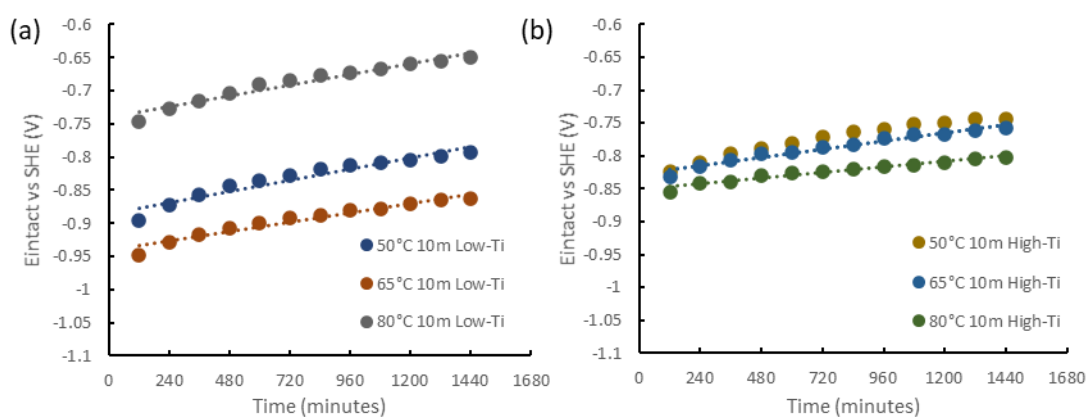king 60 minutes to initiate. The remaining HDG washed at the other cleaning conditions typically take between 60 – 240 minutes for delamination to initiate.

The scanning Kelvin probe work conducted alongside the time-lapse shows similar cathodic disbondment behaviour over the first 24 hours of the experiment, with no delamination occurring on all pre-treated substrates. As no delamination rate data can be calculated due to no delamination occurring, the variation in the intact potential (E_{intact}) of the PVB coating as a function of the amount of HFT and alkaline cleaning parameters was calculated. What is shown through the intact potential measurements is the E_{intact} becomes more anodic as time the experiment proceeds, which would indicate that the pre-treatment is suppressing the corrosion reactions that would usually occur at the steel/electrolyte and coating/electrolyte interfaces by providing a barrier preventing the electrolyte from interacting with the steel. [12] This increased positive potential can also be explained in electrochemical terms as the addition of HFT aids in suppression of the anodic metal dissolution reaction that would occur without the addition of HFT, and the increasing anodic potentials shown illustrates that the kinetics of oxygen reduction are faster than that of metal dissolution. [12] The average E_{intact} of the coating is measured between -0.95 and -0.65V, compared to measured E_{intact} of -0.6 to -0.4V measured for HDG without HFT applied. This cathodic shift in the E_{intact} can be attributed to strong inhibition of the oxygen reduction reaction. [13]

5.4. Conclusion

XPS analysis of HFT coating on steel indicates presence titanium dioxide and polymeric oxygen and carbon which aid in adhesion of model PVB coating, alongside other inorganic components such as Mn, P and F. Addition of HFT results in deposition of titania on the surface, with the titanium weighting as measured by XRF increasing when additional pre-treatment is applied, although the uniformity of this Ti layer is unknown. The addition of HFT would appear to suppress the corrosion driven cathodic disbondment of PVB coating, with increased alkaline cleaning intensity and increasing amount of HFT coating resulting in decreased delamination rate and delamination distance. The addition of pre-treated changes

the rate kinetic behaviour from parabolic (as seen in untreated HDG) to linear, illustrating the pre-treatment completely supresses cation migration in the electrolyte and also appears to suppress the electron transfer reactions occurring on the surface due to reduction in delamination rates as cleaning intensity increases. The addition of HFT almost doubles the anodic passive region when anodically polarised and suppresses additional reduction reactions when cathodically polarised, but is more reactive compared to untreated HDG with a much larger increase in the current when cathodically polarised. Polarisation resistance is increases upon addition of HFT compared to uncoated HDG steel and increasing alkaline cleaning time of the steel substrate results in much greater polarisation resistances being generated. Compared to uncoated HDG, the addition of HFT greatly improves corrosion performance of the model PVB coating in time-lapse experiments and shows better performance in electrochemical tests.

5.5. References

1. Chen XB, Chong K, Abbott TB, Birbilis N, Easton MA. Biocompatible strontium-phosphate and manganese-phosphate conversion coatings for magnesium and its alloys. In: *Surface Modification of Magnesium and Its Alloys for Biomedical Applications*. Vol 2. Elsevier Inc.; 2015:407-432. doi:10.1016/B978-1-78242-078-1.00015-3

2. Ryntz RA. Coating adhesion to low surface free energy substrates. *Prog Org Coatings*. 1994;25(1):73-83. doi:10.1016/0300-9440(94)00503-6

3. A New Standard For Facades - Architecture Today. https://architecturetoday.co.uk/new-standard-facades/. Accessed March 20, 2023.

4. Stankiewicz A. Self-healing nanocoatings for protection against steel corrosion. In: *Nanotechnology in Eco-Efficient Construction*. Elsevier; 2019:303-335. doi:10.1016/b978-0-08-102641-0.00014-1

5. Chromium-free conversion coating treatment of aluminum. May 1994. https://patents.google.com/patent/US5584946. Accessed March 15, 2019.

6. Composition and process for treating metal. April 1995. https://patents.google.com/patent/US5534082. Accessed March 15, 2019.

7. Le Bozec N, Compère C, L'Her M, Laouenan A, Costa D, Marcus P. Influence of stainless steel surface treatment on the oxygen reduction reaction in seawater. *Corros Sci*. 2001;43(4):765-786. doi:10.1016/S0010-938X(00)00113-X

8. Babić R, Metikoš-Huković M. Oxygen reduction on stainless steel. *J Appl Electrochem*. 1993;23(4):352-357. doi:10.1007/BF00296691

9. Dafydd H, Worsley DA, McMurray HN. The kinetics and mechanism of cathodic

oxygen reduction on zinc and zinc-aluminium alloy galvanized coatings. *Corros Sci*. 2005;47(12):3006-3018. doi:10.1016/J.CORSCI.2005.05.036

10. Geraint W, McMurray HN, Williams G, McMurray H. Chromate inhibition of corrosion driven organic coating delamination studied using a scanning Kelvin probe technique. *J Electrochem Soc*. 2001;148(10):B377. doi:10.1149/1.1396336

11. Geraint W, McMurray HN, Worsley DA, Williams G, McMurray H. Cerium(III) inhibition of corrosion-driven organic coating delamination studied using a scanning Kelvin probe technique. *J Electrochem Soc*. 2002;149(4):B154. doi:10.1149/1.1457983

12. Fu AQ, Cheng YF. Characterization of corrosion of X65 pipeline steel under disbonded coating by scanning Kelvin probe. *Corros Sci*. 2009;51(4):914-920. doi:10.1016/J.CORSCI.2009.01.022

13. Stratmann M, Leng A, Fürbeth W, Streckel H, Gehmecker H, Große-Brinkhaus KH. The scanning Kelvin probe; a new technique for the in situ analysis of the delamination of organic coatings. *Prog Org Coatings*. 1996;27(1-4):261-267. doi:10.1016/0300-9440(94)00542-7

Chapter 6 – Influence of ageing of Ti-based pre-treatment addition on surface chemistry and corrosion driven cathodic disbondment on galvanised steel.

6.1. Introduction

The work contained in this chapter focuses on how ageing of pre-treatments after alkaline cleaning and how re-treatment deposition influences performance under corrosion testing. The motivation for the work described in this chapter derives from industry observations that the performance of pre-treated (passivated) samples changes over time after production when the sample is left to "age" before further processing, usually as a result of line capacity limits, plant downtime or a lower volume of orders from consumers. Passivated surfaces show better corrosion performance after they have been stored loosely following production when compared to coil storage. However, storage of passivated over time (ageing) is slower when stored as coil, especially in the centre. Ageing is also slower when stored at room temperature compared to storage at 35°C. Coil storage of pre-treated steel coils shows a high sensitivity to water once they are produced, with water contact angles being lower for newly produced samples, and higher angles produced when aged in air.. Reports generated show that titanium based pre-treatments which have been aged at room temperature for 2-17 hours show better corrosion resistance under accelerated salt spray and humidity tests when compared to freshly produced samples. Literature on the influence of ageing on conversion coatings can be seen in Section 1.6.5.

This chapter will focus on how titanate-based pre-treatment performs under polarisation and corrosive environments and how the surface chemistry changes when aged at room temperature for 24, 168 and 672 hours after alkaline cleaning. In this chapter, the pre-treatment applied to the surface as seen in Chapter 5 is kept in storage for extended periods of time before analysis of the surface and before application of model PVB coating. The results shown are the results gathered at a 65°C cleaning temperature with low and high Ti-weights, with the results of all cleaning temperatures (50°C, 65°C, 80°C) discussed and results presented in the appendix.

6.2. Experimental Details

6.2.1. Materials

Bonderite U-187 alkaline cleaner was provided by Henkel via Tata Steel UK. Hot dip galvanized steel was provided by Tata Steel UK, with a gauge of 0.7mm mild steel and a zinc layer of 20µm. Bonderite 1445 M-NT hexaflourotitanate (HFT) pre-treatment wipes manufactured by Henkel were purchased online. Samples were created by cutting the HDG into coupons of 50 x 50mm. Polyvinyl butyral-co-vinyl alcohol-co-vinyl acetate (PVB), molecular weight 70,000-100,000, was obtained from Sigma Aldrich Chemical Co. and was at an analytical grade purity. The PVB solution was prepared in ethanol to 15.5% w/w with the required amount of PVB added stepwise to the solvent using a high shear mixer.

6.2.2. Experimental Methodology

Samples of pre-treated HDG were prepared for experimentation by being cut into coupons of the relevant size necessary for analysis. Samples a were degreased with ethanol before using Bonderite U-187 alkaline washing solution which was heated at 50°C, 65°C, and 80°C for between 30 seconds Samples were rinsed with de-ionised water to remove any residual cleaning solution and dried with a hairdryer. Pre-treatment was then applied using a Henkel pre-treatment wipe to apply pre-treatment to the surface, this was done by applying with either one or 10 applications by wiping across the surface with minimal pressure and left to air cure for 15 minutes before being wrapped in foil and stored at ambient laboratory conditions for 24 hours, 168 hours, or 672 hours before testing or coating application. The full description of the instrumentation, calibration, experimental set-up and analysis of XRF XPS, SKP, time-lapse photography and potentiodynamic polarisation can be found in Chapter 2.

6.3. Results

6.3.1. Surface characterisation of aged hexaflourotitanate pre-treatment on hot dipped galvanised steel

6.3.1.1 Titanium quantification of aged hexaflourotitanate coated hot dipped galvanised steel.

Titanium specific XRF was used to determine the coating weight of Ti in the aged HFT coating. Much like the quantification of Ti in the HFT coating, the influence of ageing the coating in air on the Ti content of the HFT pre-treatment can be seen below.
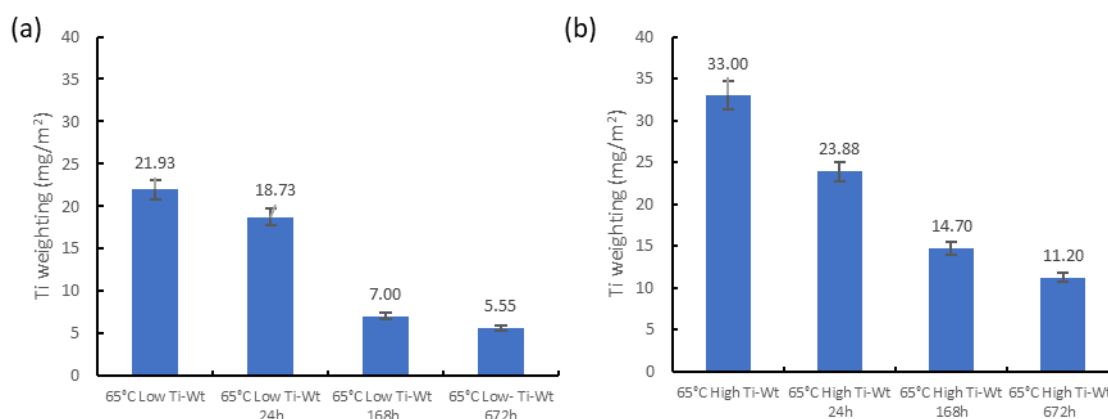

Figure 6.1. Comparison of Ti-weighting when cleaned at 65°C for 30 seconds a varying ageing times: (a) Low Ti-Wt; (b) High Ti-Wt

As can be seen above in Figures 6.1, there is a clear decrease in the Ti-weight as ageing time increases and at both low and high Ti-weighting. At Low Ti-Weight the Ti-weight does not drop by any large degree between a week aged and a month aged. At high Ti-weight there is a constant drop in the measured weight as the ageing time increases, and the measured Ti-weighting is higher when 10 wipes of HFT are applied compared to 1 wipe. At low and high Ti-weightings, the Ti-weight does not show any net negative or positive changes in the measured Ti-Weight when the cleaning temperature is increased, with the weights staying relatively constant at the same ageing times. When 1 wipe is applied, the largest decrease in Ti-Wt occurs between 24 and 168 hours and when 10 wipes are with the largest decrease in Ti-Wt occurring after 24 hours. For 1 wipe applications, the drop in Ti-Wt stabilises after 168

hours at all cleaning conditions, for 10 wipe applications the Ti-Wt continues to decrease, although the decrease is not as great as that seen in the first 24 hours. Use of multiple wipes does show more Ti-loss in the first 24 hours compared to using 1 wipe, however, 1 wipe shows greater loss over the ageing window. A possible explanation as to why the Ti-% is decreasing provided by industrial contacts was that as ageing increases there is longer room temperature curing of the coating which could be creating a more compact coating. As a result of this increased compactness the lab-scale XRF used in the lab was potentially not measuring one of the two TiO_2 layers nearest to the steel substrate.

6.3.1.2 X-ray photoelectron quantification

To investigate how ageing influences the HFT pre-treatment alkaline affects the corrosion driven cathodic delamination behaviour, XPS was utilised to identify and quantify the elemental composition of the pre-treatment layer after ageing. Figure 6.2 displays a typical survey spectrum for pre-treated HDG, demonstrating the surface consists of Zn, C, O, Ti, Mn, P and F.
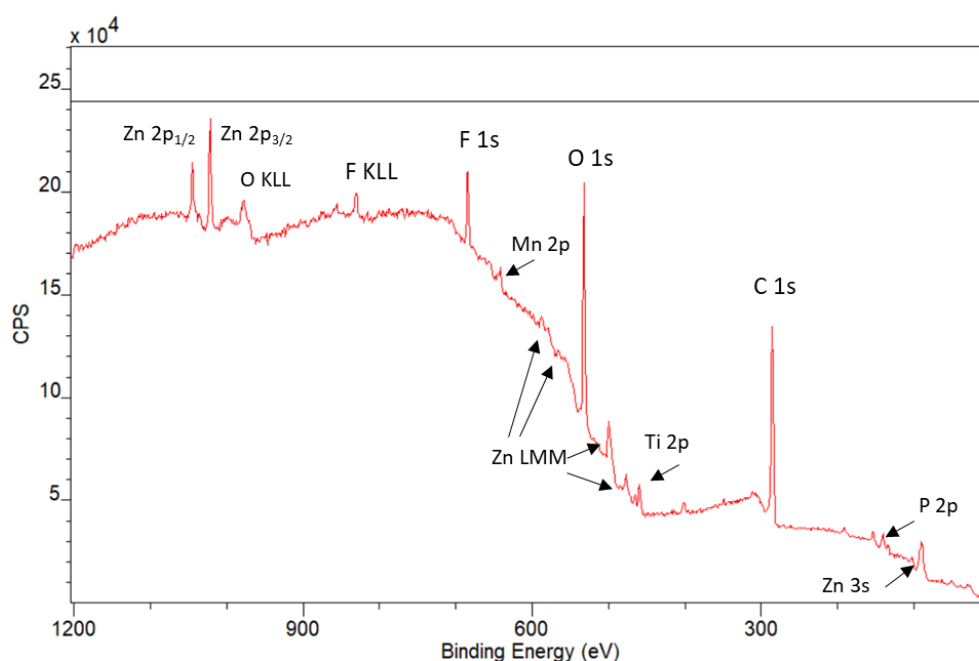

Figure 6.2. XPS spectral survey scan of HDG steel coated with HFT.

The main C 1s peak is centred at 284.8eV, identified as C-C, and is accompanied by two smaller peaks identified as C-O-C located at 286.82 eV and result from surface

contamination. Zinc peaks generated are centred around 1022.1 eV and 1045.2 eV, with the zinc Auger peak generated at 499.6 eV. A Fluoride 1s peak is generated at 684.5 eV, indicating the presence of a metal fluoride, combined with the zinc Auger peak this is shown to be zinc fluoride. Phosphorous 2p generates a peak at 133.6 eV, and Mn 2p generates peaks cantered around 642 eV, both of which illustrate the existence of manganese phosphate and manganese oxides on the surface. Oxygen 1s generates an oxide based peak at 530.9 eV and a carbon-based oxygen peak at 532.5 eV. Titanium 2p generates a peak at 458.3, indicating the presence of TiO_2.

Figure 6.3 Quantifiable. X-ray photolectron spectroscopy analysis of HDG with HFT aged for 24 hours (a) wide spectral analysis (b) carbon analysis; (c) zinc analysis; (d) oxygen analysis; (e) fluorine analysis; (f) manganese analysis; (g) titanium analysis; (h) phosphorus analysis. Key; Red – Low Ti-Wt, Green – High Ti-Wt

Figure 6.4 Quantifiable X-ray photolectron spectroscopy analysis of HDG with HFT aged for 168 hours (a) wide spectral analysis (b) carbon analysis; (c) zinc analysis; (d) oxygen analysis; (e) fluorine analysis; (f) manganese analysis; (g) titanium analysis; (h) phosphorus analysis. Key; Red – Low Ti-Wt, Green – High Ti-Wt
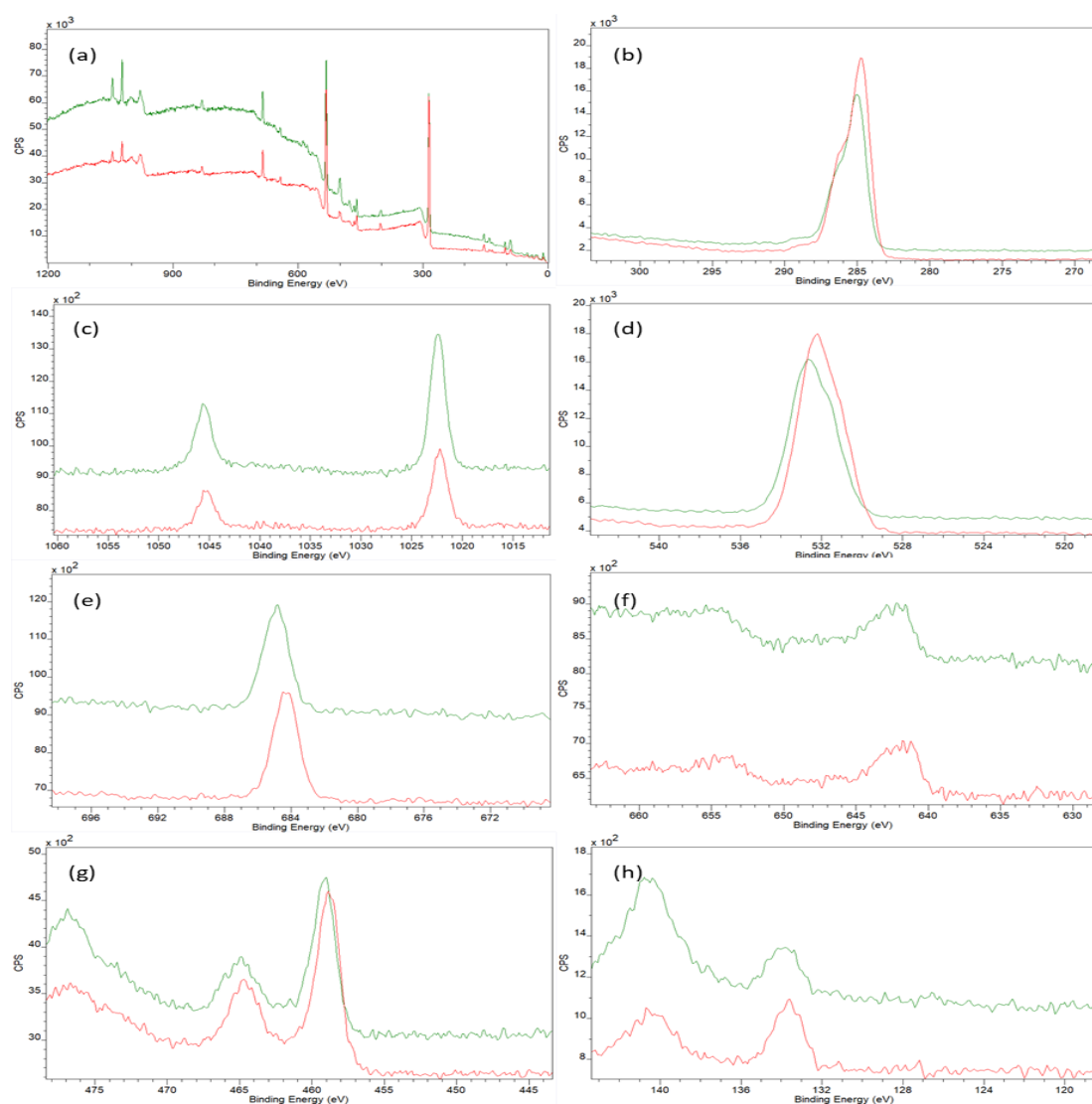
Figure 6.5. Quantifiable X-ray photolectron spectroscopy analysis of HDG with HFT aged for 672 hours (a) wide spectral analysis (b) carbon analysis; (c) zinc analysis; (d) oxygen analysis; (e) fluorine analysis; (f) manganese analysis; (g) titanium analysis; (h) phosphorus analysis. Key; Red – Low Ti-%, Green – High Ti-%
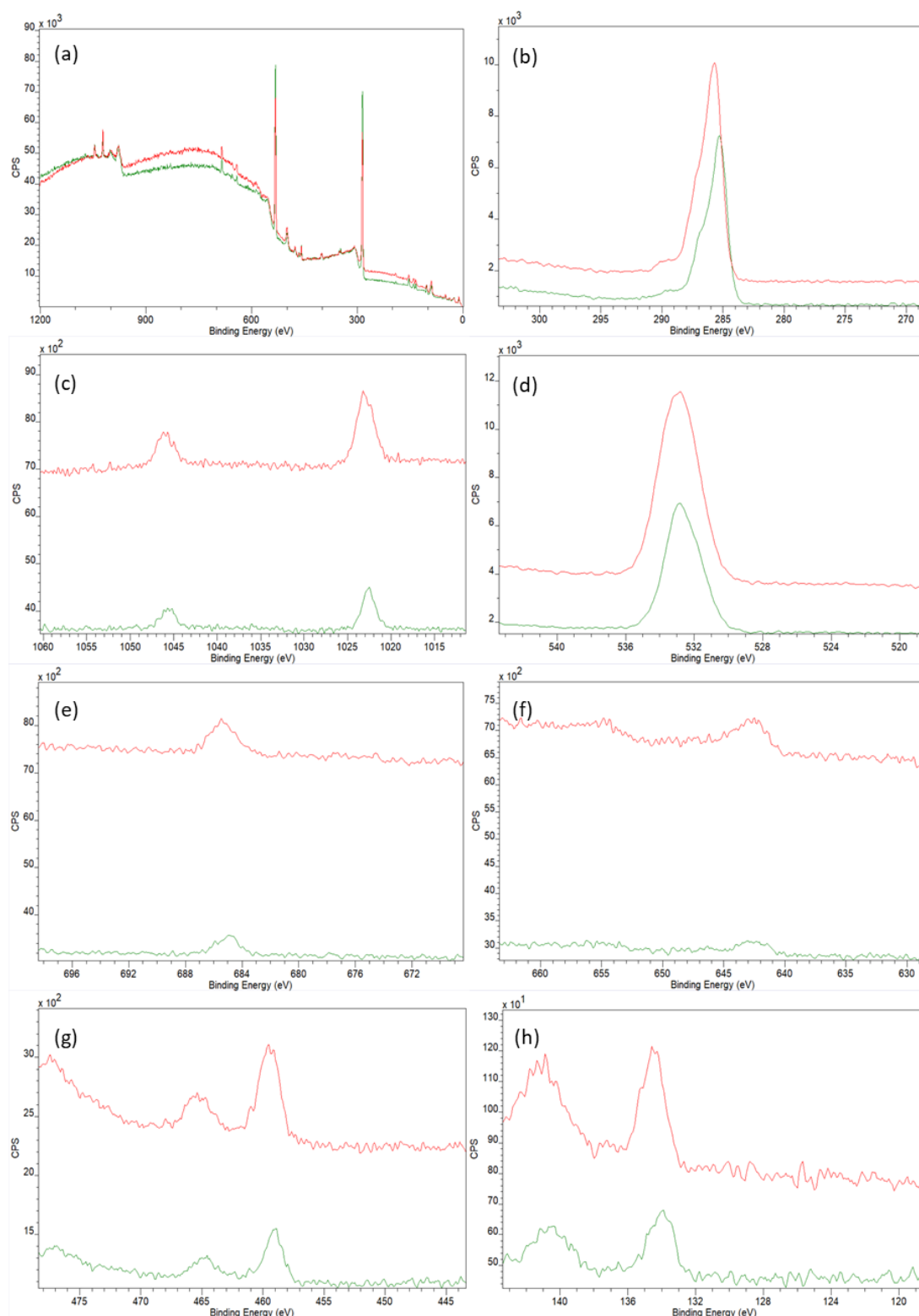
214
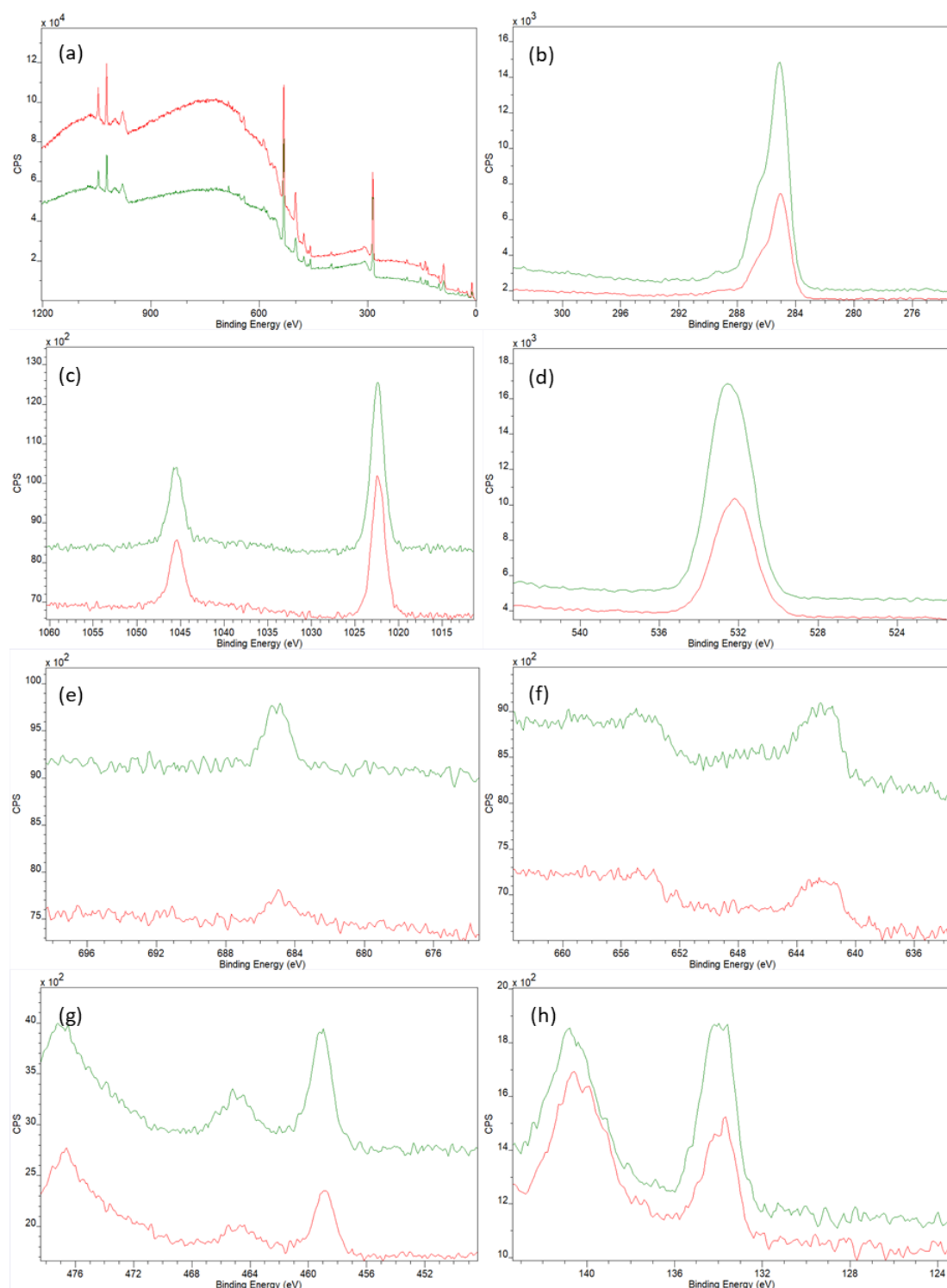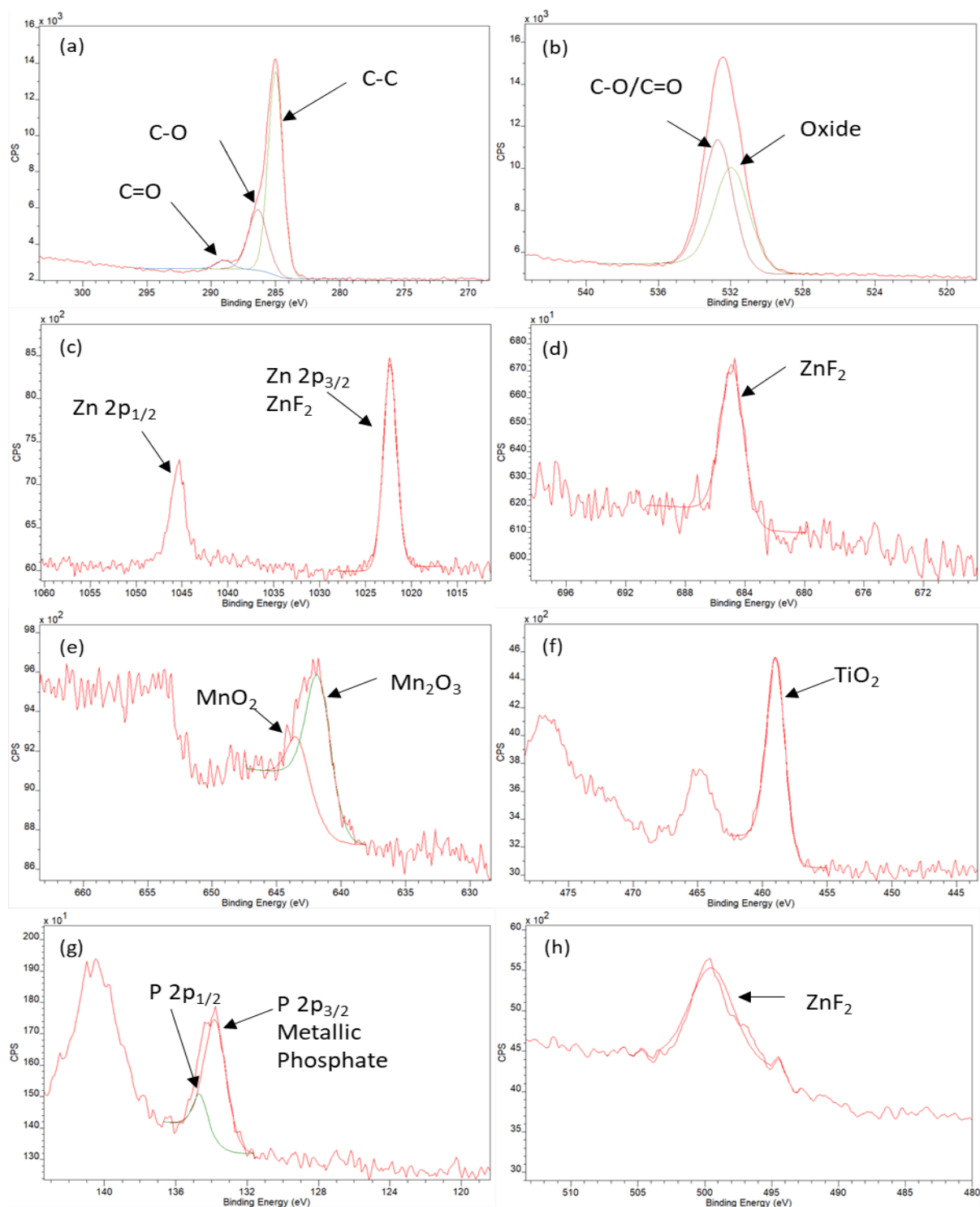

Figure 6.6. X-ray photoelectron spectroscopy analysis of elemental components of HDG coated with aged HFT. (a) wide spectral analysis (a) carbon analysis; (b) zinc analysis; (d) oxygen analysis; (e) zinc Auger analysis; (f) aluminium analysis

The average atomic concentrations in percentage have been derived from the corresponding element peak and are summaries below.

Table 6.1 XPS derived elemental content of aged pre-treatment

Sample	Ageing Time	Elemental Content (%)						
		C	O	Zn	F	P	Mn	Ti
65°C 30s Low Ti-Wt	24 hours	64.75	27.92	0.83	4.12	0.57	1.29	1.19
65°C 30s High Ti-Wt	24 hours	64.15	28.87	0.91	3.38	0.94	1.34	1.12
65°C 30s Low Ti-Wt	168 hours	67.02	28.21	0.75	1.84	0.98	1.27	0.7
65°C 30s High Ti-Wt	168 hours	71.04	25.48	0.39	1.37	0.86	0.68	0.51
65°C 30s Low Ti-Wt	672 hours	63.5	25.99	1.5	1.49	0.28	1.66	0.83
65°C 30s High Ti-Wt	672 hours	67.59	16.81	0.9	1.68	0.29	1.33	0.67

As shown above in Table 6.1, carbon and oxygen dominate the surface composition of all samples, with polymeric carbon and oxide species being the prevalent compounds of these elements. Like un-aged HFT, the remaining elements (Ti/Mn/P/Zn/F) are also present. Over the ageing period, there is variability in the contents of the elements on the surface, however, the Ti content is lower than that shown by fresh HFT samples, which show contents of 1.2-2.11%, compared to the 0.07-1.19% contents showed by aged samples. Compared to fresh samples, the fluorine content is typically lower for aged samples, with the Zn and P contents in the same content range. The manganese content is higher for aged samples, this could be due to the reduced fluorine content increasing the comparative content of other elements.

XPS analysis of aged HFT coating on steel indicates a very similar surface chemistry to that of freshly deposited HFT surfaces, with the presence of corrosion inhibitors such as manganese phosphate and titanium dioxide and polymeric oxygen and carbon which aid in adhesion of model PVB coating present on the surface. The carbon content of all HFT coated HDG steel is 65.62 $^{+}/_{-}$ 5.57% The oxygen content is calculated at 23.78 $^{+}/_{-}$ 4.08%. The contribution to the oxygen content is largely consisting of polymeric oxygen species with concentration of 10-20% and metal oxide contribution of 1-10%, much like that produced by fresh HFT. Titanium contributes 1.29 $^{+}/_{-}$ 0.53%, which consists entirely of TiO_2 and is lower than that produced by fresh HFT. Inhibitor species such as Mn, P, Zn and F contribute between 3-12%. In terms of trends of the elements with regards to the ageing time, the Ti-%,

F-%, and P-% decrease at every cleaning temperature as ageing time increases, the Zn-%, and Mn-% increases as ageing time increases at every cleaning temperature, with the C-%, and O-% showing small positive and negative trends at each cleaning temperature, although, the concentration changes are small in regards to the total concentrations of each of these elements.

6.3.1.3. Scanning Electron Microscopy and Energy Dispersive X-ray analysis of aged pre-treated HDG surface.

Surface images of HDG coated with 1 wipe and 10 wipes of HFT pre-treatment and aged for 672 hours using Scanning Electron Microscopy (SEM) and Energy Dispersive X-Ray (EDX) were taken to investigate whether the topology of the surface changes when the pre-treatment is aged. Seen in Figures 6.7 – 6.9 are SEM and EDX images of pre-treated steel aged for 672 hours.
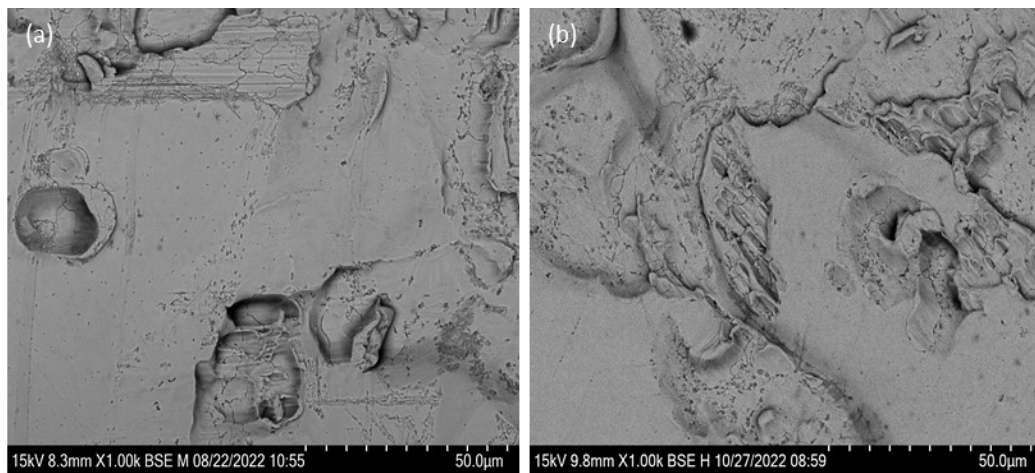

Figure 6.7. SEM images of HDG steel with 10 wipes of HFT applied; (a) freshly applied HFT; (b) HFT aged for 672 hours.
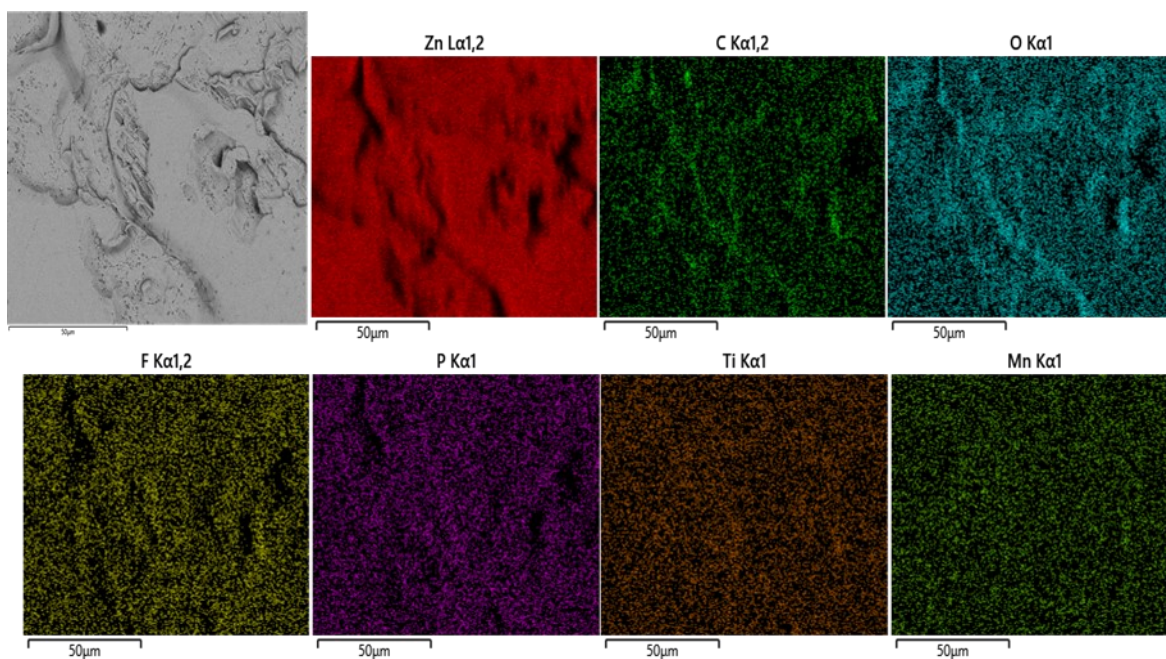
Figure 6.8. SEM image of HDG steel alkaline cleaned at 65°C for 30 seconds with 1 wipe of pretreatment applied aged for 672 hours, and EDX maps of zinc, oxygen, carbon, flourine, phosphorus, titanium, and manganese.

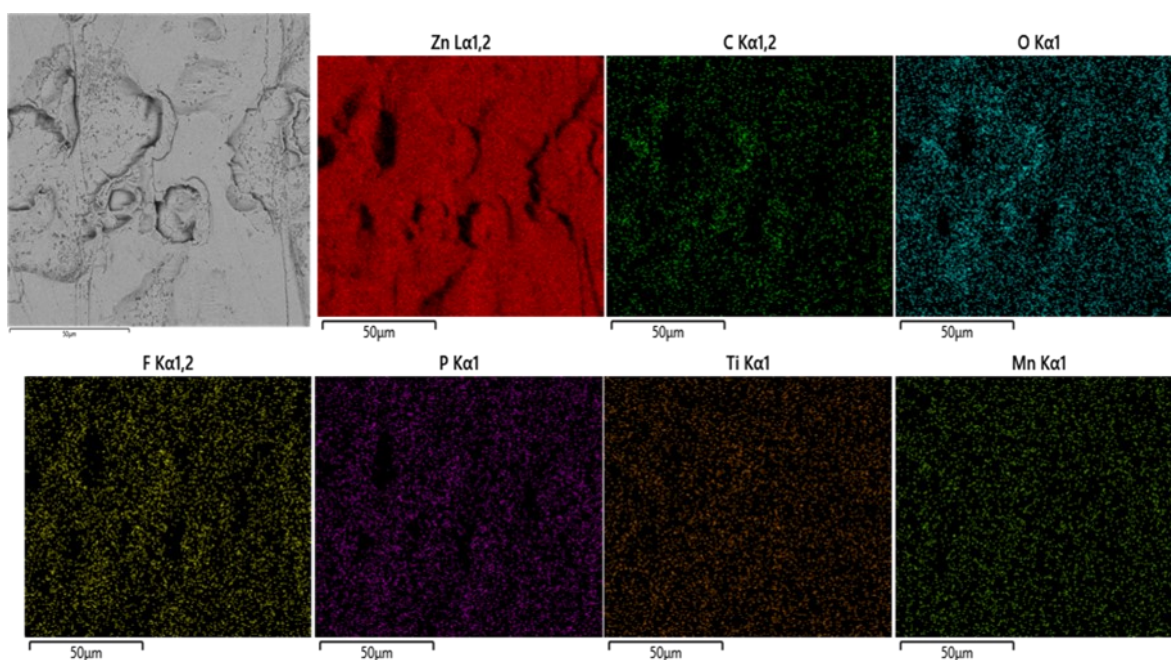*Figure 6.9. SEM image of HDG steel alkaline cleaned at 65°C for 30 seconds with 10 wipes of pretreatment applied aged for 672 hours, and EDX maps of zinc, oxygen, carbon, flourine, phosphorus, titanium, and manganese.*

As shown in Figures 6.7-6.9, the influence of ageing does not appear to make any observable change to the topography of the pre-treatment layer on the surface, with the EDX images being dominated by the zinc of the steel substrate below.

6.3.2. Influence of pre-treatment ageing on electrochemical response using anodic, cathodic and linear polarisation.

Polarisation experiments were performed as described in section 2.1 to evaluate the corrosion behaviour of HDG cleaned in alkaline solution at either 50°C, 65°C and 80°C for 30 seconds, pre-treated using HFT and aged for different times , upon immersion in 5wt.% NaCl (aq) pH 7, using methodology previously described in Chapter 2. Due to the large amount of data produced, only aged pre-treatment deposited on HDG surfaces cleaned at 65°C are shown here, with the remaining data made available in the Appendix.

6.3.2.1. Anodic polarisation of aged pre-treatment on HDG

Anodic polarisation curves of alkaline cleaned HDG substrates coated with HFT aged for extending periods of time were conducted to see how the influence of surface conditioning and pre-treatment ageing influences the metal oxidation reaction that occurs on the surface when in 5wt.% NaCl solution. The Open Circuit Potential (OCP) of samples were taken before applying an anodic-going polarisation sweep which started from of the OCP and was halted at an applied potential of +0.5V of the OCP. The curves have been displayed to a measured potential of -0.5V vs SHE in order to better resolve any differences between substrates immediately after polarising.
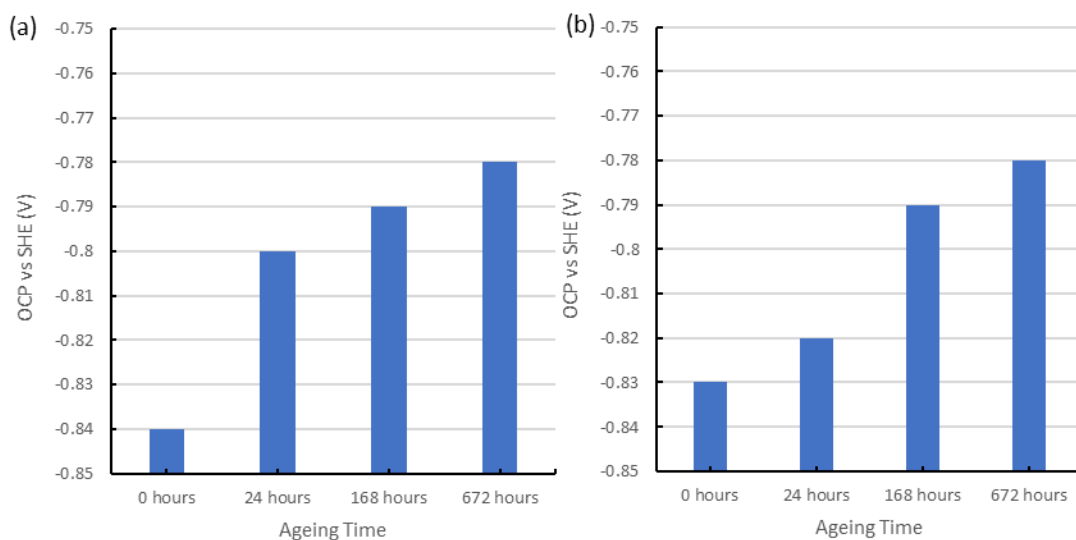
Figure 6.10. OCP measurements of aged pre-treatment applied to the surface of HDG (a) low Ti-weight; (b) high Ti-weight
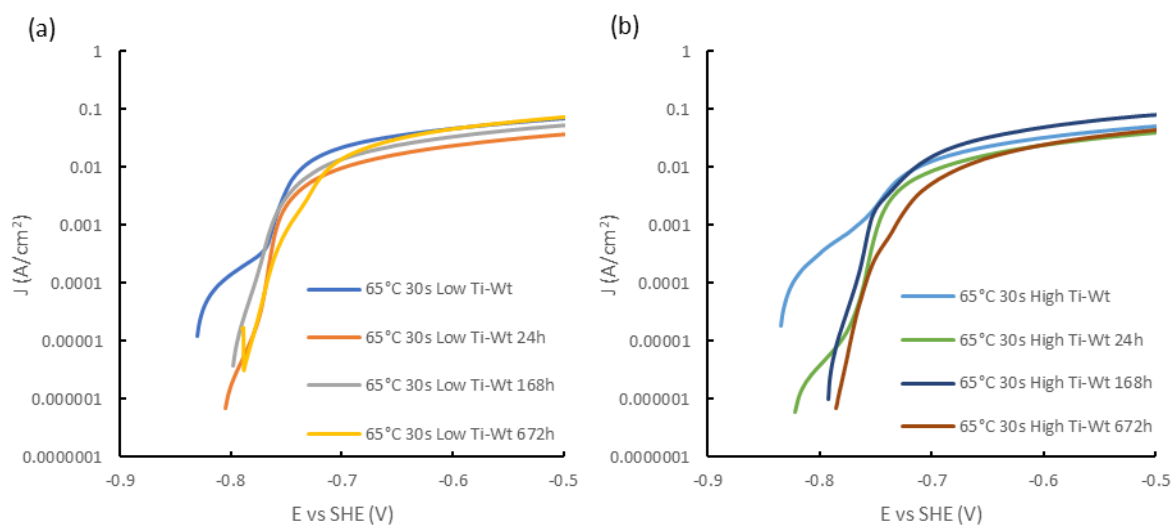

Figure 6.11. Anodic polarisation curve of HDG wash at 65°C with HFT applied aged for varying time in 5wt.% NaCl solution

There is a consistent shift in the OCP towards less negative potentials (i.e more anodic) as seen in Figure 6.10, which would indicate suppression of the anodic reaction would occur on the surface. A general trend can be observed of a slight decrease in anodic current density values with increased ageing over the same range of applied potentials. Anodic-going polarisation curves of aged pre-treatment surfaces can be seen in Figure 6.11, and there is

very little difference in the observed passive regions of aged surfaces compared to a freshly applied pre-treatment.

6.3.2.2. Cathodic polarisation of aged pre-treatment on HDG

Cathodic polarisation curves of alkaline cleaned HDG substrates were conducted to see how the influence of aged pre-treatment has on the cathodic oxygen reduction reaction that occurs on the surface when in 5wt.% NaCl solution. The Open Circuit Potential (OCP) of samples were taken before cathodic-going polarisation of the sample from the OCP to -0.5 V of the OCP.
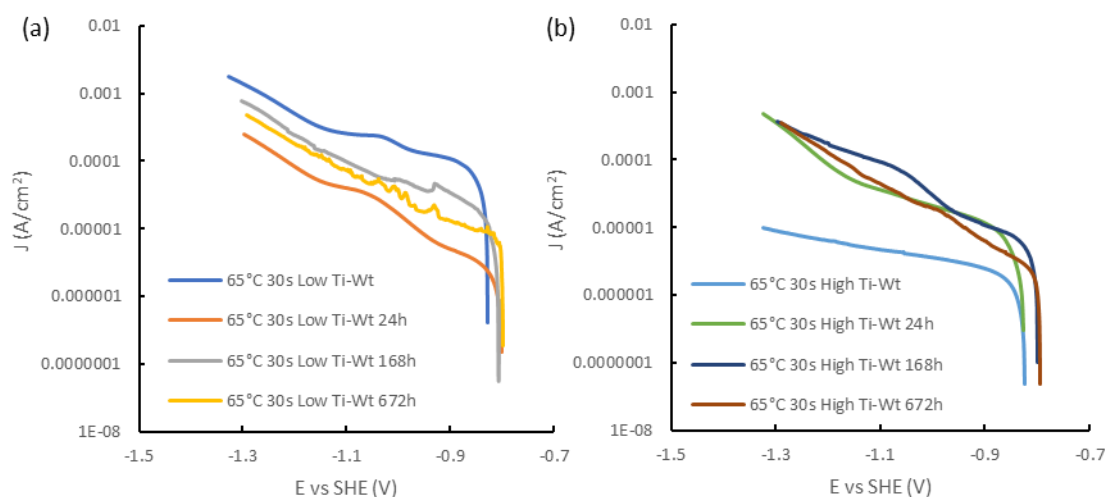

Figure 6.12. Cathodic polarisation curve of HDG with HFT applied aged for 168 hours in 5wt.% NaCl solution

What can be noted from Figures 6.12 is that ageing of the HFT layer results in the suppression of the inflection that is observed on the cathodic-going polarisation curve of HDG, much like a freshly applied pre-treatment layer. As shown in the anodic branch the OCP shifts to slightly more anodic potentials as shown in Figure 6.10. Measured current density change upon polarising the sample shows no observable trend in how cleaning conditions and ageing have on the current density of the surface. Measured currents at -0.9V and -1.2V (vs SHE) also illustrate that there is no observable trend in how increasing ageing time influences the surface when polarised in a cathodic-going potential. Figures of measured current densities can be seen in the appendix to illustrate this.

6.3.2.3. Linear polarisation of aged pre-treatment on HDG

Linear Polarisation of HDG substrates with aged HFT were conducted to see how the influence of ageing of the HFT pre-treatment influences the metal oxidation and oxygen reduction reactions that occurs on the surface when in 5wt.% NaCl solution. The Open Circuit Potential (OCP) of samples were taken before polarisation of the sample, with the potential shifting from -0.01 V below the OCP to +0.01 greater than the OCP. After polarisation, samples were held at the OCP for 30 minutes before polarisation was conducted again. This was done every 30 minutes for 210 minutes to ascertain the corrosion properties of the different substrates over time. From the linear polarisation curves, the polarisation resistance of the substrate can be gathered from the change in current and potential, which subsequently allows for calculation of the corrosion rate, which allows for direct comparisons in the performance and behaviour of tested samples. Polarisation curves and subsequent calculation of polarisation resistances and corrosion rates, it was observed that ageing of the HFT on the surface showed no observable trend in how ageing of the pre-treatment influences the corrosion rate and R_{pol} of the coating. Linear polarisation curves, and calculated R_{pol} and corrosion values can be seen in the appendix.

6.3.3. Investigation of corrosion driven cathodic disbondment kinetics using time-lapse photography and Scanning Kelvin Probe

Time-lapse photography and Scanning Kelvin Probe (SKP) were used to investigate the kinetics of corrosion driven cathodic disbondment of polyvinyl-butyral coatings applied to alkaline cleaned and pre-treated HDG steel substrates. Stratmann cells were created to create a defect region to allow for the initiation of cathodic disbondment and samples were exposed to a 95% relative humidity atmosphere and disbondment was initiated using 5% wt.v sodium chloride solution. Time-lapse images were taken every hour for 120 hours and SKP potentials were measured every hour for 24 hours and the kinetics of coating failure was analysed. Due to the large amount of data produced, only aged pre-treatment deposited on HDG surfaces cleaned at 65°C are shown, with the remaining data shown in the Appendix.

6.3.3.1. Use of time-lapse photography to analyse kinetics of corrosion driven cathodic disbondment

The delamination rate, initiation time and delamination distance of PVB coatings were calculated from measuring the distance covered by coating failure over 120 hours. The influence of variation in the temperature of alkaline cleaning of HDG steel and the application of one or ten applications, denoted low Ti-Wt and high Ti-Wt, on the performance of PVB coatings can be seen below. The delamination distance of cathodic disbondment of PVB on HDG which has been washed in 50°C, 65°C and 80°C for 30 seconds then pre-treated with 1 or 10 wipe application and aged for 24, 168 and 672 hours. The delamination performance of these aged pre-treatment cleaned at 65°C can be seen in Figure 6.13
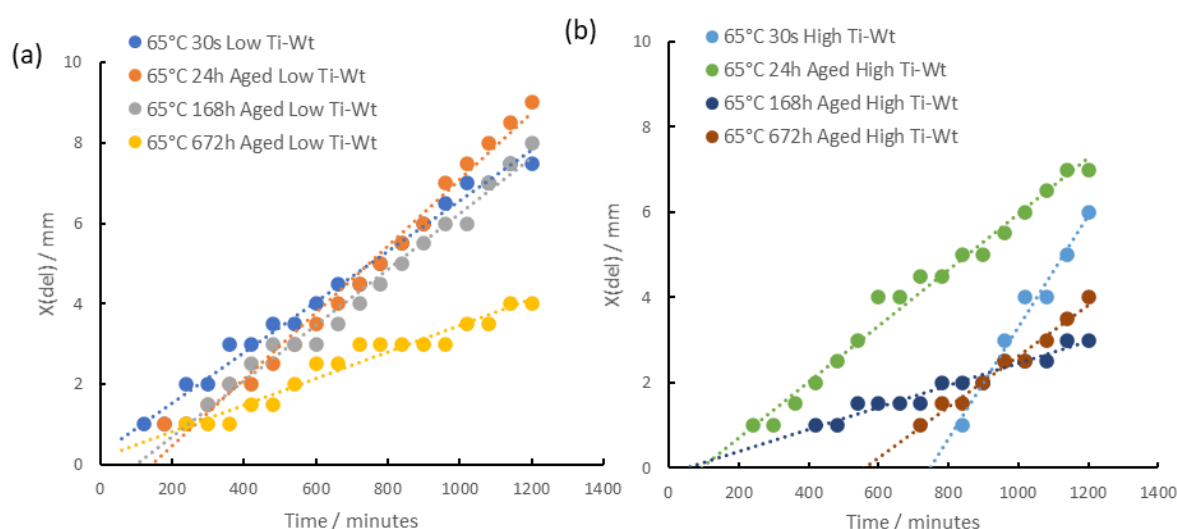

Figure 6.13 Delamination distance versus time plots obtained for aged HFT and PVB coated-HDG steel which had previously been alkaline cleaned at for 30 seconds at varying temperatures; (a) Low Ti-Wt; (b) High Ti-Wt

What can be seen through measurement of the cathodic disbondment under time-lapse conditions is that increasing the ageing time of the HFT applied to the surface typically results in improved delamination performance, with samples aged for 672h showing a reduced maximum delamination distance compared to a fresh pre-treatment layer. Surfaces with 10 wipes of HFT applied also show decreased X_{del} compared to surfaces with only one wipe of HFT applied. The temperature used to clean the surface prior to pre-treatment

application does appear to influence the distance of delaminated PVB, with surfaces cleaned at 80°C with a high Ti-Wt delaminating less than that of surfaces cleaned at 65°C and 50°C. When only 1 wipe of HFT is applied, ageing appears to influence the delamination more than cleaning temperature, with delamination decreasing as ageing time increases, with the three different temperatures showing similar delaminated coating distances of 3.5-8mm at ageing times over 168 hours.

As can be seen in Figure 6.14 ageing of HFT plays a big role in the delamination performance of PVB. There is a clear trend in the relationship between ageing time and delamination distance with the delamination distance reached decreasing as ageing time increases. At 24 and 168 hour ageing times, there is a decrease in the delamination distance as cleaning temperature increases, which also agrees with the data presented in Chapter 5. When the number of wipes applied increase from 1 to 10 wipes, the delamination distance decreases after ageing for 24 and 168 hours, however, the distances measured after 672 hours of ageing all show very similar delamination distances regardless of HFT deposition.
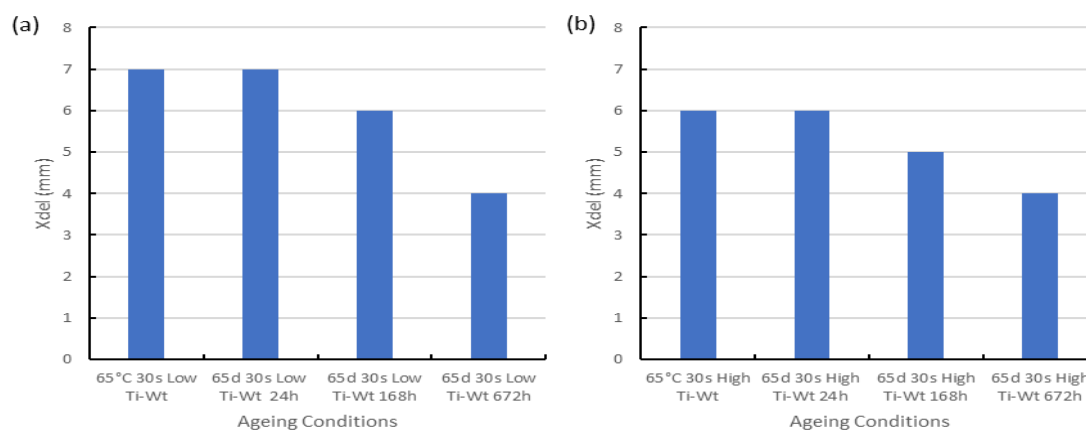

Figure 6.14 Delamination distance from defect of PVB on the surface of alkaline cleaned HDG with and without HFT applied; (a) Surface cleaned at 65°C for 30 seconds; (b) Surface cleaned at 65°C for 10 minutes

The determination of the rate kinetics of pre-treated HDG was calculated by plotting the delamination distance against the square root of time and gives an indication of how cleaning and amount of HFT applied can influence the delamination kinetics. Figures 6.16 show the delamination kinetics of samples cleaned for 30 seconds at 65°C at the varying ageing times, and varying amounts of HFT applied to the surface. What can be seen through the kinetics plot is all samples regardless of cleaning conditions and HFT application show linear

delamination kinetics. This would indicate that the application of HFT on the surface slows the electrochemical reactions that typically occur on the surface, so the electron transfer that occurs between anodic and cathodic sites at the delamination front is impeded.
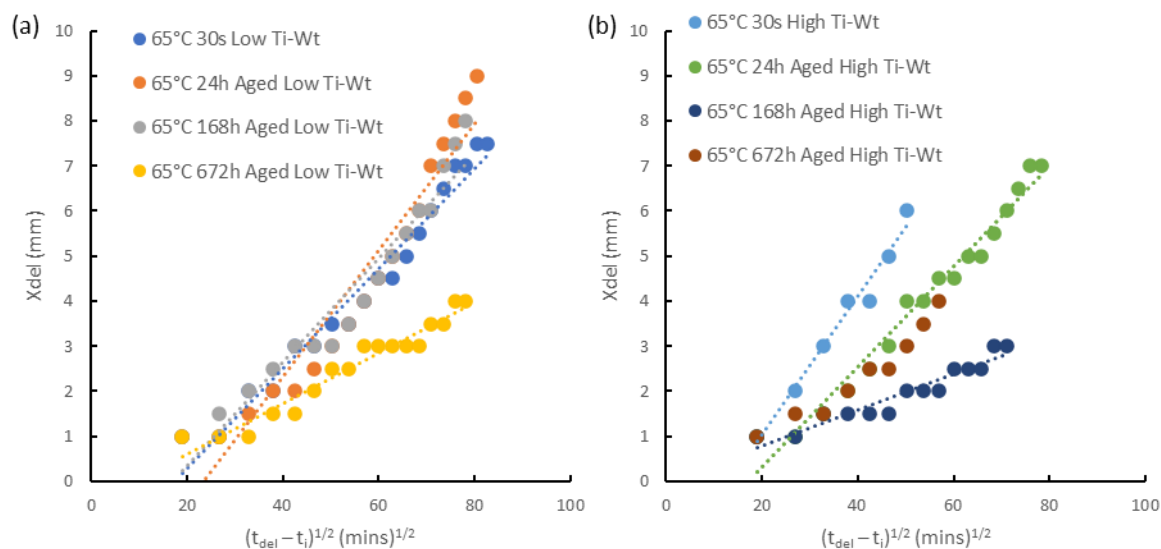

Figure 6.15. Plot of Xdel vs $(t_{del} - t_i)^{1/2}(mins)^{1/2}$ for HFT and PVB coated HDG which had been alkaline cleaned for 30 seconds at varying temperatures; (a) Low Ti-Wt; (b) High Ti-Wt
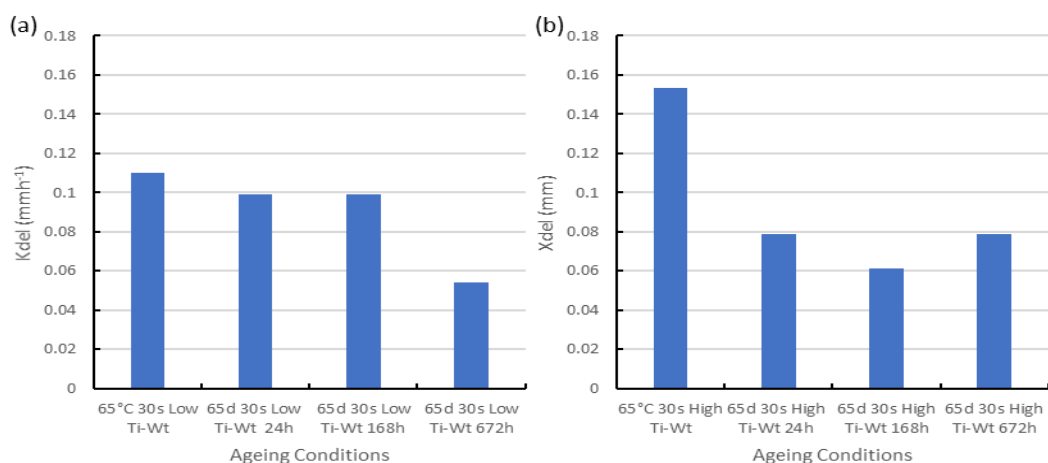

Figure 6.16. Delamination rate of PVB on the surface of alkaline cleaned HDG aged HFT applied; (a) Low Ti-weight; (b) High Ti-weight.

As seen in Figure 6.16 there is a trend in how the intensity of the alkaline wash and the amount of HFT applied influences the delamination rate, with the delamination rate slightly decreasing as ageing time increases. However, the rates are typically variable, with some

samples aged for 672 hours showing similar rates to those aged for 24 hours. The determination of the rate kinetics of the aged pre-treatment also shows similar kinetic behaviour to that produced by fresh HFT substrates. Like fresh HFT, aged HFT exhibits linear kinetics as a result of the pre-treatment acting as a corrosion inhibitor. [1,2] They also show familiar rate values, with fresh HFT showing delamination rates of 0.025 – 0.09 mmh^{-1}, and aged HFT showing delamination rates of 0.039 – 0.139 mmh^{-1}, values which indicate that ageing results in faster overall delamination rates. The temperature at which the substrates are cleaned at before application of HFT has an influence on the delamination rate when delamination is measured on prepared samples, with increasing temperatures resulting in decreased rates. This also occurs to an extent for aged samples, with there being a general decrease in the rate as the cleaning temperature increases, although there is some variability with the rate sometimes increasing by up to 0.1 mmh^{-1} as the temperature increases. The time taken for coating failure to initiate has also been displayed in Figures 6.17.
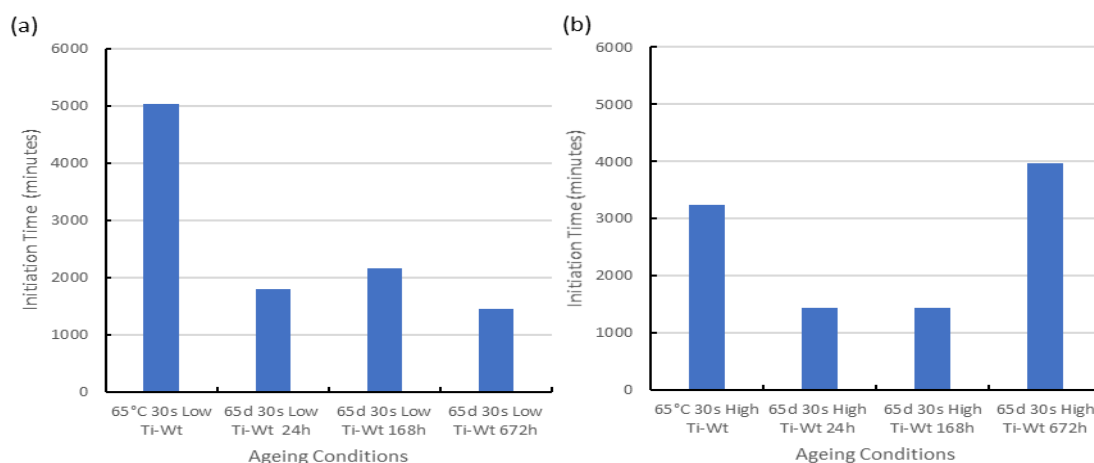

Figure 6.17. Initiation time of alkaline cleaned HDG with and without HFT applied; (a) Surface cleaned at 50°C for 30 seconds; (b) Surface cleaned at 50°C for 10 minutes

The influence of ageing also shows a trend in the initiation time, with the initiation time typically taking longer as ageing time increases. Samples aged for 24 hours will initiate delamination within 1000 – 1800 minutes, samples aged for 168 hours initiate within 1200 – 2500 minutes, and samples aged for 672 hours will initiate within 1000 – 4500 minutes. Samples with a greater amount of HFT applied and washed at identical temperatures will typically take longer to delaminate.

Pre-treated HDG (no ageing) does not begin to delaminate for at least 960 minutes and can take up to 5040 minutes for delamination to occur. Aged pre-treatment shows very similar initiation behaviour, with the earliest initiation time measured at 1080 minutes, and can take up to 4320 minutes to begin delamination. Initiation time typically increases as the amount of HFT wipes applied increases, and does also increase as ageing time increases, with the longest initiation times being shown by high-Ti% coatings aged for 672 hours. The maximum distance delamination reaches also decreases as ageing time increases. Compared to fresh HFT which shows delamination distances of 3 – 7 mm, aged HFT shows distances of 3 – 9 mm, with aged samples showing the best performance, however there isn't a large difference between PVB delamination coated with fresh or aged HFT, indicating that the presence of any HFT will inhibit delamination.

To show the difference alkaline cleaning parameters, along with ageing time, has on the cathodic disbondment of aged HFT coated HDG steel results for the delamination rate, distance, and initiation time of samples cleaned at 50°C, 65°C, and 80°C with high Ti-weight aged for 24-672 hours are shown in Figures 6.18.
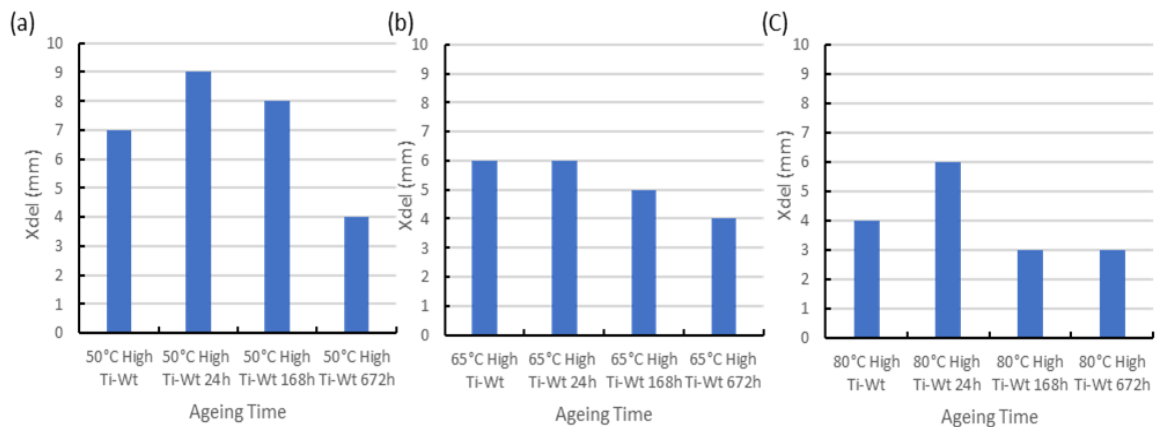

Figure 6.18. Delamination distance from defect of PVB on the surface of alkaline cleaned HDG with Hi-Ti weight HFT applied; (a) Surface cleaned at 50°C for 30 seconds; (b) Surface cleaned at 65°C 30 seconds; (c) Surface cleaned at 65°C 30 seconds

As seen in Figure 6.18 the delamination distance of an aged high Ti-weight pre-treated HDG steel sample has a tendency to decrease as ageing time increases and this occurs at each cleaning temperature. The delamination distance also decreases at cleaning time increases, much like that seen on freshly applied pre-treated surfaces.
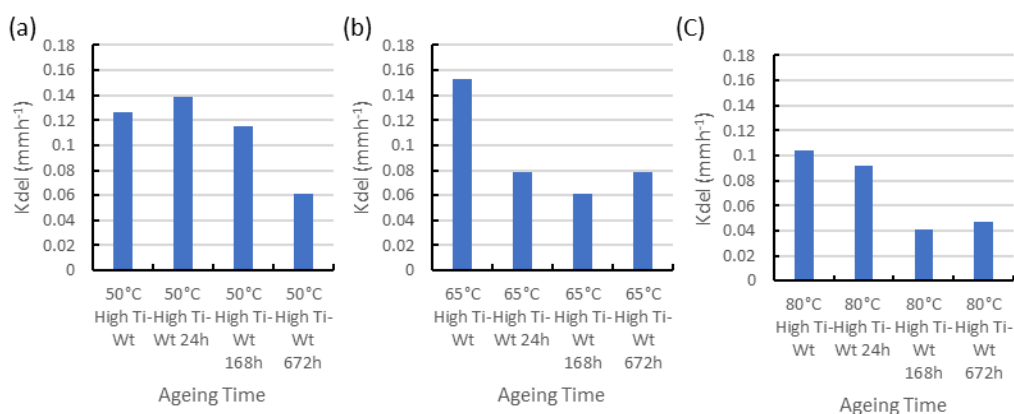
Figure 6.19. Delamination rate of PVB on the surface of alkaline cleaned HDG with Hi-Ti weight HFT applied; (a) Surface cleaned at 50°C for 30 seconds; (b) Surface cleaned at 65°C 30 seconds; (c) Surface cleaned at 65°C 30 seconds

As seen in Figure 6.19 the delamination rate of an aged high Ti-weight pre-treated HDG steel sample decreases as ageing time increases and this occurs at each cleaning temperature, although at surfaces cleaned at 65°C and 80°C the rate increases when ageing increases from 168 hours to 672 hours. The rate also decreases at the same ageing times when the cleaning temperature is increased.
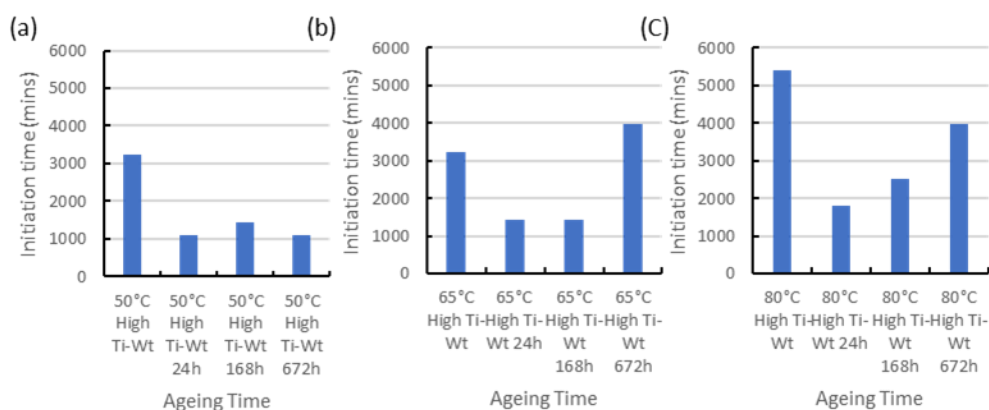

Figure 6.20. initiation time of PVB on the surface of alkaline cleaned HDG with Hi-Ti weight aged HFT applied; (a) Surface cleaned at 50°C for 30 seconds; (b) Surface cleaned at 65°C 30 seconds; (c) Surface cleaned at 65°C 30 seconds

Figure 6.20 shows that the initiation time is not influenced by cleaning time or by ageing time and appears to be completely random, with the ageing time at each temperature showing erratic initiation times.

6.3.3.2. Use of Scanning Kelvin Probe to analyse kinetics of corrosion driven cathodic disbondment

The use of scanning Kelvin probe is to analyse not only the kinetics of the cathodic disbondment of the alkaline cleaned samples with aged HFT but also how the surface potential changes with delamination of the organic coating and whether the surface conditioning changes the measured potentials. Measurements were taken using the minimum cleaning time, with 30 second washing time used at the temperatures used previously. Due to the large number of SKP profiles generated for this chapter, only a selection of SKP profiles have been used, with Figure 6.21 shows the difference in SKP profiles produced through increased ageing time of a low Ti-Wt coating on HDG steel cleaned at 65°C for 30 seconds, the remaining SKP profiles can be seen in the Appendix. The alkaline cleaning conditioned used for these profiles was 65°C for 30 seconds, with 1 or 10 HFT applications and aged for 24, 168 and 672 hours respectively before PVB application.
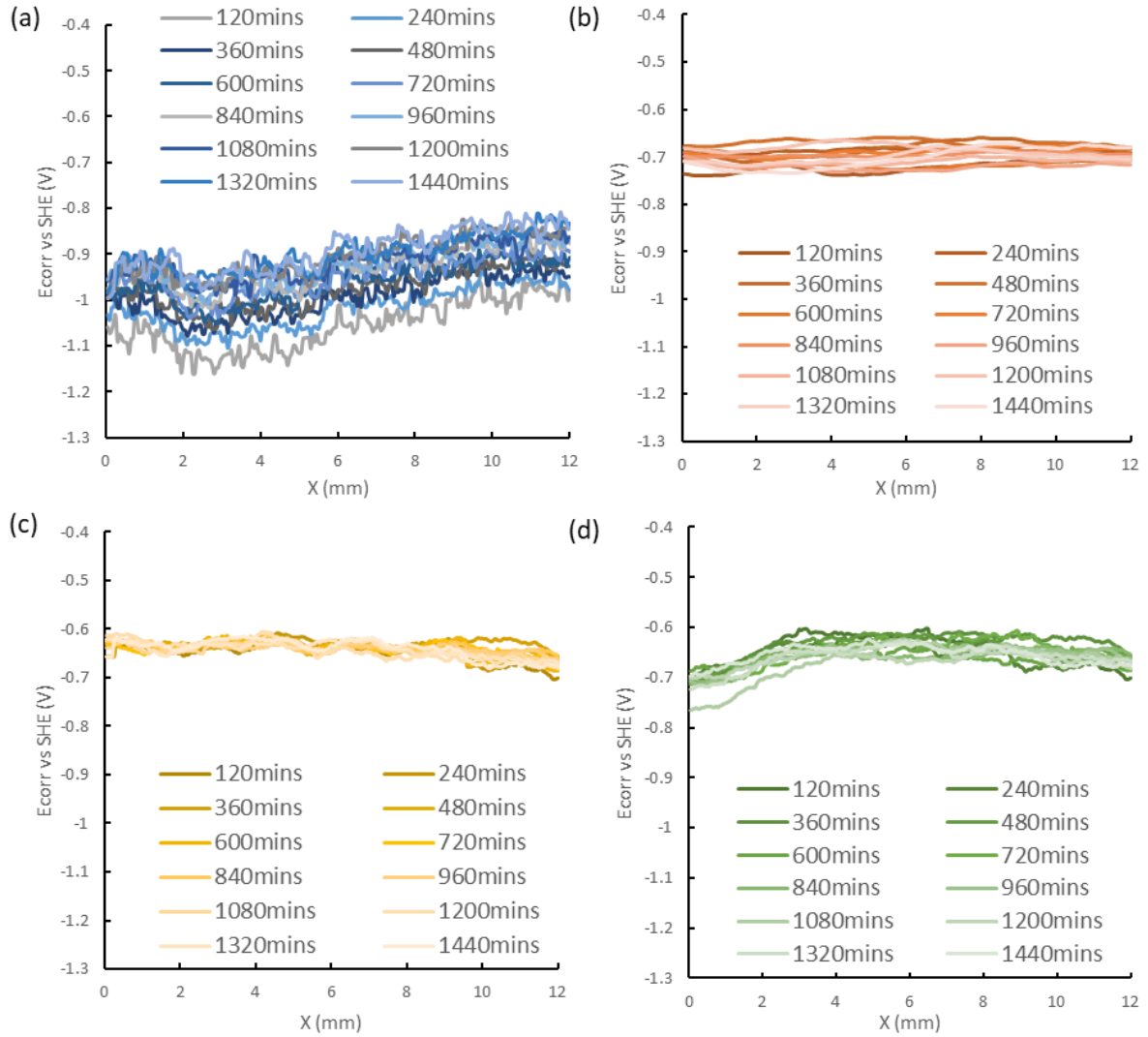
Figure 6.21. SKP profiles showing the time dependent E_{corr} measurements against distance from defect (X) for 65°C, 30 second alkaline cleaned surface with 1 wipe of HFT aged for: (a) 0 hours (b) 24 hours; (c) 168 hours; (d) 672 hours. E_{corr} measurements were taken every hour for 24 hours

Figure 6.21 shows that much like a fresh HFT coating (a), ageing the pre-treatment layer causes no delamination of the PVB coating within 24 hours, but does appear to shift the E_{corr} values to more anodic potentials. The differences in the average E_{intact} of the PVB coating can be seen in Figure 6.22, and the change in E_{intact} over 24 hours can be seen in Figure 6.23.
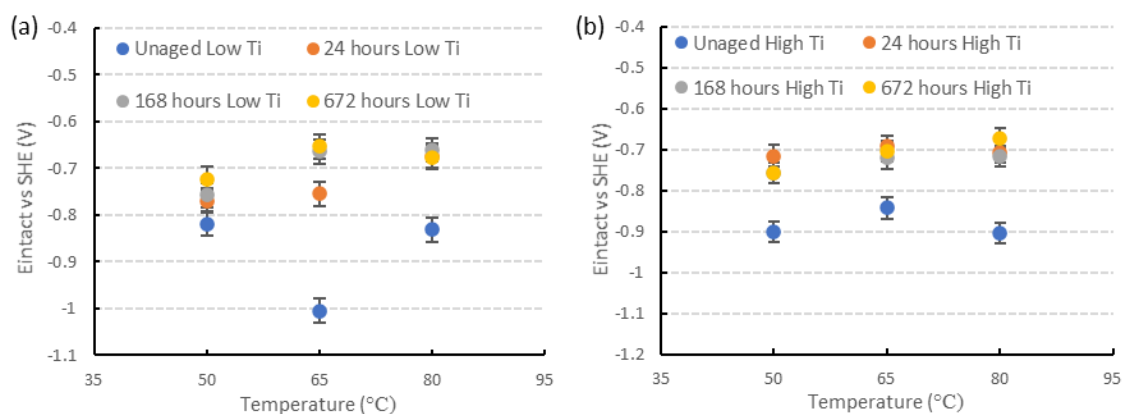
Figure 6.22 Change in average intact potential of PVB coating over time for HDG alkaline cleaned for 30 seconds at 50°C, 65°C and 80°C with aged HFT applied.
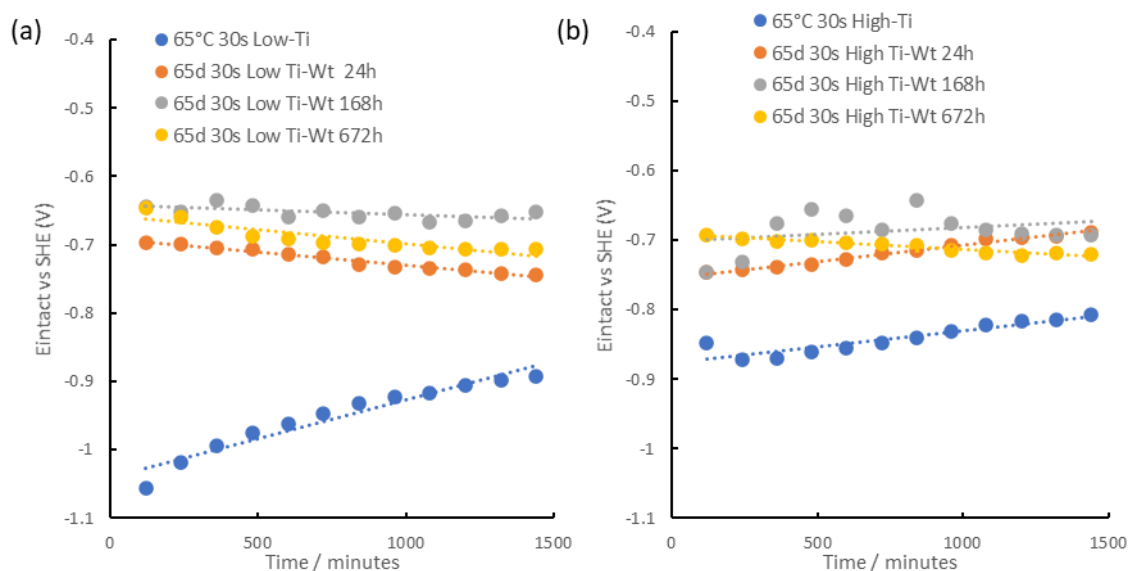

Figure 6.23. Change in intact potential of PVB coating over time for HDG alkaline cleaned for 30 seconds at 50°C, 65°C and 80°C with aged HFT applied.

The scanning Kelvin probe analysis conducted alongside the time-lapse imaging shows different observable behaviour to the results seen from time-lapse imaging. Time-lapse imagining shows that coating delamination initiates within 24 hours whereas no delamination is observed on SKP profiles. No detection of delamination could be because 24 hours is too short a timeframe for the experiment (like that seen in Chapter 5), or the intact potential is the same as the delamination zone potential. As no delamination rate data can be calculated due to no delamination occurring, the variation in the intact potential (E_{intact}) of the PVB coating as a function of the amount of HFT and ageing time was calculated. What is shown through

the intact potential measurements is the average E_{intact} becomes more anodic as ageing time is increased, however the largest difference in the average E_{inact} between samples is only 0.117 V, which is not a large enough difference in potential shift to comment on the behaviour of the intact coating. The average E_{intact} for all aged samples is also more anodic compared to that of fresh HFT, indicating ageing has an influence on the measured coating potential and likely plays a role in supressing the cathodic reduction reaction that occurs on the under-film surface, with the average E_{intact} of the coating is measured between -0.77 and -0.65 V for aged HFT, compared to measured E_{intact} of -0.95 and -0.65 V for fresh HFT. The E_{intact} of the coating over the scanning time of all aged HFT samples indicate that the pre-treatment is suppressing the corrosion reactions that would usually occur at the steel/electrolyte and coating/electrolyte interfaces by providing a barrier preventing the electrolyte from interacting with the steel. [3] The E_{intact} also tends to vary as a function of time spent in contact with electrolyte solution, with freshly deposited HFT surfaces showing increasing E_{intact} values at all cleaning temperatures, whereas the E_{intact} values of aged surfaces changes both as a function of ageing and surface cleaning temperature. There are both negative and positive trends seen in the E_{intact} at varying ageing times, however changes are typically measured as a -0.1V difference over the course of the experiment.

6.4. Conclusion

Titanium XRF measurements of aged HFT shows that Ti-weight of the coating drops as ageing time increases. XPS analysis of aged HFT coating on steel indicates a very similar surface chemistry to that of un-aged HFT surfaces, with the titanium atomic composition remaining relatively stable between 0.6-1.2%, with the presence of corrosion inhibitors such as manganese phosphate, and polymeric oxygen and carbon which aid in adhesion of model PVB coating being present on the surface.

Electrochemical tests performed show similar behaviour under anodic and cathodic conditions for aged HFT vs unaged HFT, with similar passive regions measured for aged samples compared to that seen for unaged surfaces. The cathodic polarisation curves produced illustrate similar behaviour, however the measured OCP typically becomes less negative as ageing time increases indicating the surface supresses the cathodic reaction on the surface. Linear polarisation curves and subsequent calculated polarisation resistances show that the polarisation resistance typically drops as time immersed in corrosive solution

increases, however, polarisation resistances as a function of surface cleaning time and ageing are variable. The corrosion rates calculated from polarisation resistances show that ageing has no real influence on the corrosion rate, with typical corrosion rates measured between 0-40 μm/year, with some samples (65°C low Ti-Wt. 50°C high T-Wt) showing corrosion rates up to 190 μm/year.

The corrosion driven cathodic disbondment behaviour of PVB with aged HTT behaves much like PVB applied on freshly deposited HFT, with delamination distances measured at 3 -9 mm for aged HFT and 2.5 – 7.5 mm for unaged HFT (excluding uncleaned surfaces). Much like fresh pre-treatment, the ageing of the HFT shows linear rate kinetic behaviour indicating the aged pre-treatment suppresses anodic-cathodic electron transfer. This improved behaviour can be linked to the polarisation behaviour of the surfaces, with ageing typically showing more anodic OCP measurements, which would indicate increased suppression of the anodic metal dissolution reaction. This increased delamination performance has an inverse relationship with the Ti-weight, with measured Ti-weight decreasing as ageing time increases. This would indicate that the amount of Ti on the surface is not directly linked to the cathodic disbondment behaviour, and there is a minimum deposit of Ti on the surface the coating will resist cathodic delamination. although the increased performance lined to ageing cannot be explained at this stage.

6.5. References

1.   Geraint W, McMurray HN, Williams G, McMurray H. Chromate inhibition of corrosion driven organic coating delamination studied using a scanning Kelvin probe technique. *J Electrochem Soc*. 2001;148(10):B377. doi:10.1149/1.1396336

2.   Geraint W, McMurray HN, Worsley DA, Williams G, McMurray H. Cerium(III) inhibition of corrosion-driven organic coating delamination studied using a scanning Kelvin probe technique. *J Electrochem Soc*. 2002;149(4):B154. doi:10.1149/1.1457983

3.   Fu AQ, Cheng YF. Characterization of corrosion of X65 pipeline steel under disbonded coating by scanning Kelvin probe. *Corros Sci*. 2009;51(4):914-920. doi:10.1016/J.CORSCI.2009.01.022

7. Conclusions

Alkaline cleaning has a direct influence of the surface chemistry of both HDG and 4.8%-Al steel surfaces as determined by XPS analysis. Observed elemental content of zinc oxide decreasing and metallic zinc increasing as cleaning temperature and/or time is increased. Aluminium is completely removed from steel surfaces under all alkaline cleaning parameters (50-80°C, over time periods of 30 seconds to 10 minutes).

Anodic polarisation of HDG substrates show that alkaline cleaned surfaces exhibit very little difference in observed behaviour. This was similar in all tested specimens. Similar behaviour is shown by Galvalloy substrates, with passivity being almost non-existent when polarised.

Under cathodic-going polarisation, the surface of cleaned HDG would appear to become a more active oxygen cathodes as cleaning intensity is increased, with progressive increases in current density with increased cleaning temperature and time over the same potential range. There is also an interesting increase in current that occurs -1.1V vs SHE into the cathodic branch, with zinc oxidation reoccurring on the surface that could cause a sudden inflection in current. Similar behaviour is seen in Galvalloy substrate with more intense cleaning indicating the surface becoming a more active oxygen cathode as cleaning temperatures increase or when cleaning time is increased at a set temperature There is also the inflection in current that occurs -1.1V vs SHE that occurs during cathodic-going polarisation of HDG, with an additional inflection being observed that which could indicate oxidation of aluminium and zinc on the surface when cathodically polarised.

Linear polarisation of cleaned HDG shows a drop in the polarisation resistance of substrates as time in 5% NaCl increases, and increasing the cleaning time and/or temperature results in a drop in the initial and average polarisation resistance. Polarisation resistances of HDG surfaces becomes relatively constant after 30-90 minutes immersion in 5% NaCl, with most cleaned surfaces having similar R_{pol} values of 100-400Ω. Calculation of corrosion rates shows that when the cleaning time is kept at 30 seconds, the corrosion rate decreases with increasing cleaning temperature. When the cleaning time is maintained at 10 minutes, and the cleaning temperature is increased, the corrosion rate shows the opposite trend where the rate rises with increasing temperature.

Polarisation studies of alkaline cleaned Galvalloy specimens show decreased R_{pol} compared to an uncleaned sample. Polarisation resistances stabilise after 30 minutes in electrolyte solution

and measured R_{pol} values of 100-400Ω are calculated, with cleaning temperatures of 80°C providing the lowest R_{pol}. Calculation of the corrosion rate on Galvalloy surfaces shows similar corrosion rates for all Galvalloy surfaces irrespective of cleaning parameters sued. When the temperature increases at a 30 second cleaning time the corrosion rate decreases, and when the time is held at 10 minutes the corrosion rate increases as temperature is increased. However unlike HDG, a control Galvalloy surface exhibits the lowest corrosion rate indicating the intact oxide film on the surface suppresses the corrosion rate.

Studies of the corrosion driven cathodic disbondment using time-lapse imaging and SKP techniques show that time and temperature of alkaline cleaning also have a significant effect on the observed rate of delamination of a model PVB protective coating. As the cleaning time and temperature are increased, the delamination rate increases because the immersion in alkaline cleaning solution produces a more electroactive cathode and decreases the PVB performance. As the cleaning time is increased at each temperature the delamination rate and the distance travelled by the delaminated coating over a 24h holding time also typically increases. This behaviour is also observed when the cleaning temperature is increased for a given cleaning time. The SKP profiles of alkaline cleaned HDG surfaces illustrate a greater driving force for delamination when the surface has undergone more intense cleaning, either at higher temperature or increased times. This increased driving force is demonstrated by a shift of the intact potential of the coated metal to more positive values when the cleaning temperature is increased at each cleaning time. The greater the difference between the intact potential and the corrosion potential in the defect, then the greater the driving force for cathodic delamination to occur.

Similar behaviour is observed for Galvalloy substrates, where delamination rate and disbondment distance observed within 24h both increase as cleaning intensity is increased. The performance of Galvalloy substrates in resisting corrosion-driven organic coating disbondment is improved compared to that of HDG, showing at least a 45% reduction in the coating delamination determined for identical cleaning times and temperatures. The intact potential of Galvalloy is more negative than that of HDG, although its defect potential is similar, thus indicating a reduced driving force for cathodic delamination to occur. The rate kinetics of cleaned HDG and Galvalloy typically exhibit parabolic kinetics, whereby the relationship between delamination distance and time exhibits parabolic dependence of observed delamination on time. The rate limiting step in the delamination process is transport of Na^+ cations from the defect to the cathodic disbondment front to produce the parabolic

curves. Uncleaned Galvalloy exhibits linear kinetics, which is caused by a change in the rate limiting step where cathodic oxygen reduction at the disbondment front is the slowest step. This difference in kinetics could be a result of the intact oxide film and greater aluminium content present on uncleaned Galvalloy, providing inhibition to cathodic delamination.

Hexaflourotitante pre-treatment was applied to the surface of alkaline cleaned HDG using Henkel 1445 M-NT pre-treatment wipes. Wipes were applied across the surface either once, or ten times which should increase the amount of pre-treatment on the surface. XPS analysis of HFT coating on steel indicates the presence of corrosion inhibitive compounds such as manganese phosphate and titanium dioxide, along with polymeric oxygen and carbon which aid in adhesion of model PVB coating. The application of HFT surface treatment results in deposition of titania on the surface, with XRF analysis showing an increasing in the titanium coating weight on the surface when the amount of HFT applied to the surface is increased. For substrates subjected to the same HFT pre-treatment process, XRF analysis showed that the titanium weight increased in line with both increasing alkaline cleaning temperature and exposure time.

Anodic polarisation of HFT pre-treated HDG shows a passive region in the anodic branch of ~0.1-0.15V, which is not present on untreated HDG steel. In the cathodic branch, the inflection observed at ~1.1V (vs SHE) is not present, indicating the pre-treatment layer supresses additional surface reactions. The initial increase in current density in the cathodic branch is greater for pre-treated HDG compared to the current density measured for uncoated HDG. When titania weight is increased on the surface the measured current density at the beginning of the cathodic-going polarisation curve also increases.

Polarisation resistances produced are slightly increased upon addition of one wipe of HFT compared to uncoated HDG steel, while increasing alkaline cleaning time of the steel substrate at a fixed temperature results in significantly higher polarisation resistances following HFT coating application. Corrosion rates calculated show that the alkaline cleaning of the surface prior to HFT deposition has a greater influence on measured corrosion rates than the amount of HFT applied. Surfaces cleaned at 30 seconds with low or high Ti-weights show similar corrosion rates to that of uncleaned HDG with measured rates in the 13 - 31 µm/year range. When the cleaning time increases to 10 minutes the corrosion rate is measured between 25 – 56 µm/year.

Compared to un-treated HDG, the application of HFT greatly improves the corrosion protection performance of model PVB coatings determined in time-lapse experiments. The application of HFT layer and duration of alkaline cleaning at a set pre-treatment application regime both exert a significant influence the cathodic disbondment behaviour of HDG. PVB coating delamination initiates within 6 hours using un-treated HDG, whereas this increases to ca 16h for PVB coated HFT pre-treated substrates . Increasing the titanium weight of the HFT layer on the surface further increases the time taken for coating delamination to initiate. The distance that coating disbondment front reaches on pre-treated HDG after 120 hours is also significantly reduced compared to that seen for untreated HDG after a similar holding time, and also decreases when additional HFT is applied. The delamination rate, characterised by the slopes of distance versus time plots, also shows similar behaviour, where rates are suppressed by the application of pre-treatment and linear disbondment kinetics are observed. This observation suggests that the pre-treatment provides underfilm cathodic inhibition, making oxygen reduction at the disbondment front the rate determining step in the coating failure process.

In-situ SKP analysis of PVB-coated HDG surfaces which had been HFT pre-treated beforehand showed that the intact potential was significantly depressed compared to an alkaline cleaned control. The similarity of both intact and defect potentials within the delamination cell meant that E_{corr} versus distance profiles could not be correlated with visual evidence of organic coating delamination over a 24h period. When the experiment time was extended to 72 hours, some evidence of delamination was detected from E_{corr} versus distance profiles after 40 hours, where measured potentials in the apparent delamination zone became more positive. The difference between the measured intact and defect corrosion potentials is much smaller than that those observed in the SKP profiles of untreated HDG and Galvalloy steels, indicating a much reduced driving force for delamination to occur, thus confirming the ability of the HFT layer to inhibit underfilm oxygen reduction.

Titanium XRF measurements of aged HFT layers applied to HDG showed that the Ti-weight of the coating decreased with increasing ageing time, however, XPS analysis of aged HFT coatings indicated a very similar surface chemistry to that of un-aged HFT surfaces, with the titanium atomic composition remaining relatively stable between 0.6-1.2%, but the fluoride content drops as ageing time increases and is typically lower than that seen for freshly applied HFT. The behaviour of aged HFT when anodically polarised is similar to that of freshly deposited HFT, with similar passive regions in the anodic branch. In the cathodic

branch, fresh HFT shows greater increase in current density under cathodic-going polarisation when the surface is washed at 50°C at low and high Ti-weight and at 65°C with low Ti-weight compared to aged HFT. This would indicate that aged HFT is a less reactive surface when the surface is cleaned at these conditions.

Linear polarisation curves and subsequent calculated polarisation resistances show that R_{pol} typically drops as time immersed in corrosive solution increases, however measured R_{pol} as a function of surface cleaning time and ageing are variable. The corrosion rates calculated from polarisation resistances show that ageing has no real influence on the corrosion rate, with typical corrosion rates measured between 0.19-40 μm/year, with some samples (65°C low Ti-Wt. 50°C high Ti-Wt) showing corrosion rates of up to 190 μm/year.

The corrosion driven cathodic disbondment behaviour of PVB with aged HFT behaves much like PVB applied on freshly deposited HFT, where delamination distances measured at 3 -9 mm for HDG with HFT applied aged between 24 - 672 hours and 2.5 – 7.5 mm for unaged HFT (excluding uncleaned surfaces). Aged HFT shows linear rate kinetics like fresh HFT which is in agreement with the observations made using freshly deposited HFT pre-treatment. The improved delamination performance of the model PVB coating has an inverse relationship with the Ti-weight. As the with measured Ti-weight decreases as ageing time increases, the delamination rate decreases as the ageing time is increased. At each cleaning temperature K_{del} of PVB applied on a 672 hour aged HFT surface is ca. half of that of PVB applied to a freshly applied HFT layer. Delamination kinetics remain linear for aged HFT pre-treatment indicating the same rate-limiting step as freshly deposited HFT. The observed kinetics would indicate that the amount of Ti on the surface is not directly linked to the rate limiting step during cathodic disbondment, and if there is a minimum deposit of Ti on the surface the coating will resist cathodic delamination, although the increased performance linked to ageing cannot be explained at this stage. The SKP profiles of aged HFT show that the intact potential of aged shifts to more positive potentials compared to that of unaged HFT, which would indicate that ageing may cause the HFT to be less effective and inhibiting underfilm oxygen reduction, although observation of delamination rates would contradict this observation.

8. Future Work

- Environmental corrosion testing such as humidity or salt spray testing on fully coated (no defects) steels to assess how cleaning and pre-treatment application influences coating performance and to evaluate whether rusting or blistering occurs beneath the coating.

- Analysis of corrosion products formed on pre-treated surfaces using X-ray photoelectron spectroscopy (XPS) would quantify and identify what corrosion products have formed. Understanding the chemistry of corrosion products would give evidence of inhibition mechanisms.

- Hot dipped galvanised (HDG) steel is a widely used substrate for organic coatings. Further work could be done to investigate the effect of pre-treatments on Galvalloy and other alloy steels. Changing the substrate will change the mechanism of corrosion with different ions being released and different pH values being reached in the under-film environment, and a variation in the type of corrosion products formed.

- Model coatings such as PVB are ideal for analysing how corrosion mechanisms occur on a surface, but are not typically used in industrial coating systems. Systematic trials with industrial partners varying the cleaning parameters and pre-treatment conditions prior to the application of commercially available paint systems could be conducted to assess how organically coated steel products perform when defects are introduced within the coating system.

- The surface chemistry and corrosion behaviour of aged pre-treatment compared to freshly applied pre-treatment needs to be investigated further. As ageing time is increased, XRF shows a decrease in the titanium weight, whereas XPS shows similar atomic contents of Ti on the surface, and further investigation such as using XPS depth profiling could be used to examine how the Ti content changes throughout the coating.

- Initial work into how the concentration of soluble metallic elements are removed from the surface during cleaning was conducted and is unfortunately not included in this thesis. Further work could be done to measure the concentration of soluble aluminium and zinc released into the cleaning solution from the surface of HDG and 4.8%-Al steels during cleaning through measurement using Microwave-Plasma Atomic Emission Spectroscopy (MP-AES).

- The influence of alkaline cleaning could also be conducted on other corrosion inhibitor systems using in industry such as zirconate or mixed titanate/zirconate systems to see if these systems produce similar results as the titanate system described in this thesis.

9. Appendix

Sample	AlOx (Atomic %)	Carbon (Atomic %)	Oxygen (Atomic %)	ZnOx (Atomic %)
HDG 1	16.38	30.08	48.6	4.94
HDG 2	15.68	33.38	46.52	4.42
HDG 3	13.94	40.02	41.96	4.08
HDG 4	18.68	30.34	45.81	5.16
HDG 5	17.48	32.27	46.3	3.95

Table 9.1. Quantified contents of HDG controls derived from XPS peaks.
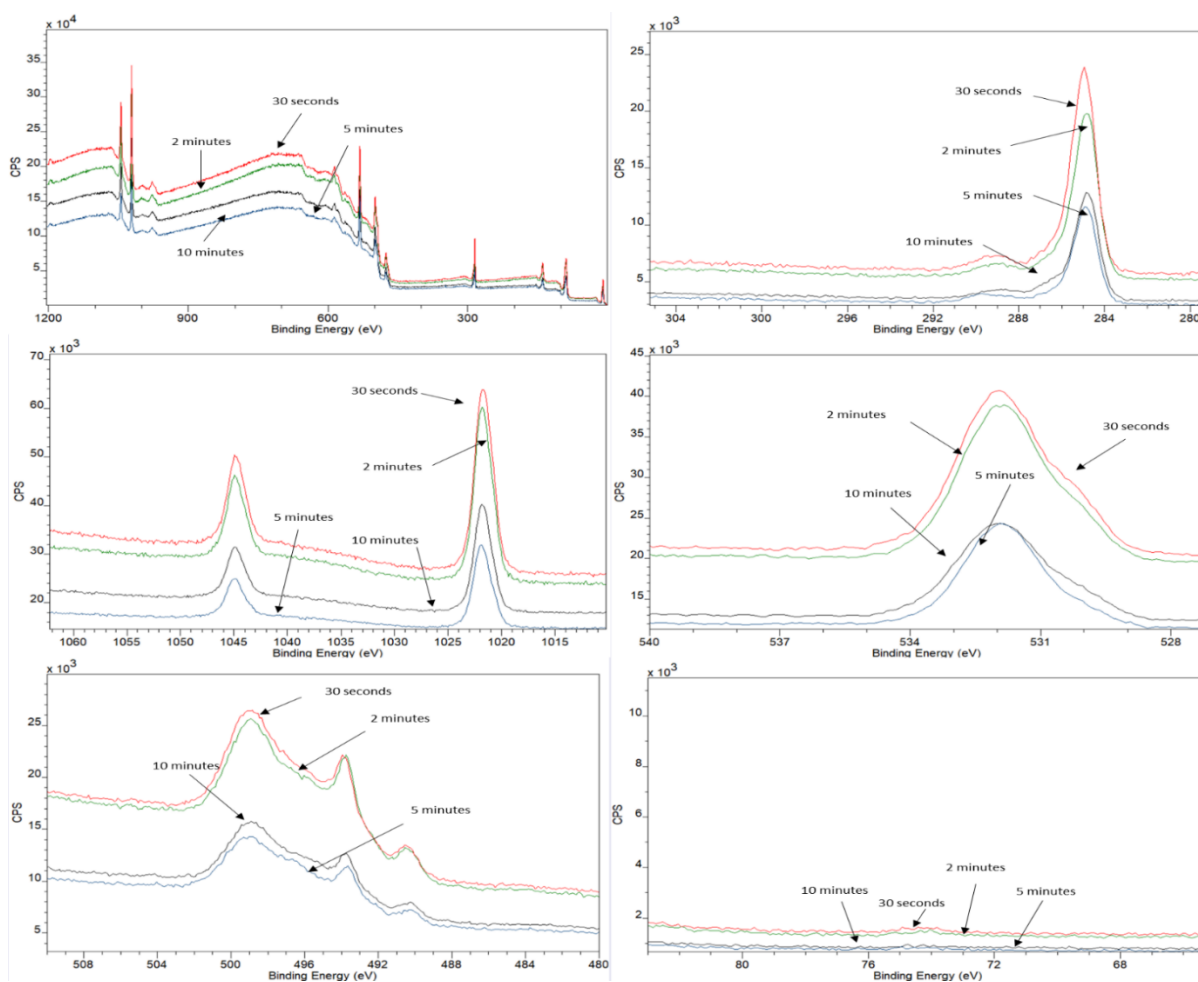
Figure 9.1. X-ray photoelectron spectroscopy analysis of HDG alkaline cleaned at 80°C for varying times. (a) wide spectral analysis (b) carbon analysis; (c) zinc analysis; (d) oxygen analysis; (e) zinc Auger analysis; (f) aluminium analysis
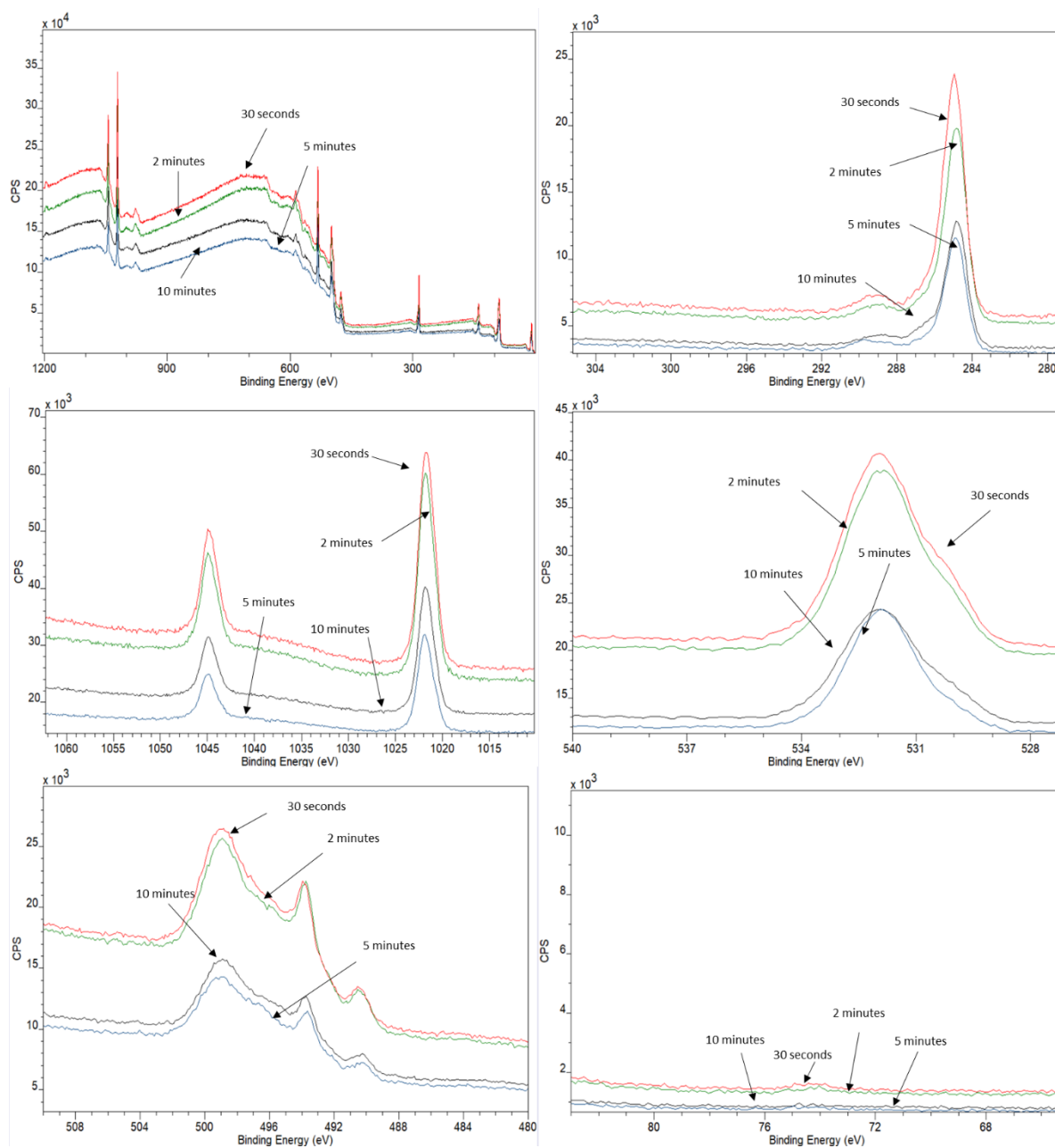
Figure 9.2. X-ray photoelectron spectroscopy analysis of HDG alkaline cleaned at 80°C for varying times. (a) wide spectral analysis (b) carbon analysis; (c) zinc analysis; (d) oxygen analysis; (e) zinc Auger analysis; (f) aluminium analysis
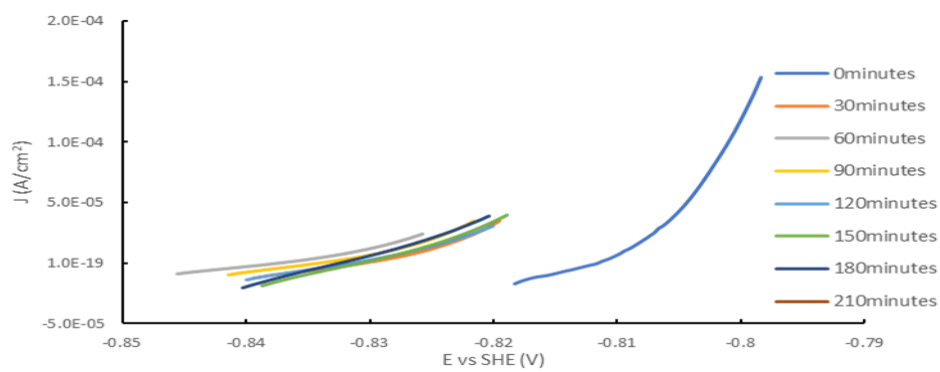
Figure 9.3. Linear Polarisation curve of HDG alkaline cleaned at 50°C for 10 minutes. Polarisation was conducted every 30 minutes for 210 minutes.
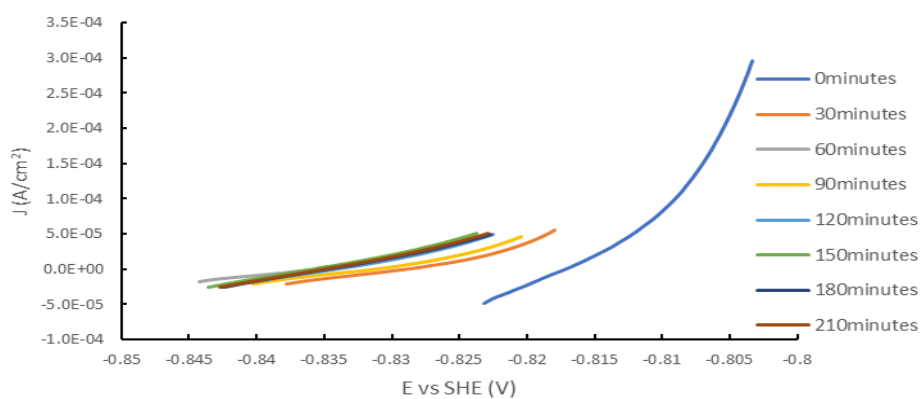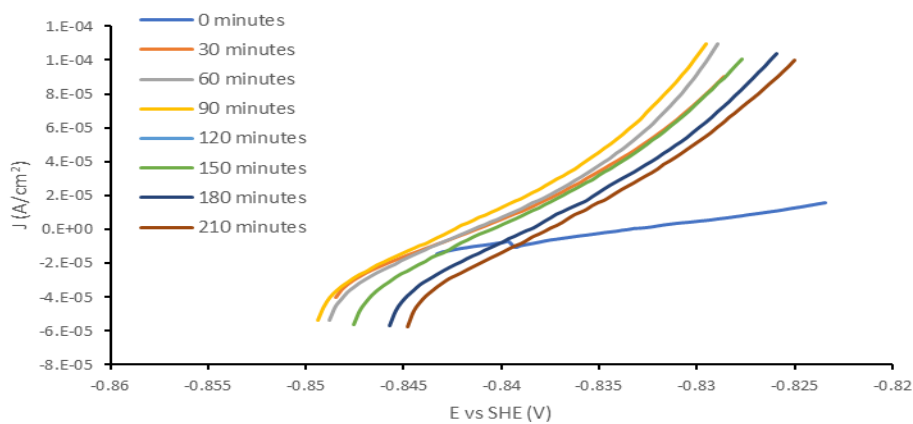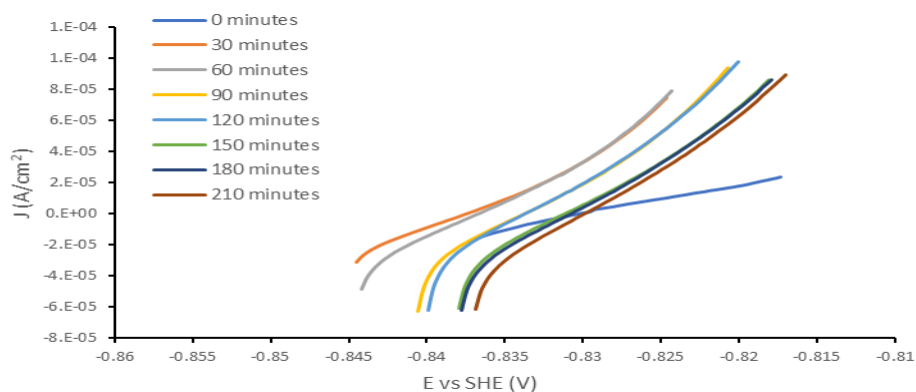

Figure 9.4. Linear Polarisation curve of HDG alkaline cleaned at 65°C for 10 minutes. Polarisation was conducted every 30 minutes for 210 minutes.
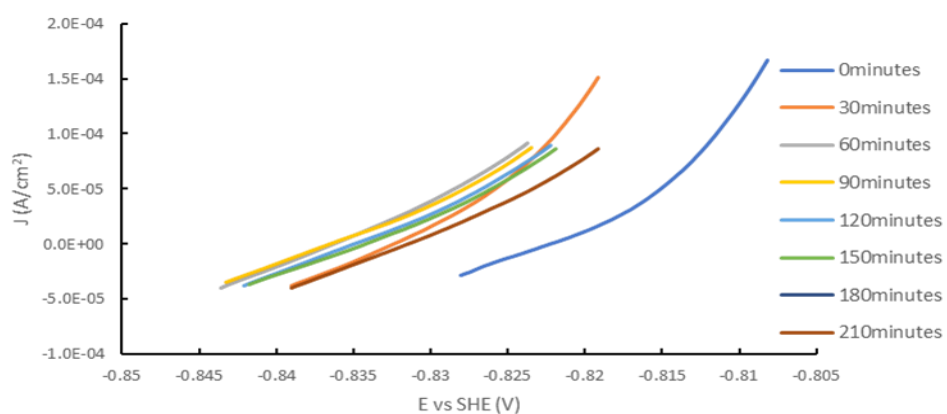
Figure 9.5. Linear Polarisation curve of HDG alkaline cleaned at 80°C for 10 minutes. Polarisation was conducted every 30 minutes for 210 minutes.
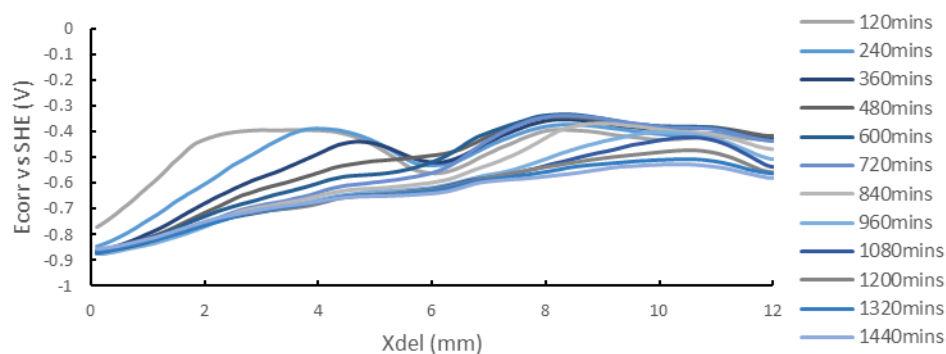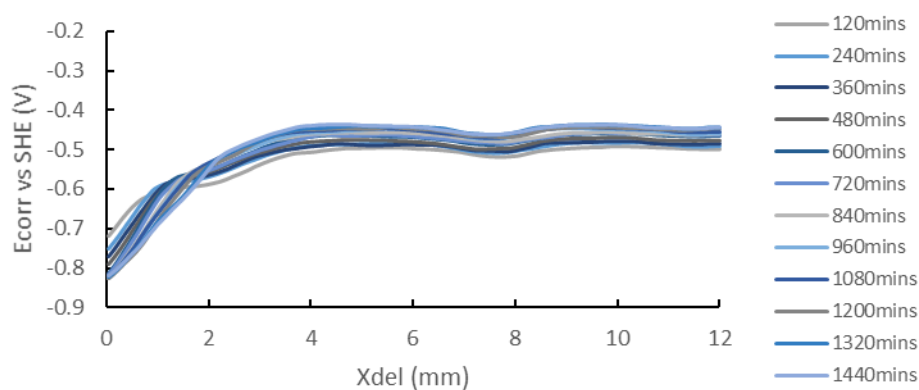
Figure 9.6 A graph showing the time dependent E_{corr} measurements against distance from defect (X) for 50 °C, 30 seconds alkaline cleaned surface with PVB coating from a HDG sample. E_{corr} measurements were taken every hour for 24 hours, with measurements shown every 2 hours.
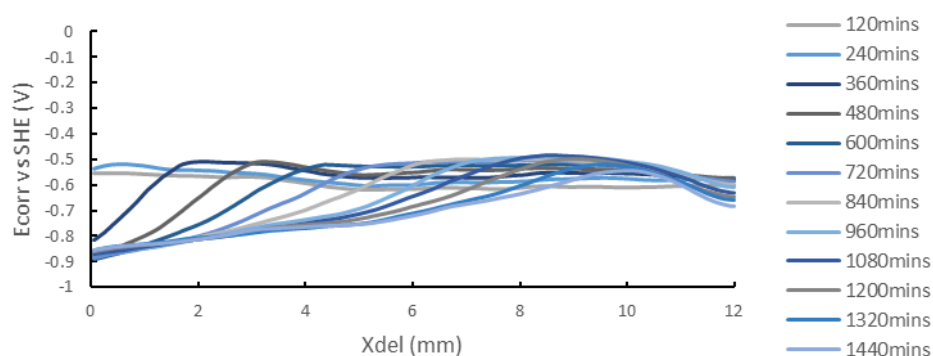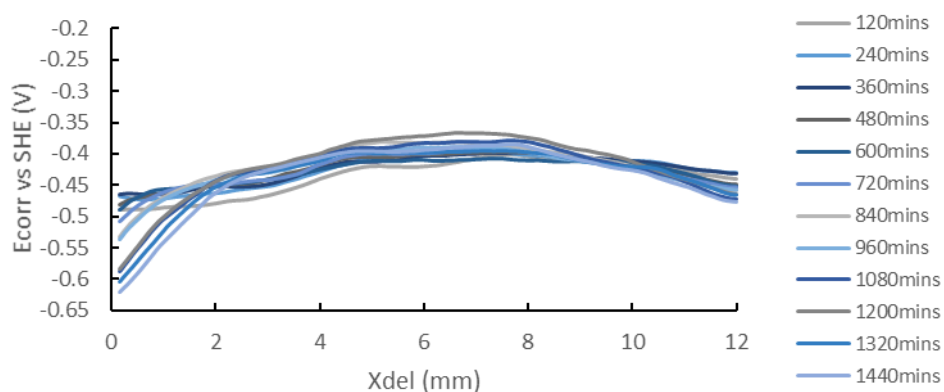

Figure 9.7 A graph showing the time dependent E_{corr} measurements against distance from defect (X) for 65 °C, 30 seconds alkaline cleaned surface with PVB coating from a HDG sample. E_{corr} measurements were taken every hour for 24 hours, with measurements shown every 2 hours.
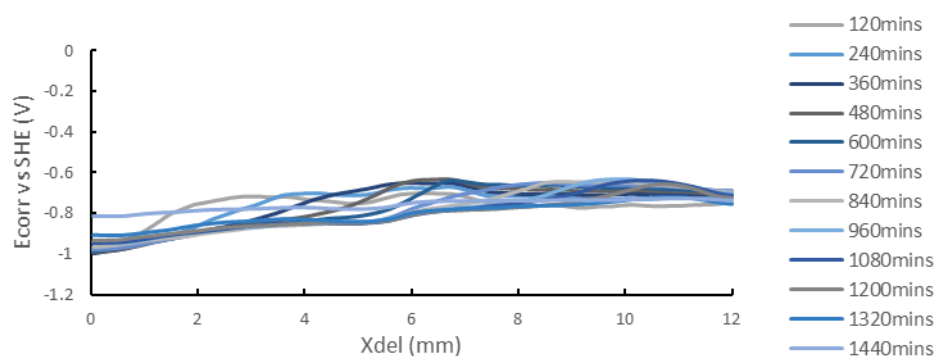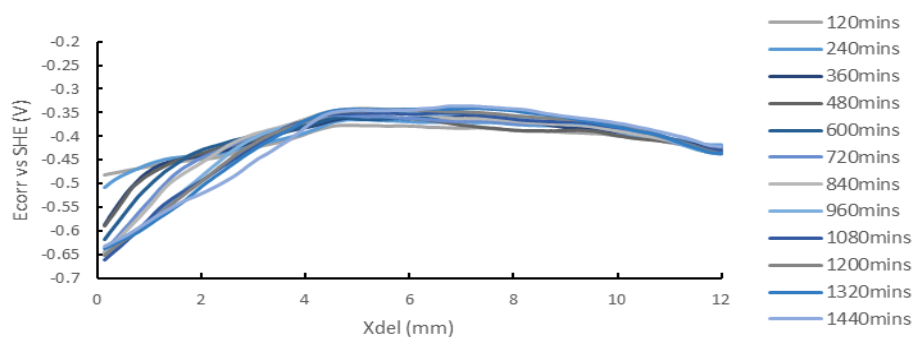

Figure 9.8 A graph showing the time dependent E_{corr} measurements against distance from defect (X) for 80°C, 30 seconds alkaline cleaned surface with PVB coating from a HDG sample. Ecorr measurements were taken every hour for 24 hours, with measurements shown every 2 hours.

Sample	AlOx (Atomic %)	Carbon (Atomic %)	Oxygen (Atomic %)	ZnOx (Atomic %)
ZA 1	19.14	29.9	45.54	5.42
ZA 2	15.07	32.25	47.5	5.18
ZA 2	16.79	31.3	47.47	4.44
ZA 3	11.24	37.98	44.52	6.26
ZA 4	25.95	27.17	44.36	2.51
ZA 5	21.72	32.27	41.66	4.35

Table 9.2. Quantified contents of Galvalloy controls derived from XPS peaks.
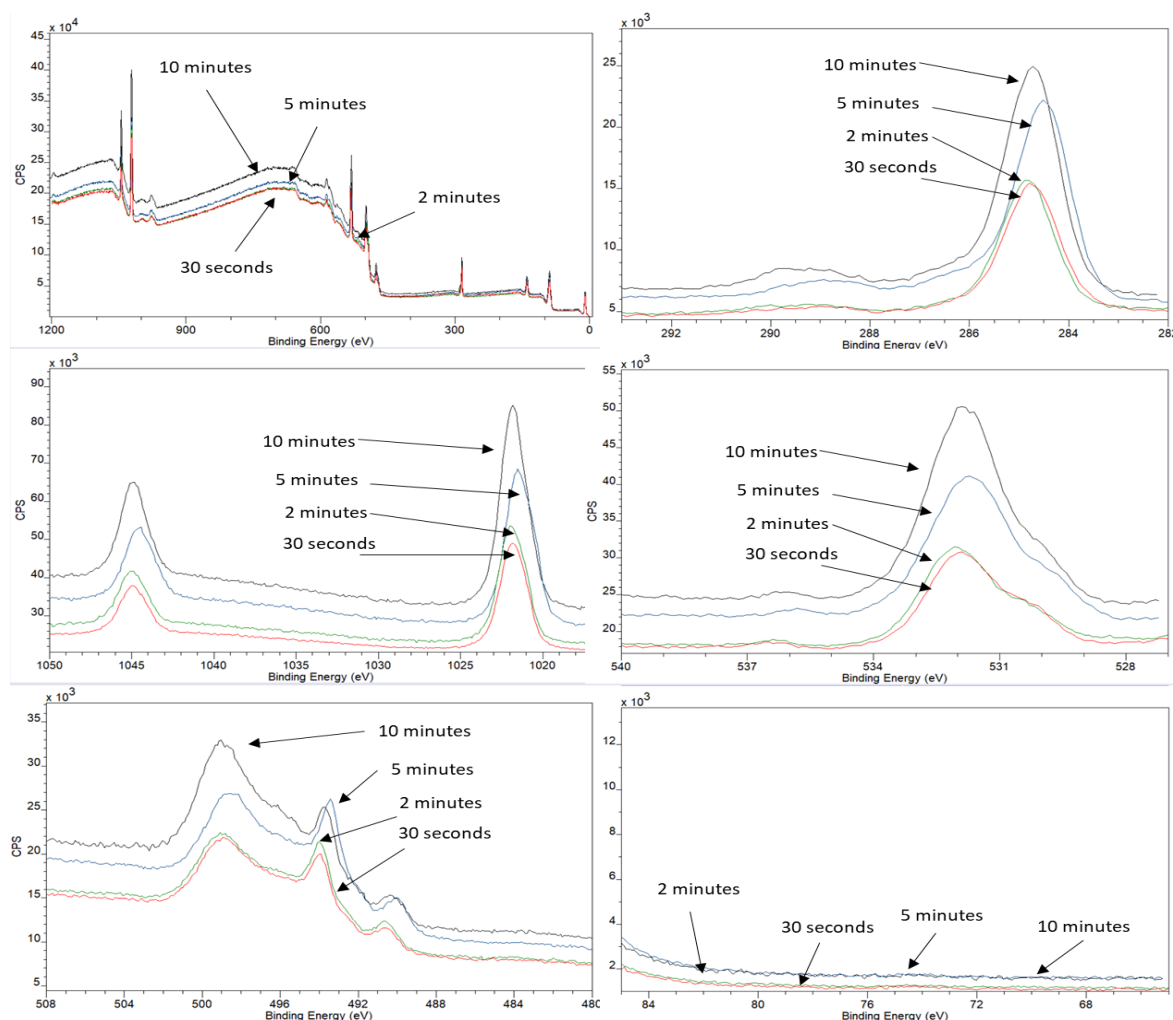
Figure 9.9. X-ray photoelectron spectroscopy analysis of Galvalloy alkaline cleaned at 50°C for varying times. (a) wide spectral analysis (b) carbon analysis; (c) zinc analysis; (d) oxygen analysis; (e) zinc Auger analysis; (f) aluminium analysis
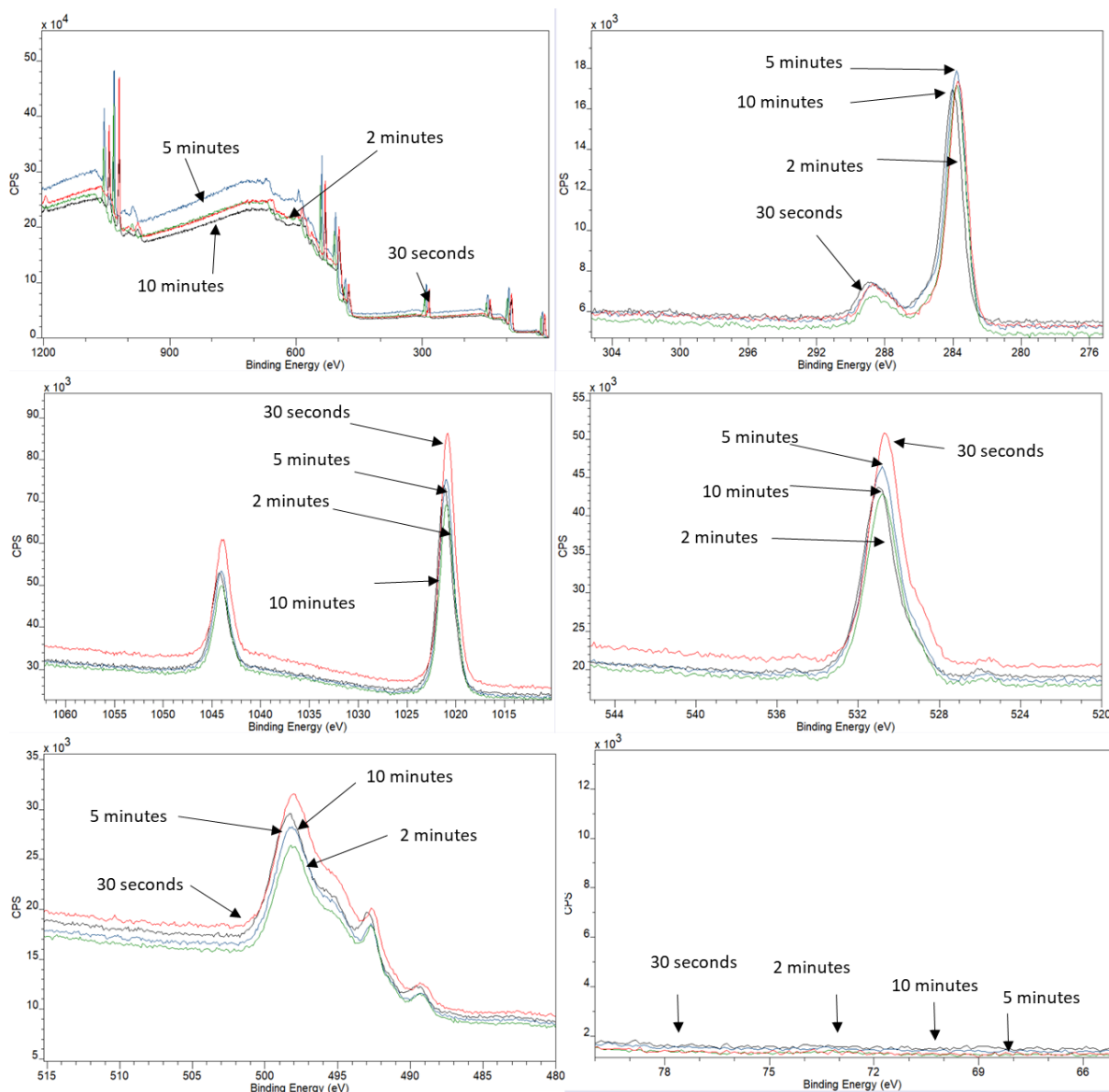
Figure 9.10. X-ray photoelectron spectroscopy analysis of HDG alkaline cleaned at 80°C for varying times. (a) wide spectral analysis (b) carbon analysis; (c) zinc analysis; (d) oxygen analysis; (e) zinc Auger analysis; (f) aluminium analysis
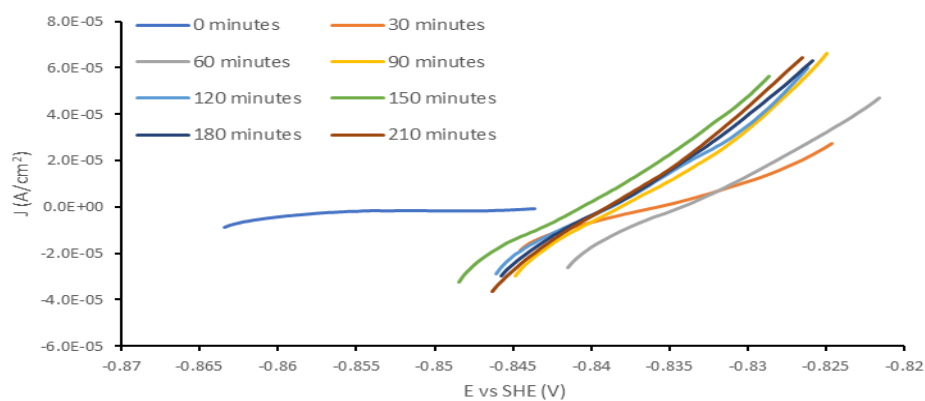
Figure 9.11. Linear Polarisation curve of HDG alkaline cleaned at 50°C for 10 minutes. Polarisation was conducted every 30 minutes for 210 minutes.

Figure 9.12. Linear Polarisation curve of HDG alkaline cleaned at 65°C for 10 minutes. Polarisation was conducted every 30 minutes for 210 minutes.

Figure 9.13. Linear Polarisation curve of HDG alkaline cleaned at 80°C for 10 minutes. Polarisation was conducted every 30 minutes for 210 minutes.
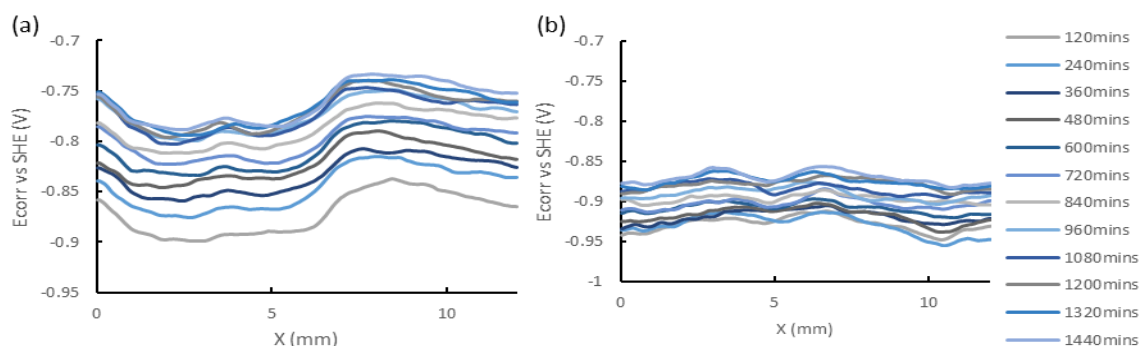
Figure 9.14. A graph showing the time dependent E$_{corr}$ measurements against distance from defect (X) for 50°C, 10 minutes alkaline cleaned surface with PVB coating from a Galvalloy sample. Ecorr measurements were taken every hour for 24 hours, with measurements shown every 2 hours.

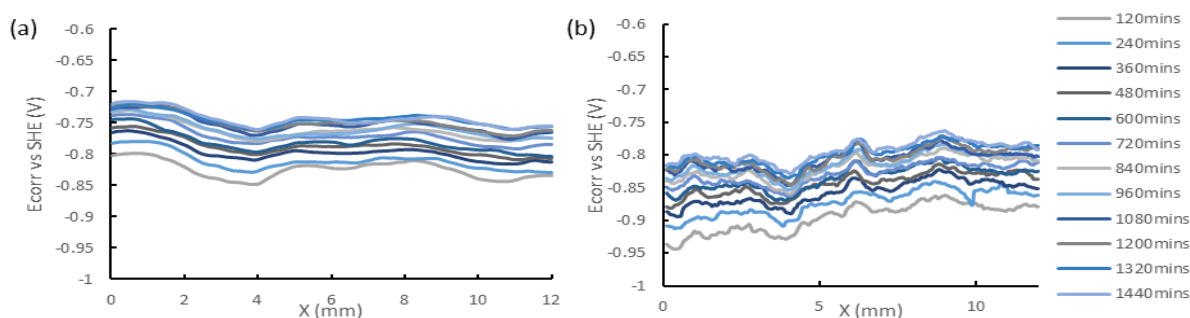*Figure 9.15. A graph showing the time dependent E$_{corr}$ measurements against distance from defect (X) for 65°C, 10 minutes alkaline cleaned surface with PVB coating from a Galvalloy sample. Ecorr measurements were taken every hour for 24 hours, with measurements shown every 2 hours*
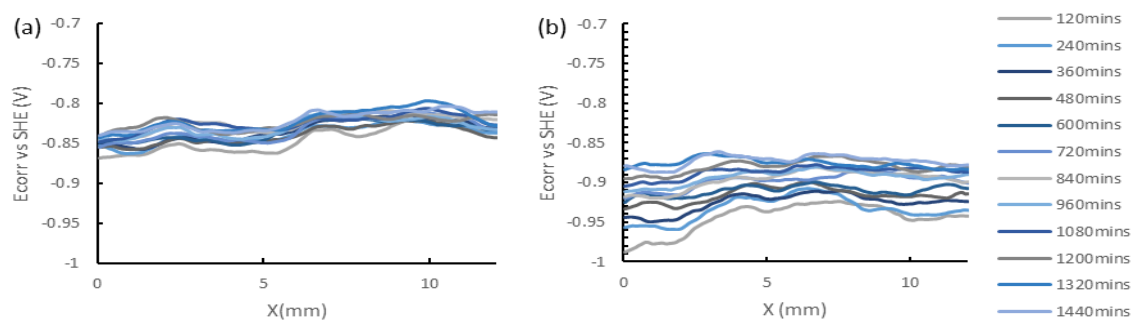

Figure 9.16. A graph showing the time dependent E$_{corr}$ measurements against distance from defect (X) for 80°C, 10 minutes alkaline cleaned surface with PVB coating from a Galvalloy sample. Ecorr measurements were taken every hour for 24 hours, with measurements shown every 2 hour.
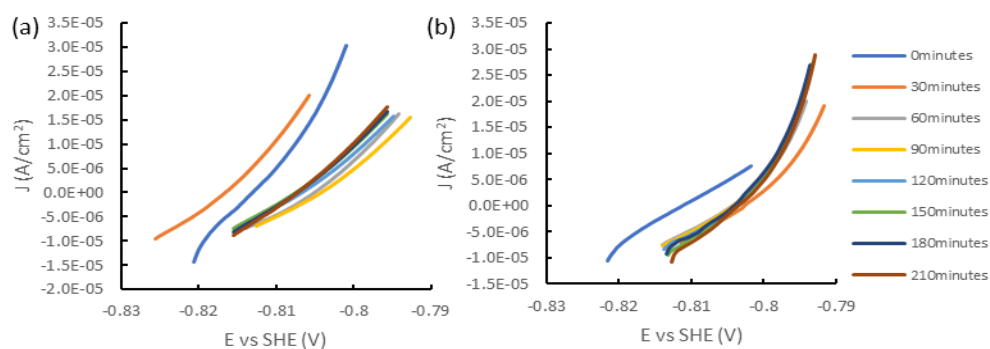
Figure 9.17. Linear Polarisation curve of HDG alkaline cleaned at; (a) 50°C for 30 seconds with low Ti-Wt coating; (b) 50 °C for 30 seconds with high Ti-Wt coating. Polarisation was conducted every 30 minutes for 210 minutes.
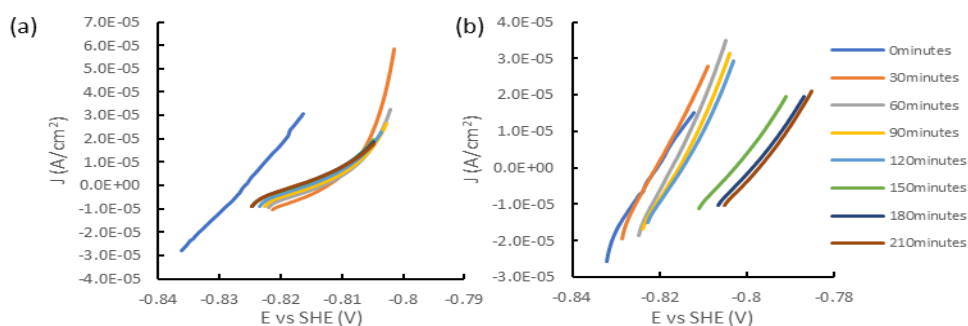
Figure 9.18. Linear Polarisation curve of HDG alkaline cleaned at; (a) 50°C for 10 minutes with low Ti-Wt coating; (b) 50°C for 10 minutes with high Ti-Wt coating. Polarisation was conducted every 30 minutes for 210 minutes.
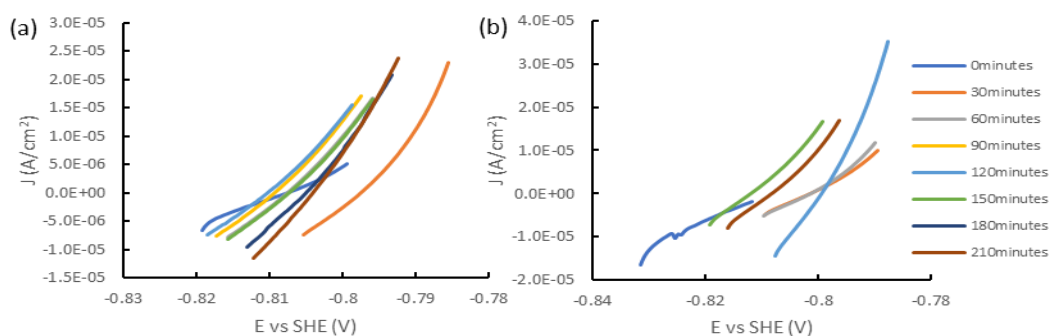
Figure 9.19. Linear Polarisation curve of HDG alkaline cleaned at; (a) 80°C for 30 seconds with low Ti-Wt coating; (b) 80°C for 30 seconds with high Ti-Wt coating. Polarisation was conducted every 30 minutes for 210 minutes.
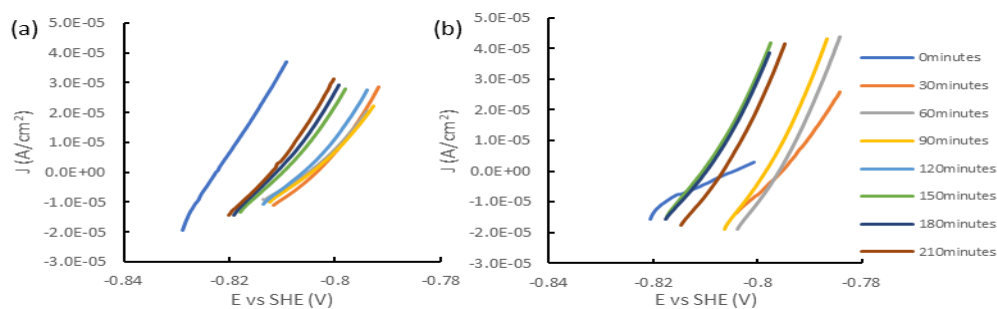
Figure 9.20. Linear Polarisation curve of HDG alkaline cleaned at 80°C for; (a) 10 minutes with low Ti-Wt coating; (b) 80°C for 10 minutes with high Ti-Wt coating. Polarisation was conducted every 30 minutes for 210 minutes
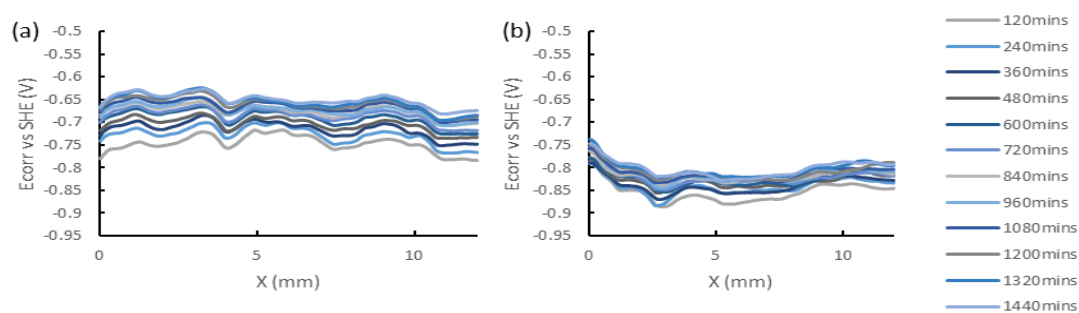

Figure 9.21. Graphs showing the time dependent E_{corr} measurements against distance from defect (X) for: (a) 50 °C, 30 seconds alkaline cleaned surface with 1 wipe of HFT and PVB coating from a HDG sample and; (b) 50 °C, 30 seconds alkaline cleaned surface with 10 wipes of HFT and PVB coating from a HDG sample. E_{corr} measurements were taken every hour for 24 hours and displayed every 2 hours .


Figure 9.22. A graph showing the time dependent E_{corr} measurements against distance from defect (X) for (a) 50°C, 10 minutes alkaline cleaned surface with 1 wipe of HFT and PVB coating from a HDG sample and; (b) 50°C, 10 minutes alkaline cleaned surface with 10 wipes of HFT and PVB coating

from a HDG sample. Ecorr measurements were taken every hour for 24 hours and displayed every 2 hours .

Figure 9.23. A graph showing the time dependent E_{corr} measurements against distance from defect (X) for: (a) 80°C, 30 seconds alkaline cleaned surface with 1 wipe of HFT and PVB coating from a HDG sample and; (b) 80°C, 30 seconds alkaline cleaned surface with 10 wipes of HFT and PVB coating from a HDG sample. E_{corr} measurements were taken every hour for 24 hours and displayed every 2 hours

Figure 9.24. A graph showing the time dependent E_{corr} measurements against distance from defect (X) for: (a) 80°C, 10 minutes alkaline cleaned surface with 1 wipe of HFT and PVB coating from a HDG sample and; (b) 80°C, 10 minutes alkaline cleaned surface with 10 wipes of HFT and PVB coating from a HDG sample. E_{corr} measurements were taken every hour for 24 hours and displayed every 2 hours.
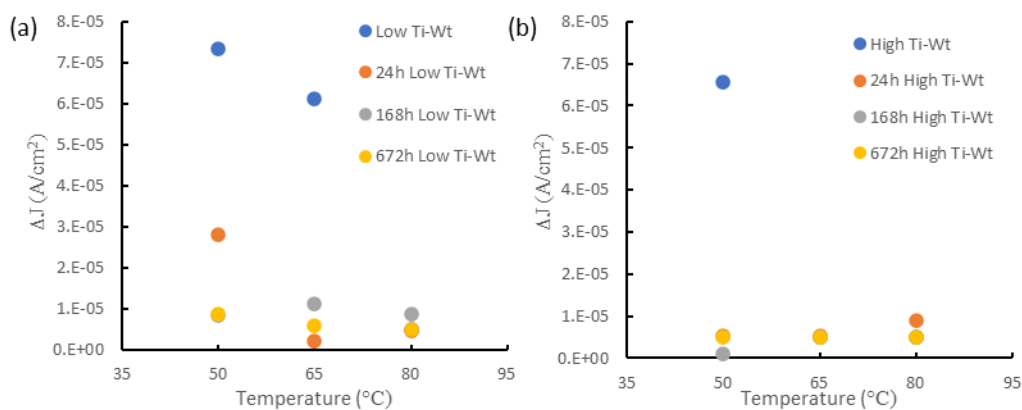
Figure 9.25. Measured current density when sample is cathodically polarised.
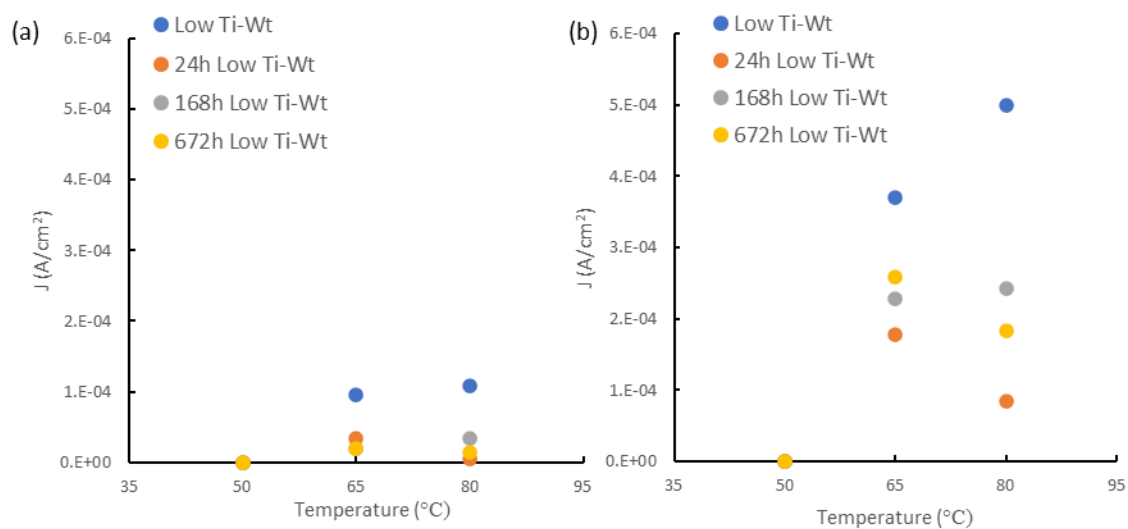
Figure 9.26. Low Ti-Wt (a)-0.9V measured current; (b) -1.2V measured current
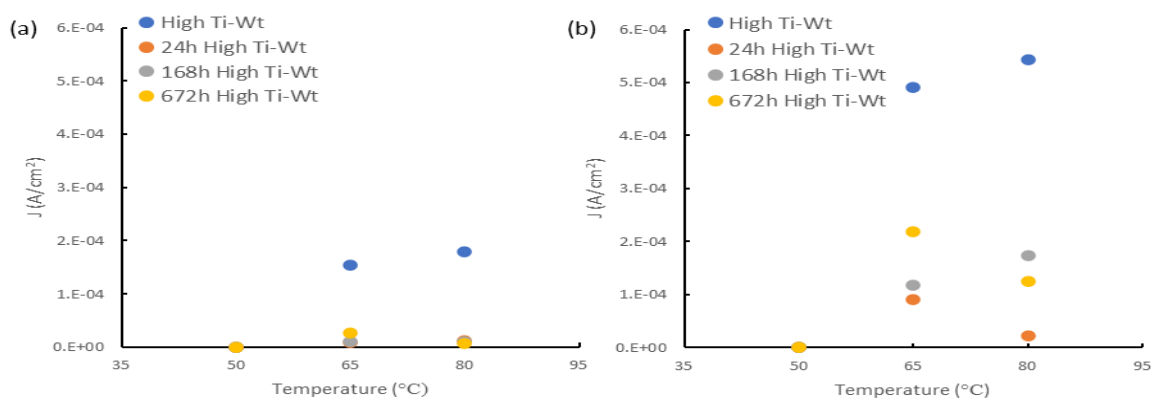
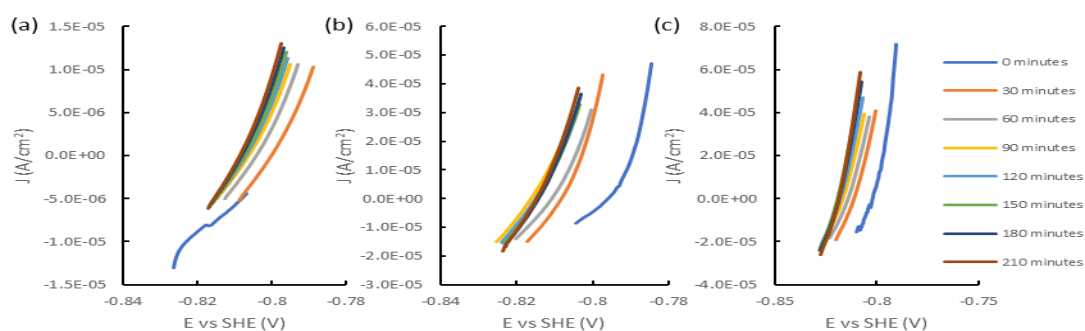*Figure 9.27. High Ti-Wt (a) -0.9V measured current; (b)-1.2V measured current*
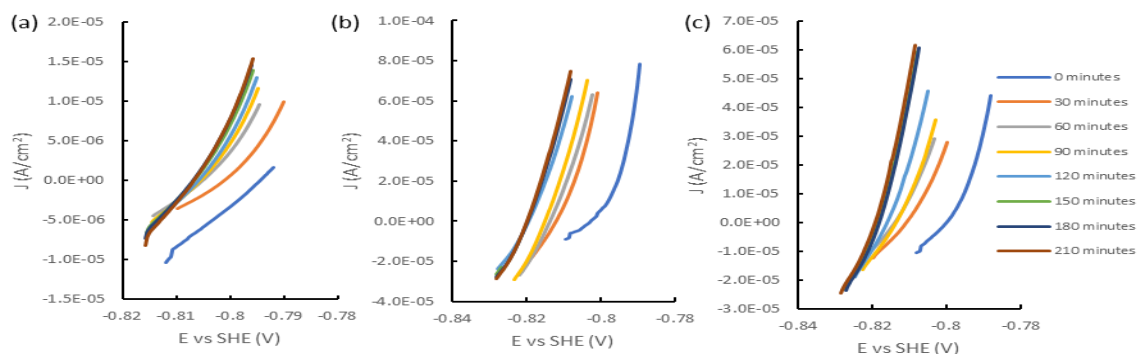
Figure 9.28. Linear Polarisation curved of HDG alkaline cleaned at; (a) 50°C for 30 seconds with one HFT application aged for 24 hours: (b)50°C for 30 seconds with one HFT application aged for 168 hours; (c) 50°C for 30 seconds with one HFT application aged for 672 hours.
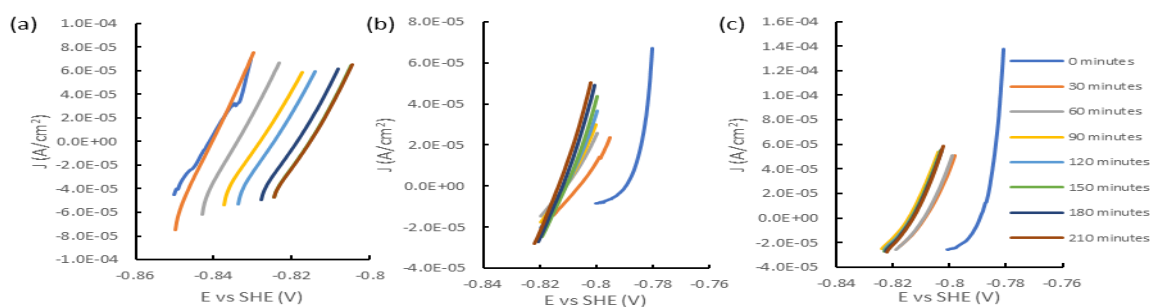

Figure 9.29. Linear Polarisation curved of HDG alkaline cleaned at; (a) 50°C for 30 seconds with ten HFT applications aged for 24 hours; (b) 50°C for 30 seconds with ten HFT applications aged for 168 hours; (c) 50°C for 30 seconds with ten HFT applications aged for 672 hours.
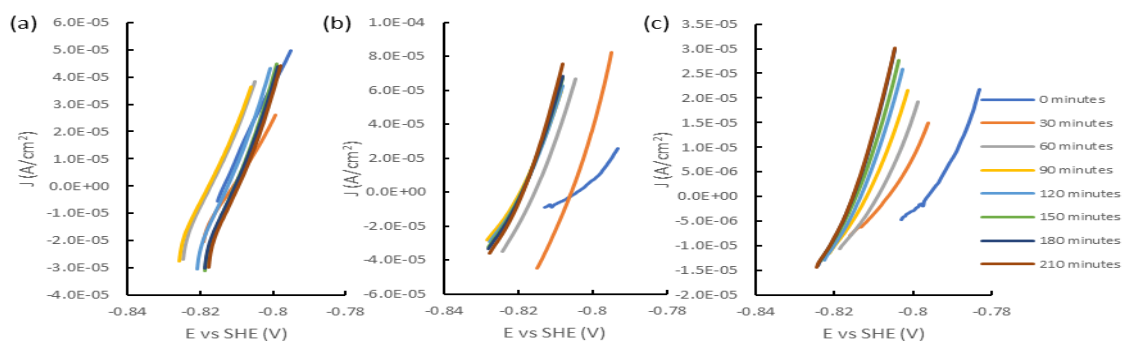
Figure 9.30. Linear Polarisation curved of HDG alkaline cleaned at; (a) 65°C for 30 seconds with ten HFT applications aged for 24 hours; (b) 65°C for 30 seconds with ten HFT applications aged for 168 hours; (c) 65°C for 30 seconds with ten HFF applications aged for 672 hours.
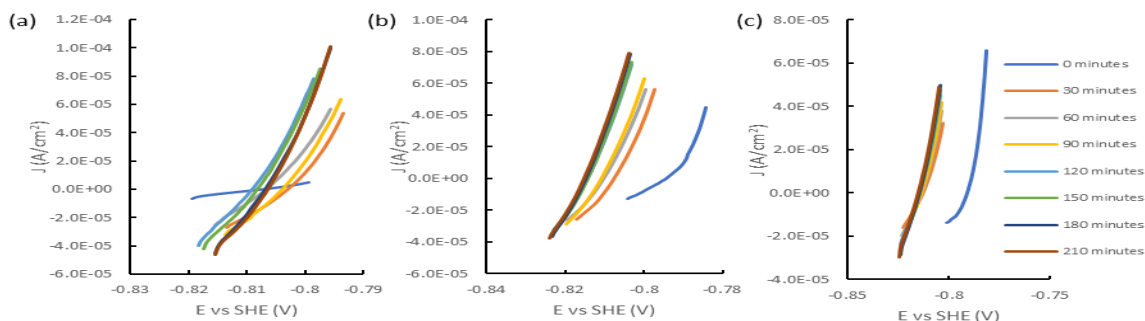
Figure 9.31. Linear Polarisation curved of HDG alkaline cleaned at; (a) 80°C for 30 seconds with one HFT application aged for 24 hours; (b) 80°C for 30 seconds with one HFT application aged for 168 hours; (c) 80°C for 30 seconds with one HFT application aged for 672 hours.

Figure 9.32. Linear Polarisation curved of HDG alkaline cleaned at; (a) 80°C for 30 seconds with ten HFT applications aged for 24 hours; (b) 80°C for 30 seconds with ten HFT applications aged for 168 hours; (c) 80°C for 30 seconds with ten HFT applications aged for 672 hours.
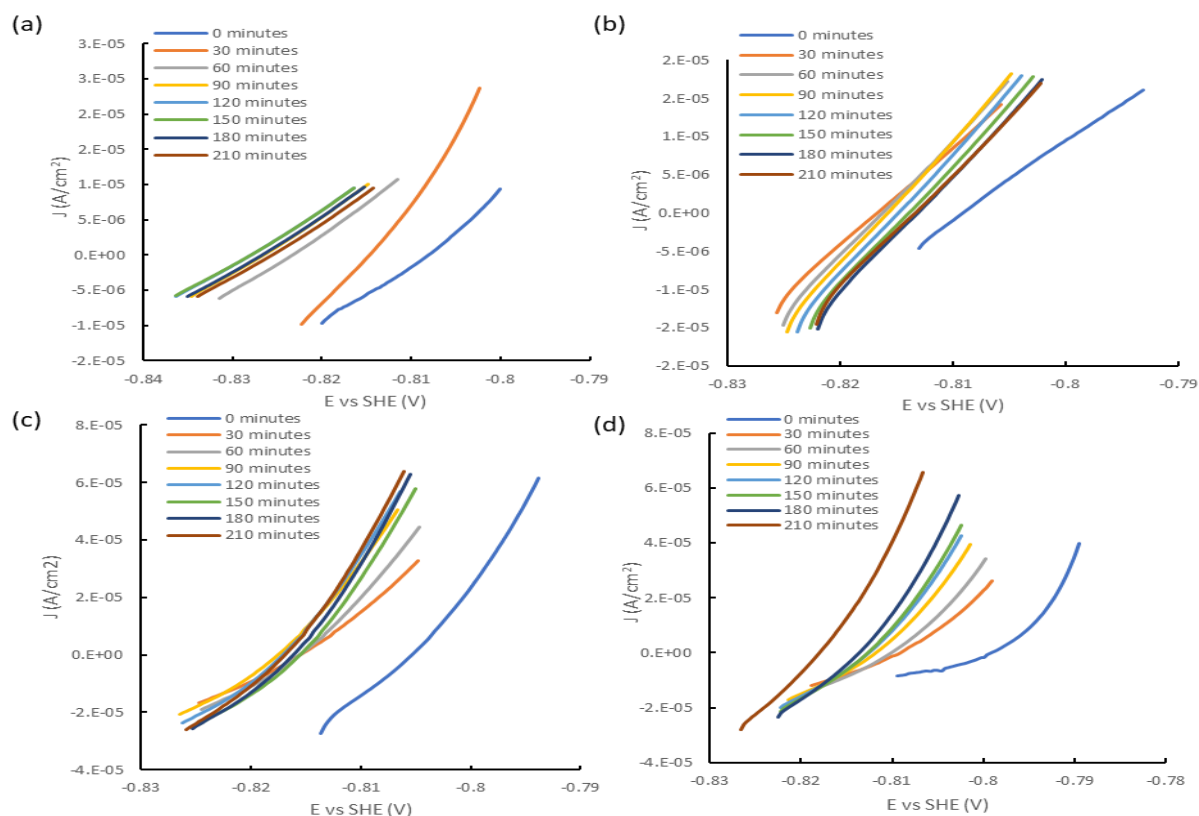
Figure 9.33. Linear Polarisation curved of HDG alkaline cleaned at 65 °C for 30 seconds with one aged HFT application: (a) Unaged; (b) 24 hours aged; (c) 168 hours aged; (d) 672 hours aged. Polarisation was conducted every 30 minutes for 210 minutes.
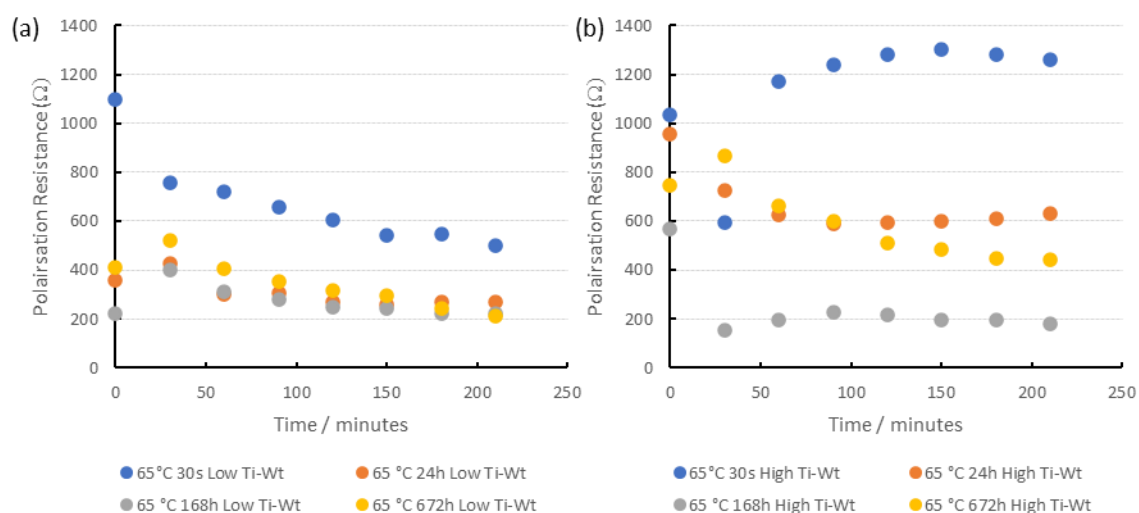
Table 9.3 Polarisation resistance of 24 hour aged HFT applied on HDG alkaline cleaned for 30 seconds at varying temperatures.

Time (minutes)	24h Low Ti-Wt (Ω)	24h High Ti-Wt (Ω)	168h Low Ti-Wt (Ω)	168h High Ti-Wt (Ω)	672h Low Ti-Wt (Ω)	672h High Ti-Wt (Ω)
0	358	953	222	566	410	744
30	423	728	402	155	520	867
60	302	623	312	194	406	660
90	308	586	278	224	350	599
120	268	591	246	215	316	509
150	260	602	240	197	292	483
180	267	609	223	194	244	449
210	267	631	220	177	212	444
Average	307	665	268	240	344	594

Figure 9.34. Polarisation resistance of 168 hour aged HFT applied on HDG alkaline cleaned for 30 seconds at varying temperatures

Table 9.4. Tafel coefficients, I_{corr} and corrosion rate values for alkaline cleaned HDG steel with HFT coating applied.

Sample	Bc (V/decade)	Ba (V/decade)	I_{corr} (A/cm^2)	CR (μm/year)
65°C 30s Low Ti-Wt	0.0026	0.2345	1.64×10^{-6}	24.67
65°C 30s Low Ti-Wt 24h	0.004	0.1373	5.41×10^{-6}	82.33
65°C 30s Low Ti-Wt 168h	0.0011	0.1937	1.76×10^{-6}	26.51
65°C 30s Low Ti-Wt 672h	0.007	0.3087	8.63×10^{-6}	129.42
65°C 30s High Ti-Wt	0.0022	0.1879	8.23×10^{-7}	12.35
65°C 30s High Ti-Wt 24h	0.00002	0.1508	1.30×10^{-6}	0.19
65°C 30s High Ti-Wt 168h	0.0006	0.2352	1.07×10^{-6}	16.16
65°C 30s High Ti-Wt 672h	0.0005	0.1839	3.63×10^{-7}	5.45
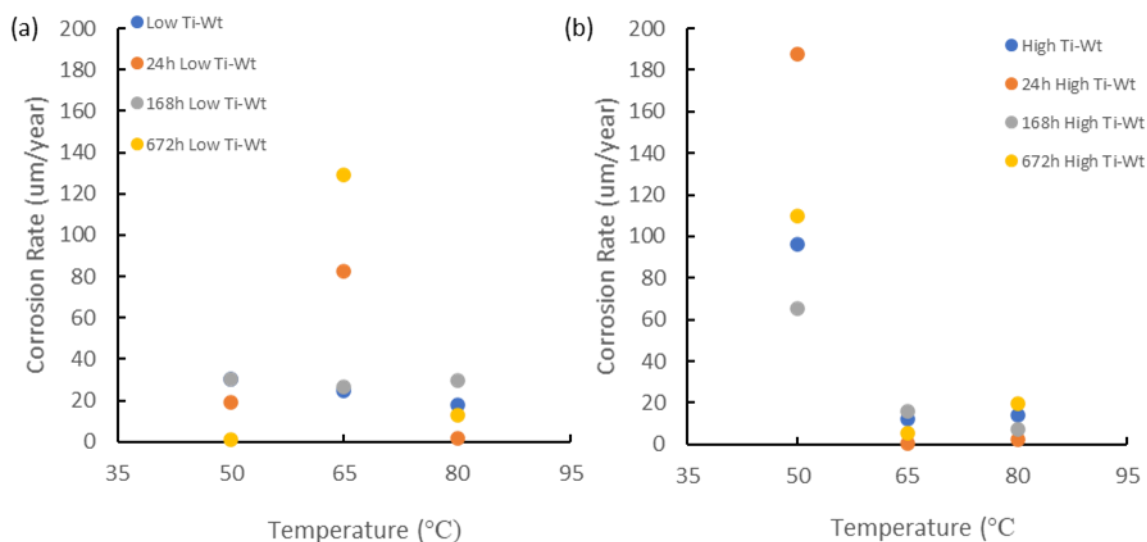
Figure 9.35. Corrosion rate of aged and unaged HFT coated HDG steel. (a) Low Ti-Wt; (b) High Ti-Wt.
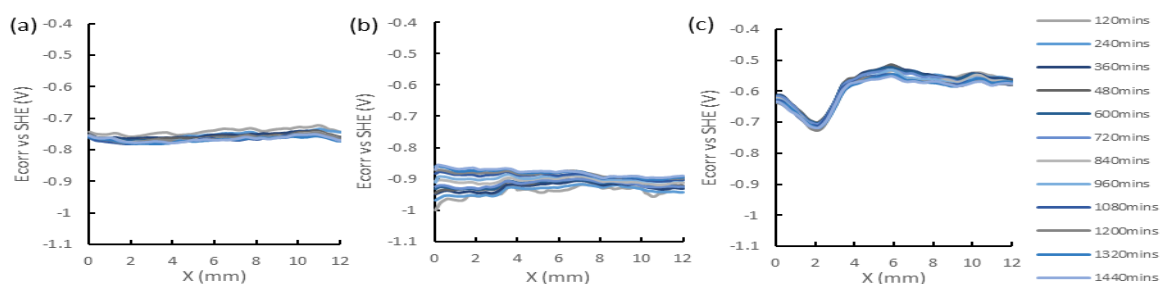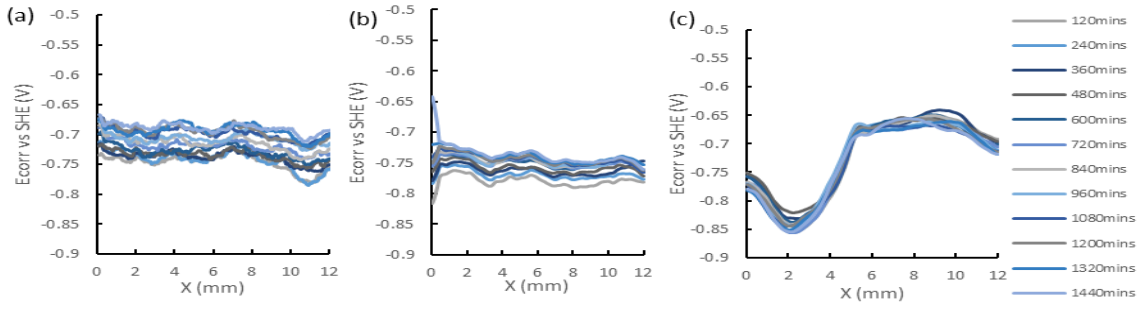

Figure 9.36. A graph showing the time dependent E_{corr} measurements against distance from defect (X) for: (a) 50°C, 30 second alkaline cleaned surface with 1 wipe of HFT aged for 24 hours; (b) 50°C, 30 second alkaline cleaned surface with 1 wipe of HFT aged for 168 hours; (c) 50°C, 30 second alkaline cleaned surface with 1 wipe of HFT aged for 672 hours. Ecorr measurements were taken every hour for 24 hours and displayed every two hours.

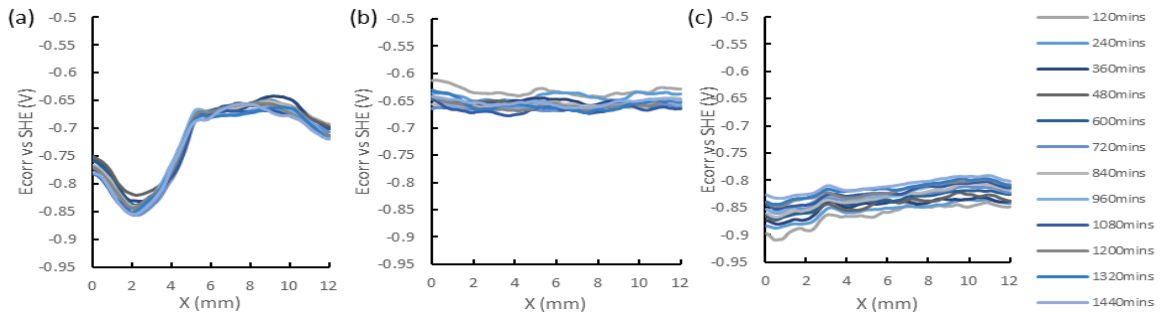*Figure 9.37. A graph showing the time dependent E*_{corr}* measurements against distance from defect (X) for: (a) 50°C, 30 second alkaline cleaned surface with 10 wipes of HFT aged for 24 hours; (b) 50°C, 30 second alkaline cleaned surface with 10 wipes of HFT aged for 168 hours; (c)50°C, 30 second alkaline cleaned surface with 10 wipes of HFT aged for 672 hours. Ecorr measurements were taken every hour for 24 hours and displayed every two hours.*
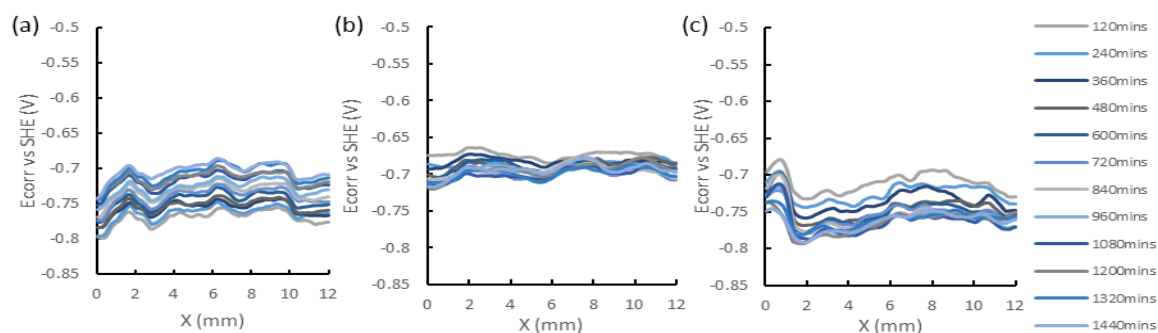

*Figure 9.38. A graph showing the time dependent E*_{corr}* measurements against distance from defect (X) for:(a) 65°C, 30 second alkaline cleaned surface with 10 wipes of HFT aged for 24 hours; (b) 65°C, 30 second alkaline cleaned surface with 10 wipes of HFT aged for 168 hours; (c) 65°C, 30 second alkaline cleaned surface with 10 wipes of HFT aged for 672 hours. Ecorr measurements were taken every hour for 24 hours and displayed every two hours*
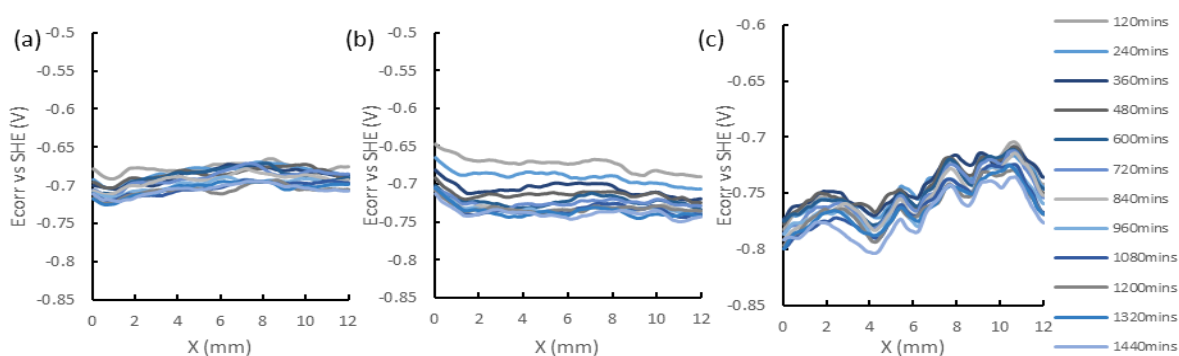
Figure 9.39. A graph showing the time dependent E$_{corr}$ measurements against distance from defect (X) for;(a) 80°C, 30 second alkaline cleaned surface with 1 wipe of HFT aged for 24 hours; (b) 80°C, 30 second alkaline cleaned surface with 1 wipe of HFT aged for 168 hours; (c) 80°C, 30 second alkaline cleaned surface with 1 wipe of HFT aged for 672 hours. Ecorr measurements were taken every hour for 24 hours and displayed every two hours.

Figure 9.40. A graph showing the time dependent E$_{corr}$ measurements against distance from defect (X) for; (a) 80°C, 30 second alkaline cleaned surface with 10 wipes of HFT aged for 24 hours; (b) 80°C, 30 second alkaline cleaned surface with 10 wipes of HFT aged for 168 hours; (c) 80°C, 30 second alkaline cleaned surface with 10 wipes of HFT aged for 672 hours. Ecorr measurements were taken every hour for 24 hours and displayed every two hours.
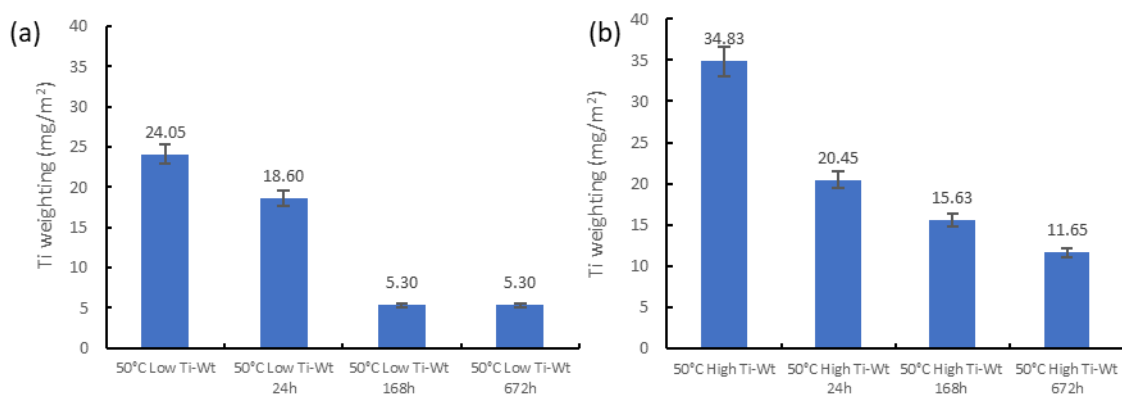
Figure 9.41 Comparison of Ti-weighting when cleaned at 50°C for 30 seconds a varying ageing times: (a) Low Ti-Wt; (b) High Ti-Wt
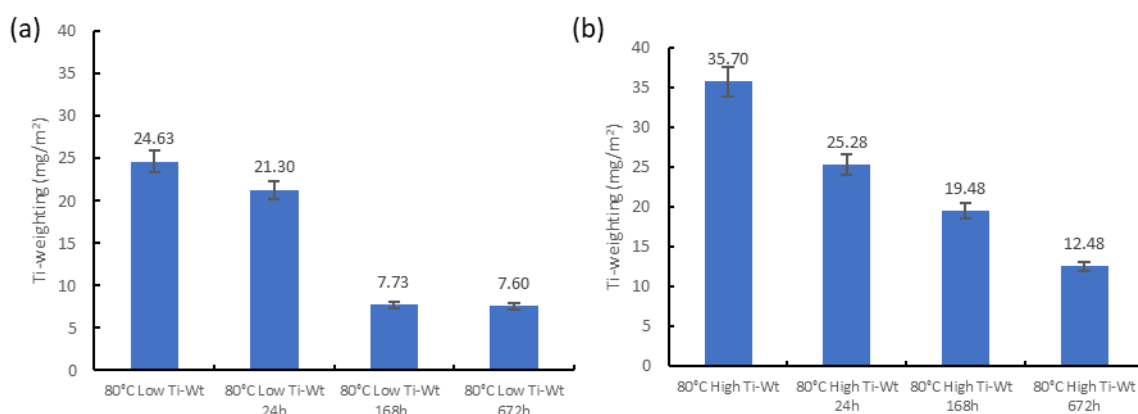

Figure 9.42. Comparison of Ti-weighting when cleaned at 80°C for 30 seconds a varying ageing times: (a) Low Ti-Wt; (b) High Ti-Wt
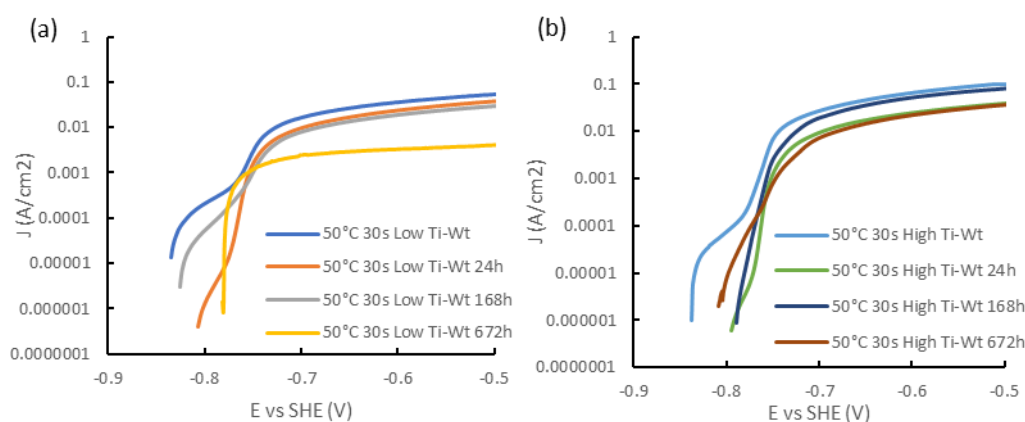

Figure 9.43. Anodic polarisation curve of HDG with HFT applied aged for 24 hours in 5wt.% NaCl solution
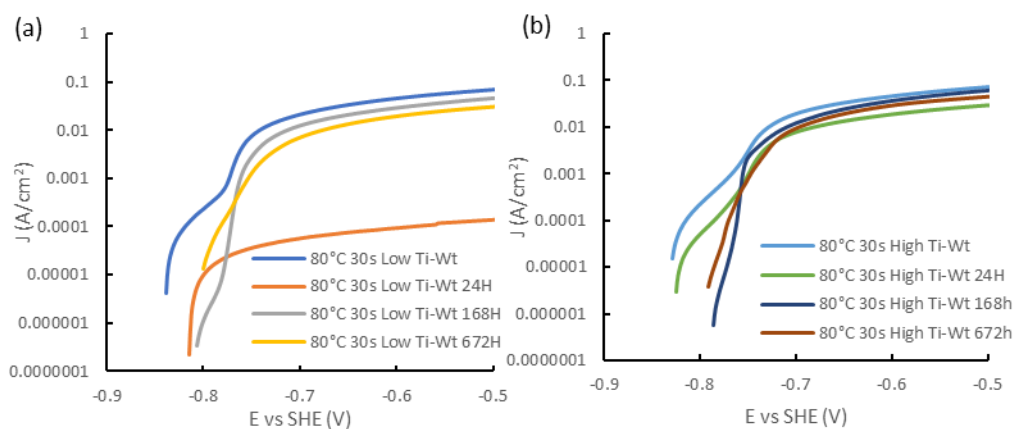
Figure 9.44. Anodic polarisation curve of HDG with HFT applied aged for 672 hours in 5wt.% NaCl solution
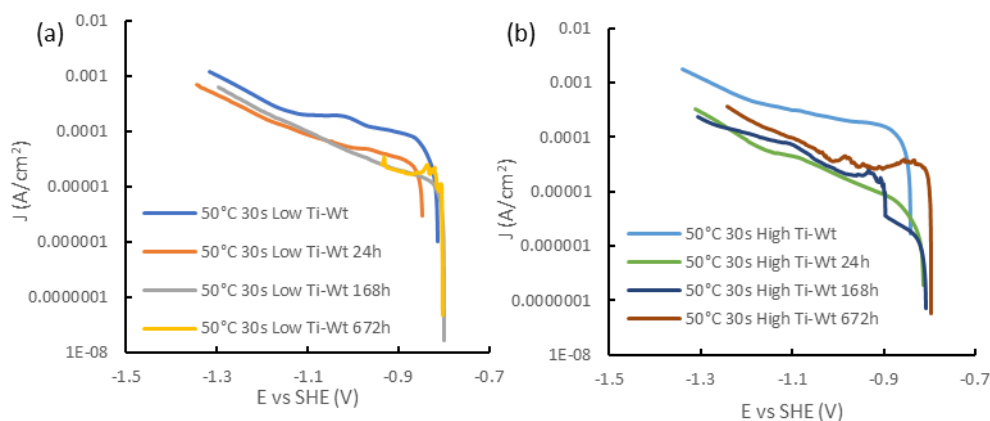

Figure 9.45. Cathodic polarisation curve of HDG with HFT applied aged for 24 hours in 5wt.% NaCl solution.
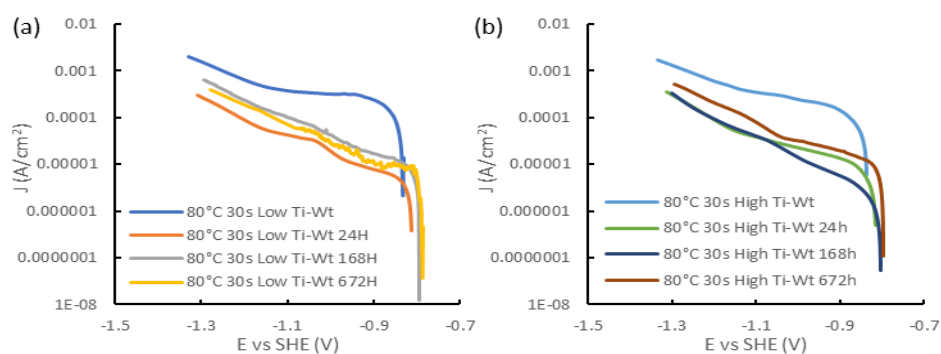

 Figure 9.46. Cathodic polarisation curve of HDG with HFT applied aged for 672 hours in 5wt.% NaCl solution